



**UNIVERSIDADE ESTADUAL DE CAMPINAS**

Faculdade de Engenharia Mecânica

**AMADEUS CAVALCANTI SALVADOR DE ALCÂNTARA**

**A Multiscale Modeling Approach for Bone Tissue  
from the Nanoscale up**

**Uma Abordagem de Modelagem Multiescala para  
Tecidos Ósseos partindo da Nanoescala**

Campinas

2024

AMADEUS CAVALCANTI SALVADOR DE ALCÂNTARA

# **Uma Abordagem de Modelagem Multiescala para Tecidos Ósseos partindo da Nanoescala**

Tese de Doutorado Acadêmico apresentada à Faculdade de Engenharia Mecânica da Universidade Estadual de Campinas como parte dos requisitos exigidos para a obtenção do título de Doutor em Engenharia Mecânica, na Área de Mecânica dos Sólidos e Projeto Mecânico.

Orientador: Prof. Dr. Munir Salomão Skaf

ESTE TRABALHO CORRESPONDE À VERSÃO FINAL DA TESE DE DOUTORADO ACADÊMICO DEFENDIDA PELO ALUNO AMADEUS CAVALCANTI SALVADOR DE ALCÂNTARA, E ORIENTADA PELO PROF. DR. MUNIR SALOMÃO SKAF.

Campinas

2024

Ficha catalográfica  
Universidade Estadual de Campinas  
Biblioteca da Área de Engenharia e Arquitetura  
Rose Meire da Silva - CRB 8/5974

AL16m Alcântara, Amadeus Cavalcanti Salvador de, 1994-  
A multiscale modeling approach for bone tissue from the nanoscale up /  
Amadeus Cavalcanti Salvador de Alcântara. – Campinas, SP : [s.n.], 2024.

Orientador: Munir Salomão Skaf.  
Tese (doutorado) – Universidade Estadual de Campinas, Faculdade de  
Engenharia Mecânica.

1. Fratura óssea. 2. Osteoporose. 3. Colágenos fibrilares. 4. Biocompósito.  
5. Abordagem multiescala. 6. Dinâmica molecular. 7. Propriedades mecânicas.  
I. Skaf, Munir Salomão, 1963-. II. Universidade Estadual de Campinas.  
Faculdade de Engenharia Mecânica. III. Título.

### Informações Complementares

**Título em outro idioma:** Uma abordagem de modelagem multiescala para tecidos ósseos partindo da nanoescala

**Palavras-chave em inglês:**

Bone fracture

Osteoporosis

Collagen fibrils

Biocomposite

Multiscale approach

Molecular dynamics

Mechanical properties

**Área de concentração:** Mecânica dos Sólidos e Projeto Mecânico

**Titulação:** Doutor em Engenharia Mecânica

**Banca examinadora:**

Munir Salomão Skaf [Orientador]

Marco Lúcio Bittencourt

Vitor Rafael Coluci

Mario Milazzo

Markus Jochen Buehler

**Data de defesa:** 08-03-2024

**Programa de Pós-Graduação:** Engenharia Mecânica

**Identificação e informações acadêmicas do(a) aluno(a)**

- ORCID do autor: <https://orcid.org/0000-0003-4493-0827>

- Currículo Lattes do autor: <http://lattes.cnpq.br/4286810579460176>

**UNIVERSIDADE ESTADUAL DE CAMPINAS  
FACULDADE DE ENGENHARIA MECÂNICA**

**TESE DE DOUTORADO ACADÊMICO**

# **A Multiscale Modeling Approach for Bone Tissue from the Nanoscale up**

Autor: Amadeus Cavalcanti Salvador de Alcântara

Orientador: Prof. Dr. Munir Salomão Skaf

A Banca Examinadora composta pelos membros abaixo aprovou esta Tese de Doutorado Acadêmico:

**Prof. Dr. Munir Salomão Skaf**  
**DFQ/IQ/UNICAMP**

**Prof. Dr. Marco Lúcio Bittencourt**  
**DMC/FEM/UNICAMP**

**Prof. Dr. Vitor Rafael Coluci**  
**FT/UNICAMP**

**Prof. Dr. Mario Milazzo**  
**DICI/UNIFI**

**Prof. Dr. Markus Jochen Buehler**  
**CEE/MIT**

A Ata de Defesa com as respectivas assinaturas dos membros encontra-se no SIGA/Sistema de Fluxo de Dissertação/Tese e na Secretaria do Programa da Unidade.

Campinas, 8 de Março de 2024

## ACKNOWLEDGEMENTS

There are many people whom I want (and should!) thank, so I'll have to limit myself to the most significant ones, who have been closest and for the longest time over these almost seven years. Here, I am taking the liberty to write also in Portuguese.

Aos Professores:

Meu agradecimento especial vai para o Prof. Paulo Sollero, com quem iniciei meu Mestrado, e meu Doutorado Direto após aplicarmos para a bolsa FAPESP. O Prof. Sollero foi meu orientador durante grande parte da minha pós-graduação. Por questões pessoais e de saúde, ele precisou interromper minha orientação, tendo o Munir, nesse tempo meu co-orientador, assumido minha orientação.

Caro Sollero, obrigado por tudo! Pela oportunidade de vir para Unicamp, pela confiança, conversas, e puxadas de orelha. Sei o quanto o trabalho com osteoporose era importante para você. Te desejo muita saúde, e sobretudo força! Forte abraço!

Caro Munir, desde nossa primeira reunião, quando você iniciou minha co-orientação, fiquei encantado com a fluidez de nossa conversa e como você já então me explicava conceitos da dinâmica molecular e modelagem atomística. Sou muito grato por você ter aceitado assumir a minha orientação. Obrigado por todo ensino, suporte, atenção e confiança até aqui. É um prazer e alegria trabalhar com você.

Dear Markus, thank you not only for hosting me at LAMM/MIT, but for being so kind and welcoming. The depth of experiences, both personal and professional, I've gathered is truly invaluable.

Thanks also to all professors/lecturers/teaching staff who collaborated with us at some point, taught courses I've taken, or participated in one of the two committees. I've learned valuable lessons from each of you.

Aos familiares:

Pai e mãe, vocês sempre me motivaram e me encorajaram a ser o que eu queria ser. Talvez eu ainda não tenha descoberto o que quero, mas sei que posso ser o que eu quiser. Obrigado pelo carinho, amor e suporte de sempre.

Minha irmãs, obrigado pelo carinho de sempre. Mari, você em especial, sua dedicação a música, aquilo que ama, é uma grande fonte de inspiração.

Aos amigos, colaboradores, group members, and labmates:

Querido Israel, sem você talvez nada disso tivesse acontecido. Foi você quem me convenceu a vir fazer o mestrado na Unicamp e com quem passei madrugadas na FEM, escrevendo e quebrando cabeça discutindo sobre mecânica do contínuo, osso, e sobre como reescrever cada frase, sem pressa, até ela ficar clara. Você também me motivava a continuar quando quis desistir de tentar o doutorado. Sua contribuição na escrita do projeto e no paper de revisão é inestimável. Aprendi muito com você sobre escrita científica, e a dar valor aos detalhes e a teoria. Você é genial. Obrigado por tudo!

Caio, Carlos e Pedro, o grupo do BEM, vocês, junto também com o Israel, Adyllyson, Jack e Bruno, sempre me motivaram a ser mais analítico, mais 'matemático'. Nossas conversas (sérias e descontraídas) e brincadeiras foram essenciais para balancear descontração e trabalho. É bonito ver o quanto vocês admiram e se interessam por matemática, métodos numéricos e engenharia (afinal, todas andam juntos). Obrigado pela parceria de sempre.

Obrigado a todos com quem em algum momento trabalhei junto ou compartilhei sala no grupo do Sollero, Andrés, Daniel, Lucas, João, e Hugo, e no grupo do Munir, Alberto, Clauber, Carlos, Artur, Lucas, Carol, Eduard, Shabir, Felipe e Jéssica.

Levi, obrigado pela colaboração frutífera e por sempre estar disposto a discutir sobre meus problemas com modelagem e simulação atomística. Aprendi muito sobre LAMMPS com você. LAMM members at MIT, thank you for welcoming me as part of the group. Our insightful discussions and collaborative efforts made me grow as a research. I deeply appreciate the contributions of each lab member, especially those whom I interacted most with, Talia, Bo, Eesha, Sabrina, Yiwen, Wei, Nic, Rachel, Jesse, Zhenze, Michael, Sofia, Irina, Andrew, Bella, Mario, Marcin, and Darsh.

A special thanks also to Rosabelli and Marygrace who made it possible for me to go to MIT.

Agradeço também a todas as pessoas com quem morei e compartilhei meu tempo nesses quase sete anos. Primeiramente a Tangas, a primeira república onde morei. Obrigado a todos pelo companheirismo e parceria de sempre, sobretudo Rafa, Arthur, Eliezer, Mauro, e também o Medina e o Ali.

Gi, obrigado por toda parceria e companheirismo durante nosso tempo juntos. Você, o Leko, e a Laka, me ajudaram a passar por um período complicado, de pandemia e no qual eu estava perdido na pesquisa, com sanidade e alegria.

Aos amigos da música e da Capoeira, que me fazem sempre lembrar que a vida vai além da

universidade. Me manter fisicamente ativo e ter com quem compartilhar minha paixão pela música foi, e é, imprescindível para todo o resto. Prof. Lars, obrigado por me receber no IA como um de seus alunos de violoncelo e membro do Unicamp Cello Ensemble. Arthur e Marina, tocar e viajar com o trio Sabiá foi, e sempre será, motivo de orgulho para mim.

Amigos da quarta do Choro e do Choro em Boston, obrigado por me receberem tão bem nas rodas. Um agradecimento especial a Catherine Bent, Luiz Antônio, e Ricardo Henrique, com quem aprendi e aprendo tanto.

Por fim, agradeço minha namorada, Carol, pelo apoio constante e compreensão durante a elaboração desta tese. Sua presença ao meu lado trouxe uma dose extra de motivação e conforto nessa reta final.

### **Funding**

This study was financed in part by the São Paulo Research Foundation (FAPESP) grants #2018/18503-2, #2022/03410-4, the Center for Computing in Engineering & Sciences (CCES/UNICAMP) FAPESP grant #2013/08293-7, and the Coordenação de Aperfeiçoamento de Pessoal de Nível Superior – Brasil (CAPES) – Finance Code 001.

This work also used resources of the “Centro Nacional de Processamento de Alto Desempenho em São Paulo” (CENAPAD-SP), MIT-Brazil, and workstations kindly provided by Prof. Paulo Sollero and Prof. Munir S. Skaf.

## ABSTRACT

Bones are complex living biomaterials with a multi-scale structure centered on mineralized collagen fibrils. Mutations and structural changes at its molecular scale can lead to microscopic defects and failures that result in macroscopic fractures. For instance, osteoporosis-induced bone fracture is a major health concern not yet fully understood. The improvement of bone fracture prediction and diagnosis currently requires two critical components: a comprehensive understanding of the mechanical behavior of bones at the nanoscale, and an elucidation of the interrelation and impact of these behaviors on higher lengthscales.

This thesis is structured as a compendium of articles. It starts with a review paper that provides a state-of-the-art framework for advancing patient-specific bone multiscale modelling, fracture simulation and risk analysis. Next, the thesis focus on the nanomechanics of bones. Both the modeling of bone molecular models as well as a thorough investigation of their mechanical properties are presented. Our nanoscale investigations highlight the key role of minerals within the extrafibrillar region of mineralized collagen fibrils in bone nanomechanics, serving as primary load-bearing components.

Additionally, this thesis provides a roadmap for devising realistic patient-specific bone fracture simulations which is here presented as a novel approach to the early diagnosis of osteoporosis-induced bone fracture. This approach suggests the combination of macro- and microscopic patient-specific data with atomistic-derived properties for osteoporosis risk analysis. Although not yet fully implemented, the integration presented in this approach represents a significant contribution and novelty in the field, possibly enhancing the precision and comprehensiveness of osteoporosis risk assessment.

By shedding light on the intricate interplay between structural components at the nanoscale and with the presented multiscale approach, our work lays the groundwork for more refined and sensitive bone fracture simulations.

**Keywords:** bone failure; bone fracture; osteoporosis; patient-specific bone models; bone multiscale structure; bone multiscale modelling; fracture risk analysis; mineralized collagen fibrils; molecular dynamics;

## RESUMO

Os ossos são biomateriais vivos complexos com uma estrutura multiescala centrada em fibrilas de colágeno mineralizadas. Mutações e alterações estruturais em sua escala molecular podem levar a defeitos e falhas microscópicas que resultam em fraturas macroscópicas. Por exemplo, a fratura óssea induzida por osteoporose é um grande problema de saúde ainda não totalmente compreendida. A melhoria da predição e diagnóstico de fraturas ósseas atualmente requer dois componentes críticos: uma compreensão abrangente do comportamento mecânico dos ossos na escala nanométrica e um esclarecimento da inter-relação e impacto desses comportamentos em escalas de comprimento maiores.

Esta tese é estruturada como um compêndio de artigos. Ela começa com um artigo de revisão que apresenta o estado da arte e fornece um arcabouço para o avanço da modelagem multiescala de ossos, simulação de fraturas e análise de riscos específicas do paciente. Em seguida, a tese se concentra na nanomecânica dos ossos. Tanto a modelagem de modelos moleculares de ossos quanto uma investigação minuciosa de suas propriedades mecânicas são apresentadas. Nossas investigações em nanoscala destacam o papel fundamental dos minerais na região extrafibrilar de fibrilas de colágeno mineralizadas na nanomecânica óssea, servindo como componentes primários de suporte de carga.

Além disso, esta tese fornece um roteiro para a elaboração de simulações realistas de fraturas ósseas específicas do paciente, que aqui é apresentada como uma abordagem inovadora para o diagnóstico precoce de fraturas ósseas induzidas por osteoporose. Esta abordagem sugere a combinação de dados específicos do paciente em macro- e microescala com propriedades derivadas atomisticamente para análise de risco de osteoporose. Embora ainda não totalmente implementada, a integração apresentada nesta abordagem representa uma contribuição significativa e uma novidade no campo, possivelmente aprimorando a precisão e a compreensão da avaliação de risco de osteoporose.

Ao lançar luz sobre a intrincada interação entre componentes estruturais na escala nanométrica e com a abordagem multi-escalar apresentada, nosso trabalho estabelece bases para simulações de fraturas ósseas mais refinadas e sensíveis.

**Palavras-chave:** falha óssea; fratura óssea; osteoporose; modelos de ossos específicos do paciente; estrutura multiescala do osso; modelagem multiescala do osso; análise do risco de fratura; fibrilas de colágeno mineralizada; dinâmica molecular;

# CONTENTS

|          |   |            |
|----------|---|------------|
| <b>1</b> | <b>Introduction and Motivation</b>  | <b>11</b>  |
| <b>2</b> | <b>State-of-the-Art Bone Multiscale Modeling</b>  | <b>13</b>  |
| <b>3</b> | <b>Devising Bone Molecular Models at the Nanoscale</b>  | <b>79</b>  |
| <b>4</b> | <b>Investigating Mechanical Properties of Bone Molecular Models</b>   | <b>107</b> |
| <b>5</b> | <b>A Road Map for Future Research on Bone Multiscale Modeling</b>   | <b>125</b> |
| 5.1      | An Approach to the early Diagnosis and Prediction of Fracture in Bones  | 125        |
| 5.1.1    | Step I – Defining macro domain geometry and mechanical properties from medical imaging and imposing realistic BCs | 126        |
| 5.1.2    | Step II – Macroscale: Computing the traction and displacement fields  | 128        |
| 5.1.3    | Step III – Transitioning from the macro- to the microscale  | 130        |
| 5.1.4    | Step IV – Determining micro domain BCs  | 133        |
| 5.1.5    | Step V – Transitioning from the micro to the molecular scale: Modeling the bone cracking process                  | 134        |
| 5.1.6    | Step VI – Computing the TSL through an MD approach  | 136        |
| 5.1.7    | Step VII – Transitioning from the molecular to the microscale   | 138        |
| 5.1.8    | Step VIII – Transitioning from the micro- to the macroscale   | 139        |
| 5.1.9    | Step IX – Towards an osteoporosis diagnosis   | 140        |
| 5.2      | Future Directions   | 141        |
| <b>6</b> | <b>Other Works I have been involved with during my PhD</b>  | <b>142</b> |
| 6.1      | 3D Boundary Element Meshing for Multiscale Bone Anisotropic Analysis  | 142        |
| 6.2      | Coarse-Grain Modeling of Polymer Hydrogels  | 142        |
| 6.3      | Mechanical Properties of Plant Cell Walls   | 143        |
|          | <b>Bibliography</b>   | <b>144</b> |

# 1 INTRODUCTION AND MOTIVATION

The worldwide increasing life expectancy leads to the elderly gradually composing a larger fraction of the population. This implies that osteoporosis, a bone disease characterized by low bone mineral density and a consequent increase in fragility fracture risk, will become commonplace. If current predictive diagnosis techniques remain unimproved, osteoporosis-induced fractures will increasingly strain healthcare systems financially and hinder social well-being worldwide. The improvement of bone fracture prediction and diagnosis currently requires two critical components: **(1.)** a comprehensive understanding of the mechanical behavior of bones at the nanoscale, and **(2.)** an elucidation of the interrelation and impact of these behaviors on higher lengthscales.

Bones and tendons are complex living biomaterials with a multiscale structure centered on collagen fibrils. However, in bones, collagen fibrils undergo mineralization and organize into intricate composites at higher length scales. The study of bone mechanics is multidisciplinary and requires laborious investigations, e.g., time-consuming modeling and experiments. It is an open field of research. To fully understand the structure and properties of bones is a challenge that (has and) will demand decades of collaborative research endeavors to be solved, if solvable.

This thesis is motivated by the worldwide necessity and our<sup>1</sup> willingness to contribute to the improvement of **(1.)** and **(2.)**. Structured as a compendium of published scientific articles, it not only sheds light on the intricate interplay between structural components at the nanoscale of bone, but also presents a framework for investigating the interrelation between the multiple length scales of bones.

Chapter 2 presents a review paper that provides a starting point for those interested in an up-to-date literature survey on state-of-the-art patient-specific bone multiscale modelling, fracture simulation and risk analysis ([Alcântara \*et al.\*, 2020](#)). It introduces and discusses topics related to components **(1.)** and **(2.)**, serving as an introductory literature survey chapter. This paper distinguishes itself from any other review paper for not being a simple list of citations. Much more than that, its innovative and straight-to-the-point textual organization and notation points to important remarks, highlights and open issues in the field. This extensive literature

---

<sup>1</sup> In this thesis, 'we' and 'us' refer to collaborators and myself. I'm grateful for their support and collaborations during my graduate studies.

survey hints at a framework, at an approach, for devising realistic patient-specific bone fracture simulations. This is later discussed in Chapter 5.

Next, we focus on the nanoscale of bones. Chapter 3 provides a detailed prescription on how to devise and perform molecular dynamics with all-atom bone molecular models that consider both intra- and extrafibrillar mineralization (Alcântara *et al.*, 2022). To our knowledge, it was the first molecular model presented in the literature to take into account this important element of the biology, chemistry, and mechanics of fibers in bones.

Chapter 4, presents a paper in which we investigate structural and mechanical properties of all-atom bone molecular models composed of type-I collagen, hydroxyapatite, and water, by means of fully atomistic molecular dynamics (MD) simulations (Alcântara *et al.*, 2023). We subjected our nanoscale models to tensile loads and analyzed their mechanical responses using LAMMPS (Thompson *et al.*, 2022). An analysis of the stress distribution showed that the extrafibrillar region plays a crucial role in the mechanical response of the bone nanoscale models.

These two papers constitute a novel, and crucial, contribution for the improvement of (1.). They were motivated by the fact that the current literature exhibits limited resources on how to model bone at the nanoscale and on its nanomechanics. Modeling and simulating the nanoscale of bone is laborious and demands high performance computing.

Chapter 5 serves as a road map for future research on patient-specific multiscale modeling. It introduces an approach to improve current prediction of fracture in bones. We aim to contribute to (2.) by sharing this clear and detailed framework.

Finally, Chapter 6 briefly present other works I have been involved with during my PhD.

## **2 STATE-OF-THE-ART BONE MULTISCALE MODELING**

As mentioned earlier, bone is a living complex multiscale material. The interrelations between its different structure requires multidisciplinary understanding that involves biology, medicine, mathematics, physics, and engineering. Given that the literature exhibited only limited resources that could be used as a starting point for those new to the field, we prepared an up-to-date literature survey on state-of-the-art patient-specific bone multiscale modelling, fracture simulation and risk analysis. This literature survey distinguishes itself from most review papers for its innovative and straight-to-the-point textual organization and notation that points to important remarks, highlights and open issues in the field. The review goes from discussing the impact of osteoporosis on health care systems worldwide, to describing multiscale physico-mathematical approaches to model bone using continuum mechanics and molecular dynamics.

This paper makes its contribution to the field by both thoroughly describing each step involved in modeling and simulating bone in a multiscale context, and by revealing paths and frameworks for the improvement of the broad field of bone mechanics. Indeed, this extensive literature survey hints at a framework for devising realistic patient-specific bone fracture simulations, which is discussed in Chapter 5.

Review

# Patient-Specific Bone Multiscale Modelling, Fracture Simulation and Risk Analysis—A Survey

Amadeus C. S. Alcântara <sup>1</sup>, Israel Assis <sup>2</sup>, Daniel Prada <sup>1</sup>, Konrad Mehle <sup>3</sup>, Stefan Schwan <sup>4</sup>,  
Lúcia Costa-Paiva <sup>5</sup>, Munir S. Skaf <sup>6</sup>, Luiz C. Wrobel <sup>7,8</sup> and Paulo Sollero <sup>1,\*</sup>

- <sup>1</sup> Department of Computational Mechanics, School of Mechanical Engineering, University of Campinas—UNICAMP, Campinas, Sao Paulo 13083-860, Brazil; amadeus.alcantara@fem.unicamp.br (A.C.S.A.); daniel.prada@fem.unicamp.br (D.P)
- <sup>2</sup> Department of Integrated Systems, School of Mechanical Engineering, University of Campinas—UNICAMP, Campinas, Sao Paulo 13083-860, Brazil; israel.dynamics@gmail.com
- <sup>3</sup> Department of Engineering and Natural Sciences, University of Applied Sciences Merseburg, 06217 Merseburg, Germany; konrad.mehle@hs-merseburg.de
- <sup>4</sup> Fraunhofer Institute for Microstructure of Materials and Systems IMWS, 06120 Halle/Saale, Germany; stefan.schwan@imws.fraunhofer.de
- <sup>5</sup> Department of Obstetrics and Gynecology, School of Medical Sciences, University of Campinas—UNICAMP, Campinas, Sao Paulo 13083-887, Brazil; paivaepaiva@uol.com.br
- <sup>6</sup> Institute of Chemistry and Center for Computing in Engineering and Sciences, University of Campinas—UNICAMP, Campinas, Sao Paulo 13083-860, Brazil; skaf@unicamp.br
- <sup>7</sup> Institute of Materials and Manufacturing, Brunel University London, Uxbridge UB8 3PH, UK; Luiz.Wrobel@brunel.ac.uk
- <sup>8</sup> Department of Civil and Environmental Engineering, Pontifical Catholic University of Rio de Janeiro, Rio de Janeiro 22451-900, Brazil
- \* Correspondence: sollero@fem.unicamp.br

Received: 13 November 2019; Accepted: 17 December 2019; Published: 24 December 2019



**Abstract:** This paper provides a starting point for researchers and practitioners from biology, medicine, physics and engineering who can benefit from an up-to-date literature survey on patient-specific bone fracture modelling, simulation and risk analysis. This survey hints at a framework for devising realistic patient-specific bone fracture simulations. This paper has 18 sections: Section 1 presents the main interested parties; Section 2 explains the organization of the text; Section 3 motivates further work on patient-specific bone fracture simulation; Section 4 motivates this survey; Section 5 concerns the collection of bibliographical references; Section 6 motivates the physico-mathematical approach to bone fracture; Section 7 presents the modelling of bone as a continuum; Section 8 categorizes the surveyed literature into a continuum mechanics framework; Section 9 concerns the computational modelling of bone geometry; Section 10 concerns the estimation of bone mechanical properties; Section 11 concerns the selection of boundary conditions representative of bone trauma; Section 12 concerns bone fracture simulation; Section 13 presents the multiscale structure of bone; Section 14 concerns the multiscale mathematical modelling of bone; Section 15 concerns the experimental validation of bone fracture simulations; Section 16 concerns bone fracture risk assessment. Lastly, glossaries for symbols, acronyms, and physico-mathematical terms are provided.

**Keywords:** bone fracture; patient-specific bone models; osteoporosis; bone multiscale structure; bone multiscale modelling; fracture risk analysis

## 1. Interested Parties Concerning this Survey

This paper surveys a multidisciplinary topic. Bone is a not fully understood biological material. Professionals from biology and medicine have been working with physicists and engineers to better

understand bone mechanical properties with the goal of anticipating and preventing bone fracture. Bone diseases, specially osteoporosis, have proven to be a major health concern. Governments and philanthropists are putting more effort into minimizing the social and financial consequences of bone fragility fractures. Most fragility fractures are impact-induced fractures occurring in the elderly when performing routine activities. Table 1 shows the main interested parties involved in bone fracture risk analysis and which sections of this paper are most interesting for each party.

**Table 1.** Main interested parties involved in bone fracture and which sections of this paper are most interesting for each party.

| Specialization, Interested | Related Sections  |
|----------------------------|---|
| <b>Biology</b>             | Section 3. Motivating Patient-Specific Bone Fracture Simulation<br>Section 4. Motivating this Literature Survey<br>Section 6. The Physico-Mathematical Approach to Bone Fracture<br>Section 7. Modelling Bone as a Continuum<br>Section 8. Categorizing the Surveyed Literature into a Continuum Mechanics Framework<br>Section 9. Patient-Specific Geometry of Bone<br>Section 10. Mechanical Properties Categorization for Computational Bone Models<br>Section 13. The Multiscale Structure of Bone  |
| <b>Medicine</b>            | Section 3. Motivating Patient-Specific Bone Fracture Simulation<br>Section 4. Motivating this Literature Survey<br>Section 6. The Physico-Mathematical Approach to Bone Fracture<br>Section 7. Modelling Bone as a Continuum<br>Section 8. Categorizing the Surveyed Literature into a Continuum Mechanics Framework<br>Section 9. Patient-Specific Geometry of Bone<br>Section 10. Mechanical Properties Categorization for Computational Bone Models<br>Section 11. Mathematical Model of Bone Trauma-inducing Accident—The Boundary Conditions<br>Section 15. Validating Bone Fracture Simulation<br>Section 16. Assessing Fracture Risk   |
| <b>Physics</b>             | Section 3. Motivating Patient-Specific Bone Fracture Simulation<br>Section 4. Motivating this Literature Survey<br>Section 6. The Physico-Mathematical Approach to Bone Fracture<br>Section 7. Modelling Bone as a Continuum<br>Section 8. Categorizing the Surveyed Literature into a Continuum Mechanics Framework<br>Section 9. Patient-Specific Geometry of Bone<br>Section 10. Mechanical Properties Categorization for Computational Bone Models<br>Section 11. Mathematical Model of Bone Trauma-inducing Accident—The Boundary Conditions<br>Section 12. Simulating Bone Fracture<br>Section 13. The Multiscale Structure of Bone<br>Section 14. Multiscale Modelling of Bone<br>Section 15. Validating Bone Fracture Simulation<br>Section 16. Assessing Fracture Risk |
| <b>Engineering</b>         | Section 3. Motivating Patient-Specific Bone Fracture Simulation<br>Section 4. Motivating this Literature Survey<br>Section 6. The Physico-Mathematical Approach to Bone Fracture<br>Section 7. Modelling Bone as a Continuum<br>Section 8. Categorizing the Surveyed Literature into a Continuum Mechanics Framework<br>Section 9. Patient-Specific Geometry of Bone<br>Section 10. Mechanical Properties Categorization for Computational Bone Models<br>Section 11. Mathematical Model of Bone Trauma-inducing Accident—The Boundary Conditions<br>Section 12. Simulating Bone Fracture<br>Section 13. The Multiscale Structure of Bone<br>Section 14. Multiscale Modelling of Bone<br>Section 15. Validating Bone Fracture Simulation<br>Section 16. Assessing Fracture Risk |
| <b>Government</b>          | Section 3. Motivating Patient-Specific Bone Fracture Simulation<br>Section 4. Motivating this Literature Survey<br>Section 16. Assessing Fracture Risk  |
| <b>Philanthropy</b>        | Section 3. Motivating Patient-Specific Bone Fracture Simulation<br>Section 4. Motivating this Literature Survey<br>Section 16. Assessing Fracture Risk  |

## 2. Reading This Paper—Textual Organization and Notation

Throughout this paper, six extra text environments are used to organize ideas intuitively and to facilitate the reading.

|                              |   |
|------------------------------|---|
| <b>Characteristic Length</b> | Numerical values, surveyed from the literature, that characterize major geometric features of a specific bone lengthscale, see Definition 8.  |
| <b>Definition</b>            | Non-mathematical definitions that may be differently understood by specialists from different fields. Mathematical definitions are not presented here due to their complexity. Rigorous mathematical definitions are found in the references present in Appendix C. |
| <b>Highlight</b>             | A statement that plays a major role in the argumentation.   |
| <b>Illustration</b>          | A non-mathematical explanation of a physical phenomenon.  |
| <b>Open Issue</b>            | Issues and problems not clearly defined or completely solved within the surveyed literature.  |
| <b>Remark</b>                | Relevant notes.   |

To make the text less wordy and to shorten sentences whenever possible, a notation has been devised. For instance:  $\mathbf{S}\mathcal{A}_i$  represents the  $i$ -th concept within the concept group  $\mathcal{A}$  in section  $\mathbf{S}$ .

Some figures and tables are gridded in rows and columns, which, in turn, are labeled by either numbers or letters. For instance, the label Figure 1 row XII refers to the solid's homogeneity (a solid continuum can be either homogeneous or inhomogeneous); Table 2(1A) refers to the box at column 1 and row A in Table 2, which is titled "CT".

At the end of this paper, glossaries for symbols, acronyms, and physico-mathematical terms are provided, see Appendixes A, B and C.

## 3. Motivating Patient-Specific Bone Fracture Simulation

An increase in life expectancy implies that the elderly gradually compose a larger fraction of the population. Thus, diseases common among the elderly, e.g., osteoporosis, will occur more frequently, leading to an increase in occurrence of bone fragility fracture. The following Sections 3.1–3.3 present evidence for this argument.

### 3.1. Ageing Population

Life expectancy has been increasing by about 3 years per decade since 1950 [1]. Due to accelerated scientific and technological development, countless medical breakthroughs have been achieved, enabling people worldwide to live longer [2].

Projections show an intensified increase in the elderly population worldwide. While data from 2018 shows that only 13 countries have at least 20% of their population aged 65 or older, 82 countries are projected to have at least 20% of their population in the same age bracket by 2050 [3]. Furthermore, about 16% of the total world population in 2050 will be aged 65 and older, compared to 9% in 2018 [3]; about 1.5 billion of a projected population of 9.5 billion will be 65 and older in 2050. These projections are confirmed by other reports [4,5].

Analysing individual groups of countries, these same conclusions can be drawn in different magnitudes. A brief compilation of projections on the ageing population of America, Europe and Asia is presented in the next six paragraphs.

*Brazil*—by 2050, the number of people over 50 years old will represent 37% of the population [6]. In parallel, the population over 70 will increase by about 314% in comparison to 2011.

*Latin America*—in the 3 economies with the highest GDP after Brazil, the population over 70 will increase: by 321% in Mexico, by 129.6% in Argentina and by 348% in Colombia [6].

*The United Kingdom*—24% of the population will be 65 years and older in 2037 [7], taking the  $\geq 65$  years age bracket to 20.4 million people.

Europe—29% of the population will belong to the  $\geq 65$  age bracket in 2050, vs. 19% in 2016. In parallel, 13% of the population will be above 80 vs. 4% in 2016 [8].

The United States of America—exhibits a trend similar to that of Latin America and Europe [9].

Asia—will concentrate 62.3% of the world population in the  $\geq 65$  age bracket by 2050 [10].

### 3.2. Osteoporosis—A Major Health Concern

A longer life does not necessarily translate into a better life. The rising average life expectancy implies that a greater fraction of the population will be afflicted by several aging-related bone diseases. In particular, by osteoporosis, a chronic condition characterized by low Bone Mineral Density (BMD) and a consequent increase in fragility fracture risk [11,12]. Menopausal women are major victims of osteoporosis [13–15].

Understanding the mechanical behaviour of bone under osteoporosis and conditions such as weightlessness [16,17], radiation and vitamin D deficiency is of vital interest, for instance, to the cause of manned space travel.

**Highlight 1.** *This paper focuses on osteoporosis, which is the most frequent aging-related bone disease. Other bone diseases not addressed by this paper can be studied by applying the same methodology.*

### 3.3. Osteoporosis—Consequences and Costs

Bone fragility fractures are costly to treat. The associated decrease in quality of life implies further social and financial burden. Besides physical pain and disability, these fractures often lead to clinical death [18,19]. The treatment of bone diseases, e.g., osteoporosis, involves medical imaging, diagnosis and pharmacotherapy [20]. In case of fracture, surgery is often mandatory, implying hospitalization and rehabilitation. These fracture-triggered events produce a chain of financially heavy costs.

It is unsettling that osteoporosis can be clinically silent. As an example, it has been demonstrated that, without prevention and early diagnosis, the costs of osteoporotic fracture-related morbidity and mortality will burden the U.S. health-care system [21]. Logically, if preventive diagnosis methodologies are ignored, the burdening of every health-care systems worldwide is to be expected.

**Highlight 2.** *If current predictive diagnosis techniques remain unimproved, bone fragility fracture will become a heavier financial burden for health care systems and a social hindrance for people worldwide [22–24].*

## 4. Motivating This Literature Survey

Given Highlight 1, it immediately follows the question **4A<sub>0</sub>**.

**4A<sub>0</sub>**: How to accurately predict bone fragility fracture?

The definitive answer to **4A<sub>0</sub>** is unknown. Trying to answer **4A<sub>0</sub>**, this paper makes the assumptions **4B<sub>1</sub>–4B<sub>4</sub>**.

**4B<sub>1</sub>**: It is possible to use bone fracture simulations to identify bone structure failure criteria.

**4B<sub>2</sub>**: It is possible to correlate bone structure failure criteria to early signs of bone deterioration.

**4B<sub>3</sub>**: It is possible to correlate early signs of bone deterioration to bone fracture risk.

**4B<sub>4</sub>**: It is possible to predict fragility fractures from bone fracture risk analysis.

If **4B<sub>1</sub>–4B<sub>4</sub>** are true, improvement in predictive diagnosis is an immediate consequence and part of the unknown answer to **4A<sub>0</sub>** lies in answering questions **4A<sub>1</sub>–4A<sub>3</sub>**.

**4A<sub>1</sub>**: How to simulate bone fracture?

**4A<sub>2</sub>**: How to estimate fracture risk?

**4A<sub>3</sub>**: How to combine the answers to **4A<sub>1</sub>–4A<sub>2</sub>** to answer **4A<sub>0</sub>**?

Any coarse literature review indicates that several approaches have been applied to answer **4A<sub>1</sub>–4A<sub>2</sub>**. Furthermore, there has not been enough effort to answer **4A<sub>3</sub>**. Making a single literature survey encompassing the papers that answer **4A<sub>1</sub>–4A<sub>2</sub>** is this paper's contribution to answering **4A<sub>3</sub>**.

The surveyed literature was critically revisited and herein summarized in a structured view, updating specialists, those listed in Table 1, on bone fracture modelling, simulation and risk analysis. Ultimately, every specialist must be aware of pertinent open issues and know how to work with other specialists in order to collectively propose solutions.

## 5. Collecting Bibliographical References

This survey was performed using the platforms: *Web of Science*, *Scopus*, *PubMed* and *Google Scholar*. Some of the keywords searched in these platforms were: bone fracture, osteoporosis, bone mechanical properties, bone multiscale modelling, patient-specific bone model, multiscale bone analysis, fracture risk analysis. Papers suggested by these searches as well as other papers referenced by them were analyzed and selected for this survey.

Bone fracture simulation with risk analysis, like any other multidisciplinary topic, see, for instance, ref. [25], exhibits a vast array of relevant papers and applications. Thus, only a limited number of papers could be reviewed. The non-citation of a particular paper is unrelated to the paper's merit.

**Highlight 3** (Usage of the Word *Model*). *The word model has different meanings depending on the context. In this paper, a mathematical model is labelled "a model", i.e., "to model" means "to devise a mathematical model"; a computer-based likeness of a bone sample is referred to as "a geometry model".*

**Highlight 4** (Usage of the Word *Simulation*). *In this paper, performing mathematical calculations is labelled "simulation".*

**Highlight 5** (The Focus of This Survey). *The focus of this survey lies in papers that applied physico-mathematical approaches to bone fracture modelling and simulation.*

## 6. The Physico-Mathematical Approach to Bone Fracture

Physics and mathematics provide the most accurate descriptions of natural phenomena [26]. Accurate prediction of bone fragility fracture requires such mathematical and physical description. This description consists of equations that have physical, and, thus, biological, interpretations.

Continuum mechanics is a mature field of research and, for this reason, the ubiquitous theory when studying deformation and fracture processes. Continuum mechanics assumes the material to be continuous, i.e., a continuum: between every two points in the spatial domain of the body there always exists another point. A rigorous formulation of a continuum is founded upon, among other mathematical concepts, the basis coordinate frame axes's Dedekind-density and on Cauchy-continuity [27].

**Remark 1** (Continuum Mechanics Concepts). *Appendix C presents the list of references for physical and mathematical enunciations to the continuum mechanics concepts used in the text. Biologico-medical concepts can only be incorporated into computer simulations by means of adequate mathematical objects. The mathematical objects required by a consistent physico-mathematical description of bone fracture must mimic physical reality as much as possible.*

## 7. Modelling Bone as a Continuum

Figure 1 schematizes the possibilities for modelling patient-specific bone as a continuum and for evaluating, over the entire bone sample, the stresses and strains caused by imposed boundary conditions. Thus, Figure 1 presents what is required to model and simulate patient-specific bone fracture.

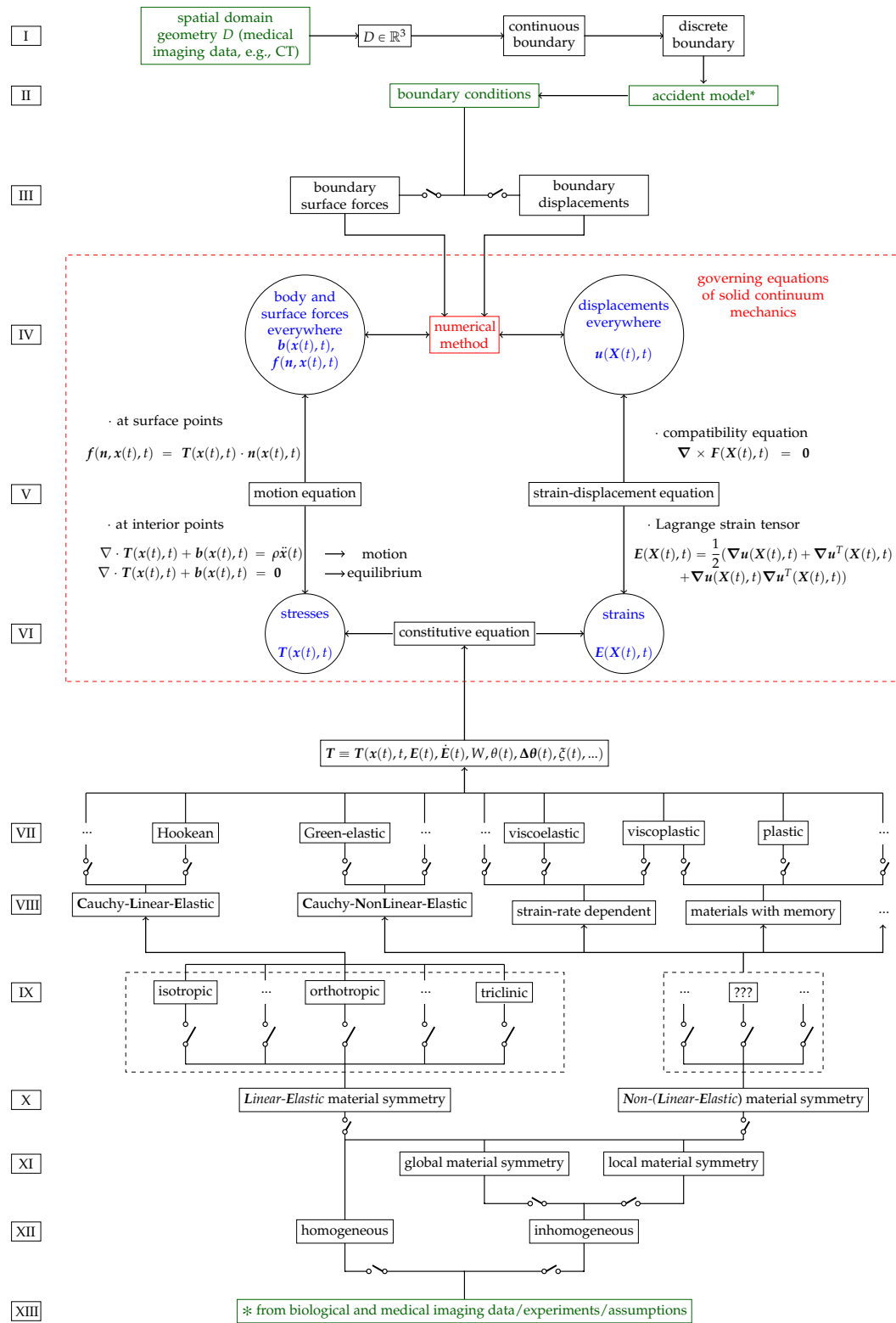


Figure 1. Modelling of a solid continuum mechanics problem for bone.

Figure 1, inspired by [28] (p. 145), is divided into 13 rows, from I to XIII.

- Row I of Figure 1 illustrates the modelling of patient-specific bone geometry and is further described in Section 9. The spatial domain plus the boundary of a solid bone constitutes its geometry.

**Remark 2** (Continuous Boundary). *In this paper, the term continuous boundary is used to describe the finest possible geometry discretization given by the resolution of the medical imaging to a computer geometry model. In fact, all geometry models created from medical imaging techniques have a discrete resolution, i.e., a finite number of pixels/voxels.*

Domain and boundary are mathematically defined in the references of Appendix C, but may not be clear for specialists who are not used to definitions of Partial Differential Equations (PDEs) and continuum mechanics.

**Illustration 1** (Domain and Boundary). *Picture a potato. In continuum mechanics, the spatial domain of the body represents the interior of the potato. The boundary of the body represents the potato's skin. Domain plus boundary comprise the entire body.*

- Row II of Figure 1 illustrates the derivation of boundary conditions from accident models which are further described in Section 11.

It is at the boundary of the body, through boundary conditions, where bone models can use information provided by accident models representative of common physical trauma among the elderly, see Section 11. The definition of boundary condition in the context of PDEs may not be clear for non-specialists. In the bone fracture literature, boundary conditions are often labelled as loading or constraint conditions.

**Illustration 2** (Boundary Condition). *Boundary conditions (BCs) represent the effects of the exterior domain (everything that is not the body) onto the body. BCs describe the interactions between the domain of the body and the exterior domain through the boundary. In structural analysis, BCs are usually represented by surface forces (or tractions) and displacements [29] (p. 11). Boundary conditions require a predefined domain, i.e., geometry. In the diagram of Figure 1 BCs transmit information about the geometry to the set of governing equations, see Section 12, between rows IV and VI.*

- Row III of Figure 1 illustrates the two types of BCs for solid continuum mechanics problems which are briefly described in Section 11.
- Row IV of Figure 1 illustrates the inputs (body forces in the domain, if present, and surface forces and displacements on the boundary, i.e., as BCs) and outputs (surface forces and displacements everywhere) of solid continuum mechanics problems which are further discussed in Section 11.
- Row V of Figure 1 illustrates the motion and strain-displacement equations which are further described in Section 12.
- Row VI of Figure 1 illustrates the relationships between stresses and strains given by constitutive equations which are further described in Section 10.
- Rows VII to VIII of Figure 1 illustrate different types and categorizations of constitutive equations which are further described in Section 10.

**Remark 3** (On the Reticences Displayed in the Scheme of Figure 1). *Theorists and experimentalists in the field of mechanics of materials should consider any possible material symmetry and constitutive equation, see 15.A<sub>1</sub>. The most well-known constitutive equations can only describe bone behaviour up to a certain accuracy. Indeed, if a key variable of bone mechanics is not being considered, it is possible that numerical calculations will never match experimental results. Time, position within the material's spatial domain, strain, strain rate,*

temperature, temperature gradients and strain-energy are only a few of the variables that may have an influence on the mechanical behaviour of a material, e.g., bone.

- Rows IX to X of Figure 1 illustrate different types and categorizations of material symmetry regarding mechanical properties which are further described in Section 10.
- Rows XI to XII of Figure 1 illustrate homogeneity regarding mechanical properties, i.e., material symmetry and constitutive equations, which are further described in Section 10.
- Row XIII of Figure 1 illustrates the experiment-based categorization of mechanical properties, i.e., homogeneity, material symmetry and constitutive equations, which are further described in Sections 10, 13 and 15.

Green coloured texts illustrate the inputs of the modelling process.

Blue coloured texts illustrate the output of the simulation.

Red coloured texts illustrate where the simulation is performed.

Switches in parallel indicate that only one box at a time must be selected when modelling a solid continuum, e.g., a material is either orthotropic or isotropic, but not simultaneously both. Note that inhomogeneous materials are, in fact, globally inhomogeneous, but locally homogeneous. For each homogeneous subdomain of a globally inhomogeneous material, a material symmetry and a constitutive equation must be selected.

Each stage on the diagram of Figure 1 must be modelled and validated as accurately and realistically as possible, so the final results can be used in medical clinics.

**Remark 4** (Model Accuracy and Validation). *Geometry, discretization, mechanical properties, full model, boundary conditions, evaluation of stresses, strains, forces and displacements. Accuracy and validation of the current stage on the diagram of Figure 1 depends directly on the accuracy and validation of the previous stage of the diagram, see Section 15.*

One of the main objectives of the continuum mechanics is to study how solids, subjected to certain BCs (e.g., external forces), deform and move. This is achieved through the coupling of strain-displacement, equilibrium and constitutive equations (the governing equations), see Figure 1 and Section 12. The references in Appendix C give more detailed information on continuum mechanics.

## 8. Categorizing the Surveyed Literature into a Continuum Mechanics Framework

Most surveyed papers performing bone simulations, patient-specific or not, of fracture or not, modelled bone as a continuum, following a strategy similar to the diagram in Figure 1. The surveyed literature was categorized regarding its bone computational modelling. The assumptions and considerations made by each reference are registered in Table 2, where tendencies and possible open issues become visible.

**Table 2.** Categorization of surveyed literature that modelled bone as a solid continuum [30–147].

|   | 1   | 2   | 3   | 4  | 5   | 6   | 7   | 8  |
|---|---|---|---|--|---|---|---|--|
|   | Geometry Modeling   | Motion equation   | Strain-Displacement Equation  | Constitutive Equation  | Material Symmetry   | Homogeneity   | Material Properties Source  | Boundary Conditions Origin   |
| A | CT<br>[30–126]  | Static, Quasi-Static Equilibrium<br>[33,34,36,37,40,41,46,50,52–55,60,61,64,65,69,71,76,80,83,90,92,99–102,105,110,111,124,125,135,141,143–147]       | Linear<br>[38,40,41,52–54,56,61,65,84,88,89,95,100,112,135,143,144]   | Elastic (CLE + CNLE)<br>[30–32,34,36–41,44,46,48,50–55,57–61,65,66,68,69,71,73,74,76,77,79–83,85,87–93,95,97,98,102,103,106–119,121–123,125–129,132–145,147] | Isotropic<br>[30–34,36–49,51,52,54,56–61,63,64,66–77,79–83,85–99,101–122,124–133,135–145,147] | Homogeneous<br>[30,42,51,52,64,79,83,134,142,144–147]                     | from experiment<br>[61,139]   | Human motion representative-Deterministic<br>[32,35,39–41,44,49,54,69–75,81,82,99,100,105,106,108–114,117,118,120–123,127–130,147]                               |
| B | DXA<br>[56,97,127–129]  |   |   | Viscous<br>[42,43,45,75,143]   |   |   |   |  |
| C | MRI<br>[48,53,83,130,131]                                       | Motion<br>[39,75,126]   | Nonlinear<br>[43,55,67,84,94,124,133,137]   | Elastic-Plastic<br>[33,42,43,45,47,49,56,64,67,70,72,75,84,86,94,96,99–101,104,105,120,124,130,131,146]  | Transversally isotropic<br>[42,45,50,52,54,64,65,69,74,84,99,115,124,139–141,146]             | Inhomogeneous<br>[30–34,36–41,43,44,46–51,54–58,60–63,65–72,74–77,81–143] | from medical imaging<br>[30–32,36–41,43,44,46,47,49–51,54–56,58,60,62,63,65–72,74–77,81,82,84–121,125–131]    | Experiment representative<br>[30,31,33,34,36–38,42,43,45–48,50–52,55,57,58,60–68,79,80,83,84,86,88–90,92–98,101–104,111,115,116,119,125,131,132,134–138,144–147] |
| D | Microscopy<br>[83,132–134]                                      |   |   | Damageable<br>[42,45,54,56,60,64,73,75,76,80,124,143]  | Orthotropic<br>[42,44,53,55,57,73,74,81,83,96,115,124,134,138,143]                            |   |   |  |
| E | Illustration from Biology, Experimental studies<br>[61,135–144] | Unspecified / Other<br>[30–32,35,38,42–45,47–49,51,56–59,62,63,66–68,70,72–74,77–79,81,82,84–89,91,93–98,103,104,106–109,112–123,127–134,136–140,142] | Unspecified / Other<br>[30–37,39,42,44–51,56–60,62–64,66,68–83,85–87,90–93,96–99,101–111,113–123,125–132,134,136,138–142,145–147] | Porous<br>[123,144]  |   |   | from specialized literature<br>[33–35,42,45,48,49,51–54,56,57,59,61,64,69,73,74,78–81,83,115,122–124,132–147] | Human motion representative-Stochastic<br>[126]  |
| F | Unspecified / Other<br>[54,69,145–147]                          |   |   | Unspecified / Other<br>[35,62,63,76,78]  | Unspecified / Other<br>[35,61,62,78,100,123,140–142]  | Unspecified / Other<br>[35,45,53,59,73,78,80,123,134]                     |   | Arbitrary, Unspecified / Other<br>[53,56,59,76–78,85,87,91,107,124,133,139–143]  |

Table 2 categorizes the surveyed literature regarding 8 different aspects of solid continuum mechanics modelling. Each column regards one of these aspects:

- Column 1 of Table 2 categorizes the surveyed literature based on how bone geometry is modelled, see Section 9.
- Column 2 of Table 2 categorizes the surveyed literature based on if the inertial term of the motion equation was neglected or not, see Section 12.
- Column 3 of Table 2 categorizes the surveyed literature based on if the non-linear term of the strain-displacement equation was neglected or not, see Section 12.
- Column 4 of Table 2 categorizes the surveyed literature regarding the constitutive equation of their models, see Section 10.
- Column 5 of Table 2 categorizes the surveyed literature regarding the material symmetry of their models, see Section 10.
- Column 6 of Table 2 categorizes the surveyed literature based on the homogeneity regarding the mechanical properties of their models, see Section 10
- Column 7 of Table 2 categorizes the surveyed literature based on the source of the mechanical properties of their models, see Section 10.

- Column 8 of Table 2 categorizes the surveyed literature based on the BCs imposed on their models, see Section 11.

Some references may be repeated within a column in Table 2.

**Remark 5** (Multiplicity of References in Table 2). *Reasons for repeating references in the same column are: (1.) There is more than one model in the reference, each set up differently; (2.) The reference considers a multiscale model and each lengthscale is modelled differently (3.) The model is inhomogeneous and each locally homogeneous subdomain is modelled differently.*

The authors tried their best at categorizing each analyzed reference into the most appropriate row of Table 2. However, some references do not clearly or directly reveal how they created their model. Sometimes a bit of interpretation and common sense of the authors was needed to find the best suitable categorization for each reference.

**Remark 6** (Lack of Clarity). *It is worth to note that some references do not specify their models, see Table 2 row F. The boxes “Unspecified/Other” indicate that the analyzed reference either does not specify its model creation/assumption or uses another, less usual, procedure/assumption not shown in Table 2. The vast majority of references in these boxes do not specify their models. It is very likely that these references assumed the most mature and easy-to-implement modelling strategy. For example, the material was assumed isotropic when no material symmetry was specified, see Table 2 column 5. Complex models tend to be described in detail. Very uncommon assumptions are highlighted throughout this survey.*

Remark 6 leads to Remark 7.

**Remark 7** (Unifying Framework for Bone Continuum Modeling). *The large number of unspecified modelling data suggests that the literature in the field of bone fracture simulation should be more clear and direct about their modelling. A brief paragraph, or even better a table, addressing all information for continuum modelling shown in Table 2 should be present. In addition, further information on used mechanical properties and numerical techniques, as shown in Table 2 of [148], would facilitate the understanding and reproducibility of the simulations.*

In addition to assuming bone as a continuum, several of the reviewed papers considered the multiscale structure of bone, see Section 13, and modelled bone as a multiscale material, see Section 14. At the molecular lengthscale, however, bone is not a continuum, but rather a discrete material, or a non-continuum, constituted of molecules, and atoms connected by chemical bonds. Between atoms there is vacuum. Bone is mostly made of vacuum. However, continuum mechanics does not consider the empty spaces between the atoms and is, thus alone not able to foresee where a gummy-bear will break since a continuum has no weakness [149]. Cracks must be first artificially created before propagated.

New multiscale approaches considering molecular structures have arisen to improve the accuracy and precision of material behaviour’s prediction. In the ideal case, bones are modelled as a bunch of (countless) interacting atoms. Nonetheless, this is computationally very expensive and currently impracticable. Today’s greatest clusters can simulate, in a reasonable time, no more than very small cubes with millions, maybe billions of atoms.

As once said by the mathematician Terence Tao: “Well, just about any useful mathematical model makes non-physical assumptions—for instance, fluids are almost always modelled by a continuum, when in reality they are composed of a huge number of interacting particles. But if the model is robust enough, one can still expect it to give an accurate prediction of reality, even if at an ontological level it is quite distinct” (<https://terrytao.wordpress.com/2011/08/04/localisation-and-compactness-properties-of-the-navier-stokes-global-regularity-problem/>).

Physicists and engineers should try to take meaningful *macroscale* information from reduced *molecular* simulations, rather than to simulate all particles within the bone. Continuum mechanics has proved itself to be, in many applications, e.g., fracture mechanics, “robust enough”.

**Remark 8** (Challenges & Limits). *Current Limits of the Patient-Specific Fracture Simulation are:*

**6.A<sub>1</sub>**: *viability of in vivo experiments for the assessment of patient-specific bone mechanical properties, see Section 10 and 15.A<sub>1</sub>;*

**6.A<sub>2</sub>**: *viability of in vivo experiments for validation of computer simulations, see 15.A<sub>2</sub>;*

**6.A<sub>3</sub>**: *computing processor and memory for simulation (mesh refinement increases the number of DOF and so the computing time. Molecular modelling requires an almost infinite number of DOF).*

## 9. Patient-Specific Geometry of Bone

Every bone is unique in its geometry and mechanical properties. Bone fracture models cannot be generalized for all bones, i.e., fracture risk and traction and displacement fields evaluated within the geometry of a specific bone for a given set of BCs are not interchangeable with other bones.

**Illustration 3.** *Two equally manufactured steel beams behave (at least quasi) equally when subjected to equal BCs. The mathematical description of bone behavior, however, may depend on an infinite number of variables, since there are infinitely possible constitutive equations, relevant physical properties and environmental, e.g., host tissue conditions. Most of the variables considered in mathematical descriptions of living tissue are time-varying and depend on biochemical complexity, animal and human habits, interaction with the environment. For instance, bone undergoes a continuous remodelling process, see Remark 19.*

Thus, bones are *patient-specific*. Each bone is differently “manufactured”.

**Definition 1** (Patient-Specific: in vivo vs. in vitro). *The term patient-specific denotes each bone in each patient is unique in its geometry and mechanical properties. Thus, bone geometry and mechanical properties are directly assessed from the studied bone. Patient-specific refers to a bone of a living patient, i.e., to in vivo bone. In vivo indicates bone from inside a living organism. Dual to in vivo experiments, in vitro bone experiments are more feasible. In vitro indicates bone outside a living organism.*

Patient-specific: some models can be it, some models cannot be it.

**Remark 9.** *Patient-specific data comes from non-destructive techniques. For instance, the geometry of computational bone models is acquired through non-destructive and non-intrusive medical imaging techniques [50,150]. When not possible, e.g., due to insufficient resolution for specific lengthscale dimensions, to acquire certain patient-specific information, data usually comes from experiments or physical assumptions. For instance, ref. [133] constructs an inhomogeneous, see section Section 10, simulation domain at the microscale, see Section 13, based on simplifying geometric assumptions derived from microscopy.*

**Definition 2** (Computational Bone Model). *A computational bone model refers to computer files that contain bone geometry and mechanical properties data.*

**Open Issue 1.** *The validation of patient-specific bone fracture simulations is a major challenge in the field of biomechanics, see Section 15. In vitro experiments do not validate patient-specific bone. However, since there is still no possible way of validating bone computational models by performing in vivo experiments, in vitro experiments are the best way to compare simulations with the real-world.*

Subject-specific and specimen-specific are not the same as patient-specific.

**Definition 3** (Subject-Specific and Specimen-Specific). *Differently from patient-specific, both subject-specific and specimen-specific terminologies refer either to in vivo non-human bones or to in vitro-experimented bones. A given bone fracture simulation methodology may be applied to bone samples designated by any of the three aforementioned terminologies.*

This section features three non-invasive medical imaging techniques plus microscopy, which is not patient-specific, but is commonly used to model bone micro- and lower-scales-geometry, see Definition 9:

**Computed Tomography** (CT), or X-ray computed tomography, is the most used medical imaging technique among the surveyed literature, as demonstrated in Table 2. CT is argued to be the most accurate 3D medical imaging technique for the creation of computational bone models [151]. However, CT is not recommended for routine clinical examinations due to associated high radiation dosages [152].

**Remark 10** (CT Resolution). *Ordinary CT-scans have a limited spatial resolution of about 0.5 mm [153]. Thus, they are unable to delineate bone geometry at the microscale, see Section 13. Microscale geometry of bones can be assessed through higher resolution CT techniques, such as High-Resolution peripheral-CT (HR-pCT) and Micro Computed Tomography ( $\mu$ CT).*

**HR-pCT** is a high-radiation CT restricted to the peripheral sites of the body, e.g., distal skeleton. HR-pCT provides in vivo imaging with spatial resolution smaller than 100  $\mu$ m [75,81,153,154]. Similarities between the micro-geometry of peripheral bones and the micro-geometry of non-peripheral bones were discussed and considered by [154,155]. Though HR-pCT is being increasingly used for in vivo bone research, its use has been limited to the distal radius and tibia [156].

**$\mu$ CT** features a spatial resolution of about 1  $\mu$ m, higher than that of HR-pCT, enabling delineation of the trabecular microstructure [157,158]. Due to high associated radiation dosages, its usage is restricted to biopsy specimens [153,159]. In comparison to HR-pCT,  $\mu$ CT captures the trabecular porosity more accurately [160].

The reviewed literature features a certain confusion between the usage of HR-pCT and  $\mu$ CT terminologies [161]. For instance, it could be argued that [159,162] misplaces terminology. HR-pCT reaches at most  $\sim 10$   $\mu$ m; its associated radiation dosage is small enough to allow in vivo rapid tests and is capable of providing a detailed analysis of bone morphology, i.e., geometry [153,161].  $\mu$ CT displays a finer resolution; its associated radiation dosage restricts applicability to in vitro analysis [161].

**Remark 11** (QCT and HR-pQCT). *The Q in QCT and HR-pQCT stands for Quantitative and indicates that a calibration phantom is included in the scanning for the calculation of BMD. However, if a computational model is not aimed, it is preferable to calculate BMD using DXA, see below, because it is more accessible and less expensive [163].*

**Dual-Energy X-ray Absorptiometry** (DEXA, DXA) is the clinical standard to diagnose osteoporosis and fracture risk by measuring areal Bone Mineral Density (aBMD) [97,164,165]. DXA can also contain non-BMD parameters that are correlated to bone fracture [128,166]. The main advantage of DXA over CT is that DXA requires minimal radiation exposure. However, ref. [97,163,167] present a “3D-DXA” method capable of assessing the bone femoral shape and density distribution from 2D DXA images. They are based on statistical shape and appearance models and show good correlations between 3D-DXA and CT. However, DXA is still not as accurate as CT in, e.g., predicting femoral strength [97].

**Magnetic Resonance Imaging** (MRI) is the most suitable technique method for in vivo 3D geometry modelling since it emits no harmful ionizing radiation. However, although comparable to CT-based geometry models, MRI-based geometry models are not as accurate as CT-based geometry models [151]. The bone microstructure can be effectively imaged by  $\mu$ MRI [53,83].  $\mu$ MRI-based models are also effective in assessing mechanical properties, but  $\mu$ CT-based models are still more accurate [48,130].

**Microscopy** provides very fine and detailed images featuring the nano and even sub-nano lengthscale bone geometry. However, this technique is invasive and only able to prove 2D geometry [83,132–134]. Microscopy-based 3D geometry models can be created when the third dimension is idealized [134], e.g., when a circle is turned into a cylinder. However, creating the third dimension from scratch is not considered subject-specific.

**Remark 12.** *Very few works in the literature compare two medical imaging techniques to the same bone sample, e.g., [56,151], see column I of Table 2.*

**Remark 13.** *Scanning and accurately modelling macroscale bone geometry through medical imaging techniques is a mature field of research. However, though HR-pCT,  $\mu$ CT and  $\mu$ MRI allow the determination of bone microscale geometry with some accuracy, techniques capable of accessing non-macro lengthscales must be improved.*

Analytical fracture analysis of complex bone geometries is currently impossible. Numerical methods, see Section 12, used in engineering for structural analysis (including fracture) require discretization of the spatial domain, i.e., a mesh.

**Remark 14 (Mesh Generation).** *The reviewed literature presents two mesh generation procedures for patient-specific bone geometry: (1.) Voxel-based meshing defines the mesh contour as the voxel contour [74,83,168,169]. Each voxel turns into a hexahedron-shaped volume, i.e., cube or rectangular cuboid. This type of mesh generation requires no material mapping strategy, see Section 10. However, it may exhibit locations (corners) where stress is concentrated and can only accurately represent the surface of the bone geometry when the mesh is sufficiently fine. Very fine meshes increase the number of nodes and sub-domains and are thus computationally more expensive; (2.) Geometry-based meshing defines the mesh contour based on the surface of the geometry model [119,168]. It requires a material mapping strategy, see Section 10. Geometry-based meshing is difficult to implement computationally, but several commercial software packages (Ansys, Abaqus, Hypermesh, Gmesh, et cetera) already provide it.*

Completion of the following procedures  $9A_1 \rightarrow 9A_5$ , see Figure 1 row I, constitute patient-specific bone 3D geometry modelling and discretization:

**9A<sub>1</sub>:** Scanning—The patient’s bone is scanned by medical imaging equipments, which create a DICOM (Digital Imaging and Communications in Medicine—<http://dicom.nema.org/>) file. DICOM files contain information on the patient (e.g., age, sex, health condition) in addition to collections of images.

**9A<sub>2</sub>:** Image segmentation—Medical imaging techniques create images that contain bones, nearby soft tissue and fat. A segmentation must be performed in order to separate bone from non-bone tissues. This can be done manually or automatically [170] by using domestic algorithms or software packages, e.g., InVesalius [171], MIMICS, Simpleware and Amira.

**9A<sub>3</sub>:** Geometry surface—From segmented DICOM files, an .STL (STereoLithography) file, describing only the surface geometry of the 3D object, i.e., the hip bone, is obtained by using domestic algorithms or software packages, e.g., InVesalius [171], MIMICS, Simpleware and Amira.

**9A<sub>4</sub>:** 3D solid geometry model—Using domestic algorithms or software packages, e.g., MIMICS, Simpleware or CATIA, the .STL file is converted into a .STEP (STandard for the Exchange of Product model data) file, which provides a readily-modifiable 3D solid model of the bone.

**9A<sub>5</sub>:** 3D mesh—A 3D mesh with  $n$  nodes and  $s$  sub-domains is created using domestic algorithms or software packages, e.g., ANSYS, Altair HyperMesh, Gmsh or 3ds Max, from the .STEP file. The mesh is described by a node matrix, which contains the coordinates of each node, and an incidence matrix, which relates  $n$  nodes to  $s$  sub-domains.

The modelling of the patient-specific bone geometry and thereafter creation of 3D bone meshes are a mature field of research [54,172].

## 10. Mechanical Properties Categorization for Computational Bone Models

Computational bone models require spatially-local data on domain geometry and mechanical properties. Such data can be obtained by applying the standard scientific method:

**10A<sub>1</sub>**: observation of and experimentation on bone;

**10A<sub>2</sub>**: identification of pertinent physical characteristics and phenomena;

**10A<sub>3</sub>**: selection of mathematical descriptions that match the physical characteristics and phenomena identified in step **10A<sub>2</sub>**.

When performing **10A<sub>3</sub>**, most of the *continuum mechanics*-based bone models require, as shown in columns 4, 5 and 6 of Table 2, assumptions regarding:

**10B<sub>1</sub>**: a constitutive equation;

**10B<sub>2</sub>**: a type of material symmetry;

**10B<sub>3</sub>**: homogeneity, i.e., the spatial configuration of material and mechanical properties, of **10B<sub>1</sub>** and of **10B<sub>2</sub>**.

**Open Issue 2.** Most of the surveyed literature does not provide justification, based on **10A<sub>1</sub>** and **10A<sub>2</sub>**, for their particular **10A<sub>3</sub>**. **Open Issue 2** aims to hint on what the lack of such justification consists of, by presenting some literature on how **10A<sub>2</sub>** influences **10A<sub>3</sub>**. Some of these influences are mathematically described by appropriate choices of **10B<sub>1</sub>**, **10B<sub>2</sub>** and **10B<sub>3</sub>**.

The surveyed literature points to four groups of open issues regarding the influence of **10A<sub>2</sub>** on **10A<sub>3</sub>**. These groups consist of open issues related to: (1.) bone sample geometry, (2.) bone intensive properties, (3.) phenomenological aspects of bone observation/experimentation and (4.) patient-specific characteristics that influence issues (1)–(3).

(1) Some issues regarding bone sample geometry:

OI 10.11 Geometric irregularities at the transverse cross-section: contrary to longitudinal geometric irregularities, they contribute significantly to the linearly elastic torsional behaviour of long bones [173,174].

OI 10.12 Bone aspect ratio: long bone failure may be more dependent on deformation rather than on stress [175].

OI 10.13 Microstructure: influences the fatigue life of bone [176,177]. The vascular pattern of bone affects its Young's Modulus [178].

(2) Some issues regarding bone intensive properties:

OI 10.21 Temperature: influences the fatigue life of bone [176,177].

OI 10.22 Water content: influences the stiffness, strength and toughness of bone [179,180]; the Young's Modulus of dead (dry) and living (wet) bones tend to be different [178]. Furthermore, viscoelastic [181] properties of bones are also influenced by the water content. The water content of bone is related to the molecular scale, see Section 13.

OI 10.23 Mineral content: porosity and mineral content influence bone Young's Modulus [182–184]. The mineral content of bone is related to the molecular scale, see Section 13.

OI 10.24 Bone density: exhibits a *p*-value based highly significant positive correlation with bone fatigue life [176,177]. Furthermore, density influences bone stiffness and strength [185].

OI 10.25 Porosity: alongside bone mineral content, influences bone Young's Modulus [182].

(3) Some issues regarding bone phenomenological aspects when under observation/experimentation:

OI 10.31 Strain-rate: is directly proportional to bone Young's Modulus under tension and under compression [186] and influences bone compressive strength [187].

OI 10.32 Loading condition: [178] presents a comparison of bone Young's Modulus for femur and tibia under tension, compression and bending. Experiments performed by [188] exhibited the same mechanical properties for tension and compression in bone.

- OI 10.33 *Stress duration: influences bone Young's Modulus in a phenomenon labelled elastic after-effect [178].*
- OI 10.34 *Cyclic loading frequency: influences bone Young's Modulus [189].*
- OI 10.35 *Stress amplitude: influences the fatigue life of bone [176,177].*

(4) *Some issues regarding patient-specific bone characteristics:*

- OI 10.41 *Patient age: affects ultimate tensile strength, elastic modulus, maximum deformation, and Brinell hardness [190] and the bone structure in such a way that increases its fracture risk [191].*
- OI 10.42 *Diseases: affect the rate of bone remodelling, see Remark 19, and consequently the percentage of bone mineral content (OI 10.23) and BMD distribution, i.e., the mechanical properties of bone [192–194]. Fracture risk analysis in unhealthy, e.g., metastatic, bones is currently even less accurate than fracture risk analysis in healthy bones [195].*
- OI 10.43 *Nutrition: a well-balanced diet (including plant-based diets [196–200]) alongside an adequate intake of Calcium and Vitamin D (sunlight exposure time) may reduce osteoporosis-induced fracture risk and hospital costs [196,201].*
- OI 10.44 *Physical activity: increases not only quality of life [202,203], but also BMD and bone mechanical properties values [204]. Furthermore, regular exercise enhances bone mass and strength, and reduces bone fracture risk [205].*

A comprehensive review on the relationships between physical, geometrical and mechanical properties of bone was made by ref. [185].

The physical assumptions underlying the conclusion of an experiment may imply an inaccurate mathematical description. For instance, consider a bibliographical reference that states an issue of Young's Modulus inhomogeneity; this issue may be readily solved using a numerical method, see Section 12, that considers a value of Young's Modulus that is specific to each discretized unit (or subdomain); perhaps the experiment calculated an equivalent numerical value for Young's Modulus uniformly distributed in the bone. If a CT were to be used, the conclusions on the same sample would be different.

A mathematical description, despite not explicitly considering all bone physics at the experimental conclusions, can still agree with the experiment. Consider an experiment. A material exhibits properties X and Z of different categories. It may be the case that a change in Z is almost totally reflected as a change in X alone. If X is already considered in the current mathematical description, it may not be necessary to consider any mathematics for Z. The converse can also be true, that is: if, for the same value of X, the outcome of the same experiment is considerably different, it may be the case that Z must be included in the mathematical description.

For instance, if nutrition (OI 10.43), diseases (OI 10.42), patient age (OI 10.41) and density (OI 10.24) have their effects fully captured by the knowledge of, e.g., bone mineral content (OI 10.23), it is reasonable to assume that these variables are unlikely to appear in an accurate mathematical description. To consider only bone mineral content would suffice for an accurate mathematical description.

The ultimate goal of studying bone fracture is to predict fracture propagation at the macro scale, a task highly dependent on  $\mathbf{10B}_1\text{--}\mathbf{10B}_3$ . The choice of  $\mathbf{10B}_1\text{--}\mathbf{10B}_3$  must be guided by what is observed in experiments. The surveyed literature indicates that  $\mathbf{10A}_1$  implies several mechanical characteristics of bone that are, in a purely macroscopic continuum model, not readily accounted for. Thus, specific models are needed for these mechanical characteristics and their lengthscales. For instance, it is impossible to go straight from the macroscale to the molecular scale. These specific models need to be integrated, from which is known that a non-multiscale approach is incomplete. From the multiscale approach, it is possible to accurately predict fracture propagation at the macro scale through an appropriate choice of  $\mathbf{10B}_1\text{--}\mathbf{10B}_3$ , see Section 14. These choices can not be accurately

made without proper knowledge of all length scales, see Section 13. Then it is possible to know if it is a matter of tuning the macroscale model or modeling these different physics someplace else. Multiscale is a consequence of experimental observation.

**Remark 15** (Insufficiency of Biological Considerations). *Biology, e.g., using microscopy, provides only the conceptual framework for the material categorization, i.e., for the selection of appropriate  $10\mathcal{B}_1$ ,  $10\mathcal{B}_2$  and  $10\mathcal{B}_3$ . It is through engineering and physics experiments that quantitative mechanical properties are more realistically estimated.*

### 10.1. Constitutive Equation

Calculating stresses and strains over solid bodies using *continuum mechanics*-based bone models requires at least one equation correlating stresses and strains, i.e., a constitutive equation, see Appendix C. There are infinite possible materials, each material described by one or more constitutive equations [206]. Currently known constitutive equations enable simulation-based design of robust materials, e.g., for aircraft. Strain-displacement and motion equations are independent of the material properties, see Figure 1 and Section 12.

**Open Issue 3.** *Currently known constitutive equations, regarding the mechanical behaviour of living tissues to different loading conditions, do not (or do not accurately) account for, e.g., rapid changes of living tissues over time, e.g., bone remodelling, see Remark 19. Possible dependence on still unknown mechanical properties must be studied.*

This paper found eight constitutive equations used for the creation of computational bone models, listed in column 4 of Table 2: elastic, plastic, viscoelastic and -plastic, poroelastic and -plastic, elastic and plastic-damageable materials.

**Elastic materials**, see Appendix C, can be either Cauchy-Linear-Elastic (CLE) or Cauchy-NonLinear-Elastic (CNLE), see Figure 1 row VIII. **CLE-materials** display spring-like behaviour according to Hooke's law:  $T(x(t), t) = \mathbb{C}E(X(t), t)$ . A CLE-material may not comply to Hooke's Law when there are unknown contributions to the stiffness tensor  $\mathbb{C}$  that are implicitly, but not explicitly, dependent on the strain tensor  $E$ . Most of the surveyed literature, as seen in Table 2 column 4, assume that bone is an elastic material; all literature in Table 2(4A) assumes bone complies to Hooke's Law. Though many materials can be accurately modelled as CLE, the literature on bone mechanical properties rarely reports experimental verifications of CLE-behaviour in bones. **CNLE-materials** are usually modelled by constitutive equations that correlate stress and strain-energy:  $T \equiv T(x(t), t, W(E))$ . Non-linear stress-strain correlations may be linearized into affine approximations [207], which are still not linear correlations. Though none of the surveyed literature reports bone to be CNLE, human soft tissue, also present at muscle-bone connection sites, displays Green-elastic (hyperelastic) behaviour [125,208]. For exhibiting *quasi*-brittle fracture in experiments, bone is sometimes assumed to be a CLE-material [112], e.g., strain measurements performed by [113] have shown this to be a reasonable assumption for femurs. Furthermore, ref. [129,209] assume that the proximal femur behaves as a CLE-material up to fracture, i.e., that the post-yield behaviour, i.e., the plastic behaviour, can be neglected.

**Remark 16 (Linear Material Terminology).** *A material is labelled linear, e.g., Hookean, if it can be accurately modelled by a constitutive equation that exhibits a linear relationship between stress  $T$  and strain  $E$ . Though not all elastic materials are linear, e.g., Green-elastic materials, only elastic materials may be labelled linear. Viscoelastic materials are, misleadingly, labelled linear materials [210,211] even though they are modelled by a constitutive equation that exhibits a linear relationship between stress  $T$  and strain-rate  $\dot{E}$  instead of between stress  $T$  and strain  $E$ . Figure 1 row X classifies materials into Linear-Elastic (LE) and Non-(Linear-Elastic) (NLE). Emphasis on the subtle distinction between NLE- and CNLE-materials: the first refers to the set of all materials excluding the LE-materials, the latter refers to the set of all elastic materials excluding CLE-materials.*

Bone can be considered an LE-material for several purposes [212]. However, it is expected that for bone fracture purposes, more “complete” constitutive equations that account for the nonelastic behaviour of bone, may improve the model accuracy and thus the accuracy in predicting fractures.

**Plastic materials**, see Appendix C, feature one or more particles that do not return to their unstressed spatial position after unloaded, thus exhibiting long-term memory of previous stresses and strains. Among the NLE constitutive equations, plastic constitutive equations (or elastic–plastic, elastoplastic) are the most frequently used for modelling bone [184,213–216]. Plastic constitutive equations may accurately predict the failure of vertebrae [217]. Some of the surveyed literature does not explicitly justify the choice of assuming bone as a plastic material [33]. Nevertheless, the entanglement of different molecules that compose bone may justify its plastic behaviour [218].

**Remark 17** (Elastic-Plastic Materials). *No physical material is exclusively elastic or exclusively plastic. The perceived material behaviour depends on experimental setups and local conditions. A certain constitutive equation may better fit the numerical values of the experimentally measured deformations. All materials exhibit elasticity and, after reaching the Yield Stress, plasticity. Thus, the term elastic materials refers to pure elastic materials. The higher the ratio between the Yield Strain and the Ultimate Strain, the higher is the degree of elasticity  $\mathcal{E}$  of a material; the degree of plasticity is  $\mathcal{P} = 1 - \mathcal{E}$ . Thus, all plastic materials are, in fact, Elastic-Plastic, or elastoplastic, materials.*

**Elasticity** and **Plasticity** are modelled by stress-strain constitutive equations. As stated in Remark 3, constitutive equations are not limited to stresses and strains. Constitutive equations can be systems of equations accounting for several phenomena affecting the stress-strain relationship. This paper presents three such phenomena: **Viscosity**, **Porosity** and **Damageability**.

**Elastic-Viscous materials**, or viscoelastic materials, see Appendix C, exhibit stresses dependent on strain-rate:  $T \equiv T(x(t), t, E, \dot{E})$ . Other physical phenomena of viscous materials include stress-strain hysteresis, creep and stress relaxation [219] (p. 436), [220]. Phenomena identified by [178], who studies only aspects **10.A<sub>1</sub>**, **10.A<sub>2</sub>** were interpreted by [221] as implying that a viscoelastic constitutive equation was an accurate mathematical model for the execution of step **10.A<sub>3</sub>**. Usage of viscoelastic constitutive equations may also be justified by the fact that bone mass is  $\approx 30\%$  collagen, see Section 13.1, which has been experimentally characterized as viscoelastic [206,222,223]. It has been experimentally verified that biological soft-tissue, which is mostly composed of collagen, can be accurately modelled by the Voigt, Maxwell and Kelvin viscoelastic constitutive equations, see [206,224,225] and references therein.

A recent study by [226] showed that boneviscoelasticity is affected by the composition of the molecular scale. Viscoelastic parameters measured at the macroscale may not be directly related to viscoelastic parameters measured at lower-scales, see Definition 9. A new microscopic viscous-hyperelastic constitutive equation for human trabecular bone based on depth-sensing indentation tests was presented by [227].

**Plastic-Viscous materials**, or viscoplastic materials, see Appendix C, are plastic materials that exhibit post-yield strain-rate dependency, which has been experimentally verified at the macroscale [228–231]. Still, few works ventured to model bone as a viscoplastic material.

**Highlight 6.** *An Elastic-Plastic-Viscous constitutive equation for the analysis of trabecular bone under compression is presented by [232].*

The water content within bone may also explain its viscous (both viscoelastic and viscoplastic) behaviour [233].

**Definition 4** (Porous Material). *Porous materials consist of a solid body topologically defined over a simply connected spatial domain whose convex hull features non-solid gaps. The non-solid gaps are known as pores.*

**Elastic-Porous materials**, or poroelastic materials, see Appendix C, in which fluid flows through porous elastic solids, are modelled by equations from the theories: of elasticity, of viscous fluid flow and of fluid flow through porous media, see [222,234] and references therein. When devising a multiscale poroelastic cortical bone model, ref. [144] found that the fluid flow influences the stiffness of bone. A constitutive equation accounting for the pressure both in the *material pores*  $10C_1$  and over interconnected *fluid compartments*  $10C_2$  within a porous solid is studied in [235]; in bone,  $10C_1$  may refer to the collagen-water-hydroxyapatite-lattice lengthscale, see Section 13, and  $10C_2$  may refer to the bone marrow-filled intertrabecular pores, see Section 13.

**Plastic-Porous materials**, or poroplastic materials, see Appendix C, in which fluid flows through porous plastic solids, are modelled by equations from the theories: of plasticity, of viscous fluid flow and of fluid flow through porous media. From a generic poroplastic model for binary mixtures, where the mixture may be assumed as consisting of solid bone and biomaterial, ref. [236] estimated the yield stress associated with the outset of remodelling, see Remark 19.

**Definition 5** (Damageable Materials). *In this paper's terminology, Damageable Materials refers to materials accurately modelled by damage-accounting constitutive equations, see Appendix C—Damage Mechanics. Such constitutive equations are obtained by modifying any non-damage-accounting constitutive equation; these modifications include, in a known constitutive equation, a damage variable which is a mathematical representation for an ensemble of microdefects in the spatial domain of the material [237].*

**Elastic-Damageable materials** have been considered by [60,76].

**Plastic-Damageable materials** have been considered by [54,56,64,73,75,80,124].

Other materials, modelled using constitutive equations combining Elastic-Plastic-Viscous-Porous-Damageable materials are possible. For instance, by devising a trabecular bone model with both *poro-* and viscoelastic constitutive equations, [238] argued that, at certain lengthscales, viscoelasticity, not poroelasticity, accounts for almost the entirety of the “total stress” over a cubic bone sample.

**Remark 18.** *The specialized experimental literature shows that bone may be accurately modelled as an elastic-plastic-viscous-porous-damageable material. Indeed, it is reasonable to assume that bone (and any other material) exhibits a -as complex as possible/accounting for all variables- mechanical behaviour. However, when modelling bone fracture, it is not necessary to account for all possible variables to reach accurate fracture predictions. For example, metals are in reality anisotropic, see Section 10.2, but isotropic computational models of metals exhibit accurate predictions used by design and structural engineers. It is thus important that physicists and engineers find out which variables and which constitutive equation satisfactorily models and predicts bone fracture.*

**Remark 19** (Bone Remodelling). *In brief, Wolff's law (originally in German, Das Gesetz der Transformation der Knochen [239] enunciates that: living bones tend to become stiffer and denser when periodically loaded; on the other hand, when not periodically loaded, bones shrink and become more fracture-susceptible. Wolff's law is best described by bone remodelling [240], which is basically characterized by two processes [241–243]: (1.) bone resorption, i.e., bone tissue erosion by osteoclasts; (2.) bone formation, i.e., bone synthesis by osteoblasts. Osteoporosis and several other bone diseases are a consequence of bone remodelling malfunction [244,245], i.e., higher ration of bone resorption in comparison with bone formation.*

Wolff's law and bone remodelling explain, for instance, a phenomenon known as **stress shielding**, see Definition 6, and also why astronauts exhibit thinner bones. In space, astronauts are exposed to lower levels of gravity than on earth, meaning that their bones will be subjected to lower stresses.

**Definition 6** (Stress Shielding). *Bone implants are usually made of materials that exhibit much higher stiffness (and general mechanical properties) than bones. The stresses applied on a bone in contact with an implant tend to*

be shielded from that bone by the implant. This bone tends, therefore, to become less dense and stiff, as described by Wolff's law, see Remark 19. This loss of density and stiffness caused by much stiffer bone implants is labeled stress shielding [246].

Furthermore, Wolff's research on femoral heads found out that trabecular bone adapts its orientation in the direction of applied forces, seeking an optimal inner structure with minimum stress concentration. This change in geometry follows the forces acting within the trabeculae and is mathematically describable, i.e., it behaves following mathematical laws [147,243,247,248].

## 10.2. Material Symmetry

Material symmetry regarding mechanical properties [249] (p. 84), defined for LE-materials only, may be assumed as being of one type out of eight possible types [222,250]: isotropic, cubic, transversally isotropic, tetragonal, trigonal, orthotropic, monoclinic and triclinic. Materials featuring symmetry types 2–7 are labeled anisotropic. Though it is not impossible for a NLE-material to feature a type of material symmetry, no material symmetry categorization for such materials exists, as seen in Figure 1. Every possible material is either LE or NLE, see Remark 16.

The survey found 3 main types of material symmetry used to devise LE computational bone models; they are listed in column 5 of Table 2 and are further discussed

**Isotropic materials**, see Appendix C, are the most implemented material symmetry among the surveyed literature, see Table 2(5A). Isotropic materials are easier to implement than anisotropic materials (they possess only two independent constants out of twenty-one possible, triclinic). Patient-specific, e.g., QCT-based, estimation of anisotropic material symmetry is still a non-mature field of research [31,36]. This might be another reason why isotropic materials are more often implemented, especially among patient-specific computational bone models.

**Open Issue 4 (Isotropy Assumption).** *Depending on the conditioning of the elastic stiffness matrix, a theoretically anisotropic bone can be accurately represented as an isotropic material, e.g., small differences between stresses and displacements calculated assuming isotropic and orthotropic patient-specific mechanical properties have been presented by [44]. Anisotropic models, when compared with isotropic models, sometimes exhibit a minimum effect on the correlation between macroscale analysis and experiments [81,115,127,251,252], sometimes exhibit relevant improvements.*

**Transversal Isotropic materials**, see Appendix C, are the most implemented anisotropic material symmetry among the surveyed literature, see Table 2(5C). Bone exhibited experimental transversely isotropic material symmetry in some works [233,253,254]. Recent works modelled bone as a transversally isotropic material [220,255].

**Orthotropic materials**, see Appendix C, are considered to best describe bone material symmetry. Bone exhibits orthotropic material behaviour in many works, e.g., [44,212,256]. However, small differences between stresses and displacements calculated assuming isotropic and orthotropic patient-specific mechanical properties have been found, e.g., by [44].

Though bone consistently seems to be orthotropic, its LE-symmetry is subject-specific, and thus patient-specific [222]. The same bone from different individuals may present different material symmetry.

**Triclinic materials**, or general anisotropic materials, and other types of material symmetry, see Appendix C, and their application to model bone is still a non-mature field of research. In vitro experiments have not shown such behaviours. That is mainly because triclinic material symmetry could not be experimentally measured and identified [212]; triclinic symmetry could only be assumed. Later, however, experimental methodologies for determination of all triclinic symmetry parameters was presented [257,258].

Few works are found in the literature applying a material symmetry not shown in column 5 of Table 2. Although no definite statement can be made on the real in vivo behaviour of bone, in vitro bone experiments exhibit anisotropic mechanical properties [221,259]. Yet, the great majority of the literature assumed bone and its components (e.g., hydroxyapatite, collagen) to be isotropic, see Table 2.

Modelling bone as an anisotropic material may improve fracture risk predictions, but anisotropy might not be obtained from medical imaging, i.e., may not be obtained from patient-specific methods [36].

### 10.3. Homogeneity Regarding Constitutive Equation and Anisotropy

Solid bodies, in regard to the spatial distribution of their mechanical properties, can either be homogeneous or inhomogeneous, see Appendix C. Computational bone models listed in column 6 of Table 2 assumed bone to be at times homogeneous, at times inhomogeneous.

**Homogeneous materials**, see Appendix C, feature, at any arbitrary pair of points within their spatial domain, mechanical properties of the same numerical value. Though some materials can be accurately modelled as homogeneous, no real-world material fits such description. Computer implementation of a homogeneous material is a mature field of research.

**Inhomogeneous materials**, see Appendix C, feature, at any arbitrary pair of points within their spatial domain, mechanical properties that are not necessarily of the same numerical value. Estimation of inhomogeneous mechanical properties from medical imaging-based geometry models is straightforward and has been performed by many of the references in Table 2(6C).

**Open Issue 5.** *Devising standardized material tests for the obtention of experimental measurements bone mechanical properties remains an open issue. The multiscale structure of bone makes mechanical properties both lengthscale- and bone site-dependent, see Section 13.*

Patient-specific inhomogeneous bones are most commonly modelled by splitting the spatial domain into smaller homogeneous subdomains and assigning specific mechanical properties to each subdomain. These subdomain-specific mechanical properties can be computed from medical imaging data, e.g., CT. The definition of subdomains requires domain discretization, see Remark 14 and 9A5.

**Remark 20** (A General Remark on the Physics of Bone Modelling). *Though outside the scope of this review, some scarcely studied phenomena include: the effect of fiber orientation; the rate of loading; the velocity of impact; the spatial distribution of calcium; the dependence of Young's Modulus and damping on bone site; piezoelectricity; bone aspect ratio; stiffness reduction after the initial formation of small cracks [260]; the decrease of stress concentration factor around holes in the presence of couple-stress effects [261]; creep effects [262]; application of micropolar theory and couple stress theory [263]; drying and re-wetting effects [264]; osteonal microstructure and cortical porosity differences that may be adaptations related to regional differences in strain mode and/or strain magnitude [265]; disparity in mechanical properties of compact bone in tension vs. compression; the influence of bone integrity [266]; work of fracture [267]; Terzaghi's effective stress [268].*

### 10.4. Patient-Specific Mechanical Properties

Medical imaging techniques have often been used to estimate bone patient-specific mechanical properties, see Table 2(7C). CT is the most used technique for assigning patient-specific homogeneous, LE, isotropic properties to sub-domains of a mesh, see Table 2(1A), [38,97,98,111,112,118,119,269–273].

CT cross-sectional images (CT-images or CT-slices) are created by X-ray tubes and detectors, which rapidly rotate around the patient's body while the patient is slowly moved through the ring-shaped CT-equipment. The emitted radiation penetrates the patient's body and is either totally or partially absorbed. The detectors receive the residual radiation and send electrical signals to computers. Calculations generate cross-sectional images of the patient's body. Each CT-image is interpreted by the computer as a pixel-matrix. Pixels (picture elements) are the elements of the matrix (3D pixels are

labelled voxels, i.e., volume elements or volumetric pixels). Each pixel is assigned a linear attenuation coefficient, which is converted into Hounsfield Units (HU) [274] by

$$CT_{\text{num}}(\mu_{\text{tissue}}) = 1000 \frac{(\mu_{\text{tissue}} - \mu_{\text{H}_2\text{O}})}{\mu_{\text{H}_2\text{O}}} [\text{HU}] \quad \text{or} \quad CT_{\text{num}}(\mu_{\text{tissue}}) = 1000 \frac{(\mu_{\text{tissue}} - \mu_{\text{H}_2\text{O}})}{(\mu_{\text{H}_2\text{O}} - \mu_{\text{air}})} [\text{HU}] \quad (1)$$

where  $CT_{\text{num}}$  indicates the CT-number, i.e., grayscale pixel-value given in HU; and  $\mu_{\text{tissue}}$  and  $\mu_{\text{H}_2\text{O}}$  represent the attenuation coefficients of the tissue (pixel) and water, respectively. The Hounsfield Unit was created such that the CT-number of water and air are set to 0 and  $-1024$  HU, respectively. It provides a more tangible reference for values seen in the grayscale CT-images. Figure 2 illustrates the Hounsfield-scale for different kinds of biological tissues.

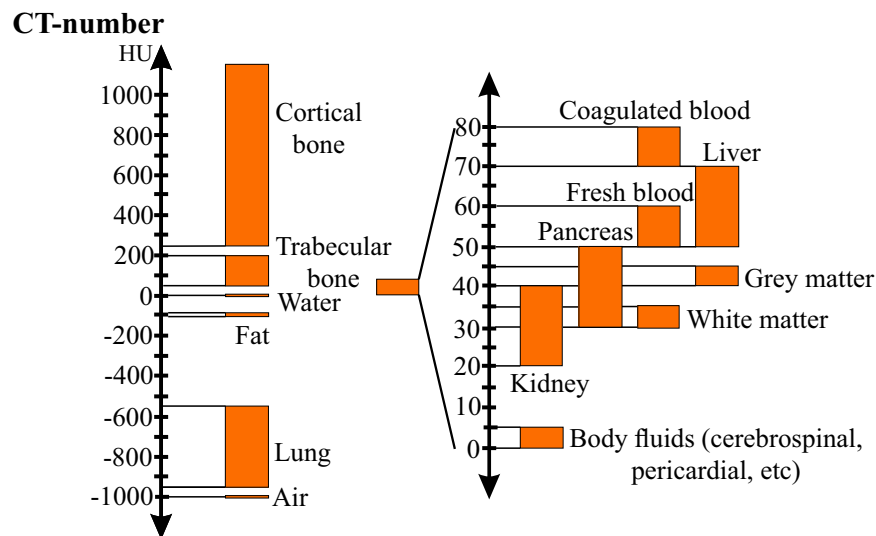


**Figure 2.** Hounsfield-Scale for different kinds of tissues (adapted from © Institut für Anatomie, Universität Bern (<https://elearning.medizin.unibe.ch/morphomed/radioanatomie/ct-mrt-des-rumpfs/ct-mrt-einf%C3%BChrung/hounsfield-skala>)).

When a calibration phantom is scanned with the bone, HU-values can be converted into volumetric bone mineral density (vBMD), also labelled as radiological density or quantitative equivalent CT-density ( $\rho_{\text{QCT}}$ ), using an affine function [36,153,275,276]:

$$\rho_{\text{QCT}} = a \cdot CT_{\text{num}}(\text{HU}) + b \quad (2)$$

**Remark 21** (vBMD). *CT is not the only medical imaging technique able to quantify vBMD. MRI-images, though not as suited to estimate bone density as CT-images [150,277], were used to accurately quantify in vivo vBMD of a patella by [278] and to estimate CLE-properties [48,131].*

**Highlight 7** (Patient-Specific Phantomless Estimation of BMD). *Very recently, a phantomless method of estimating vBMD from HU was proposed by [279].*

In the context of bones, depending on experimental measurements, density can be defined in different ways [280]. The three most relevant density measures in the context of patient-specific material properties estimation are [187,275,276]:

$$\text{Real density: } \rho_{\text{real}} = \frac{\text{wet mass}}{\text{solid volume}}; \quad \text{Apparent density: } \rho_{\text{app}} = \frac{\text{wet mass}}{\text{bulk volume}}; \quad \text{Ash density: } \rho_{\text{ash}} = \frac{\text{ash mass}}{\text{bulk volume}};$$

where bulk volume is the total volume of the solid and non-solid material,  $V_{\text{bulk}} = V_{\text{solid}} + V_{\text{non-solid}}$ . The solid volume is the volume occupied by the solid material only, not including porosity.

The different types of bone density are directly correlated. The literature on the relationships used in the conversion of  $\rho_{\text{QCT}}$  measures to  $\rho_{\text{ash}}$ ,  $\rho_{\text{app}}$ , and  $\rho_{\text{real}}$  (or tissue density) as well as the relationships between these densities and the CLE-properties of patient-specific bone was reviewed by [275].

The existence of density-elasticity relationships, i.e., relationships between CT-estimated bone density and LE properties, e.g., Young's Modulus  $Y$ , has been empirically studied by [102,118,169,281,282] and the works therein. Density-elasticity relationships are usually represented by a power function and have a great influence on the prediction of the CLE-properties of bone [36,68].

$$Y = k \cdot \rho_{\text{ash/app}}^p \quad (3)$$

where the coefficients  $k$  and  $p$  are experimentally estimated. Though most commonly estimated through experiments, density-elasticity relationships can be determined by inverse computational approaches [36,283,284]. Due to the uniqueness of each bone, there is no density-elasticity relationship that accurately estimates macroscopic mechanical properties for all bones [214,280]. In the hypothesis of [68] that each bone specimen has its individual density-elasticity relationship, bone CLE-properties are assumed to be patient-specific, suggesting that a density-elasticity relationship should be determined for each bone.

According to [102], who compares several density-elasticity relationships, some of the published relationships are unsuitable for strain prediction in bones. However, subject-specific models that used the density-elasticity relationship proposed by [281] showed very good accuracy in predicting strains [102,111]. Relationships proposed by [256,285] showed less accuracy. The density-elasticity relationship proposed by [281] also exhibits good strain and strain-energy predictions in long bones [116] and in shoulders [30].

**Remark 22** (Bone Mechanical Properties from Continuum Micromechanics). *It is possible to replace purely empirical, CT-based, HU-density-elasticity relationships by other relationships based on continuum micromechanics that consider the micro-morphological features of bone within each voxel of a CT-image. Such relationships account for voxel-specific: bone structure, vascular porosity and volume fractions of HA, CLG and H<sub>2</sub>O, see Section 13. Usage of such relationships may improve mechanical behaviour prediction [115,140,286–291]. Emphasis on [115], the first to consider an inhomogeneous Poisson's ratio for bone. Continuum micromechanics may be coupled with ultrasonic experiments, instead of being coupled with CT, to estimate the CLE-properties of bone [292].*

The process of assigning homogeneous mechanical properties  $\mathbf{10B}_1$ ,  $\mathbf{10B}_2$  from medical images onto sub-domains of a 3D-mesh  $\mathbf{9A}_5$  of an inhomogeneous computational bone model, see Definition 2, is labeled *material mapping* [75,98,118,119]. The strategy used to perform a material mapping can have a great impact on the assignment of bone CLE-properties [118,119].

There are several software packages that perform a material mapping. SimpleWare ScanIP and MIMICS are the most consolidated. Several works used the freeware Bonemat to perform material mapping [38,119,120,269,270]. Bonemat was also used as a reference to develop and validate other material mapping strategies tools [97,118,271,272].

**Open Issue 6.** *CT-images are two-dimensional and CT-voxels are points in space, therefore, a voxel does not contain local anisotropy. However, different techniques and approaches to extract anisotropic mechanical properties from CT-data were proposed in the literature [44,73,74,81,168,221,251,286,293]. Most commonly, different values of  $k$  and  $p$ , see Equation (3), are given for different directions. The micromechanics-based approach shown in [115,140,286–291] does not derive anisotropic properties purely from CT-images, but correlates each CT-voxel to an anisotropic tensor based on the voxel-specific volume fractions of HA, CLG and H<sub>2</sub>O, see Section 13.*

*Yet, as mentioned in Section 10, the influence of anisotropy on the accuracy of the model's behaviour, as the extraction of anisotropic properties from medical images, is still an open issue [81,251].*

Cortical and trabecular bones exhibit different geometries and mechanical properties, see Section 13, thus, they require different density-elasticity relationships [44,90,92,93,106,115,121]. Further, some works define an upper limit for the Young's Moduli (or HU values) evaluated using density-elasticity relationships, since external interferences or error by the scanning may occur [44,87,269].

### 11. Mathematical Model of Bone Trauma-Inducing Accident—The Boundary Conditions

BCs for patient-specific fracture simulations should preferably be derived from realistic models of common accidents among the elderly. In a solid mechanics problem, for instance, BCs are usually represented as surface forces and displacements.

Figure 3 illustrates examples of falls, backwards and forwards, that may originate fragility fractures. The “\*” in the accident model box in Figure 1 row II indicates that this stage is represented in Figure 3.

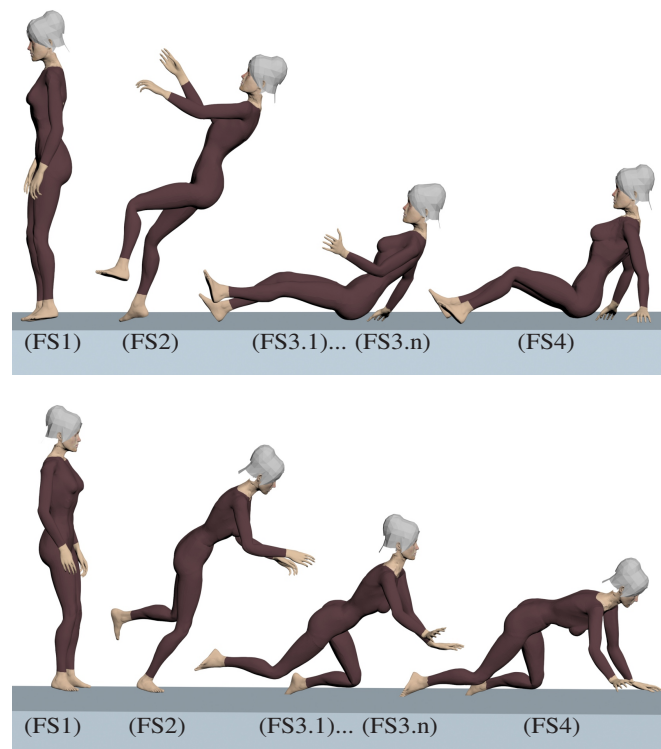


**Figure 3.** Backwards and forwards fall.

Both backwards and forwards falls can be seen as a sequence of instantaneous motions, illustrated in Figure 3 by Fall Stages (FSs).

- FS 1** Normal human gait, i.e., walk or run. The individual is in motion through the movements of the legs, e.g., at stance position.
- FS 2** Tip over, or equilibrium loss. This stage characterizes the fall. The equilibrium loss occurs when the challenge to balance is greater than the ability or strength to stay upright.
- FS 3.1** 1st environment collision. The first collision between the body and a solid surface from the environment, e.g., the floor. It is usually the most intense and fracture-susceptible collision. The first collision is usually followed by a series of other collisions caused by inertial movements. Picture a bouncing ball; the idea is the same. As long as the inertial forces are greater than the ability to stop them, collisions will follow.

- FS 3.2** 2nd environment collision. The second collision may have one or more contact points, or zones, between the body and environment, e.g., the individual may hit the floor with both hands or with hip and a hand at the same time.
- FS 3.i** *i*-th environment collision. The *i*-th collision may have one or more contact points, or zones, between the body and the environment.
- FS 3.n** *n*-th environment collision. Similar to the second collision, the *n*-th, and last, collision may have one or more contact points, or zones, between the body and environment. It is often the least fracture-susceptible collision. The first collisions have already absorbed most of the kinetic energy of the fall.
- FS 4** Final position. Characterizes the accommodation of the body. Here there is only minor motion. There is no more collision with the environment. The individual has already fallen and looks for a rest position. The accommodating motion is not relevant for fracture.

This description of FSs is valid for any bone and any fall. Side-ways falls have not been illustrated in Figure 3, but exhibit similar FSs. Depending on environment obstacles, individual reflex and motor skills, a different bone can first collide with the environment at FS 3.1. Furthermore, all instantaneous motion described by FSs can be considered a *quasi*-static equilibrium. Thus, it is reasonable to evaluate the motion equation in a *quasi*-static sense, i.e., equilibrium equation [147,294], see Governing Equation (1).

In Figure 3, the collision happens between the body and the environment. However, most of the surveyed papers simulate bone individually, i.e., external forces are applied directly on the bone; neighbour-tissues are neglected. Forces applied on the exterior part of the body, i.e., on the skin, are not the same as the forces acting directly on the bone at the interior of the body.

**Open Issue 7** (Body BC vs. Bone BC). *The tissues between the bone and the contact point partially absorb the impact, displaying a damping effect. When transporting BCs from contact points to the boundary of the bone, the energy absorbed by these tissues should be taken into account.*

*Very recently, a model which predicts the fraction of the collision force that is transferred to the boundary of bones was presented by [126]. This model takes into account damping effects due to flooring elements (i.e., carpets), protector devices (if present), all active tissues (muscles) that contract at the instant of impact and all passive soft tissues interposed between the point of impact on the skin and the lateral aspect of the greater trochanter of the femur.*

In general, the simulated bone should always be assumed as the limiting bone, i.e., as the bone that will fracture first. Each kind of fall has its limiting bone. For instance: (1.) if you fall on your hand(s), the wrist is the most fracture-susceptible bone; (2.) if you fall on your back, the spine is the most fracture-susceptible bone; (3.) if you fall on your backside, the hip bone is the most fracture-susceptible bone, (4.) if you fall on your knees, the femur is the most fracture-susceptible bone.

Neighbour-bones of the limiting bone are also usually affected by the collision, but less directly and critically. The forces acting on these bones have been already damped by other tissues. Furthermore, between FS3.1 and FS3.n there are multiple collisions with the environment. It may be argued that only the most intense and fracture-susceptible collision should be modelled for being the most relevant one, however, a sequence of many less intense collisions may also lead the bone to fracture.

**Remark 23** (Multiple Collisions). *No fracture resulting from multiple collisions was considered in the surveyed literature.*

Highlight 8 summarizes the surveyed papers with major contributions and interesting findings on deriving BCs from dynamic models and imposing them onto the bone surface.

**Highlight 8.** A model accounting for fall rate, stochasticity of fall scenarios including fall kinematics, postural reflex and fall impact attenuation conditions was presented by [126].

The interaction between body and ground using a mass-spring-damper system and patient-specific variables, e.g., hip soft tissue thickness, body mass index, body height and weight, was modelled by [35,295,296]. Conclusions showed that patient-specific dynamic models can improve the accuracy of hip fracture risk analysis.

The influence of loading direction on strength and fracture sites of the proximal femur is presented by [100]. A CT-based FEM, see Section 12, is used to determine loading directions under which the proximal femur is most fracture-susceptible.

Patient-specific loading forces acting on the proximal femur during a sideways fall is estimated by [39].

Loading conditions mimicking typical sideways falls on the hip are modelled by [41]. Femoral neck internal rotation angles varying from  $-30^\circ$  to  $45^\circ$  at  $15^\circ$  intervals are selected to simulate a range of possible falling configurations.

A free library available by <http://www.orthoload.com> provides a direct approach to estimate force BCs acting in human joints [160].

Homogenized yield properties of human femoral trabecular bone are evaluated and compared in [297] by applying kinematic uniform BCs and periodicity-compatible mixed uniform.

Using basic principles of kinematics and dynamics, ref. [298] estimates peak impact forces on the greater trochanter in sideways falls from standing height.

A comprehensive database of hip contact forces and simultaneously measured gait data for improvements of hip implants is provided by [299].

Very recently, ref. [300] studied the influence of BCs on bone fracture assessed using the FEM, see Section 12.

BCs should very closely imitate *in-vivo* situations and be as simple as possible so simulations can be experimentally validated [160], see Section 15. The estimation of the forces exerted by muscles, ligaments constraints, and joint reactions is still a major scientific challenge [111]. BCs strongly influence elastic-plastic mechanical properties of heterogeneous materials estimated by homogenization techniques, see Section 14, [297], and are of major relevance for the accuracy of fracture simulation.

The main goal of determining appropriate and realistic BCs from fall models is to calculate stress and strain fields within the bone geometry, which can be further related to fracture.

In Table 2(8A), many of the surveyed references estimate BCs from very simple accident models. A specific force is simply and directly applied on the femur's head and said to be the representation of a side-ways fall or stance position [91,105,106,108–112,121,122,129].

## 12. Simulating Bone Fracture

Figure 1 illustrates the PDEs that describe (or “govern”, see Remark 24) the solid continuum mechanics. Motion and strain-displacement equations are briefly discussed in this section. Constitutive equations are discussed in Section 10.

**Remark 24** (Governing Equation). *Governing equations are mathematical equations that describe phenomena, natural or otherwise. Solving governing equations provides the values of previously unknown dependent variables based on changes of known independent variables and on the numerical value of relevant physical constants.*

**Governing Equation 1** (Motion Equation). *The macroscopic geometry defines the spatial macrodomain  $D \in \mathbb{R}^3$ . A patient-specific macroscopic geometry is devised through a mesh, see Remark 14. The motion equation, see Appendix C, is the governing equation of  $D$  and stems from the balance of linear momentum; it can either describe accelerated motion or an equilibrium configuration, see Figure 1 row V.*

*The motion equation represents an equilibrium and is labeled equilibrium equation when the inertial term is neglected [147,294], i.e.,  $\ddot{\mathbf{x}}(t) \approx 0$ , and hence  $\nabla \cdot \mathbf{T}(\mathbf{x}(t), t) + \mathbf{b}(\mathbf{x}(t), t) = \mathbf{0}$ . This is appropriate when inertial*

forces in Figure 3 are much smaller than body and surface forces. For instance, a fall from standing height may be considered a quasi-static equilibrium [71,105,147,294,301].

**Governing Equation 2** (Strain-Displacement Equation). *The strain-displacement equation, see Appendix C, relates the strain tensor  $E(\mathbf{u}(\mathbf{X}(t), t), \mathbf{X}(t), t)$  and the displacement vector field  $\mathbf{u}(\mathbf{X}(t), t)$ . When only relatively small strains, displacements and rotations are considered, the non-linear, i.e., second-order terms, of the strain-displacement equation, i.e.,  $\nabla \mathbf{u}(\mathbf{X}(t), t) \nabla \mathbf{u}^T(\mathbf{X}(t), t)$ , are neglected, and hence  $E(\mathbf{u}(\mathbf{X}(t), t), \mathbf{X}(t), t) = \frac{1}{2}(\nabla \mathbf{u}(\mathbf{X}(t), t) + \nabla \mathbf{u}^T(\mathbf{X}(t), t))$ , see Figure 1 row V.*

**Governing Equation 3** (Compatibility Equation). *The compatibility equation guarantees that there is a single-valued displacement vector field  $\mathbf{u}(\mathbf{X}(t), t)$  associated to each point of the spatial domain  $D$ . The compatibility equation is needed in a continuum solid mechanics problem only when strains  $E(\mathbf{u}(\mathbf{X}(t), t), \mathbf{X}(t), t)$  are given as inputs. In bone fracture analysis, however, displacements  $\mathbf{u}(\mathbf{X}(t), t)$  are given as inputs, i.e., as BCs, see Figure 1 rows IV to VI. Thus, the compatibility equation is usually not necessary in the algorithm for a computer simulation.*

Different forms and assumptions of the governing PDEs may have specific terminologies that are commonly misused by the literature on bone fracture and continuum mechanics.

**Remark 25** (Misleading Term—Nonlinear Analysis). *Terms such as nonlinear analysis may be misleading. For instance, [99,101,131] speak of non-linear analysis, but do not specify the type or source of non-linearity. There are mainly four types/sources of non-linearity in a solid continuum mechanics problem [302] (p. 85), [303] (p. 8): (1.) material nonlinearity, i.e., when an NLE constitutive equation is used, see Remark 16; (2.) geometric nonlinearity, i.e., the strain-displacement equation does not include the second-order term, see Governing Equation (2); (3.) kinematic non-linearity, i.e., when the displacement BCs depend on the deformations of the structure; and (4.) force nonlinearity, i.e., when the applied forces depend on the deformation of the structure.*

The PDEs that describe deformations in solid continuum mechanics problems cannot be solved analytically for complex geometries, e.g., bones. Numerical methods capable of solving PDEs through approximations are required. Three main numerical methods can be applied in solid continuum mechanics:

The **Finite Element Method** (FEM) subdivides the spatial domain into subdomains (or elements) and approximates the governing equations by traditional variational methods over each subdomain [303]. The FEM is by far the most used numerical method in the bone fracture literature [148,160,304]. Most probably because there are many commercial software with friendly user interfaces that facilitate its operation, and because the FEM is a mature field of research which has been optimized for several applications. For instance, FAIM, a finite element solver optimized for solid mechanics simulations of bone, was developed by [305,306].

The **Boundary Element Method** (BEM) requires discretization of the boundary only and, for this reason, usually requires a smaller number of DOF than the FEM to achieve accurate results [307,308]. A discretization of the spatial domain into subdomains, commonly labelled subregions by the literature on BEM, is required when the analyzed material is inhomogeneous [307,309], see Section 10. The BEM has been scarcely used in the field of bone fracture. However, some works have used the BEM for bone remodelling simulation [310–315].

The **Finite Difference Method** (FDM) is simple in formulation, but exhibits some difficulties in modelling complex geometries and, for this reason, has been scarcely used for solid mechanics problems in recent years [316,317]. FDM was used by [318] to simulate bone remodelling, see Definition 19.

Other numerical methods are also available, e.g., method of characteristics, finite volume method, et cetera; these are outside our paper because, to the best of the authors' knowledge, they have not yet been applied to bones.

**Open Issue 8** (Exploring BEM and FDM). *The BEM and the FDM have been scarcely used by the literature on bone fracture. The BEM is, however, particularly recommended for fracture mechanics problems [309]. The FDM succeeded in fluid dynamics and is mostly used when studying fluid and wave propagation within bones [319,320].*

**Remark 26** (Inputs for Numerical Methods). *A mesh covering the geometry (Remark 14), mechanical properties  $10\mathcal{B}_1$ – $10\mathcal{B}_3$  and BCs, see Section 11. The non-mathematical reader should know that all numerical solution procedures share these same inputs.*

The primary goal of fracture simulation is to evaluate strain and stress fields and to associate them with failure criteria. A recent review made by [148] has shown that stress- and strain-based failure criteria may improve the prediction of fractures [112,321].

There are several different ways of approaching fracture mechanics problems [322–325]. **Linear Elastic Fracture Mechanics** (LEFM), the classical and mature cracking process mathematical model, is restricted to elastic materials. Though largely applied, LEFM is not the most appropriate approach to describe crack propagation in bones [326]. **Elastic-Plastic Fracture Mechanics** (EPFM), though more recommended for materials exhibiting large plastic zones (of the same order of magnitude as the crack size) at the crack tip, has been less successful than LEFM in predicting fracture when large yielding prevails [324]. The **Cohesive Zone Model** (CZM) is based on considering fracture separation occurring at an extended zone ahead of the crack tip (also labelled “cohesive zone”). Two reasons make the CZM superior to LEFM for bone fracture analysis: (1.) Bone fracture experimental data analysis performed by [327] demonstrated the need for a nonlinear model considering a spatial stress distribution at the fracture zone. (2.) Unlike the LEFM, the CZM can remove stress singularities ahead of the crack tip; i.e., ahead of the furthest extent of damage [143]. Furthermore, both LEFM and EPFM require a pre-existing initial crack, whereas the CZM can be modelled at the interface between continuum elements (spatial sub-domains) [328].

**Remark 27** (Animal Bone Modelling and Simulation). *Parallel to the work conducted on modelling human bone, there have been efforts to model bone of several animals. Studies range from small animals such as mice [287,329–336], rats [288,337–343] and zebrafish [344], to medium-sized animals such as dogs [345], as well as large animals such as pigs [346–352], sheep [353–355], bovine [220,356–363] and horses [273,364].*

*As it is done with human bone, subject-specific animal bone geometry models are created from CT-data [345,365], see Section 9. The influence of CT resolution was investigated by [357,363,366]. Some works used  $\mu$ CT to create high-resolution animal bone geometry models [287,344,365,366].*

*There are not many dynamic models of animal motion [364,365,367]. Due to this apparent lack of interest in animal motion simulation, most animal bone simulations use BCs representative of experiments, see Table 2(8C), e.g., compression [340], 3-point bending tests [357,361] and 4-point bending tests [349]. Thus, simulations of clinically relevant situations in animal models is not those of human models.*

*Fabricating specimens, see Definition 7, from animal whole bone samples compromises experiment reliability, even more so in the case of small animals. Thus, most experiments are made on whole bones. It is difficult to hold small animal bone samples, e.g., mice bone [336], in a fixed position during experiments due to the presence of asymmetrical loadings, e.g., twisting of the sample at the areas touching experimental apparatus can easily occur [330,335].*

*Bones, human and animal alike, are modelled and simulated using the same techniques to: acquire bone geometry, see Section 9; estimate mechanical properties, see Section 10; use equations based on continuum mechanics, see Section 4; solve said equations using numerical methods, see Section 12. Furthermore, models of*

mechanical and reconstructive properties of animal bones, e.g., osseointegration, bone ingrowth and bone marrow reconstruction were investigated by [333,337,339,341,347,359,368].

Research directives within the field of animal bone modelling and analysis include **12.A<sub>1</sub>–12.A<sub>3</sub>**.

**12.A<sub>1</sub>**: Usage of animal bone experimental data to estimate mechanical properties [220,287,288,330,331,340,342,347,363,369] and conception of animal bone failure models [331,338,349,351,356,358,362] that may be similar to human bone failure models [342,344,370]. This directive includes studies in which pathological changes to the skeleton are purposefully induced in test animals by genetic manipulation [371] or malnutrition [332,338,354] in order to create models to study osteoporosis [338,354].

**12.A<sub>2</sub>**: Biocompatibility evaluation, via *in vivo* experiments, of implant materials [339,355,356,360,372,373], implant designs [352,374], and surgical techniques [353], with the host tissue. These evaluations, are first performed on animal tissues as a stepping stone towards application in human tissues.

**12.A<sub>3</sub>**: Conception of models that: explain animal bone mechanical behaviour [369,375]; compute key variables of animal implant design [376]; and help in designing treatment procedures [345,348,350]. These studies mostly focus on domestic and farm animals.

**Definition 7** (Specimen). *A specimen is a standardized material sample meant to represent larger quantities of the same material and built for controlled laboratory experiments.*

### 13. The Multiscale Structure of Bone

To improve bone fracture risk analysis, more accurate simulations are required. To perform more accurate simulations, more realistic models are needed. To create more realistic models, a deep knowledge of the multiscale structure of bone is required. The multiscale structure of bone refers to the complex network of different physical structures and mechanical properties present throughout bone tissue down to the atomic scale, where fracture ultimately originates.

The geometry and mechanical properties **10.B<sub>1</sub>–10.B<sub>3</sub>** of each lengthscale of bone are influenced by the geometry and mechanical properties of lower-scales, see Definition 9. Similarly, the geometry and mechanical properties of the lowest possible continuum lengthscale is affected by molecular features, e.g., by the arrangement and distribution of the molecular structure. Geometry, mechanical properties and several lengthscale-specific physical features of bone, see Open Issue 2, can be quantified, or estimated, through medical imaging techniques, observation and experiments **10.A<sub>1</sub>, 10.A<sub>2</sub>**.

There are three main reasons to perform multiscale fracture analysis on bone [377,378]:

**13.A<sub>1</sub>**: each lengthscale exhibits specific geometries, mechanical properties and physical features;

**13.A<sub>2</sub>**: each lengthscale is directly influenced by the geometry, mechanical properties and physical features of the nearest lower-scale, see Definition 9;

**13.A<sub>3</sub>**: fracture and several other physical phenomena start at the molecular scale.

**Remark 28** (Scales Classification). *There is no “standard” classification for devising bone lengthscales. The surveyed literature sometimes refers to the same lengthscale geometry or physical feature at different lengthscales. For example, unlike [139], ref. [378] does not define a mesoscale. Furthermore, what [378] illustrates as the sub-nanoscale, ref. [139] illustrates as the nanoscale of bone. Thus, when modelling different bone lengthscales, it is important to define the geometric features and characteristic length of each lengthscale.*

Figure 4 illustrates the bone lengthscales found in the reviewed literature. Each lengthscale is discussed in the following subsections.

The continuum mechanics approach shown in Figure 1 can be applied to any lengthscale that is coarse enough to be modelled as a continuum. The molecular scale should best be assumed as a non-continuum.

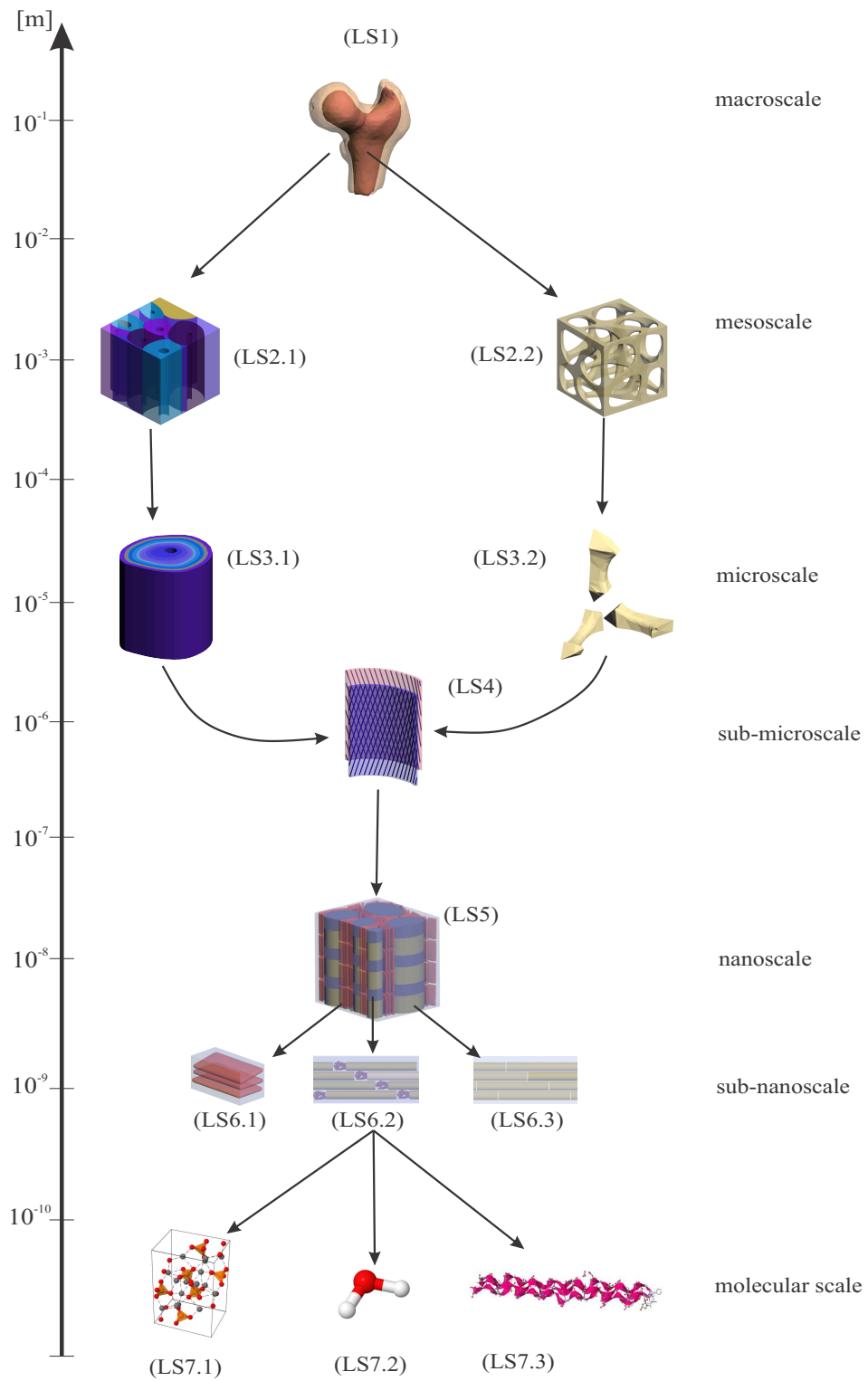


**Figure 4.** The multiscale structure of bone.

### 13.1. Molecular Scale— $H_2O$ -CLG-HA Lengthscale

At the molecular scale, see Figure 4, bone is composed of three components: water LS7.2, an organic phase LS7.3 and an inorganic phase LS7.1. Water ( $H_2O$ ) represents approximately 10% of total bone mass. The organic phase represents 30% of total bone mass and is 90% constituted by of type I ColLaGen (CLG) and 10% by of a combination of other collagen types (III and VI) plus non-collagenous proteins. The inorganic phase of bone is a ceramic crystalline-type mineral labelled hydroxyapatite (HA):  $Ca_{10}(PO_4)_6(OH)_2$  [61,379] and represents 60% of total bone mass [380].

#### Characteristic Length 1 (Molecular Scale).

|                                      |              |            |                              |
|--------------------------------------|--------------|------------|------------------------------|
|                                      | HA length    | 20–200 nm  | [61,139,191,378,379,381–383] |
|                                      | HA width     | 15–70 nm   | [61,139,191,378,379,382,383] |
| HA mineral crystal and CLG molecule: | HA thickness | 1.5–5 nm   | [61,139,191,378,379,382,383] |
|                                      | CLG diameter | 1.5–3.5 nm | [61,139,378]                 |
|                                      | CLG length   | 300 nm     | [61,139,222,378,384]         |

**Remark 29** (Proportion of HA, CLG and  $H_2O$  Contents). *Bone's HA, CLG and  $H_2O$  contents vary from species to species, from individual to individual and from one anatomical location to another. Yet, the average chemical composition of healthy bone inside a large-enough cube-shaped volume remains constant in space (i.e., across all cube-shaped volumes comprising the whole bone) and in time (i.e., along the aging process, starting from early adulthood) [115,140]. Since bone CLE-properties depend mostly on the proportion between its HA, CLG and  $H_2O$  contents, different proportions translate into correspondingly different CLE-properties [115,140,286–291,385].*

Collagen alone displays a multiscale structure [386–388]. A single collagen molecule, a tropocollagen, is a helical structure consisting of three left-handed polypeptide chains coiled around each other to form a right-handed superhelix. What is known as collagen is actually tropocollagen, the basic triple-helical structural unit of collagen, i.e., a single collagen molecule.

It is in the molecular lengthscale where vitamin deficiency, sunlight exposure time, physical activities and other variables presented in Open Issue 2 are hidden. They alter, among others, the distribution and arrangement of atoms and molecules. Changes in the physical structure and chemical composition at the molecular lengthscale imply changes in geometry and mechanical properties at higher-scales, see Definition 9. These changes have a direct influence on osteoporosis and bone fracture.

### 13.2. Sub-Nanoscale—Mineralized Collagen Fibrils Lengthscale

At the sub-nanoscale, a collection of axially connected CLG molecules located next to each other in a thread-like structure with a high length-to-diameter ratio forms a collagen fibril. The fibrillar structure exhibits an axial periodicity, with gaps between the end of the collagen molecules of  $\sim 40$  nm [383]. Zones across the length of a fibril with gaps are labelled gap zones, see Figure 4 LS6.2. Zones across the length of a fibril with no gaps are labelled overlap zones, see Figure 4 LS6.3. Gap and overlap zones appear periodically with a characteristic distance (D) of  $\sim 67$  nm [383,389,390]. Deposition of the HA crystals, see Figure 4 LS6.1, occurs within gap zones [384]. A CLG fibril with HA deposition is labelled mineralized CoLlaGen fibril (mCLGf), see Figure 4 LS6.2.

HA crystals are also found surrounding and oriented parallel to mCLGfs, i.e., in the extra-fibrillar volume. The extra-fibrillar volume is a foamlike structure basically composed of HA crystals and filled with  $H_2O$  and a small portion of non-collagenous organic matter [61,391]. The major portion of HA crystals, in bone, is located in the extra-fibrillar volume. HA crystals located in the extra-fibrillar volume are larger than HA crystals located within the gap zones of mCLGf. Several experimental approaches confirm the existence of HA in the extra-fibrillar volume, e.g., neutron diffraction [392,393] and electron microscopy [380,382,383,391,394–396]. Furthermore, many works have modelled bone considering HA to be also outside CLG fibrils [142,385,397–399].

**Remark 30** (Mineral Within Bone). *As well explained in [380], there are two views of the sub-nanoscale of bone: an older—and nowadays less accepted—view, which considers HA to be located only within the gap zones of collagen fibrils, building mCLGfs; and a more recent—and more consistent—view, which considers HA to be mostly located in the extra-fibrillar volume, outside mCLGfs.*

**Characteristic Length 2** (Sub-nanoscale).

|                              |                |                  |                          |
|------------------------------|----------------|------------------|--------------------------|
| Mineralized Collagen Fibril: | mCLGf diameter | 20–150 nm        | [61,139,378,379,400–402] |
|                              | mCLGf length   | 10,000–30,000 nm | [401,403,404]            |
|                              | CLGs gaps      | 35–44 nm         | [61,139,222,378,379]     |

**Highlight 9.** *The influence of mechanical properties of the mCLGf and of the extra-fibrillar volume (or matrix) on the mechanical properties of trabecular bone was recently investigated by [405]. The extent of modifications in energy to failure during mCLGf rupture and separation relative to the changes in the properties of the mCLGf and the extra-fibrillar volume was quantified.*

13.3. Nanoscale—Collagen Fiber Lengthscale

At the nanoscale, arranged bundles of collagen fibrils, separated from each other by a thin layer of extra-fibrillar volume, form collagen fibers [206,222,381], see Figure 4 LS5.

**Characteristic Length 3** (Nanoscale).

|                  |                    |                               |                       |
|------------------|--------------------|-------------------------------|-----------------------|
| Collagen Fibers: | CLG fiber diameter | 0.15–0.25/2–3 $\mu\text{m}$   | [378]/[402,406]       |
|                  | CLG fiber length   | $\approx$ 10–30 $\mu\text{m}$ | several mCLGf lengths |

**Remark 31** (Fibers and Fibrils). *Some of the surveyed literature seems to interchange the words fiber and fibril. Both are thread-like structures with a high length-to-diameter ratio, but fibers are larger and thicker than fibrils. A bundle of fibrils characterizes a fiber [222].*

13.4. Sub-Microscale—Lamella Lengthscale

A group of collagen fiber layers, each layer containing an arrangement of unidirectional fibers, is labelled lamella, see Figure 4 LS4.

**Characteristic Length 4** (Sub-microscale).

|          |                   |                                   |                             |
|----------|-------------------|-----------------------------------|-----------------------------|
| Lamella: | lamella length    | $\approx$ 10–30 $\mu\text{m}$     | several CLG fiber lengths   |
|          | lamella width     | $\approx$ 0.15–0.25 $\mu\text{m}$ | several CLG fiber diameters |
|          | lamella thickness | 3–7 $\mu\text{m}$                 | [61,139,191,379]            |

13.5. Microscale—Osteon and Trabecula Lengthscale

Different assemblies of lamellae give origin to two different types of bone: cortical and trabecular. The cortical bone consists of osteons and Haversian canals, see Figure 4 LS3.1. The trabecular bone consists of many single trabeculae, rod-like structures, arranged in a porous way, see Figure 4 LS3.2. Osteons and trabecula are the lengthscale elements that define the microstructure of cortical and trabecular bone, respectively.

**Characteristic Length 5** (Microscale).

|                       |                     |                                       |                  |
|-----------------------|---------------------|---------------------------------------|------------------|
| Osteon and Trabecula: | osteon length       | 10,000–20,000/1000–3000 $\mu\text{m}$ | [222]/[379]      |
|                       | osteon diameter     | 200–300 $\mu\text{m}$                 | [191,222,379]    |
|                       | trabecula length    | 1000 $\mu\text{m}$                    | [191]            |
|                       | trabecula thickness | 50–300 $\mu\text{m}$                  | [61,139,191,379] |

**Remark 32** (Bone Porosities). *At the microscale, bone is composed of a solid structure with porosities. The solid structure, composed of lamellae, is commonly labelled solid bone matrix or bone ultrastructure and may be considered tissue-independent [385]. Cortical bone exhibits pores as Haversian and Volkmann's canals.*

*Trabecular bone exhibits several pores in the intertrabecular spaces. Bone pores are filled either with a fluid or a gel, e.g., blood vessels, nerves, fat, bone marrow, et cetera [222].*

### 13.6. Mesoscale—Cortical and Trabecular Bone Lengthscale

The cortical bone, see Figure 4 LS2.1, also labelled compact bone, and the trabecular bone, see Figure 4 LS2.2, also labelled cancellous or spongy bone, constitute the lengthscale that lays between the micro- and macroscales. This scale is commonly labelled mesoscale in the literature of bone multiscale modelling.

**Remark 33** (Mesoscale—Multiscale Literature). *The multiscale modelling literature defines mesoscale as any intermediate lengthscale, i.e., any lengthscale that is not the finest or the coarsest modelled lengthscale [407] (pp. 6, 214). For example, in the case of three lengthscales consideration, the mesoscale is defined as a scale with a characteristic length  $L_{\text{meso}} \mid L_{\text{micro}} < L_{\text{meso}} \ll L_{\text{macro}}$ , where  $L_{\text{micro}}$  and  $L_{\text{macro}}$  are the characteristic length of the micro- and macroscales, respectively [385,408,409], see Definition 8.*

**Characteristic Length 6** (Mesoscale—Representative Volume Element (RVE)). *Defined in the Multiscale literature as a scale between any two lengthscales, see Remark 33, bone mesoscale is usually referred to as the scale between the macro- and microscale in the literature regarding bone modelling. The mesoscale is characterized by an RVE, usually cube-shaped, that contains several elements of the microscale, e.g., a bunch of osteons or a bunch of trabeculae, see Figure 4 LS2.1 and LS2.2. An appropriate characteristic length for the mesoscale of bone is 10 to 100 times the characteristic length of the microscale.*

### 13.7. Macroscale—Whole Bone Lengthscale

At the macroscale, the whole bone, consisting of cortical and trabecular bone, is considered, see Figure 4 LS1.

**Characteristic Length 7** (Macroscale—Whole Bone). *Different bones have different sizes. The femur is the longest human bone. The mean ratio of femur length to human stature is approximately 26.74% [410]. For instance, a 1.7 m tall person has a 45 cm long femur. The stapes is the smallest bone in humans. The distance between the surface of the head of the stapes to the surface of its footplate, i.e., its greater length, is approximately 3.19 mm [411].*

At the macroscale, bone can be classified based on its skeletal site, shape and structure [412]. According to its structure, bone can be classified into cortical and trabecular bone, see Figure 4 LS2.1, LS2.2. According to their shape, bones can be classified into five different groups: (1.) long bones; (2.) short bones; (3.) flat bones; (4.) irregular bones; (5.) sesamoid bones. The huge majority literature on bone fracture simulation focuses on long bones, probably due to its beam-like geometry that enables simplified analytical calculations and experimental reproducibility.

Other types of tissue found in bone, but not discussed in detail in this paper, include bone marrow, endosteum, periosteum, nerves, blood vessels and cartilage. They also play a role in bone fracture.

References [61,96,139,180,191,206,222,378,379,381,384–386,400,402,412–417] constitute the main literature concerning the elaboration of Section 13 and are recommended for further details.

## 14. Multiscale Modelling of Bone

Multiscale modelling of bone starts when bone is assumed to comprise at least two of the lengthscales presented at Section 13, and consists of linking at least two different lengthscales. Each scale is distinguished by its characteristic length, see Definition 8.

**Definition 8** (Characteristic Length). *The characteristic length of a lengthscale quantitatively describes the physical space occupied by the RVE of this lengthscale. An RVE must contain enough physical space to enclose*

a fully defined example of all physical phenomena that were assumed to take place at a certain lengthscale. For example, in the case of cubic-shaped RVEs, the edge length of the RVE is, in most cases, the most suitable choice of characteristic length.

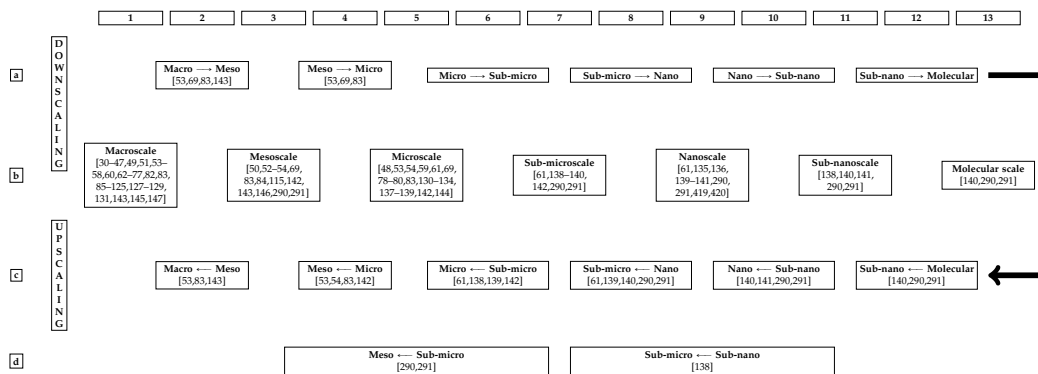
The linking between lengthscales can either be done by transitioning from a certain scale  $LS_x$  to a lower-scale (Downscaling)  $LS_{x+1}$  or from a certain scale  $LS_x$  to a higher-scale (Upscaling)  $LS_{x-1}$ , see Definition 9.

**Definition 9** (Higher- and Lower-Scales). *Picture two lengthscales. The higher lengthscale, or higher scale, is the lengthscale with greater characteristic length. The lower lengthscale, or lower-scale, is the lengthscale with shorter characteristic length.*

At a certain lengthscale  $LS_x$ , the domain of a solid body can either be described as a continuum or as a conjunction of discrete particles, i.e., non-continuum. Two distinct lengthscales may have one of three possible relationships outlined in [418]: hierarchical, semi-concurrent and concurrent; further discussion of these three relationships is outside the scope of this survey. All 3 relationships may characterize continuum–continuum scale transitions or continuum–discrete scale transitions.

Table 3 shows the bone lengthscales modelled by the surveyed papers. Papers which performed multiscale analysis are present in more than one box in Table 3. There are difficulties in applying hierarchical multiscale models to fracture [418].

**Table 3.** Bone multiscale modelling [30–80,82–125,127–147,290,419,420].



14.1. Continuum Downscaling

In a solid continuum, the transition from a certain lengthscale  $LS_x$  to a lower-scale  $LS_{x+1}$  is commonly labelled Downscaling or Localization [407]. Details on localization techniques are presented in [418,421]. Within the surveyed literature, continuum downscaling consists in transferring the displacement and surface force vector fields or stress and strain tensor fields calculated at points inside the spatial domain of  $LS_x$  as suitable BCs to the boundaries of the RVEs of  $LS_{x+1}$  [422–426].

There are three main classes of BCs used for downscaling: **Periodic Boundary Conditions** (PBCs) are the most used BCs for spatial downscaling. As an advantage, they provide the fastest convergence of physical and mechanical properties of  $LS_x$ . As a disadvantage, the fact that they restrict the deformation to obey the structural frame periodicity of  $LS_{x+1}$  imposes unphysical deformation constraints over localization zones (i.e., regions of relative extremely high deformation gradient where micro-cracks occur) [425,426]. **Minimal Kinematic Boundary Conditions** (MKBCs) ensure effective deformation shear strain but overestimate the number of localization zones near the domain boundary [425]. **Tesselation Boundary Conditions** (TBCs) maintain the point-to-point conditions imposed by PBCs while shifting the periodicity frame to correspond to the developing localization zone. In biomaterials, e.g., bones, when transitioning from  $LS_x$  to  $LS_{x+1}$ , TBCs may give the least-error

estimation of stresses and strains at  $LS_x$  [426]. Four references feature bone multiscale analyses with downscaling: [53,69,83,143], see Table 3. To transition from the macroscale to the mesoscale, ref. [69] used a displacement interpolation procedure. To transition from the mesoscale to the microscale, ref. [69] transferred mesoscale displacements as BCs to the microscale. Likewise, ref. [143] transitioned from the macroscale to the mesoscale by applying displacements computed from the macroscale strain tensors as BCs on the boundary of the mesoscale RVE.

To transition from the macroscale to the microscale, and vice versa, [53,83] used intermediate scales, i.e., mesoscales. This transition was performed using octree hierarchical multiresolution geometric data structure. This kind of transition consists in mesh refinement. There is little controversy regarding the assumption of mesh refinement as a multiscale approach.

#### 14.2. Continuum Upscaling

In a solid continuum, the transition from a certain lengthscale  $LS_x$  to a higher-scale  $LS_{x-1}$  is commonly labelled Upscaling or Homogenization [407]. Details on homogenization techniques are presented in [418,421,427]. Within the surveyed literature, continuum upscaling consists of averaging the displacement and surface force vector fields or stress and strain tensor fields calculated in points inside the spatial domain of  $LS_x$  to displacement and traction vector fields at  $LS_{x-1}$  by using averaging-based homogenization techniques [423,424].

Consider a stress tensor  $\mathbf{T}^{LS_{x-1}}$  and a strain tensor  $\mathbf{E}^{LS_{x-1}}$  at  $LS_{x-1}$ , and a point  $\mathbf{x}$  inside an RVE's domain  $\Omega_{LS_x}$  at  $LS_x$ , i.e.,  $\mathbf{x} \in \Omega_{LS_x}$ . Homogenization evaluates, at any time instant  $t$ ,  $\mathbf{T}^{LS_{x-1}}$  and  $\mathbf{E}^{LS_{x-1}}$  as the volume average of  $\mathbf{T}^{LS_x}$  and  $\mathbf{E}^{LS_x}$  over  $\Omega_{LS_x}$  [422,424]:

$$\begin{aligned} T_{ij}^{LS_{x-1}}(\mathbf{x}(t), t) &= \langle T_{ij}^{LS_x}(\mathbf{x}(t), t) \rangle = \frac{1}{|\Omega_{LS_x}|} \int_{\Omega_{LS_x}} T_{ij}^{LS_x}(\mathbf{x}(t), t) d\Omega_{LS_x} \\ E_{ij}^{LS_{x-1}}(\mathbf{x}(t), t) &= \langle E_{ij}^{LS_x}(\mathbf{x}(t), t) \rangle = \frac{1}{|\Omega_{LS_x}|} \int_{\Omega_{LS_x}} E_{ij}^{LS_x}(\mathbf{x}(t), t) d\Omega_{LS_x} \end{aligned} \quad (4)$$

where  $|\Omega_{LS_x}|$  is the volume of  $\Omega_{LS_x}$  in absolute value. All of the surveyed literature concerning upscaling procedures in bone used Equation (4), see Table 3 rows c and d. For example, ref. [140,141] present a cascade homogenization procedure for transitioning between several lengthscales. When transitioning from any  $LS_x$  to any corresponding  $LS_{x-1}$ , Equation (4) interprets any spatial discontinuity within the RVE of  $LS_x$  as a uniform volumetric redistribution of  $\mathbf{T}^{LS_x}$  and  $\mathbf{E}^{LS_x}$  over all space enclosed by the RVE.

#### Molecular Scale as a Non-Continuum Material

At the molecular scale, bone is composed of a colossal number of interacting molecules, see Section 13. Each molecule comprises several atoms participating in interatomic bonds. Assuming that modelling each atom as a solid particle is accurate enough, the molecular domain is defined, in conclusion, as a gathering of discrete particles, i.e., a non-continuum. The molecular scale of bone is mostly studied through Molecular Dynamics (MD) simulations [386,428,429].

**Remark 34** (Linking Continuum and Non-Continuum Scales). *None of the surveyed literature transitions, in bone, between a lengthscale modelled as a continuum and a lengthscale modelled as a non-continuum. Within the surveyed literature, only [140,290,291] model the molecular scale alongside larger lengthscales of bone, see Table 3; however, ref. [140,290,291] model the molecular scale as a continuum using a multiscale micromechanics-based approach. This approach can estimate bone anisotropic CLE-properties from  $H_2O$ , HA and CLG, the basic constituents of bone, see Section 13, and may be combined with CT-data to estimate patient-specific CLE-properties [61,115,140,286–291].*

The transition between a lengthscale modelled as a non-continuum and a lengthscale modelled as a continuum can be performed using several approaches; ref. [427] further comments on these possible approaches. This literature survey emphasizes an approach consisting in finding parameters for Traction-Separation Equations (TSEs) through MD simulations, as outlined in [418,430,431]. TSEs describe fracture at any lengthscale that is modelled as a continuum material. The TSE parameters are used by CZMs that describe fracture as element-wise interface disconnection; lastly, the CZM is coupled with the Governing Equations (1)–(3) [430,432–435].

MD simulations, as proposed by [436], and performed in bone by [191,414,415,419,420,437,438], consist in solving Newton's 2nd Law of Motion at a material's molecular scale whose spatial domain contains  $a$  atoms interacting with up to  $n$  neighbour atoms:

$$m_a \frac{d^2 \mathbf{r}_a(t)}{dt^2} = \sum_{n_1=1}^n \mathbb{f}_2(\mathbf{r}_a(t), \mathbf{r}_{n_1}(t)) + \dots + \sum_{n_1=1}^n \sum_{\substack{n_2=1 \\ n_2 \neq n_1}}^n \dots \sum_{\substack{n_k=1 \\ n_k \neq n_1, n_2, \dots}}^n \mathbb{f}_n(\mathbf{r}_a(t), \mathbf{r}_{n_1}(t), \dots, \mathbf{r}_{n_k}(t)) \quad (5)$$

where, for each  $a$ -th atom:  $\mathbf{r}_a$  is the position vector;  $m_a$  is the mass,  $\mathbb{f}_2$  is a force vector function that describes pairwise atomic interactions; similarly,  $\mathbb{f}_n$  describes  $n$ -atom interactions. Each  $\mathbb{f}_n$  is the time-derivative of an energy function that accounts for up to  $n$ -body and quantum interactions. The total energy of the  $a$ -th atom is a function of an  $a$ -th atom's position  $\mathbf{r}_a(t)$  and of its  $n$  neighbours' positions  $\mathbf{r}_1(t), \dots, \mathbf{r}_n(t) \in \mathbb{R}^3$ .

MD simulations of bone commonly account for the presence of CLG, HA and H<sub>2</sub>O, see Section 13 and [191,386,414,415,419,420,428,429,437,438]. For each inter- and intra-molecular interaction there are specific potential energy functions (or simply potentials), some of which are found in the literature referred to in Table 4.

**Table 4.** Bibliographical references for interatomic potential function parameters.

| Interaction | CLG–CLG              | CLG–HA    | CLG–H <sub>2</sub> O | HA–HA                              | HA–H <sub>2</sub> O | H <sub>2</sub> O–H <sub>2</sub> O |
|-------------|----------------------|-----------|----------------------|------------------------------------|---------------------|-----------------------------------|
| Reference   | [413,415] apud [439] | [440,441] | [440,441]            | [442] apud [437], [414] apud [443] | [440,441]           | [413] apud [444]                  |

When formulating energy functions for the CLG–HA, CLG–H<sub>2</sub>O and HA–H<sub>2</sub>O inter-molecular interactions, the Lorentz-Berthelot mixing rule [440,441] is usually used, as in [414,415].

Once  $\mathbb{f}_2, \dots, \mathbb{f}_n$  are defined, the next step of an MD simulation consists either in solving: (1.) an initial-value problem, which requires the atoms' initial positions  $\mathbf{r}(0)$  and velocities  $\dot{\mathbf{r}}(0)$ ; or (2.) a boundary-value problem, which requires the atoms' positions at an initial time instant  $\mathbf{r}(t_i)$  and at a final time instant  $\mathbf{r}(t_f)$ . Both (1.) and (2.) require potential energy functions.

MD simulations provide the position  $\mathbf{r}_a(t)$  and velocity  $\dot{\mathbf{r}}_a(t)$  of every  $a$ -th atom in the molecular spatial domain at each time step. The accuracy of MD simulation results depends strongly on the inter- and intra-molecular potential's validity. Therefore, the before mentioned 6 inter- and intra-molecular potentials must be selected according to their accuracy in modelling bone mechanics at the molecular scale [413,414].

**Highlight 10** (Multiscale Modelling and Bone Remodelling). *Bone remodelling, see Definition 19, has been recently incorporated into multiscale models. The first approach to study bone remodelling by coupling models of systems biology and multiscale continuum micromechanics is presented in [445]. Follow-up papers studied the relationship between oscillating hydrostatic pore pressure and bone cells activity [446,447], which is presented from a biological perspective in [448].*

*A comprehensive multiscale model of bone remodelling multiscale model, accounting for hormonal regulation and biochemical coupling of bone cell populations is presented by [245]. Structural changes induced by osteoclasts and osteoblasts at the "cellscale" change bone density at higher-scales in the model proposed by [449].*

**Open Issue 9** (Simulations Coupling 6 or More Lengthscales). *No paper has been found modelling and linking all the lengthscales illustrated in Figures 4 and Table 3. Among the surveyed literature, ref. [290,291] devised the multiscale model with the largest number of linked lengthscales: 5.*

**Remark 35** (Scales Jumps). *Table 3 row d shows scale jumps performed by [138,290,291]. Jumping from the sub-nanoscale directly to the sub-microscale, as in [138], may be justified by the fact that mCLGf and CLG fibers exhibit the same geometry. CLG fibers are nothing but a bunch of mCLGfs. Thus, it may be reasonable to skip the transition between the sub-nanoscale and the nanoscale of bone. Jumping from the sub-microscale directly to the mesoscale, as in [290,291], may be justified by the fact that the microscale is composed of, in the case of cortical bone, a single osteon and the mesoscale is a bunch of osteons, see Characteristic Length 6.*

## 15. Validating Bone Fracture Simulation

Simulations should imitate reality as accurately as possible. The way to validate solid continuum mechanics models is by performing simulations that imitate real-world experiments. A model is labeled validated when the numerical value of a variable computed in a simulation satisfactorily matches the numerical value from the experimental measurement of the same variable. For instance, the numerical value of a strain computed from a simulation must match the numerical value of a strain measured in an experiment representative of said simulation.

There are mainly two classes of experiments on bone material: **15A<sub>1</sub>** and **15A<sub>2</sub>**. Both involve highly sensitive procedures that must be carefully performed, see guidelines on biomechanical experiments by [233].

**15A<sub>1</sub>**: Experiments for Bone Material Characterization—give insight into the mechanical behaviour of bone under specific loading conditions and into how Open Issue 2 affects bone mechanical properties. **15A<sub>1</sub>** are related to the bone modelling categorization shown in Table 2 and described in Section 10: **10B<sub>1</sub>–10B<sub>3</sub>**. **15A<sub>1</sub>** must comprehend the largest possible number of variables, see Remark 3. **15A<sub>1</sub>** must test the specimen: at all possible lengthscales, see Section 13; at all possible loading conditions, e.g., tension, compression, shear, torsion; at all directions, i.e., assuming every planes of symmetry, e.g., assuming the material to be triclinic; under different strain rates; under different thermal conditions, e.g., different temperatures, temperature change rates. Furthermore, **15A<sub>1</sub>** must characterize: the plastic region; fracture toughness mechanisms and other important features [221,326,450–452]. **10B<sub>1</sub>–10B<sub>3</sub>** that best suit experimental results must be sought after.

**15A<sub>2</sub>**: Experiments on Bone Materials under Generic Environmental Conditions—must imitate in vivo, see Definition 1, conditions (when possible) and consider several issues to assure reproducibility, e.g., bone conservation, hydration, temperature, et cetera.

**Remark 36** (Validation and Experiments—An Iterative Process). *Mechanical properties of bone must be modelled based on preliminary **15A<sub>1</sub>** that estimate **10B<sub>1</sub>–10B<sub>3</sub>**. Simulated variables, e.g., strains, displacements, et cetera, are validated by being compared to **15A<sub>2</sub>**. When simulated variables do not match **15A<sub>2</sub>** (assuming both experiments and simulations were correctly performed), a new model, with different assumptions, based on new **15A<sub>1</sub>**, is required. This is an iterative process. **15A<sub>1</sub>** are required pre-simulation. **15A<sub>2</sub>** are required post-simulation.*

**Remark 37** (Validated?). *Some references in Table 2 made simple assumptions, e.g., [30,81,115,127] modelled bone only at the macroscale and/or as an isotropic homogeneous CLE-material, and validated their simulations, i.e., their simulation showed good agreement with **15A<sub>2</sub>**. It is reasonable to question such results: bone is most probably not isotropic and does not fit an LE constitutive equation, see Section 10. **15A<sub>1</sub>** may even reveal some particular bone sample to behave like a quasi-isotropic homogeneous CLE-material; however, these findings may stop being valid under the slightest change in local conditions, e.g., bones in vivo vs. bones in vitro, et cetera.*

Experiments and simulations contain errors and approximations; thus, they are always questionable.

**Remark 38** (Towards Realistic Fracture Predictions). *Most realistic fracture predictions stem from the best-achievable fracture simulations. To achieve such simulations the following issues should be considered: (1.) the multiscale structure of bone, see Sections 13 and 14; (2.) the most robust physico-mathematical approach, see Sections 6–8 and 12; (3.) the most realistic mechanical properties, see Section 10; (4.) the most realistic BCs, see Section 11; (5.) proper validation, see Section 15.*

## 16. Assessing Fracture Risk

Current available osteoporosis and fracture risk assessment tools are fundamentally based on BMD and qualitative medical variables (e.g., sex, age, weight, patient’s case history), most commonly labelled Clinical Risk Factors (CRFs) [453].

There are single-variable and multi-variable fracture risk predictors and assessment tools.

### 16.1. Single-Variable Risk Analysis

**BMD** measurements are the current clinical standard to diagnosis osteoporosis. According to the WHO, women with a BMD that lies 2.5 SD or more below the average value for young healthy women are classified as *osteoporotic* (T-score  $\leq$  2.5 SD) [11]. However, BMD alone is unable to accurately assesses fracture risk [454]. Patients classified as osteoporotic will not invariably suffer a fragility fracture; non-osteoporotic patients may also suffer a fragility fracture [11,14,455]. BMD can be used in conjunction with CRFs and available fracture assessment tools to improve the accuracy of fracture predictions. CRFs provide information on fracture risk that are unrelated to BMD [165]. As mentioned in Section 9, DXA is the clinical standard technique to measure BMD. QCT and ultrasound measurements are alternative techniques for the quantification of BMD [14,153].

**TBS**, an acronym for Trabecular Bone Score, is a grayscale-based (or HU-based) texture measurement influenced by the geometry of bone at the meso- and microscales [456]. A low TBS value may indicate thin trabeculae and a highly porous mesostructure, see Figure 4 (LS2.2, LS3.2) [457]. TBS contains structural information that are not captured by BMD measurements [457,458]. TBS can be used, though not very accurately, to assess fracture risk independently of BMD and CRFs [453,459]. TBS has been used in conjunction with BMD alone and with BMD and CRFs in available fracture risk assessment tools such as FRAX, to improve the accuracy of bone fracture predictions [458]. In the study performed by [459], however, TBS did not improve BMD and FRAX fracture predictions. TBS depends on HU variations obtained in vivo, which can have many causes [457] and is most commonly estimated using DXA. For more information on TBS see [14,459–462].

**BTMs**, an acronym for Bone Turnover Markers, are measurable indicators of bone turnover, e.g., blood and urine tests. Bone turnover, i.e., bone replacement, is the effect, the cause (mechanism) of which is bone remodelling, see Definition 19. Bone turnover refers to the volume of replaced bone per unit time [463]. Deterioration of bone microstructure, i.e., bone structure at the microscale, translates into a high value of bone turnover. BTMs indicate the degree of deterioration of the bone microstructure and, may thus, independently of BMD, predict a person’s fracture risk. Furthermore, BTMs can be used in conjunction with BMD to improve the accuracy of fracture risk assessment tools [464]. The use of BTMs in the osteoporotic risk analysis and in monitoring the efficacy of osteoporosis treatment is rapidly increasing [465–468].

### 16.2. Multi-Variable Risk Analysis

**FRAX** (<https://www.sheffield.ac.uk/FRAX/>), the Fracture Risk Assessment tool, estimates individualized ten-year probability of hip, spine, forearm and proximal humerus osteoporotic fracture [469,470]. FRAX integrates eight main CRFs (prior fragility fracture, parental hip fracture, smoking, systemic glucocorticoid use, excess alcohol intake, body mass index, rheumatoid arthritis, and other causes of secondary osteoporosis), which, in addition to age and sex, contribute to fracture risk analysis independently of BMD. FRAX does not consider risk factors such as BTM and those associated with falls, lower dietary calcium intake and Vitamin D deficiency [464], but has BMD as

an optional input variable [165,469,470]. FRAX predictions can become more accurate when used in conjunction with, e.g., BMD and TBS [458]. For more information on FRAX, see [41,91,453,471–475].

**QFracture** (<https://qfracture.org/>) predicts individual risk of osteoporotic and hip fracture based on several distinct CRFs (age, body mass index, ethnic origin, alcohol intake, smoking status, chronic obstructive pulmonary disease or asthma, any cancer, cardiovascular disease, dementia, diagnosis or treatment for epilepsy, history of falls, chronic liver disease, Parkinson's disease, rheumatoid arthritis or systemic lupus erythematosus, chronic renal disease, type 1 and 2 diabetes, previous fracture, endocrine disorders, gastrointestinal malabsorption, any antidepressants, corticosteroids, unopposed hormone replacement therapy and parental history of osteoporosis), needing no quantitative measurements [476,477]. When compared with FRAX, QFracture shows some evidence of improved discrimination and calibration for hip fracture [476]. BMD cannot be used in conjunction with QFracture.

**Garvan**, short for Garvan Fracture Risk Calculator [478,479], estimates individualized five- to ten-years risk of total fracture and hip fracture by combining BMD and several CRFs (age, body weight, height, daily physical activity level, daily calcium intake, smoking, history of falls in the preceding 12 months, history of fractures in the past five years, et cetera [480]).

Comparisons between FRAX, Qfracture and Garvan discussing approaches to osteoporosis risk analysis worldwide can be found in [481–484]. The use of such risk assessment tools in conjunction with BMD, TBS, genetic data, BTMs and new CRFs could improve their accuracy in predicting fracture risk [481,485]. Furthermore, artificial intelligence could also enhance the accuracy of these tools, e.g., machine learning methods can be used to assess the risk of osteoporotic fractures [486].

Others fracture risk assessment tools are available in the literature: The DVO-Tool developed by the German Osteology Society [487,488], the fracture risk score model based on in-hospital treated patients to predict osteoporotic fractures [489], and the FRACTURE Index [490] are only a few of them. A brief schematic overview of the evolution of the diagnosis of osteoporosis since 1940 is given in [491].

Current available fracture risk assessment tools generally evaluate individual fracture risks based on a cohort of statistical data. However, current tools do not account for bone mechanical properties and/or bone quantitative fracture mechanics variables. Fracture simulation of patient-specific computational models could give already existing risk assessment tools its contribution by adding diagnostic quantitative information based on multiscale simulations.

**Open Issue 10 (Quantitative Risk Factors).** *Mathematical calculations can accurately assess the fracture risk of many different materials (e.g., steels, iron, composites) subject to specific BCs. It can possibly also accurately assess the fracture risk of biological materials. Continuum mechanics, fracture mechanics, multiscale modelling and molecular mechanics enable the designing of robust structures capable of supporting extreme (e.g., loading and thermal) conditions. Quantitative Risk Factors (QRFs), e.g., Young's Modulus and Yield strength, could improve the accuracy of current fracture risk assessment tools.*

As shown in Section 13, bone presents different geometries and thus mechanical properties, see Section 10, at different lengthscales. The analysis of patient-specific fracture risk is a multiscale problem and requires consideration of as many bone lengthscales as possible [214]. Adding, from patient-specific bone computational models, quantitative multiscale fracture mechanics-based variables to current fracture risk assessment tools may be crucial to the improvement of current fracture risk analysis, being the next step towards an improved fracture-predictive diagnosis [128,214,481,485,492,493]. Not only osteoporosis, but several others bone diseases and conditions could profit from patient-specific fracture risk simulations and assessment tools, e.g.: osteomalacia, osteitis fibrosa, osteopenia (or bone loss), osteogenesis imperfecta, brittle bone disease, et cetera [194].

**Author Contributions:** Conceptualization, A.C.S.A., I.A., K.M., S.S., D.P., L.C.-P., M.S.S., L.C.W. and P.S.; methodology, A.C.S.A., I.A., K.M., S.S., L.C.-P., M.S.S., L.W. and P.S.; investigation, A.C.S.A., I.A., K.M., S.S., L.C.-P., M.S.S., L.C.W. and P.S.; resources, M.S.S. and P.S.; writing—original draft preparation, A.C.S.A. and I.A.; writing—review and editing, A.C.S.A., I.A., K.M., S.S., D.P., L.C.-P., M.S.S., L.C.W. and P.S.; visualization, A.C.S.A., I.A. and D.P.; supervision, M.S., L.C.W. and P.S.; project administration, M.S.S. and P.S.; funding acquisition, A.C.S.A., M.S.S. and P.S.

**Funding:** This study was financed in part by the São Paulo Research Foundation (FAPESP) grant #2018/18503-2, the Center for Computing in Engineering & Sciences (CCES/UNICAMP) grant #2013/08293-7, the Coordenação de Aperfeiçoamento de Pessoal de Nível Superior—Brasil (CAPES). This material is based upon work supported by the Air Force Office of Scientific Research under award number FA9550-18-1-0113.

**Conflicts of Interest:** The authors declare no conflict of interest.

## Appendix A. Glossary of Symbols

| Symbol:                | Meaning:  |
|------------------------|---|
| $i, j, k, l = 1, 2, 3$ | spatial components of Einstein's summation or notation, or Index/Subscript/Tensor notion                    |
| $T_{ij}$               | an element of the Cauchy stress tensor $\mathbf{T}$ [ $N/m^2$ ] $\in \mathbb{R}^{3 \times 3}$               |
| $b_i$                  | an element of the body force vector $\mathbf{b}$ [ $N/m^3$ ] $\in \mathbb{R}^{3 \times 1}$                  |
| $f_i$                  | an element of the surface force vector $\mathbf{f}$ [ $N$ ] $\in \mathbb{R}^{3 \times 1}$                   |
| $E_{ij}$               | an element of the strain tensor $\mathbf{E}$ $\in \mathbb{R}^{3 \times 3}$                                  |
| $n_j$                  | an element of the unit normal vector $\mathbf{n}$ $\in \mathbb{R}^{3 \times 1}$                             |
| $\rho$                 | a density [ $g/m^3$ ] $\in \mathbb{R}^1$  |
| $X_i$                  | an element of the material point $\mathbf{X}$ [ $m$ ] $\in \mathbb{R}^{3 \times 1}$ [494] (p. 61)           |
| $x_i$                  | an element of the spatial point $\mathbf{x}$ [ $m$ ] $\in \mathbb{R}^{3 \times 1}$ [494] (p. 61)            |
| $F_{ij}$               | an element of the deformation gradient $\mathbf{F}$ $\in \mathbb{R}^{3 \times 3}$                           |
| $u_i$                  | an element of the displacement vector $\mathbf{u}$ [ $m$ ] $\in \mathbb{R}^{3 \times 1}$                    |
| $C_{ijkl}$             | an element of the stiffness tensor $\mathbb{C}$ [ $N/m^2$ ] $\in \mathbb{R}^{3 \times 3 \times 3 \times 3}$ |
| $W$                    | the strain-energy density function [ $J$ ] $\in \mathbb{R}^1$   |
| $t$                    | the time [ $s$ ] $\in \mathbb{R}^1$   |
| $\theta$               | the temperature [ $K$ ] $\in \mathbb{R}^1$  |
| $\Delta\theta_i$       | an element of the temperature gradient $\Delta\theta$ [ $K/s$ ] $\in \mathbb{R}^{3 \times 1}$               |
| $\zeta$                | an unknown internal variable [?] $\in \mathbb{R}^?$   |
| $Y$                    | a unidirectional Young's Modulus [ $N/m^2$ ] $\in \mathbb{R}^1$   |

## Appendix B. Glossary of Acronyms

| Acronym:                  | Full form:  |
|---------------------------|---|
| <b>BEM</b>                | Boundary Element Method                                     |
| <b>BC</b>                 | Boundary Condition  |
| <b>MKBC</b>               | Minimal Kinematic Boundary Condition                        |
| <b>PBC</b>                | Periodic Boundary Condition                                 |
| <b>TBC</b>                | Tesselation Boundary Condition                              |
| <b>BMD</b>                | Bone Mineral Density  |
| <b>BTM</b>                | Bone Turnover Marker  |
| <b>CLG</b>                | CoLlaGen  |
| <b>mCLGf</b>              | mineralized CoLlaGen fibril                                 |
| <b>CT</b>                 | Computed Tomography   |
| <b><math>\mu</math>CT</b> | Micro Computed Tomography                                   |
| <b>QCT</b>                | Quantitative Computed Tomography                            |
| <b>HR-pQCT</b>            | High-Resolution Peripheral Quantitative Computed Tomography |
| <b>CZM</b>                | Cohesive Zone Model   |
| <b>DICOM</b>              | Digital Imaging and Communications in Medicine              |
| <b>DOF</b>                | Degrees of Freedom  |
| <b>DXA or DEXA</b>        | Dual Energy X-ray Absorptiometry                            |
| <b>FDM</b>                | Finite Difference Method                                    |

|             |                                    |
|-------------|------------------------------------|
| <b>FEM</b>  | Finite Element Method              |
| <b>EPFM</b> | Elastic-Plastic Fracture Mechanics |
| <b>LEFM</b> | Linear Elastic Fracture Mechanics  |
| <b>FS</b>   | Fall Stage                         |
| <b>GDP</b>  | Gross Domestic Product             |
| <b>HA</b>   | HydroxyApatite                     |
| <b>HU</b>   | Hounsfield Units                   |
| <b>LE</b>   | Linear-Elastic                     |
| <b>CLE</b>  | Cauchy-Linear-Elastic              |
| <b>CNLE</b> | Cauchy-NonLinear-Elastic           |
| <b>NLE</b>  | Non-Linear-Elastic                 |
| <b>LS</b>   | Lengthscale                        |
| <b>MD</b>   | Molecular Dynamics                 |
| <b>MRI</b>  | Magnetic Resonance Imaging         |
| <b>μMRI</b> | Micro Magnetic Resonance Imaging   |
| <b>PDE</b>  | Partial Differential Equation      |
| <b>RVE</b>  | Representative Volume Element      |
| <b>CRF</b>  | Clinical Risk Factor               |
| <b>QRF</b>  | Quantitative Risk Factor           |
| <b>SD</b>   | Standard Deviations                |
| <b>TBS</b>  | Trabecular Bone Score              |
| <b>TSE</b>  | Traction Separation Equation       |
| <b>WHO</b>  | World Health Organization          |

### Appendix C. Glossary of PDE, Continuum Mechanics and Theory of Elasticity Concepts

References to several concepts important to the understanding of PDEs, continuum mechanics and theory of elasticity are listed here. These concepts have mathematical and physical enunciations. The mathematical enunciations are rigorous and contain all the details that computer simulations require. The physical enunciations give an intuitive idea, but are not mathematically rigorous and, in most cases, do not contain the necessary data required by the algorithm of a computer simulation. However, the physical interpretations facilitate interaction between biologists, physicians, engineers and physicists. Biologists and physicians need to understand definitions in physical terms to make suggestions to engineers and physicists so they can create more realistic bone models.

Some of the references listed on the physical definitions may also contain a mathematical definition. They are classified as a physical definition because they explain the concept in a more intuitive way. The references for the physical definition present the mathematical definition usually in a more easy-to-grasp way, sometimes not as complete and rigorous as the references for the mathematical definition. Furthermore, terms with multiple references may present slightly different approaches or interpretations in each reference.

| Term:  | Mathematical definition:  | Physical definition:  |
|--|---|---|
| Domain   | ([495] p. 222, same as <i>Gebiet</i> ), [496] (p. 1, same as <i>Region</i> )    | see Illustration 1  |
| Boundary   | [497] (pp. 25, 28, same as <i>Frontier</i> )                                    | see Illustration 1  |
| Boundary Condition   | [498] (p. 23)   | see Illustration 2  |
| Constitutive equation  | [499] (p. 170), [219] (p. 69), [500] (p. 1644), [494] (p. 276)                  | [222] (p. 170), [499] (p. 169), [206] (p. 35), [219] (p. 69), [501] (p. 273), [502] (p. 2), [494] (p. 223), [500] (p. 1642) |
| Elastic material (or Cauchy-elastic material)  | [503] (p. 170), [504] (p. 207) [499] (p. 175), [502] (p. 117), [494] (p. 297)   | [505] (p. 201), [506] (pp. 1, 444), [28] (p. 147)   |
| Hyperelastic material (or Green-elastic)   | [219] (p. 520), [503] (p. 171) [499] (p. 206), [502] (p. 294), [506] (p. 444)   | [219] (p. 519), [502] (p. 13), [499] (p. 206), [28] (p. 148), [501] (p. 282)  |
| Plastic (or elasto-plastic) material   | [219] (p. 148), [506] (p. 131), [210] (p. 57)                                   | [219] (p. 1480), [506] (p. 131), [210] (p. 52), [507] (p. 75)   |
| Viscoelastic material  | [503] (p. 174), [211] (p. 5)  | [211] (p. 5), [222] (pp. 59, 217), [210] (p. 65)  |
| Viscoplastic (or elasto-viscoplastic) material   | [219] (p. 450)  | [506] (p. 133), [210] (p. 65), [219] (p. 435)   |
| Poroelectricity  | [222] (p. 249)  | [222] (p. 247)  |
| Poroplasticity   | [508] (p. 226)  | [508] (p. 225)  |
| Poroviscoelasticity  | [508] (p. 261)  | [508] (p. 261)  |
| Poroviscoplasticity  | [508] (p. 273)  | [508] (p. 272)  |
| Damage mechanics   | [509] (p. 8) [510] (pp. 16, 142)  | [511] (p. 1) [510] (p. 3) [512] (p. 1)  |
| Isotropic material   | [503] (p. 234), [502] (p. 78), [513] (p. 60), [504] (p. 243)                    | [514] (p. 25), [250] (p. 41), [505] (p. 203), [499] (p. 170)  |
| Anisotropic material   | [503] (p. 234), [502] (p. 78), [513] (p. 60), [504] (p. 243)                    | [514] (p. 25), [250] (p. 41), [505] (p. 203)  |
| Linear elastic anisotropy: triclinic, monoclinic, orthotropic (or rhombic), trigonal, tetragonal, transversally isotropic (or hexagonal), cubic, isotropic | [250] (p. 44), [222] (p. 150), [257] (p. 10)                                    | [250] (p. 44), [222] (p. 150), [257] (p. 10)  |
| Homogeneous material   | [504] (p. 237), [502] (p. 58,59)  | [502] (pp. 58, 59), [514] (p. 25), [505] (p. 203)   |
| Inhomogeneous (or non-homogeneous, heterogeneous) material   | [504] (p. 237)  | [514] (p. 25), [505] (p. 203)   |
| Properties (not only mechanical properties): global and local  | [515] (p. 83)   | [515] (p. 83), [516] (p. 532)   |
| Cauchy's equation of motion (equilibrium equation)   | [504] (p. 223), [503] (pp. 153, 204), [499] (p. 148), [494] (pp. 139, 273, 307) | [222] (p. 129), [222] (p. 196)  |
| Strain-displacement equation (or Lagrange strain tensor, strain)   | [503] (p. 272), [505] (p. 84)   | [206] (p. 29), [505] (p. 84)  |
| Stress (or Cauchy stress tensor)   | [504] (p. 174), [503] (p. 150) [494] (p. 137)                                   | [206] (p. 25), [222] (p. 122), [505] (p. 157)   |
| Displacement (or displacement vector)  | [503] (p. 272), [494] (p. 297)  | [206] (p. 30), [505] (p. 81)  |
| Body force   | [504] (p. 151), [503] (p. 97), [494] (p. 132)                                   | [499] (p. 144), [494] (p. 132)  |
| Surface force (or surface traction, stress vector, Cauchy traction field)  | [503] (p. 97), [494] (p. 133)   | [494] (p. 133), [206] (p. 26), [505] (p. 155)   |
| Materials with memory  | [504] (p. 201)  | [502, XVIII preface to third edition]   |
| Hookean Material (or generalized Hooke's law, Hooke's law)   | [506] (pp. 2, 127), [505] (p. 204), [206] (p. 38)                               | [222] (p. 58), [211] (p. 4)   |

## References

- World Health Organization. World Health Statistics 2016: Monitoring Health for the SDGs, Sustainable Development Goals. 2016. Available online: [https://www.who.int/gho/publications/world\\_health\\_statistics/2016/en/](https://www.who.int/gho/publications/world_health_statistics/2016/en/) (accessed on 2 December 2019).
- United Nations, Department of Economics and Social Affairs, Population Division. World Population Prospects: The 2015 Revision, Key Findings and Advance Tables. Working Paper No. ESA/P/WP. 241. 2015. Available online: <http://wedocs.unep.org/handle/20.500.11822/18246?show=full> (accessed on 2 December 2019).
- Kaneda, T.; Greenbaum, C.; Patierno, K. 2018 World Population Data Sheet With Focus on Changing Age Structures. 2018. Available online: <https://www.prb.org/2018-world-population-data-sheet-with-focus-on-changing-age-structures/> (accessed on 2 December 2019).
- United Nations. *World Population Ageing 2017 Highlights. Statistical Papers—United Nations (Ser. A); Population and Vital Statistics Report*; UN: New York, NY, USA, 2018; p. 42, [CrossRef]
- He, W.; Goodkind, D.; Kowal, P. *An Aging World: 2015*; U.S. Census Bureau-International Population Reports. Available online: <https://www.fiapinternacional.org/en/an-aging-world-2015-international-population-reports-united-states-census-bureau-march-2016/> (accessed on 2 December 2019).
- International Osteoporosis Foundation—IOF. The Latin America Regional Audit—Epidemiology, Costs & Burden of Osteoporosis in 2012. 2012. Available online: [https://www.iofbonehealth.org/sites/default/files/media/PDFs/Regional%20Audits/2012-Latin\\_America\\_Audit\\_0\\_0.pdf](https://www.iofbonehealth.org/sites/default/files/media/PDFs/Regional%20Audits/2012-Latin_America_Audit_0_0.pdf) (accessed on 2 December 2019).
- Office for National Statistics—UK. Overview of the UK population: November 2018. 2018. Available online: <https://www.ons.gov.uk/peoplepopulationandcommunity/populationandmigration/populationestimates/articles/overviewoftheukpopulation/november2018> (accessed on 2 December 2019).
- European Commission. *The 2018 Ageing Report: Underlying Assumptions and Projection Methodologies*; European Commission: Brussels, Belgium, 2017; Volume 65, [CrossRef]
- Ortman, J.M.; Velkoff, V.A.; Hogan, H. An Aging Nation: The Older Population in the United States. Technical Report. 2014. Available online: <https://www.census.gov/library/publications/2014/demo/p25-1140.html> (accessed on 2 December 2019).
- He, W.; Goodkind, D.; Kowal, P. An Aging World: 2015. Technical Report. 2016. Available online: <https://www.census.gov/library/publications/2016/demo/P95-16-1.html> (accessed on 2 December 2019).
- World Health Organization. Assessment of Fracture Risk and Its Application to Screening for Postmenopausal Osteoporosis: Report of a WHO Study Group Meeting Held in Rome from 22 to 25 June 1992. Technical Report. 1994. Available online: <https://apps.who.int/iris/handle/10665/39142> (accessed on 2 December 2019).
- Osterhoff, G.; Morgan, E.F.; Shefelbine, S.J.; Karim, L.; McNamara, L.M.; Augat, P. Bone mechanical properties and changes with osteoporosis. *Injury* **2016**, *47*, S11–S20. [CrossRef]
- Woolf, A.D.; Akesson, K. *OSTEOPOROSIS, An Atlas of Investigation and Management*; Clinical Publishing: Oxford, UK, 2008.
- Kanis, J.A. Diagnosis of osteoporosis and assessment of fracture risk. *Lancet* **2002**, *359*, 1929–2936. [CrossRef]
- Kanis J.A.; on behalf of the World Health Organization Scientific Group. *Assessment of Osteoporosis at the Primary Health-Care Level*; Technical Report; World Health Organization Collaborating Centre for Metabolic Bone Diseases, University of Sheffield: Sheffield, UK, 2007. Available online: [https://www.sheffield.ac.uk/FRAX/pdfs/WHO\\_Technical\\_Report.pdf](https://www.sheffield.ac.uk/FRAX/pdfs/WHO_Technical_Report.pdf) (accessed on 4 December 2019).
- Laurence, V.; van Rietbergen Bert.; Nicolas, V.; Marie-Thérèse, L.; Hervé, L.; Myriam, N.; Mohamed, Z.; Maude, G.; Nicolas, B.; Valery, N.; et al. Cortical and Trabecular Bone Microstructure Did Not Recover at Weight-Bearing Skeletal Sites and Progressively Deteriorated at Non-Weight-Bearing Sites During the Year Following International Space Station Missions. *J. Bone Miner. Res.* **2017**, *32*, 2010–2021. [CrossRef]
- Grimm, D.; Grosse, J.; Wehland, M.; Mann, V.; Reseland, J.E.; Sundaresan, A.; Corydon, T.J. The impact of microgravity on bone in humans. *Bone* **2016**, *87*, 44–56. [CrossRef]
- Bhandari, M.; Swiontkowski, M. Management of Acute Hip Fracture. *N. Eng. J. Med.* **2017**, *377*, 2053–2062. [CrossRef]

19. Hannan, E.L.; Magaziner, J.; Wang, J.J.; Eastwood, E.A.; Silberzweig, S.B.; Gilbert, M.; Morrison, S.; McLaughlin, M.A.; Orosz, G.M.; Siu, A.L. Mortality and locomotion 6 months after hospitalization for hip fracture. Risk factors and risk-adjusted hospital outcomes. *JAMA* **2001**, *285*, 2736–2742. [[CrossRef](#)]
20. O'Connor, K.M. Evaluation and Treatment of Osteoporosis. *Med. Clin. N. Am.* **2016**, *100*, 807–826. [[CrossRef](#)]
21. Kling, J.M.; Clarke, B.L.; Sandhu, N.P. Osteoporosis Prevention, Screening, and Treatment: A Review. *J. Womens Health* **2014**, *23*, 563–572. [[CrossRef](#)]
22. Morales-Torres, J.; Gutiérrez-Ureña, S. The burden of osteoporosis in Latin America. *Osteoporos. Int.* **2004**, *15*, 625–632. [[CrossRef](#)]
23. Odén, A.; McCloskey, E.V.; Kanis, J.A.; Harvey, N.C.; Johansson, H. Burden of high fracture probability worldwide: Secular increases 2010–2040. *Osteoporos. Int.* **2015**, *26*, 2243–2248. [[CrossRef](#)]
24. Holzer, L.A.; Leithner, A.; Holzer, G. The Most Cited Papers in Osteoporosis and Related Research. *J. Osteoporos.* **2015**, *2015*, 12. [[CrossRef](#)] [[PubMed](#)]
25. Housner, G.W.; Bergman, L.A.; Caughey, T.K.; Chassiakos, A.G.; Claus, R.O.; Masri, S.F.; Skelton, R.E.; Soong, T.T.; Spencer, B.F.; Yao, J.T.P. Structural Control: Past, Present, and Future. *J. Eng. Mech.* **1997**, *123*, 897–971. [[CrossRef](#)]
26. Castiglione, F.; Pappalardo, F.; Bianca, C.; Russo, G.; Motta, S. Modeling Biology Spanning Different Scales: An Open Challenge. *BioMed Res. Int.* **2014**, *2014*, 1–9. [[CrossRef](#)] [[PubMed](#)]
27. Katz, K.U.; Katz, M.G. Cauchy's Continuum. *Perspect. Sci.* **2011**, *19*, 426–452. [[CrossRef](#)]
28. Chen, W.; Saleeb, A. *Constitutive Equations for Engineering Materials: Elasticity and Modeling*; Studies in Applied Mechanics; Elsevier Science: Amsterdam, The Netherlands, 2013.
29. Marsden, J.; Hughes, T. *Mathematical Foundations of Elasticity*; Dover Civil and Mechanical Engineering; Dover Publications: Mineola, NY, USA, 2012.
30. Knowles, N.K.; Langohr, G.; Faieghi, M.; Nelson, A.J.; Ferreira, L.M. A comparison of density–modulus relationships used in finite element modeling of the shoulder. *Med. Eng. Phys.* **2019**, *66*, 40–46. [[CrossRef](#)]
31. Yosibash, Z.; Padan, R.; Joskowicz, L.; Milgrom, C. A CT-Based High-Order Finite Element Analysis of the Human Proximal Femur Compared to In-vitro Experiments. *J. Biomech. Eng.* **2006**, *129*, 297–309. [[CrossRef](#)]
32. Helgason, B.; Taddei, F.; Pálsson, H.; Schileo, E.; Cristofolini, L.; Viceconti, M.; Brynjólfsson, S. A modified method for assigning material properties to FE models of bones. *Med. Eng. Phys.* **2008**, *30*, 444–453. [[CrossRef](#)]
33. Dall'Ara, E.; Luisier, B.; Schmidt, R.; Kainberger, F.; Zysset, P.; Pahr, D. A nonlinear QCT-based finite element model validation study for the human femur tested in two configurations in vitro. *Bone* **2013**, *52*, 27–38. [[CrossRef](#)]
34. Hambli, R. A quasi-brittle continuum damage finite element model of the human proximal femur based on element deletion. *Med. Biol. Eng. Comput.* **2013**, *51*, 219–231. [[CrossRef](#)]
35. Sarvi, M.N.; Luo, Y. A two-level subject-specific biomechanical model for improving prediction of hip fracture risk. *Clin. Biomech.* **2015**, *30*, 881–887. [[CrossRef](#)]
36. Eberle, S.; Göttliger, M.; Augat, P. An investigation to determine if a single validated density–elasticity relationship can be used for subject specific finite element analyses of human long bones. *Med. Eng. Phys.* **2013**, *35*, 875–883. [[CrossRef](#)] [[PubMed](#)]
37. Keyak, J.; Meagher, J.; Skinner, H.; Mote, C. Automated three-dimensional finite element modelling of bone: A new method. *J. Biomed. Eng.* **1990**, *12*, 389–397. [[CrossRef](#)]
38. Viceconti, M.; Davinelli, M.; Taddei, F.; Cappello, A. Automatic generation of accurate subject-specific bone finite element models to be used in clinical studies. *J. Biomech.* **2004**, *37*, 1597–1605. [[CrossRef](#)] [[PubMed](#)]
39. Enns-Bray, W.; Bahaloo, H.; Fleps, I.; Pauchard, Y.; Taghizadeh, E.; Sigurdsson, S.; Aspelund, T.; Büchler, P.; Harris, T.; Gudnason, V.; et al. Biofidelic finite element models for accurately classifying hip fracture in a retrospective clinical study of elderly women from the AGES Reykjavik cohort. *Bone* **2019**, *120*, 25–37. [[CrossRef](#)] [[PubMed](#)]
40. Falcinelli, C.; Schileo, E.; Pakdel, A.; Whyne, C.; Cristofolini, L.; Taddei, F. Can CT image deblurring improve finite element predictions at the proximal femur? *J. Mech. Behav. Biomed.* **2016**, *63*, 337–351. [[CrossRef](#)]
41. Nishiyama, K.K.; Ito, M.; Harada, A.; Boyd, S.K. Classification of women with and without hip fracture based on quantitative computed tomography and finite element analysis. *Osteoporos. Int.* **2014**, *25*, 619–626. [[CrossRef](#)]

42. Pahr, D.H.; Schwiedrzik, J.; Dall'Ara, E.; Zysset, P.K. Clinical versus pre-clinical FE models for vertebral body strength predictions. *J. Mech. Behav. Biomed.* **2014**, *33*, 76–83. [[CrossRef](#)]
43. Keyak, J.H.; Falkinstein, Y. Comparison of in situ and in vitro CT scan-based finite element model predictions of proximal femoral fracture load. *Med. Eng. Phys.* **2003**, *25*, 781–787. [[CrossRef](#)]
44. Peng, L.; Bai, J.; Zeng, X.; Zhou, Y. Comparison of isotropic and orthotropic material property assignments on femoral finite element models under two loading conditions. *Med. Eng. Phys.* **2006**, *28*, 227–233. [[CrossRef](#)]
45. Zysset, P.; Pahr, D.; Engelke, K.; Genant, H.K.; McClung, M.R.; Kandler, D.L.; Recknor, C.; Kinzl, M.; Schwiedrzik, J.; Museyko, O.; et al. Comparison of proximal femur and vertebral body strength improvements in the FREEDOM trial using an alternative finite element methodology. *Bone* **2015**, *81*, 122–130. [[CrossRef](#)]
46. Gustafson, H.M.; Crompton, P.A.; Ferguson, S.J.; Helgason, B. Comparison of specimen-specific vertebral body finite element models with experimental digital image correlation measurements. *J. Mech. Behav. Biomed.* **2017**, *65*, 801–807. [[CrossRef](#)] [[PubMed](#)]
47. Chen, G.; Wu, F.; Liu, Z.; Yang, K.; Cui, F. Comparisons of node-based and element-based approaches of assigning bone material properties onto subject-specific finite element models. *Med. Eng. Phys.* **2015**, *37*, 808–812. [[CrossRef](#)] [[PubMed](#)]
48. Rajapakse, C.S.; Magland, J.F.; Wald, M.J.; Liu, X.S.; Zhang, X.H.; Guo, X.E.; Wehrli, F.W. Computational biomechanics of the distal tibia from high-resolution MR and micro-CT images. *Bone* **2010**, *47*, 556–563. [[CrossRef](#)] [[PubMed](#)]
49. Koivumäki, J.E.; Thevenot, J.; Pulkkinen, P.; Kuhn, V.; Link, T.M.; Eckstein, F.; Jämsä, T. Ct-based finite element models can be used to estimate experimentally measured failure loads in the proximal femur. *Bone* **2012**, *50*, 824–829. [[CrossRef](#)]
50. Hussein, A.I.; Louzeiro, D.T.; Unnikrishnan, G.U.; Morgan, E.F. Differences in Trabecular Microarchitecture and Simplified Boundary Conditions Limit the Accuracy of Quantitative Computed Tomography-Based Finite Element Models of Vertebral Failure. *J. Biomech. Eng.* **2018**, *140*, 021004. [[CrossRef](#)]
51. Zhang, Y.; Zhong, W.; Zhu, H.; Chen, Y.; Xu, L.; Zhu, J. Establishing the 3-D finite element solid model of femurs in partial by volume rendering. *Int. J. Surg.* **2013**, *11*, 930–934. [[CrossRef](#)]
52. Gamez, B.; Divo, E.; Kassab, A.; Cerrolaza, M. Evaluation of fatigue crack growing in cortical bone using the BEM. *Int. J. Health Tech. Manag.* **2010**, *11*, 202–221. [[CrossRef](#)]
53. Podshivalov, L.; Fischer, A.; Bar-Yoseph, P. 3D hierarchical geometric modeling and multiscale FE analysis as a base for individualized medical diagnosis of bone structure. *Bone* **2011**, *48*, 693–703. [[CrossRef](#)]
54. Fish, J.; Hu, N. Multiscale modeling of femur fracture. *Int. J. Numer. Methods Eng.* **2017**, *111*, 3–25. [[CrossRef](#)]
55. Gray, H.A.; Taddei, F.; Zavatsky, A.B.; Cristofolini, L.; Gill, H.S. Experimental Validation of a Finite Element Model of a Human Cadaveric Tibia. *J. Biomech. Eng.* **2008**, *130*, [[CrossRef](#)]
56. Dall'Ara, E.; Eastell, R.; Viceconti, M.; Pahr, D.; Yang, L. Experimental validation of DXA-based finite element models for prediction of femoral strength. *J. Mech. Behav. Biomed.* **2016**, *63*, 17–25. [[CrossRef](#)] [[PubMed](#)]
57. Grassi, L.; Väänänen, S.P.; Yavari, S.A.; Weinans, H.; Jurvelin, J.S.; Zadpoor, A.A.; Isaksson, H. Experimental validation of finite element model for proximal composite femur using optical measurements. *J. Mech. Behav. Biomed.* **2013**, *21*, 86–94. [[CrossRef](#)] [[PubMed](#)]
58. Larrainzar-Garijo, R.; Caeiro, J.; Marco, M.; Giner, E.; Miguélez, M. Experimental validation of finite elements model in hip fracture and its clinical applicability. *Revista Española de Cirugía Ortopédica y Traumatología (Engl. Ed.)* **2019**, *63*, 146–154. [[CrossRef](#)]
59. Wolfram, U.; Gross, T.; Pahr, D.H.; Schwiedrzik, J.; Wilke, H.J.; Zysset, P.K. Fabric-based Tsai–Wu yield criteria for vertebral trabecular bone in stress and strain space. *J. Mech. Behav. Biomed.* **2012**, *15*, 218–228. [[CrossRef](#)] [[PubMed](#)]
60. Haider, I.T.; Goldak, J.; Frei, H. Femoral fracture load and fracture pattern is accurately predicted using a gradient-enhanced quasi-brittle finite element model. *Med. Eng. Phys.* **2018**, *55*, 1–8. [[CrossRef](#)]
61. Elham, H.; Iwona, J.; Andrew, Y.; YikHan, L.; Tadeusz, L. Multi-scale modelling of elastic moduli of trabecular bone. *J. R. Soc. Interface* **2012**, *9*, 1654–1673. [[CrossRef](#)]
62. Cody, D.D.; Gross, G.J.; Hou, F.J.; Spencer, H.J.; Goldstein, S.A.; Fyhrie, D.P. Femoral strength is better predicted by finite element models than QCT and DXA. *J. Biomech.* **1999**, *32*, 1013–1020. [[CrossRef](#)]

63. Anez-Bustillos, L.; Derikx, L.C.; Verdonshot, N.; Calderon, N.; Zurakowski, D.; Snyder, B.D.; Nazarian, A.; Tanck, E. Finite element analysis and CT-based structural rigidity analysis to assess failure load in bones with simulated lytic defects. *Bone* **2014**, *58*, 160–167. [[CrossRef](#)]
64. Zysset, P.K.; Pahr, E.D.P.V.D.H. Finite element analysis for prediction of bone strength. *Bonekey Rep.* **2013**, *2*, [[CrossRef](#)]
65. Crawford, R.; Cann, C.E.; Keaveny, T.M. Finite element models predict in vitro vertebral body compressive strength better than quantitative computed tomography. *Bone* **2003**, *33*, 744–750. [[CrossRef](#)]
66. Ota, T.; Yamamoto, I.; Morita, R. Fracture simulation of the femoral bone using the finite-element method: How a fracture initiates and proceeds. *J. Bone Miner. Metab.* **1999**, *17*, 108–112. [[CrossRef](#)] [[PubMed](#)]
67. Keyak, J. Improved prediction of proximal femoral fracture load using nonlinear finite element models. *Med. Eng. Phys.* **2001**, *23*, 165–173. [[CrossRef](#)]
68. Eberle, S.; Göttlinger, M.; Augat, P. Individual density–elasticity relationships improve accuracy of subject-specific finite element models of human femurs. *J. Biomech.* **2013**, *46*, 2152–2157. [[CrossRef](#)] [[PubMed](#)]
69. Ascenzi, M.G.; Kawas, N.P.; Lutz, A.; Kardas, D.; Nackenhorst, U.; Keyak, J.H. Individual-specific multi-scale finite element simulation of cortical bone of human proximal femur. *J. Comput. Phys.* **2013**, *244*, 298–311. [[CrossRef](#)]
70. Keyak, J.; Sigurdsson, S.; Karlsdottir, G.; Oskarsdottir, D.; Sigmarsdottir, A.; Zhao, S.; Kornak, J.; Harris, T.; Sigurdsson, G.; Jonsson, B.; et al. Male–female differences in the association between incident hip fracture and proximal femoral strength: A finite element analysis study. *Bone* **2011**, *48*, 1239–1245. [[CrossRef](#)] [[PubMed](#)]
71. Keyak, J.H.; Rossi, S.A.; Jones, K.A.; Skinner, H.B. Prediction of femoral fracture load using automated finite element modeling. *J. Biomech.* **1997**, *31*, 125–133. [[CrossRef](#)]
72. Keyak, J.; Koyama, A.; LeBlanc, A.; Lu, Y.; Lang, T. Reduction in proximal femoral strength due to long-duration spaceflight. *Bone* **2009**, *44*, 449–453. [[CrossRef](#)]
73. Panyasantisuk, J.; Dall’Ara, E.; Pretterklieber, M.; Pahr, D.; Zysset, P. Mapping anisotropy improves QCT-based finite element estimation of hip strength in pooled stance and side-fall load configurations. *Med. Eng. Phys.* **2018**, *59*, 36–42. [[CrossRef](#)]
74. Enns-Bray, W.S.; Owoc, J.S.; Nishiyama, K.K.; Boyd, S.K. Mapping anisotropy of the proximal femur for enhanced image based finite element analysis. *J. Biomech.* **2014**, *47*, 3272–3278. [[CrossRef](#)]
75. Enns-Bray, W.; Bahaloo, H.; Fleps, I.; Ariza, O.; Gilchrist, S.; Widmer, R.; Guy, P.; Pálsson, H.; Ferguson, S.; Crompton, P.; et al. Material mapping strategy to improve the predicted response of the proximal femur to a sideways fall impact. *J. Mech. Behav. Biomed.* **2018**, *78*, 196–205. [[CrossRef](#)]
76. Falcinelli, C.; Martino, A.D.; Gizzi, A.; Vairo, G.; Denaro, V. Mechanical behavior of metastatic femurs through patient-specific computational models accounting for bone-metastasis interaction. *J. Mech. Behav. Biomed.* **2019**, *93*, 9–22. [[CrossRef](#)] [[PubMed](#)]
77. Arjmand, H.; Nazemi, M.; Kontulainen, S.A.; McLennan, C.E.; Hunter, D.J.; Wilson, D.R.; Johnston, J.D. Mechanical Metrics of the Proximal Tibia are Precise and Differentiate Osteoarthritic and Normal Knees: A Finite Element Study. *Sci. Rep.* **2018**, *8*, [[CrossRef](#)] [[PubMed](#)]
78. Sandino, C.; McErlain, D.D.; Schipilow, J.; Boyd, S.K. Mechanical stimuli of trabecular bone in osteoporosis: A numerical simulation by finite element analysis of microarchitecture. *J. Mech. Behav. Biomed.* **2017**, *66*, 19–27. [[CrossRef](#)] [[PubMed](#)]
79. Chen, Y.; Dall’Ara, E.; Sales, E.; Manda, K.; Wallace, R.; Pankaj, P.; Viceconti, M. Micro-CT based finite element models of cancellous bone predict accurately displacement once the boundary condition is well replicated: A validation study. *J. Mech. Behav. Biomed.* **2017**, *65*, 644–651. [[CrossRef](#)] [[PubMed](#)]
80. Hambli, R. Micro-CT finite element model and experimental validation of trabecular bone damage and fracture. *Bone* **2013**, *56*, 363–374. [[CrossRef](#)] [[PubMed](#)]
81. Enns-Bray, W.; Ariza, O.; Gilchrist, S.; Soyka, R.W.; Vogt, P.; Pálsson, H.; Boyd, S.; Guy, P.; Crompton, P.; Ferguson, S.; et al. Morphology based anisotropic finite element models of the proximal femur validated with experimental data. *Med. Eng. Phys.* **2016**, *38*, 1339–1347. [[CrossRef](#)] [[PubMed](#)]

82. Falcinelli, C.; Schileo, E.; Balistreri, L.; Baruffaldi, F.; Bordini, B.; Viceconti, M.; Albisinni, U.; Ceccarelli, F.; Milandri, L.; Toni, A.; et al. Multiple loading conditions analysis can improve the association between finite element bone strength estimates and proximal femur fractures: A preliminary study in elderly women. *Bone* **2014**, *67*, 71–80. [[CrossRef](#)]
83. Podshivalov, L.; Fischer, A.; Bar-Yoseph, P. Multiscale FE method for analysis of bone micro-structures. *J. Mech. Behav. Biomed.* **2011**, *4*, 888–899. Bone Remodeling, [[CrossRef](#)]
84. Zeinali, A.; Hashemi, B.; Akhlaghpour, S. Noninvasive prediction of vertebral body compressive strength using nonlinear finite element method and an image based technique. *Phys. Med.* **2010**, *26*, 88–97. [[CrossRef](#)]
85. Yosibash, Z. p-FEMs in biomechanics: Bones and arteries. *Comput. Meth. Appl. Mech. Eng.* **2012**, *249–252*, 169–184. Higher Order Finite Element and Isogeometric Methods, [[CrossRef](#)]
86. Tanck, E.; van Aken, J.B.; van der Linden, Y.M.; Schreuder, H.B.; Binkowski, M.; Huizenga, H.; Verdonchot, N. Pathological fracture prediction in patients with metastatic lesions can be improved with quantitative computed tomography based computer models. *Bone* **2009**, *45*, 777–783. [[CrossRef](#)] [[PubMed](#)]
87. Sternheim, A.; Giladi, O.; Gortzak, Y.; Drexler, M.; Salai, M.; Trabelsi, N.; Milgrom, C.; Yosibash, Z. Pathological fracture risk assessment in patients with femoral metastases using CT-based finite element methods. A retrospective clinical study. *Bone* **2018**, *110*, 215–220. [[CrossRef](#)] [[PubMed](#)]
88. Peleg, E.; Beek, M.; Jaskowicz, L.; Liebergall, M.; Mosheiff, R.; Whyne, C. Patient specific quantitative analysis of fracture fixation in the proximal femur implementing principal strain ratios. Method and experimental validation. *J. Biomech.* **2010**, *43*, 2684–2688. [[CrossRef](#)] [[PubMed](#)]
89. Katz, Y.; Lubovsky, O.; Yosibash, Z. Patient-specific finite element analysis of femurs with cemented hip implants. *Clin. Biomech.* **2018**, *58*, 74–89. [[CrossRef](#)] [[PubMed](#)]
90. Trabelsi, N.; Yosibash, Z.; Wutte, C.; Augat, P.; Eberle, S. Patient-specific finite element analysis of the human femur—A double-blinded biomechanical validation. *J. Biomech.* **2011**, *44*, 1666–1672. [[CrossRef](#)] [[PubMed](#)]
91. Qasim, M.; Farinella, G.; Zhang, J.; Li, X.; Yang, L.; Eastell, R.; Viceconti, M. Patient-specific finite element estimated femur strength as a predictor of the risk of hip fracture: The effect of methodological determinants. *Osteoporos. Int.* **2016**, *27*, 2815–2822. [[CrossRef](#)]
92. Basafa, E.; Armiger, R.S.; Kutzer, M.D.; Belkoff, S.M.; Mears, S.C.; Armand, M. Patient-specific finite element modeling for femoral bone augmentation. *Med. Eng. Phys.* **2013**, *35*, 860–865. [[CrossRef](#)]
93. Yosibash, Z.; Trabelsi, N. Patient-Specific Simulation of the Proximal Femur’s Mechanical Response Validated by Experimental Observations. In *13th International Conference on Biomedical Engineering*; Lim, C.T., Goh, J.C.H., Eds.; Springer: Berlin/Heidelberg, Germany, 2009; pp. 2019–2022.
94. Keyak, J.; Kaneko, T.; Tehranzadeh, J.; Skinner, H. Predicting Proximal Femoral Strength Using Structural Engineering Models. *Clin. Orthop. Relat. Res.* **2005**, *437*, 219–228. [[CrossRef](#)]
95. Yosibash, Z.; Mayo, R.P.; Dahan, G.; Trabelsi, N.; Amir, G.; Milgrom, C. Predicting the stiffness and strength of human femurs with real metastatic tumors. *Bone* **2014**, *69*, 180–190. [[CrossRef](#)]
96. Zohar, Y.; David, T.; Nir, T. Predicting the yield of the proximal femur using high-order finite-element analysis with inhomogeneous orthotropic material properties. *Philos. Trans. R. Soc. A* **2010**, *368*, [[CrossRef](#)]
97. Grassi, L.; Väänänen, S.P.; Ristinmaa, M.; Jurvelin, J.S.; Isaksson, H. Prediction of femoral strength using 3D finite element models reconstructed from DXA images: Validation against experiments. *Biomech. Model. Mechanobiol.* **2017**, *16*, 989–1000. [[CrossRef](#)] [[PubMed](#)]
98. Nazemi, S.M.; Amini, M.; Kontulainen, S.A.; Milner, J.S.; Holdsworth, D.W.; Masri, B.A.; Wilson, D.R.; Johnston, J.D. Prediction of local proximal tibial subchondral bone structural stiffness using subject-specific finite element modeling: Effect of selected density–modulus relationship. *Clin. Biomech.* **2015**, *30*, 703–712. [[CrossRef](#)] [[PubMed](#)]
99. Wang, X.; Sanyal, A.; Cawthon, P.M.; Palermo, L.; Jekir, M.; Christensen, J.; Ensrud, K.E.; Cummings, S.R.; Orwoll, E.; Black, D.M.; et al. Prediction of new clinical vertebral fractures in elderly men using finite element analysis of CT scans. *J. Bone Miner. Res.* **2012**, *27*, 808–816. [[CrossRef](#)] [[PubMed](#)]
100. Bessho, M.; Ohnishi, I.; Matsumoto, T.; Ohashi, S.; Matsuyama, J.; Tobita, K.; Kaneko, M.; Nakamura, K. Prediction of proximal femur strength using a CT-based nonlinear finite element method: Differences in predicted fracture load and site with changing load and boundary conditions. *Bone* **2009**, *45*, 226–231. [[CrossRef](#)]

101. Bessho, M.; Ohnishi, I.; Matsuyama, J.; Matsumoto, T.; Imai, K.; Nakamura, K. Prediction of strength and strain of the proximal femur by a CT-based finite element method. *J. Biomech.* **2007**, *40*, 1745–1753. [[CrossRef](#)]
102. Tuncer, M.; Hansen, U.N.; Amis, A.A. Prediction of structural failure of tibial bone models under physiological loads: Effect of CT density–modulus relationships. *Med. Eng. Phys.* **2014**, *36*, 991–997. [[CrossRef](#)]
103. Wille, H.; Rank, E.; Yosibash, Z. Prediction of the mechanical response of the femur with uncertain elastic properties. *J. Biomech.* **2012**, *45*, 1140–1148. [[CrossRef](#)]
104. Nishiyama, K.K.; Gilchrist, S.; Guy, P.; Crompton, P.; Boyd, S.K. Proximal femur bone strength estimated by a computationally fast finite element analysis in a sideways fall configuration. *J. Biomech.* **2013**, *46*, 1231–1236. [[CrossRef](#)]
105. Dragomir-Daescu, D.; Op Den Buijs, J.; McEligot, S.; Dai, Y.; Entwistle, R.C.; Salas, C.; Melton, L.J.; Bennet, K.E.; Khosla, S.; Amin, S. Robust QCT/FEA Models of Proximal Femur Stiffness and Fracture Load During a Sideways Fall on the Hip. *Ann. Biomed. Eng.* **2011**, *39*, 742–755. [[CrossRef](#)]
106. Katz, Y.; Dahan, G.; Sosna, J.; Shelef, I.; Cherniavsky, E.; Yosibash, Z. Scanner influence on the mechanical response of QCT-based finite element analysis of long bones. *J. Biomech.* **2019**, *86*, 149–159. [[CrossRef](#)]
107. Weinans, H.; Sumner, D.R.; Igloria, R.; Natarajan, R.N. Sensitivity of periprosthetic stress-shielding to load and the bone density–modulus relationship in subject-specific finite element models. *J. Biomech.* **2000**, *33*, 809–817. [[CrossRef](#)]
108. Cody, D.D.; Hou, F.J.; Divine, G.W.; Fyhrie, D.P. Short Term In Vivo Precision of Proximal Femoral Finite Element Modeling. *Ann. Biomed. Eng.* **2000**, *28*, 408–414. [[CrossRef](#)] [[PubMed](#)]
109. Long, Y.; Leslie, W.D.; Luo, Y. Study of DXA-derived lateral–medial cortical bone thickness in assessing hip fracture risk. *Bone Rep.* **2015**, *2*, 44–51. [[CrossRef](#)] [[PubMed](#)]
110. McErlain, D.D.; Milner, J.S.; Ivanov, T.G.; Jencikova-Celerin, L.; Pollmann, S.I.; Holdsworth, D.W. Subchondral cysts create increased intra-osseous stress in early knee OA: A finite element analysis using simulated lesions. *Bone* **2011**, *48*, 639–646. [[CrossRef](#)] [[PubMed](#)]
111. Schileo, E.; Taddei, F.; Malandrino, A.; Cristofolini, L.; Viceconti, M. Subject-specific finite element models can accurately predict strain levels in long bones. *J. Biomech.* **2007**, *40*, 2982–2989. [[CrossRef](#)] [[PubMed](#)]
112. Schileo, E.; Taddei, F.; Cristofolini, L.; Viceconti, M. Subject-specific finite element models implementing a maximum principal strain criterion are able to estimate failure risk and fracture location on human femurs tested in vitro. *J. Biomech.* **2008**, *41*, 356–367. [[CrossRef](#)]
113. Taddei, F.; Cristofolini, L.; Martelli, S.; Gill, H.; Viceconti, M. Subject-specific finite element models of long bones: An in vitro evaluation of the overall accuracy. *J. Biomech.* **2006**, *39*, 2457–2467. [[CrossRef](#)]
114. Hölzer, A.; Schröder, C.; Woiczinski, M.; Sadoghi, P.; Scharpf, A.; Heimkes, B.; Jansson, V. Subject-specific finite element simulation of the human femur considering inhomogeneous material properties: A straightforward method and convergence study. *Comput. Meth. Prog. Biol.* **2013**, *110*, 82–88. [[CrossRef](#)]
115. Yosibash, Z.; Trabelsi, N.; Hellmich, C. Subject-Specific p-FE Analysis of the Proximal Femur Utilizing Micromechanics-Based Material Properties. *Int. J. Multiscale Comput. Eng.* **2008**, *6*, 483–498. [[CrossRef](#)]
116. Austman, R.L.; Milner, J.S.; Holdsworth, D.W.; Dunning, C.E. The effect of the density–modulus relationship selected to apply material properties in a finite element model of long bone. *J. Biomech.* **2008**, *41*, 3171–3176. [[CrossRef](#)]
117. Michalski, A.S.; Edwards, W.B.; Boyd, S.K. The Influence of Reconstruction Kernel on Bone Mineral and Strength Estimates Using Quantitative Computed Tomography and Finite Element Analysis. *J. Clin. Densitom.* **2019**, *22*, 219–228. [[CrossRef](#)] [[PubMed](#)]
118. Helgason, B.; Gilchrist, S.; Ariza, O.; Vogt, P.; Enns-Bray, W.; Widmer, R.; Fitze, T.; Pálsson, H.; Pauchard, Y.; Guy, P.; et al. The influence of the modulus–density relationship and the material mapping method on the simulated mechanical response of the proximal femur in side-ways fall loading configuration. *Med. Eng. Phys.* **2016**, *38*, 679–689. [[CrossRef](#)] [[PubMed](#)]
119. Taddei, F.; Schileo, E.; Helgason, B.; Cristofolini, L.; Viceconti, M. The material mapping strategy influences the accuracy of CT-based finite element models of bones: An evaluation against experimental measurements. *Med. Eng. Phys.* **2007**, *29*, 973–979. [[CrossRef](#)]

120. Schileo, E.; Balistreri, L.; Grassi, L.; Cristofolini, L.; Taddei, F. To what extent can linear finite element models of human femora predict failure under stance and fall loading configurations? *J. Biomech.* **2014**, *47*, 3531–3538. [[CrossRef](#)] [[PubMed](#)]
121. Yosibash, Z.; Katz, A.; Milgrom, C. Toward verified and validated FE simulations of a femur with a cemented hip prosthesis. *Med. Eng. Phys.* **2013**, *35*, 978–987. [[CrossRef](#)] [[PubMed](#)]
122. Van Rietbergen, B.; Huiskes, R.; Eckstein, F.; Rügsegger, P. Trabecular Bone Tissue Strains in the Healthy and Osteoporotic Human Femur. *J. Bone Miner. Res.* **2003**, *18*, 1781–1788. [[CrossRef](#)]
123. Villette, C.C.; Phillips, A.T.M. Microscale poroelastic metamodel for efficient mesoscale bone remodelling simulations. *Biomech. Model Mechanobiol.* **2017**, *16*, 2077–2091. [[CrossRef](#)]
124. Garcia, D.; Zysset, P.K.; Charlebois, M.; Curnier, A. A three-dimensional elastic plastic damage constitutive law for bone tissue. *Biomech. Model Mechanobiol.* **2009**, *8*, 149–165. [[CrossRef](#)]
125. Johnson, J.E.; Troy, K.L. Validation of a new multiscale finite element analysis approach at the distal radius. *Med. Eng. Phys.* **2017**, *44*, 16–24. [[CrossRef](#)]
126. Bhattacharya, P.; Altai, Z.; Qasim, M.; Viceconti, M. A multiscale model to predict current absolute risk of femoral fracture in a postmenopausal population. *Biomech. Model Mechanobiol.* **2019**, *18*, 301–318. [[CrossRef](#)]
127. Wills, C.R.; Olivares, A.L.; Tassani, S.; Ceresa, M.; Zimmer, V.; Ballester, M.A.G.; del Río, L.M.; Humbert, L.; Noailly, J. 3D patient-specific finite element models of the proximal femur based on DXA towards the classification of fracture and non-fracture cases. *Bone* **2019**, *121*, 89–99. [[CrossRef](#)] [[PubMed](#)]
128. Luo, Y.; Ahmed, S.; Leslie, W.D. Automation of a DXA-based finite element tool for clinical assessment of hip fracture risk. *Comput. Meth. Prog. Biol.* **2018**, *155*, 75–83. [[CrossRef](#)] [[PubMed](#)]
129. Nasiri, M.; Luo, Y. Study of sex differences in the association between hip fracture risk and body parameters by DXA-based biomechanical modeling. *Bone* **2016**, *90*, 90–98. [[CrossRef](#)] [[PubMed](#)]
130. Rajapakse, C.S.; Gupta, N.; Evans, M.; Alizai, H.; Shukurova, M.; Hong, A.L.; Cruickshank, N.J.; Tejwani, N.; Egol, K.; Honig, S.; et al. Influence of bone lesion location on femoral bone strength assessed by MRI-based finite-element modeling. *Bone* **2019**, *122*, 209–217. [[CrossRef](#)]
131. Rajapakse, C.S.; Hotca, A.; Newman, B.T.; Ramme, A.; Vira, S.; Kobe, E.A.; Miller, R.; Honig, S.; Chang, G. Patient-specific Hip Fracture Strength Assessment with Microstructural MR Imaging-based Finite Element Modeling. *Radiology* **2017**, *283*, 854–861. [[CrossRef](#)]
132. Wang, M.; Zimmermann, E.A.; Riedel, C.; Busseb, B.; Li, S.; Silberschmidt, V.V. Effect of micro-morphology of cortical bone tissue on fracture toughness and crack propagation. *Procedia Struct. Integr.* **2017**, *6*, 64–68. [[CrossRef](#)]
133. Idkaidek, A.; Koric, S.; Jasiuk, I. Fracture analysis of multi-osteon cortical bone using XFEM. *Comput. Mech.* **2018**, *62*, 171–184. [[CrossRef](#)]
134. Ural, A.; Mischinski, S. Multiscale modeling of bone fracture using cohesive finite elements. *Eng. Fract. Mech.* **2013**, *103*, 141–152. [[CrossRef](#)]
135. Abueidda, D.W.; Sabet, F.A.; Jasiuk, I.M. Modeling of Stiffness and Strength of Bone at Nanoscale. *J. Biomech. Eng.* **2017**, *139*. [[CrossRef](#)]
136. Lin, L.; Samuel, J.; Zeng, X.; Wang, X. Contribution of extrafibrillar matrix to the mechanical behavior of bone using a novel cohesive finite element model. *J. Mech. Behav. Biomed.* **2017**, *65*, 224–235. [[CrossRef](#)]
137. Idkaidek, A.; Jasiuk, I. Cortical bone fracture analysis using XFEM—Case study. *Int. J. Numer. Methods Biomed. Eng.* **2017**, *33*, e2809, [[CrossRef](#)] [[PubMed](#)]
138. Vaughan, T.; McCarthy, C.; McNamara, L. A three-scale finite element investigation into the effects of tissue mineralisation and lamellar organisation in human cortical and trabecular bone. *J. Mech. Behav. Biomed.* **2012**, *12*, 50–62. [[CrossRef](#)] [[PubMed](#)]
139. Hamed, E.; Lee, Y.; Jasiuk, I. Multiscale modeling of elastic properties of cortical bone. *Acta Mech.* **2010**, *213*, 131–154. [[CrossRef](#)]
140. Fritsch, A.; Hellmich, C. ‘Universal’ microstructural patterns in cortical and trabecular, extracellular and extravascular bone materials: Micromechanics-based prediction of anisotropic elasticity. *J. Theor. Biol.* **2007**, *244*, 597–620. [[CrossRef](#)]
141. Hellmich, C.; Barthélémy, J.F.; Dormieux, L. Mineral–collagen interactions in elasticity of bone ultrastructure—A continuum micromechanics approach. *Eur. J. Mech. A/Solids* **2004**, *23*, 783–810. [[CrossRef](#)]
142. Crolet, J.; Aoubiza, B.; Meunier, A. Compact bone: Numerical simulation of mechanical characteristics. *J. Biomech.* **1993**, *26*, 677–687. [[CrossRef](#)]

143. You, T.; Kim, Y.R.; Park, T. Two-Way Coupled Multiscale Model for Predicting Mechanical Behavior of Bone Subjected to Viscoelastic Deformation and Fracture Damage. *J. Eng. Mater. Technol.* **2017**, *139*, 021016. [[CrossRef](#)]
144. Perrin, E.; Bou-Saïd, B.; Massi, F. Numerical modeling of bone as a multiscale poroelastic material by the homogenization technique. *J. Mech. Behav. Biomed.* **2019**, *91*, 373–382. [[CrossRef](#)]
145. Polgar, K.; Viceconti, M.; Connor, J.J. A comparison between automatically generated linear and parabolic tetrahedra when used to mesh a human femur. *Proc. Inst. Mech. Eng. H* **2001**, *215*, 85–94. [[CrossRef](#)]
146. Li, S.; Abdel-Wahab, A.; Silberschmidt, V.V. Analysis of fracture processes in cortical bone tissue. *Eng. Fract. Mech.* **2013**, *110*, 448–458. [[CrossRef](#)]
147. Kaczmarczyk, L.; Pearce, C. Efficient numerical analysis of bone remodelling. *J. Mech. Behav. Biomed. Mater.* **2011**, *4*, 858–867. [[CrossRef](#)] [[PubMed](#)]
148. Lee, Y.; Ogihara, N.; Lee, T. Assessment of finite element models for prediction of osteoporotic fracture. *J. Mech. Behav. Biomed.* **2019**, *97*, 312–320. [[CrossRef](#)] [[PubMed](#)]
149. Bartsch, C. Atomistische und Kopplungsmodelle in der Elastizitätstheorie. Master's Thesis, TU Berlin, Berlin, Germany, 2014.
150. Wong, A.K. A comparison of peripheral imaging technologies for bone and muscle quantification: A technical review of image acquisition. *J. Musculoskelet. Neuronal Interact.* **2016**, *16*, 265–282. Available online: <https://www.ncbi.nlm.nih.gov/pubmed/27973379> (accessed on 11 December 2019). [[PubMed](#)]
151. Rathnayaka, K.; Momot, K.I.; Noser, H.; Volp, A.; Schuetz, M.A.; Sahama, T.; Schmutz, B. Quantification of the accuracy of MRI generated 3D models of long bones compared to CT generated 3D models. *Med. Eng. Phys.* **2012**, *34*, 357–363. [[CrossRef](#)] [[PubMed](#)]
152. Zysset, P.; Qin, L.; Lang, T.; Khosla, S.; Leslie, W.D.; Shepherd, J.A.; Schousboe, J.T.; Engelke, K. Clinical Use of Quantitative Computed Tomography–Based Finite Element Analysis of the Hip and Spine in the Management of Osteoporosis in Adults: the 2015 ISCD Official Positions—Part II. *J. Clin. Densitom.* **2015**, *18*, 359–392. [[CrossRef](#)] [[PubMed](#)]
153. Engelke, K.; Libanati, C.; Fuerst, T.; Zysset, P.; Genant, H.K. Advanced CT based In Vivo Methods for the Assessment of Bone Density, Structure, and Strength. *Curr. Osteoporos. Rep.* **2013**, *11*, 246–255. [[CrossRef](#)]
154. Iori, G.; Schneider, J.; Reisinger, A.; Heyer, F.; Peralta, L.; Wyers, C.; Gräsel, M.; Barkmann, R.; Glüer, C.C.; van den Bergh, J.P.; et al. Large cortical bone pores in the tibia are associated with proximal femur strength. *PLoS ONE* **2019**, *14*, 1–18. [[CrossRef](#)]
155. Alcantara, A. *Osteoporosis Diagnosis through Multiscale Modeling of Bone Fracture using the Boundary Element Method and Molecular Dynamics*; Research Project FAPESP; The São Paulo Research Foundation: São Paulo, Brazil, 2018.
156. Alsayednoor, J.; Metcalf, L.; Rochester, J.; Dall'Ara, E.; McCloskey, E.; Lacroix, D. Comparison of HR-pQCT- and microCT-based finite element models for the estimation of the mechanical properties of the calcaneus trabecular bone. *Biomech. Model. Mechanobiol.* **2018**, *17*, 1715–1730. [[CrossRef](#)]
157. Jiang, Y.; Zhao, J.; Liao, E.Y.; Dai, R.C.; Wu, X.P.; Genant, H.K. Application of micro-ct assessment of 3-d bone microstructure in preclinical and clinical studies. *J. Bone Miner. Metab.* **2005**, *23*, 122–131. [[CrossRef](#)]
158. Landis, E.N.; Keane, D.T. X-ray microtomography. *Mater. Charact.* **2010**, *61*, 1305–1316. [[CrossRef](#)]
159. Irie, M.S.; Rabelo, G.D.; Spin-Neto, R.; Dechichi, P.; Borges, J.S.; Soares, P.B.F. Use of Micro-Computed Tomography for Bone Evaluation in Dentistry. *Braz. Dent. J.* **2018**, *29*, 227–238. [[CrossRef](#)] [[PubMed](#)]
160. Pahr, D.H.; Zysset, P.K. Finite Element-Based Mechanical Assessment of Bone Quality on the Basis of In Vivo Images. *Curr. Osteoporos. Rep.* **2016**, *14*, 374–385. [[CrossRef](#)] [[PubMed](#)]
161. Fuller, H.; Fuller, R.; Pereira, R.M.R. High resolution peripheral quantitative computed tomography for the assessment of morphological and mechanical bone parameters. *Rev. Bras. Reumatol. (Eng. Ed.)* **2015**, *55*, 352–362. [[CrossRef](#)] [[PubMed](#)]
162. Kohlbrenner, A.; Haemmerle, S.; Laib, A.; Koller, B.; Ruegsegger, P. Fast 3D multiple fan-beam CT systems. In *Developments in X-Ray Tomography II*; Bonse, U., Ed.; International Society for Optics and Photonics (SPIE): Bellingham, WA, USA, 1999; Volume 3772. pp. 44–54. [[CrossRef](#)]
163. Humbert, L.; Martelli, Y.; Fonollà, R.; Steghöfer, M.; Di Gregorio, S.; Malouf, J.; Romera, J.; Barquero, L.M.D.R. 3D-DXA: Assessing the Femoral Shape, the Trabecular Macrostructure and the Cortex in 3D from DXA images. *IEEE Trans. Med. Imaging* **2017**, *36*, 27–39. [[CrossRef](#)] [[PubMed](#)]

164. El Maghraoui, A.; Roux, C. DXA scanning in clinical practice. *QJM-Int. J. Med.* **2008**, *101*, 605–617. [[CrossRef](#)] [[PubMed](#)]
165. Kanis, J.A.; Borgstrom, F.; De Laet, C.; Johansson, H.; Johnell, O.; Jonsson, B.; Oden, A.; Zethraeus, N.; Pfeleger, B.; Khaltav, N. Assessment of fracture risk. *Osteoporos. Int.* **2005**, *16*, 581–589. [[CrossRef](#)]
166. Broy, S.B.; Cauley, J.A.; Lewiecki, M.E.; Schousboe, J.T.; Shepherd, J.A.; Leslie, W.D. Fracture Risk Prediction by Non-BMD DXA Measures: The 2015 ISCD Official Positions Part 1: Hip Geometry. *J. Clin. Densitom.* **2015**, *18*, 287–308. [[CrossRef](#)]
167. Väänänen, S.P.; Grassi, L.; Flivik, G.; Jurvelin, J.S.; Isaksson, H. Generation of 3D shape, density, cortical thickness and finite element mesh of proximal femur from a DXA image. *Med. Image Anal.* **2015**, *24*, 125–134. [[CrossRef](#)]
168. Lenaerts, L.; van Lenthe, G.H. Multi-level patient-specific modelling of the proximal femur. A promising tool to quantify the effect of osteoporosis treatment. *Philos. Trans. R. Soc. A* **2009**, *367*, 2079–2093. [[CrossRef](#)]
169. Cyganik, L.; Binkowski, M.; Kokot, G.; Rusin, T.; Popik, P.; Bolechala, F.; Nowak, R.; Wrobel, Z.; John, A. Prediction of Young's modulus of trabeculae in microscale using macro-scale's relationships between bone density and mechanical properties. *J. Mech. Behav. Biomed.* **2014**, *36*, 120–134. [[CrossRef](#)]
170. Zhang, J.; Yan, C.H.; Chui, C.K.; Ong, S.H. Fast segmentation of bone in CT images using 3D adaptive thresholding. *Comput. Biol. Med.* **2010**, *40*, 231–236. [[CrossRef](#)] [[PubMed](#)]
171. Amorim, P.; Moraes, T.; Silva, J.; Pedrini, H. InVesalius: An Interactive Rendering Framework for Health Care Support. In *Advances in Visual Computing*; Bebis, G., Boyle, R., Parvin, B., Koracin, D., Pavlidis, I., Feris, R., McGraw, T., Elendt, M., Kopper, R., Ragan, E., et al., Eds.; Springer: Cham, Switzerland, 2015; pp. 45–54.
172. Liao, S.H.; Tong, R.F.; Dong, J.X. Anisotropic finite element modeling for patient-specific mandible. *Comput. Meth. Prog. Biol.* **2007**, *88*, 197–209. [[CrossRef](#)] [[PubMed](#)]
173. Kennedy, J.G.; Carter, D.R. Long Bone Torsion: I. Effects of Heterogeneity, Anisotropy and Geometric Irregularity. *J. Biomech. Eng.* **1985**, *107*, 183–188. [[CrossRef](#)] [[PubMed](#)]
174. Kennedy, J.G.; Carter, D.R.; Caler, W.E. Long Bone Torsion: II. A Combined Experimental and Computational Method for Determining an Effective Shear Modulus. *J. Biomech. Eng.* **1985**, *107*, 189–191. [[CrossRef](#)]
175. Sammarco, G.; Burstein, A.H.; Davis, W.L.; Frankel, V.H. The biomechanics of torsional fractures: The effect of loading on ultimate properties. *J. Biomech.* **1971**, *4*, 113–117. [[CrossRef](#)]
176. Carter, D.; Hayes, W. Fatigue life of compact bone—I effects of stress amplitude, temperature and density. *J. Biomech.* **1976**, *9*, 27–34. [[CrossRef](#)]
177. Carter, D.; Hayes, W.; Schurman, D. Fatigue life of compact bone—II. Effects of microstructure and density. *J. Biomech.* **1976**, *9*, 211–218. [[CrossRef](#)]
178. Smith, J.; Walmsley, R. Factors affecting the elasticity of bone. *J. Anat.* **1959**, *93*, 503–523. Available online: <https://www.ncbi.nlm.nih.gov/pmc/articles/PMC1244544/> (accessed on 2 December 2019).
179. Nyman, J.S.; Roy, A.; Shen, X.; Acuna, R.L.; Tyler, J.H.; Wang, X. The influence of water removal on the strength and toughness of cortical bone. *J. Biomech.* **2006**, *39*, 931–938. [[CrossRef](#)]
180. Granke, M.; Does, M.D.; Nyman, J.S. The Role of Water Compartments in the Material Properties of Cortical Bone. *Calcif. Tissue Int.* **2015**, *97*, 292–307. [[CrossRef](#)]
181. Sasaki, N.; Enyo, A. Viscoelastic properties of bone as a function of water content. *J. Biomech.* **1995**, *28*, 809–815. [[CrossRef](#)]
182. Currey, J. The effect of porosity and mineral content on the Young's modulus of elasticity of compact bone. *J. Biomech.* **1988**, *21*, 131–139. [[CrossRef](#)]
183. Currey, J. The mechanical consequences of variation in the mineral content of bone. *J. Biomech.* **1969**, *2*, 1–11. [[CrossRef](#)]
184. Burstein, A.; Zika, J.; Heiple, K.; Klein, L. Contribution of collagen and mineral to the elastic-plastic properties of bone. *J. Bone Jt. Surg.* **1975**, *57*, 956–961. [[CrossRef](#)]
185. Burr, D.B. The relationships among physical, geometrical and mechanical properties of bone, with a note on the properties of nonhuman primate bone. *Am. J. Phys. Anthropol.* **1980**, *23*, 109–146. [[CrossRef](#)]
186. Hansen, U.; Zioupo, P.; Simpson, R.; Currey, J.D.; Hynd, D. The Effect of Strain Rate on the Mechanical Properties of Human Cortical Bone. *J. Biomech. Eng.* **2008**, *130*, 011011. [[CrossRef](#)]
187. Galante, J.; Rostoker, W.; Ray, R.D. Physical properties of trabecular bone. *Calcif. Tissue Res.* **1970**, *5*, 236–246. [[CrossRef](#)]

188. Bargren, J.H.; Bassett, C.L.; Gjelsvik, A. Mechanical properties of hydrated cortical bone. *J. Biomech.* **1974**, *7*, 239–245. [[CrossRef](#)]
189. Black, J.; Korostoff, E. Dynamic mechanical properties of viable human cortical bone. *J. Biomech.* **1973**, *6*, 435–438. [[CrossRef](#)]
190. Vinz, H. Change in the mechanical properties of human compact bone tissue upon aging. *Polym. Mech.* **1975**, *11*, 568–571. [[CrossRef](#)]
191. Sabet, F.A.; Raeisi Najafi, A.; Hamed, E.; Jasiuk, I. Modelling of bone fracture and strength at different length scales: A review. *Interface Focus* **2016**, *6*, 20150055. [[CrossRef](#)] [[PubMed](#)]
192. Grynypas, M. Age and disease-related changes in the mineral of bone. *Calcif. Tissue Int.* **1993**, *53*, S57–S64. [[CrossRef](#)] [[PubMed](#)]
193. Roschger, P.; Paschalis, E.; Fratzl, P.; Klaushofer, K. Bone mineralization density distribution in health and disease. *Bone* **2008**, *42*, 456–466. [[CrossRef](#)] [[PubMed](#)]
194. Kuhlencordt, F.; Dietsch, P.; Keck, E.; Kruse, H.P. *Generalized Bone Diseases: Osteoporosis Osteomalacia Ostitis Fibrosa*; Springer: Berlin/Heidelberg, Germany, 1986; [[CrossRef](#)]
195. Derikx, L.C.; Verdonshot, N.; Tanck, E. Towards clinical application of biomechanical tools for the prediction of fracture risk in metastatic bone disease. *J. Biomech.* **2015**, *48*, 761–766. [[CrossRef](#)]
196. Grant, J.D. Food for thought ... and health: Making a case for plant-based nutrition. *Can. Fam. Phy.* **2012**, *58*, 917–919. Available online: <https://www.ncbi.nlm.nih.gov/pubmed/22972718> (accessed on 2 December 2019).
197. Weaver, C.M.; Proulx, W.R.; Heaney, R. Choices for achieving adequate dietary calcium with a vegetarian diet. *Am. J. Clin. Nutr.* **1999**, *70*, 543s–548s, [[CrossRef](#)]
198. Anderson, J.J. Plant-based diets and bone health: nutritional implications. *Am. J. Clin. Nutr.* **1999**, *70*, 539s–542s, [[CrossRef](#)]
199. Lanou, A.J. Soy foods: Are they useful for optimal bone health? *Ther. Adv. Musculoskel. Dis.* **2011**, *3*, 293–300. [[CrossRef](#)]
200. Weikert, C.; Walter, D.; Hoffmann, K.; Kroke, A.; Bergmann, M.; Boeing, H. The Relation between Dietary Protein, Calcium and Bone Health in Women: Results from the EPIC-Potsdam Cohort. *Ann. Nutr. Metab.* **2005**, *49*, 312–318. [[CrossRef](#)]
201. Weaver, C.M.; Bischoff Ferrari, H.A.; Shanahan, C.J. Cost-benefit analysis of calcium and vitamin D supplements. *Arch. Osteoporos.* **2019**, *14*, 50. [[CrossRef](#)]
202. Caputo, E.L.; Costa, M.Z. Influence of physical activity on quality of life in postmenopausal women with osteoporosis. *Rev. Bras. Reumatol. (Eng. Ed.)* **2014**, *54*, 467–473. [[CrossRef](#)] [[PubMed](#)]
203. Xu, X.; Ji, W.; Lv, X.Q.; Zhu, Y.C.; Zhao, J.X.; Miao, L.Z. Impact of physical activity on health-related quality of life in osteoporotic and osteopenic postmenopausal women: A systematic review. *Int. J. Nurs. Sci.* **2015**, *2*, 204–217. [[CrossRef](#)]
204. Yuan, Y.; Chen, X.; Zhang, L.; Wu, J.; Guo, J.; Zou, D.; Chen, B.; Sun, Z.; Shen, C.; Zou, J. The roles of exercise in bone remodeling and in prevention and treatment of osteoporosis. *Prog. Biophys. Mol. Biol.* **2016**, *122*, 122–130. [[CrossRef](#)] [[PubMed](#)]
205. Daly, R.M.; Via, J.D.; Duckham, R.L.; Fraser, S.F.; Helge, E.W. Exercise for the prevention of osteoporosis in postmenopausal women: an evidence-based guide to the optimal prescription. *Braz. J. Phys. Ther.* **2019**, *23*, 170–180. [[CrossRef](#)]
206. Fung, Y.C. *Biomechanics—Mechanical Properties of Living Tissues*; Springer: New York, NY, USA, 1993.
207. Masson, R.; Bornert, M.; Suquet, P.; Zaoui, A. An affine formulation for the prediction of the effective properties of nonlinear composites and polycrystals. *J. Mech. Phys. Solids* **2000**, *48*, 1203–1227. [[CrossRef](#)]
208. Weiss, J.A.; Maker, B.N.; Govindjee, S. Finite element implementation of incompressible, transversely isotropic hyperelasticity. *Comput. Meth. Appl. Mech. Eng.* **1996**, *135*, 107–128. [[CrossRef](#)]
209. Juszczak, M.M.; Cristofolini, L.; Viceconti, M. The human proximal femur behaves linearly elastic up to failure under physiological loading conditions. *J. Biomech.* **2011**, *44*, 2259–2266. [[CrossRef](#)]
210. Wriggers, P. *Nonlinear Finite Element Methods*; Springer: Berlin, Germany, 2008.
211. Flügge, W. *Viscoelasticity*; Springer: Berlin/Heidelberg, Germany, 1975; [[CrossRef](#)]
212. Rietbergen, B.V.; Odgaard, A.; Kabel, J.; Huiskes, R. Direct mechanics assessment of elastic symmetries and properties of trabecular bone architecture. *J. Biomech.* **1996**, *29*, 1653–1657. [[CrossRef](#)]

213. Burstein, A.H.; Currey, J.D.; Frankel, V.H.; Reilly, D.T. The ultimate properties of bone tissue: The effects of yielding. *J. Biomech.* **1972**, *5*, 35–44. [[CrossRef](#)]
214. David, C.; James, W.D.; Ralph, M. Multiscale modelling and nonlinear finite element analysis as clinical tools for the assessment of fracture risk. *Philos. Trans. R. Soc. A* **2010**, *368*, 2653–2668. [[CrossRef](#)]
215. An, B. Constitutive modeling the plastic deformation of bone-like materials. *Int. J. Solids Struct.* **2016**, *92–93*, 1–8. [[CrossRef](#)]
216. Natali, A.N.; Carniel, E.L.; Pavan, P.G. Constitutive modelling of inelastic behaviour of cortical bone. *Med. Eng. Phys.* **2008**, *30*, 905–912. [[CrossRef](#)] [[PubMed](#)]
217. Nguyen, L.H.; Schilling, D. A multiscale predictor/corrector scheme for efficient elastoplastic voxel finite element analysis, with application to CT-based bone strength prediction. *Comput. Meth. Appl. Mech. Eng.* **2018**, *330*, 598–628. [[CrossRef](#)]
218. Mabrey, J.D.; Fitch, R.D. Plastic deformation in pediatric fractures: Mechanism and treatment. *J. Pediatr. Orthop.* **1989**, *9*, 310–314. Available online: [https://journals.lww.com/pedorthopaedics/Abstract/1989/05000/Plastic\\_Deformation\\_in\\_Pediatric\\_Fractures\\_.10.aspx](https://journals.lww.com/pedorthopaedics/Abstract/1989/05000/Plastic_Deformation_in_Pediatric_Fractures_.10.aspx) (accessed on 11 December 2019). [[CrossRef](#)]
219. De Souza Neto, E.; Peric, D.; Owen, D. *Computational Methods for Plasticity: Theory and Applications*; Wiley: Hoboken, NJ, USA, 2011.
220. Pawlikowski, M.; Barcz, K. Non-linear viscoelastic constitutive model for bovine cortical bone tissue. *Biocybern. Biomed. Eng.* **2016**, *36*, 491–498. [[CrossRef](#)]
221. Wirtz, D.C.; Schiffers, N.; Pandorf, T.; Radermacher, K.; Weichert, D.; Forst, R. Critical evaluation of known bone material properties to realize anisotropic FE-simulation of the proximal femur. *J. Biomech.* **2000**, *33*, 1325–1330. [[CrossRef](#)]
222. Cowin, S.C.; Doty, S.B. *Tissue Mechanics*; Springer: New York, NY, USA, 2007.
223. Ji, B.; Gao, H. Mechanical properties of nanostructure of biological materials. *J. Mech. Phys. Solids* **2004**, *52*, 1963–1990. [[CrossRef](#)]
224. Fung, Y. Elasticity of soft tissues in simple elongation. *Am. J. Physiol. Legacy Content* **1967**, *213*, 1532–1544. [[CrossRef](#)]
225. Fung, Y.C. Structure and Stress-Strain Relationship of Soft Tissues. *Am. Zool.* **1984**, *24*, 13–22. [[CrossRef](#)]
226. Ojanen, X.; Tanska, P.; Malo, M.; Isaksson, H.; Väänänen, S.; Koistinen, A.; Grassi, L.; Magnusson, S.; Ribel-Madsen, S.; Korhonen, R.; et al. Tissue viscoelasticity is related to tissue composition but may not fully predict the apparent-level viscoelasticity in human trabecular bone—An experimental and finite element study. *J. Biomech.* **2017**, *65*, 96–105. [[CrossRef](#)]
227. Pawlikowski, M.; Jankowski, K.; Skalski, K. New microscale constitutive model of human trabecular bone based on depth sensing indentation technique. *J. Mech. Behav. Biomed.* **2018**, *85*, 162–169. [[CrossRef](#)] [[PubMed](#)]
228. Fondrk, M.; Bahniuk, E.; Davy, D.; Michaels, C. Some viscoplastic characteristics of bovine and human cortical bone. *J. Biomech.* **1988**, *21*, 623–630. [[CrossRef](#)]
229. Schwiedrzik, J.J.; Zysset, P.K. An anisotropic elastic-viscoplastic damage model for bone tissue. *Biomech. Model Mechanobiol.* **2013**, *12*, 201–213. [[CrossRef](#)] [[PubMed](#)]
230. Gupta, H.S.; Fratzl, P.; Kerschnitzki, M.; Benecke, G.; Wagermaier, W.; Kirchner, H.O. Evidence for an elementary process in bone plasticity with an activation enthalpy of 1 eV. *J. R. Soc. Interface* **2007**, *4*, 277–282. [[CrossRef](#)]
231. Johnson, T.; Socrate, S.; Boyce, M. A viscoelastic, viscoplastic model of cortical bone valid at low and high strain rates. *Acta Biomater.* **2010**, *6*, 4073–4080. [[CrossRef](#)]
232. Lee, C.S.; Lee, J.M.; Youn, B.; Kim, H.S.; Shin, J.K.; Goh, T.S.; Lee, J.S. A new constitutive model for simulation of softening, plateau, and densification phenomena for trabecular bone under compression. *J. Mech. Behav. Biomed.* **2017**, *65*, 213–223. [[CrossRef](#)]
233. Turner, C.; Burr, D. Basic biomechanical measurements of bone: A tutorial. *Bone* **1993**, *14*, 595–608. [[CrossRef](#)]
234. Cowin, S.C. Bone poroelasticity. *J. Biomech.* **1999**, *32*, 217–238. [[CrossRef](#)]
235. Penta, R.; Merodio, J. Homogenized modeling for vascularized poroelastic materials. *Meccanica* **2017**, *52*, 3321–3343. [[CrossRef](#)]
236. Grillo, A.; Prohl, R.; Wittum, G. A poroplastic model of structural reorganisation in porous media of biomechanical interest. *Contin. Mech. Thermodyn.* **2016**, *28*, 579–601. [[CrossRef](#)]

237. Krajcinovic, D. Damage mechanics. *Mech. Mater.* **1989**, *8*, 117–197. [CrossRef]
238. Sandino, C.; McErlain, D.D.; Schipilow, J.; Boyd, S.K. The poro-viscoelastic properties of trabecular bone: A micro computed tomography-based finite element study. *J. Mech. Behav. Biomed.* **2015**, *44*, 1–9. [CrossRef] [PubMed]
239. Wolff, J. *Das Gesetz der Transformation der Knochen—1892*; Reprint; Pro Business: Berlin, Germany, 2010.
240. Maquet, P.; Wolff, J.; Furlong, R. *The Law of Bone Remodelling*; Springer: Berlin/Heidelberg, Germany, 2012.
241. Fazzalari, N.L. Bone remodeling: A review of the bone microenvironment perspective for fragility fracture (osteoporosis) of the hip. *Semin. Cell Dev. Biol.* **2008**, *19*, 467–472. [CrossRef] [PubMed]
242. Cowin, S.C.; Hegedus, D.H. Bone remodeling I: theory of adaptive elasticity. *J. Elast.* **1976**, *6*, 313–326. [CrossRef]
243. Huiskes, R.; Ruimerman, R.; van Lenthe, G.H.; Janssen, J.D. Effects of mechanical forces on maintenance and adaptation of form in trabecular bone. *Nature* **2000**, *405*, 704–706. [CrossRef]
244. Ralston, S.H. Bone structure and metabolism. *Medicine* **2013**, *41*, 581–585. [CrossRef]
245. Lerebours, C.; Buenzli, P.R.; Scheiner, S.; Pivonka, P. A multiscale mechanobiological model of bone remodelling predicts site-specific bone loss in the femur during osteoporosis and mechanical disuse. *Biomech. Model Mechanobiol.* **2016**, *15*, 43–67. [CrossRef]
246. Engh, C.; Bobyn, J.; Glassman, A. Porous-coated hip replacement. The factors governing bone ingrowth, stress shielding, and clinical results. *J. Bone Jt. Surg. Brit. Vol.* **1987**, *69-B*, 45–55. [CrossRef]
247. Frost, H. Wolff's Law and bone's structural adaptations to mechanical usage: An overview for clinicians. *Angle Orthod.* **1994**, *64*, 175–188. <0175:WLABSA>2.0.CO;2. Available online: <http://wedocs.unep.org/handle/20.500.11822/18246?show=full> (accessed on 2 December 2019). [CrossRef]
248. Andreaus, U.; Giorgio, I.; Madeo, A. Modeling of the interaction between bone tissue and resorbable biomaterial as linear elastic materials with voids. *Z. Angew. Math. Phys.* **2015**, *66*, 209–237. [CrossRef]
249. Van Houtte, P. Anisotropic Plasticity. In *Numerical Modelling of Material Deformation Processes: Research, Development and Applications*; Hartley, P., Pillinger, I., Sturgess, C., Eds.; Springer: London, UK, 1992; pp. 84–111. [CrossRef]
250. Ting, T.C. *Anisotropic Elasticity: Theory and Applications*; Oxford University Press: Oxford, UK, 1996.
251. Baca, V.; Horak, Z.; Mikulenka, P.; Dzupa, V. Comparison of an inhomogeneous orthotropic and isotropic material models used for FE analyses. *Med. Eng. Phys.* **2008**, *30*, 924–930. [CrossRef] [PubMed]
252. Taghizadeh, E.; Reyes, M.; Zysset, P.; Latypova, A.; Terrier, A.; Büchler, P. Biomechanical Role of Bone Anisotropy Estimated on Clinical CT Scans by Image Registration. *Ann. Biomed. Eng.* **2016**, *44*, 2505–2517. [CrossRef] [PubMed]
253. Uten'kin, A.A.; Ashkenazi, E.K. The anisotropy of compact bone material. *Polym. Mech.* **1972**, *8*, 614–618. [CrossRef]
254. Yoon, H.S.; Katz, J.L. Ultrasonic wave propagation in human cortical bone—I. Theoretical considerations for hexagonal symmetry. *J. Biomech.* **1976**, *9*, 407–IN3, [CrossRef]
255. Atsumi, N.; Tanaka, E.; Iwamoto, M.; Hirabayashi, S. Constitutive modeling of cortical bone considering anisotropic inelasticity and damage evolution. *Mech. Eng. J.* **2017**, *adpub*, [CrossRef]
256. Carter, D.; Hayes, W. The Compressive Behavior of Bone as a Two-Phase Porous Structure. *J. Bone Jt. Surg.* **1977**, *59*, 954–962. [CrossRef]
257. François, M.; Geymonat, G.; Berthaud, Y. Determination of the symmetries of an experimentally determined stiffness tensor: Application to acoustic measurements. *Int. J. Solids Struct.* **1998**, *35*, 4091–4106. [CrossRef]
258. Sedláčková, P.; Seiner, H.; Zidek, J.; Janovská, M.; Landa, M. Determination of All 21 Independent Elastic Coefficients of Generally Anisotropic Solids by Resonant Ultrasound Spectroscopy: Benchmark Examples. *Exp. Mech.* **2014**, *54*, 1073–1085. [CrossRef]
259. Goulet, R.; Goldstein, S.; Ciarelli, M.; Kuhn, J.; Brown, M.; Feldkamp, L. The relationship between the structural and orthogonal compressive properties of trabecular bone. *J. Biomech.* **1994**, *27*, 375–389. [CrossRef]
260. Netz, P.; Eriksson, K.; Stromberg, L. Non-Linear Properties of Diaphyseal Bone: An Experimental Study on Dogs. *Acta Orthop. Scand.* **1979**, *50*, 139–143. [CrossRef]
261. Lakes, R.S. Dynamical Study of Couple Stress Effects in Human Compact Bone. *J. Biomech. Eng.* **1982**, *104*, 6–11. [CrossRef] [PubMed]
262. Melnis, A.Ē.; Knets, I.V.; Moorlat, P.A. Deformation behavior of human compact bone tissue upon creep under tensile testing. *Mech. Compos. Mater.* **1980**, *15*, 574–579. [CrossRef]

263. Yang, J.; Lakes, R.S. Experimental study of micropolar and couple stress elasticity in compact bone in bending. *J. Biomech.* **1982**, *15*, 91–98. [[CrossRef](#)]
264. Currey, J.D. The effects of drying and re-wetting on some mechanical properties of cortical bone. *J. Biomech.* **1988**, *21*, 439–441. [[CrossRef](#)]
265. Skedros, J.G.; Mason, M.W.; Bloebaum, R.D. Differences in osteonal micromorphology between tensile and compressive cortices of a bending skeletal system: Indications of potential strain-specific differences in bone microstructure. *Anat Rec.* **1994**, *239*, 405–413. [[CrossRef](#)]
266. Barak, M.M.; Weiner, S.; Shahar, R. Importance of the integrity of trabecular bone to the relationship between load and deformation of rat femora: an optical metrology study. *J. Mater. Chem.* **2008**, *18*, 3855–3864. [[CrossRef](#)]
267. Yan, J.; Daga, A.; Kumar, R.; Mecholsky, J.J. Fracture toughness and work of fracture of hydrated, dehydrated, and ashed bovine bone. *J. Biomech.* **2008**, *41*, 1929–1936. [[CrossRef](#)]
268. Brynk, T.; Hellmich, C.; Fritsch, A.; Zysset, P.; Eberhardsteiner, J. Experimental poromechanics of trabecular bone strength: Role of Terzaghi's effective stress and of tissue level stress fluctuations. *J. Biomech.* **2011**, *44*, 501–508. [[CrossRef](#)]
269. Zannoni, C.; Mantovani, R.; Viceconti, M. Material properties assignment to finite element models of bone structures: A new method. *Med. Eng. Phys.* **1999**, *20*, 735–740. [[CrossRef](#)]
270. Taddei, F.; Pancanti, A.; Viceconti, M. An improved method for the automatic mapping of computed tomography numbers onto finite element models. *Med. Eng. Phys.* **2004**, *26*, 61–69. [[CrossRef](#)]
271. Pegg, E.C.; Gill, H.S. An open source software tool to assign the material properties of bone for ABAQUS finite element simulations. *J. Biomech.* **2016**, *49*, 3116–3121. [[CrossRef](#)] [[PubMed](#)]
272. Alcantara, A.C.S. Implementierung verschiedener Algorithmen zur automatisierten Berechnung und Zuweisung von Materialgesetzen von CT-Daten auf FE-Netze (eng. Implementation of Various Algorithms using Matlab for an Automated Calculation and Assignment of Material Mapping of Computed Tomography Data onto Finite Element Meshes). Bachelor's Thesis, Hochschule Merseburg, Merseburg, Germany, 2017.
273. Les, C.M.; Keyak, J.H.; Stover, S.M.; Taylor, K.T.; Kaneps, A.J. Estimation of material properties in the equine metacarpus with use of quantitative computed tomography. *J. Orthop. Res.* **1994**, *12*, 822–833. [[CrossRef](#)] [[PubMed](#)]
274. Hounsfield, G. Computed medical imaging. *Science* **1980**, *210*, 22–28. [[CrossRef](#)] [[PubMed](#)]
275. Knowles, N.K.; Reeves, J.M.; Ferreira, L.M. Quantitative Computed Tomography (QCT) derived Bone Mineral Density (BMD) in finite element studies: A review of the literature. *J. Exp. Orthop.* **2016**, *3*, 36. [[CrossRef](#)]
276. Schileo, E.; Dall'Ara, E.; Taddei, F.; Malandrino, A.; Schotkamp, T.; Baleani, M.; Viceconti, M. An accurate estimation of bone density improves the accuracy of subject-specific finite element models. *J. Biomech.* **2008**, *41*, 2483–2491. [[CrossRef](#)]
277. Rajapakse, C.S.; Kobe, E.A.; Batzdorf, A.S.; Hast, M.W.; Wehrli, F.W. Accuracy of MRI-based finite element assessment of distal tibia compared to mechanical testing. *Bone* **2018**, *108*, 71–78. [[CrossRef](#)]
278. Ho, K.Y.; Hu, H.H.; Keyak, J.H.; Colletti, P.M.; Powers, C.M. Measuring bone mineral density with fat-water MRI: Comparison with computed tomography. *J. Magn. Reson. Imaging* **2013**, *37*, 237–242. [[CrossRef](#)]
279. Lee, Y.H.; Kim, J.J.; Jang, I.G. Patient-Specific Phantomless Estimation of Bone Mineral Density and Its Effects on Finite Element Analysis Results: A Feasibility Study. *Comput. Math. Methods Med.* **2019**, *2019*, 10. [[CrossRef](#)]
280. Helgason, B.; Perilli, E.; Schileo, E.; Taddei, F.; Brynjólfsson, S.; Viceconti, M. Mathematical relationships between bone density and mechanical properties: A literature review. *Clin. Biomech.* **2008**, *23*, 135–146. [[CrossRef](#)]
281. Morgan, E.F.; Bayraktar, H.H.; Keaveny, T.M. Trabecular bone modulus–density relationships depend on anatomic site. *J. Biomech.* **2003**, *36*, 897–904. [[CrossRef](#)]
282. Kopperdahl, D.L.; Morgan, E.F.; Keaveny, T.M. Quantitative computed tomography estimates of the mechanical properties of human vertebral trabecular bone. *J. Orthop. Res.* **2002**, *20*, 801–805. [[CrossRef](#)]
283. Huang, H.L.; Tsai, M.T.; Lin, D.J.; Chien, C.S.; Hsu, J.T. A new method to evaluate the elastic modulus of cortical bone by using a combined computed tomography and finite element approach. *Comput. Biol. Med.* **2010**, *40*, 464–468. [[CrossRef](#)] [[PubMed](#)]

284. Cong, A.; Buijs, J.O.D.; Dragomir-Daescu, D. In situ parameter identification of optimal density–elastic modulus relationships in subject-specific finite element models of the proximal femur. *Med. Eng. Phys.* **2011**, *33*, 164–173. [[CrossRef](#)] [[PubMed](#)]
285. Keller, T.S. Predicting the compressive mechanical behavior of bone. *J. Biomech.* **1994**, *27*, 1159–1168. [[CrossRef](#)]
286. Hellmich, C.; Kober, C.; Erdmann, B. Micromechanics-Based Conversion of CT Data into Anisotropic Elasticity Tensors, Applied to FE Simulations of a Mandible. *Ann. Biomed. Eng.* **2007**, *36*, 108–122. [[CrossRef](#)]
287. Blanchard, R.; Dejaco, A.; Bongaers, E.; Hellmich, C. Intravoxel bone micromechanics for microCT-based finite element simulations. *J. Biomech.* **2013**, *46*, 2710–2721. [[CrossRef](#)]
288. Hasslinger, P.; Vass, V.; Dejaco, A.; Blanchard, R.; Örlýgsson, G.; Gargiulo, P.; Hellmich, C. Coupling multiscale X-ray physics and micromechanics for bone tissue composition and elasticity determination from micro-CT data, by example of femora from OVX and sham rats. *Int. J. Comput. Methods Eng. Sci. Mech.* **2016**, *17*, 222–244. [[CrossRef](#)]
289. Blanchard, R.; Morin, C.; Malandrino, A.; Vella, A.; Sant, Z.; Hellmich, C. Patient-specific fracture risk assessment of vertebrae: A multiscale approach coupling X-ray physics and continuum micromechanics. *Int. J. Numer. Methods Biomed. Eng.* **2016**, *32*, e02760, [[CrossRef](#)]
290. Fritsch, A.; Hellmich, C.; Dormieux, L. Ductile sliding between mineral Crystals. followed by rupture of collagen crosslinks: Experimentally supported micromechanical explanation of bone strength. *J. Theor. Biol.* **2009**, *260*, 230–252. [[CrossRef](#)]
291. Eberhardsteiner, L.; Hellmich, C.; Scheiner, S. Layered water in crystal interfaces as source for bone viscoelasticity: Arguments from a multiscale approach. *Comput. Methods Biomech. Biomed. Engin.* **2014**, *17*, 48–63. [[CrossRef](#)]
292. Morin, C.; Hellmich, C. A multiscale poromicromechanical approach to wave propagation and attenuation in bone. *Ultrasonics* **2014**, *54*, 1251–1269. [[CrossRef](#)] [[PubMed](#)]
293. Pahr, D.H.; Dall'Ara, E.; Varga, P.; Zysset, P.K. HR-pQCT-based homogenised finite element models provide quantitative predictions of experimental vertebral body stiffness and strength with the same accuracy as  $\mu$  FE models. *Comput. Methods Biomech. Biomed. Eng.* **2012**, *15*, 711–720. [[CrossRef](#)] [[PubMed](#)]
294. Kuhl, E.; Menzel, A.; Steinmann, P. Computational modeling of growth. *Comput. Mech.* **2003**, *32*, 71–88. [[CrossRef](#)]
295. Sarvi, M.N.; Luo, Y.; Sun, P.; Ouyang, J. Experimental Validation of Subject-Specific Dynamics Model for Predicting Impact Force in Sideways Fall. *J. Biomed. Sci. Eng.* **2014**, *7*, 405–418. [[CrossRef](#)]
296. Sarvi, M.N.; Luo, Y. Improving the prediction of sideways fall-induced impact force for women by developing a female-specific equation. *J. Biomech.* **2019**, *88*, 64–71. [[CrossRef](#)]
297. Panyasantisuk, J.; Pahr, D.H.; Zysset, P.K. Effect of boundary conditions on yield properties of human femoral trabecular bone. *Biomech. Model Mechanobiol.* **2016**, *15*, 1043–1053. [[CrossRef](#)]
298. Van den Kroonenberg, A.J.; Hayes, W.C.; McMahon, T.A. Dynamic Models for Sideways Falls From Standing Height. *J. Biomech. Eng.* **1995**, *117*, 309–318. [[CrossRef](#)]
299. Bergmann, G.; Deuretzbacher, G.; Heller, M.; Graichen, F.; Rohlmann, A.; Strauss, J.; Duda, G. Hip contact forces and gait patterns from routine activities. *J. Biomech.* **2001**, *34*, 859–871. [[CrossRef](#)]
300. Altai, Z.; Qasim, M.; Li, X.; Viceconti, M. The effect of boundary and loading conditions on patient classification using finite element predicted risk of fracture. *Clin. Biomech.* **2019**, *68*, 137–143. [[CrossRef](#)]
301. Varga, P.; Schwiedrzik, J.; Zysset, P.K.; Fliri-Hofmann, L.; Widmer, D.; Gueorguiev, B.; Blauth, M.; Windolf, M. Nonlinear quasi-static finite element simulations predict in vitro strength of human proximal femora assessed in a dynamic sideways fall setup. *J. Mech. Behav. Biomed.* **2016**, *57*, 116–127. [[CrossRef](#)]
302. Kim, N. *Introduction to Nonlinear Finite Element Analysis*; Springer: New York, NY, USA, 2014.
303. Reddy, J. *An Introduction to Nonlinear Finite Element Analysis: With Applications to Heat Transfer, Fluid Mechanics, and Solid Mechanics*; Oxford University Press: Oxford, UK, 2015.
304. Parashar, S.K.; Sharma, J.K. A review on application of finite element modelling in bone biomechanics. *Perspect. Sci.* **2016**, *8*, 696–698. [[CrossRef](#)]
305. Macdonald, H.M.; Nishiyama, K.K.; Kang, J.; Hanley, D.A.; Boyd, S.K. Age-related patterns of trabecular and cortical bone loss differ between sexes and skeletal sites: A population-based HR-pQCT study. *J. Bone Miner. Res.* **2011**, *26*, 50–62. [[CrossRef](#)] [[PubMed](#)]

306. Boyd, S.K.; Müller, R.; Zernicke, R.F. Mechanical and Architectural Bone Adaptation in Early Stage Experimental Osteoarthritis. *J. Bone Miner. Res.* **2002**, *17*, 687–694. [[CrossRef](#)] [[PubMed](#)]
307. Brebbia, C.A.; Dominguez, J. *Boundary Elements: An Introductory Course*; WIT Press: Southampton, UK, 1994.
308. Wrobel, L.C.; Aliabadi, M. *The Boundary Element Method, Applications in Thermo-Fluids and Acoustics*; The Boundary Element Method; Wiley: Hoboken, NJ, USA, 2002.
309. Brebbia, C.; Telles, J.; Wrobel, L. *Boundary Element Techniques: Theory and Applications in Engineering*; Springer: Berlin/Heidelberg, Germany, 2012.
310. Sollero, P.; Noritomi, P.; da Silva, J.V.L. Transversely Isotropic Bone Remodeling Using Boundary Element Method. In Proceedings of the II. International Conference on Computational Bioengineering, Lisbon, Portugal, 14–16 September 2005.
311. Prada, D.; Galvis, A.; Sollero, P. Superficial 3D mesh generation process using multimedia software for multiscale bone analysis. In *Proceedings of the 18th International Conference on Boundary Element and Meshless Techniques-BETEQ*; EC Ltd.: Bucharest, Romania, 2017; pp. 126–131.
312. Martínez, M.; Power, M.A.H. A Boundary Element Method For Analysis Of Bone Remodelling. *WIT Trans. Model Simul.* **1996**, *14*, 8. [[CrossRef](#)]
313. Martínez, G.; Aznar, J.M.G.; Doblaré, M.; Cerrolaza, M. External bone remodeling through boundary elements and damage mechanics. *Math Comput. Simul.* **2006**, *73*, 183–199. [[CrossRef](#)]
314. Sadegh, A.; Luo, G.; Cowin, S. Bone ingrowth: An application of the boundary element method to bone remodeling at the implant interface. *J. Biomech.* **1993**, *26*, 167–182. [[CrossRef](#)]
315. Prada, D.M.; Galvis, A.F.; Alcântara, A.C.; Sollero, P. 3D Boundary element meshing for multiscale bone anisotropic analysis. *Eur. J. Comput. Mech.* **2018**, *27*, 425–442. [[CrossRef](#)]
316. Dow, J.O.; Jones, M.S.; Harwood, S.A. A generalized finite difference method for solid mechanics. *Numer. Methods Partial Differ. Equ.* **1990**, *6*, 137–152. [[CrossRef](#)]
317. Hong, J.H.; Mun, M.S.; Lim, T.H. Strain rate dependent poroelastic behavior of bovine vertebral trabecular bone. *KSME Int. J.* **2001**, *15*, 1032–1040. [[CrossRef](#)]
318. Hosokawa, A. Numerical simulation of cancellous bone remodeling using finite difference time-domain method. *AIP Conf. Proc.* **2012**, *1433*, 233–236. [[CrossRef](#)]
319. Bahrieh, M.; Fakharzadeh, A. A survey on bone metastasis by finite difference method. In Proceedings of the 2015 2nd International Conference on Knowledge-Based Engineering and Innovation (KBEL), Tehran, Iran, 5–6 November 2015; pp. 468–472. [[CrossRef](#)]
320. Hosokawa, A. Finite-Difference Time-Domain Simulations of Ultrasound Backscattered Waves in Cancellous Bone. In *5th International Conference on Biomedical Engineering in Vietnam*; Toi, V.V., Lien Phuong, T.H., Eds.; Springer: Cham, Switzerland, 2015; pp. 289–292.
321. Keyak, J.H.; Rossi, S.A. Prediction of femoral fracture load using finite element models: An examination of stress- and strain-based failure theories. *J. Biomech.* **2000**, *33*, 209–214. [[CrossRef](#)]
322. Anderson, T. *Fracture Mechanics: Fundamentals and Applications*, 4th ed.; CRC Press: Boca Raton, FL, USA, 2017.
323. Knott, J. *Fundamentals of Fracture Mechanics*; Butterworths: London, UK, 1973.
324. Jin, Z.H.; Sun, C. A comparison of cohesive zone modeling and classical fracture mechanics based on near tip stress field. *Int. J. Solids Struct.* **2006**, *43*, 1047–1060. [[CrossRef](#)]
325. Park, K.; Paulino, G.H. Cohesive Zone Models: A Critical Review of Traction-Separation Relationships Across Fracture Surfaces. *Appl. Mech. Rev.* **2013**, *64*, 060802. [[CrossRef](#)]
326. Libonati, F.; Vergani, L. Understanding the structure–property relationship in cortical bone to design a biomimetic composite. *Compos. Struct.* **2016**, *139*, 188–198. [[CrossRef](#)]
327. Cox, B.N.; Yang, Q. Cohesive zone models of localization and fracture in bone. *Eng. Fract. Mech.* **2007**, *74*, 1079–1092. [[CrossRef](#)]
328. Elices, M.; Guinea, G.; Gómez, J.; Planas, J. The cohesive zone model: Advantages, limitations and challenges. *Eng. Fract. Mech.* **2002**, *69*, 137–163. [[CrossRef](#)]
329. Begonia, M.; Dallas, M.; Johnson, M.; Thiagarajan, G. Comparison of strain measurement in the mouse forearm using subject-specific finite element models, strain gaging, and digital image correlation. *Biomech. Model Mechanobiol.* **2017**, *16*, 1243–1253. [[CrossRef](#)]
330. Pereira, A.; Javaheri, B.; Pitsillides, A.; Shefelbine, S. Predicting cortical bone adaptation to axial loading in the mouse tibia. *J. R. Soc. Interface* **2015**, *12*, 1–14. [[CrossRef](#)]

331. Ramezanzadehkoldeh, M.; Skallerud, B. MicroCT-based finite element models as a tool for virtual testing of cortical bone. *Med. Eng. Phys.* **2017**, *46*, 12–20. [[CrossRef](#)]
332. Sreenivasan, D.; Tu, P.; Dickinson, M.; Watson, M.; Blais, A.; Das, R.; Cornish, J.; Fernandez, J. Computer modelling integrated with micro-CT and material testing provides additional insight to evaluate bone treatments: Application to a beta-glycan derived whey protein mice model. *Comput. Biol. Med.* **2016**, *68*, 9–20. [[CrossRef](#)]
333. Thiagarajan, G.; Lu, Y.; Dallas, M.; Johnson, M. Experimental and finite element analysis of dynamic loading of the mouse forearm. *J. Orthop. Res.* **2014**, *32*, 1580–1588. [[CrossRef](#)] [[PubMed](#)]
334. Yang, H.; Xu, X.; Bullock, W.; Main, R. Adaptive changes in micromechanical environments of cancellous and cortical bone in response to in vivo loading and disuse. *J. Biomech.* **2019**, *89*, 85–94. [[CrossRef](#)] [[PubMed](#)]
335. Liu, C.; Carrera, R.; Flamini, V.; Kenny, L.; Cabahug-Zuckerman, P.; George, B.M.; Hunter, D.; Liu, B.; Singh, G.; Leucht, P.; et al. Effects of mechanical loading on cortical defect repair using a novel mechanobiological model of bone healing. *Bone* **2018**, *108*, 145–155. [[CrossRef](#)] [[PubMed](#)]
336. Oliviero, S.; Lu, Y.; Viceconti, M.; Dall'Ara, E. Effect of integration time on the morphometric, densitometric and mechanical properties of the mouse tibia. *J. Biomech.* **2017**, *65*, 203–211. [[CrossRef](#)] [[PubMed](#)]
337. Chennimalai Kumar, N.; Dantzig, J.; Jasiuk, I.; Robling, A.; Turner, C. Numerical modeling of long bone adaptation due to mechanical loading: Correlation with experiments. *Ann. Biomed. Eng.* **2010**, *38*, 594–604. [[CrossRef](#)]
338. Hojjat, S.P.; Beek, M.; Akens, M.; Whyne, C. Can micro-imaging based analysis methods quantify structural integrity of rat vertebrae with and without metastatic involvement? *J. Biomech.* **2012**, *45*, 2342–2348. [[CrossRef](#)]
339. Stadelmann, V.; Potapova, I.; Camenisch, K.; Nehrbass, D.; Richards, R.; Moriarty, T.; Chang, Y. In vivo MicroCT monitoring of osteomyelitis in a rat model. *BioMed Res. Int.* **2015**, *2015*, [[CrossRef](#)]
340. Torcasio, A.; Zhang, X.; Duyck, J.; Van Lenthe, G. 3D characterization of bone strains in the rat tibia loading model. *Biomech. Model Mechanobiol.* **2012**, *11*, 403–410. [[CrossRef](#)]
341. Vickerton, P.; Jarvis, J.; Gallagher, J.; Akhtar, R.; Sutherland, H.; Jeffery, N. Morphological and histological adaptation of muscle and bone to loading induced by repetitive activation of muscle. *Proc. R. Soc. B* **2014**, *281*, 20140786. [[CrossRef](#)]
342. Wehner, T.; Steiner, M.; Ignatius, A.; Claes, L.; Aegerter, C. Prediction of the time course of callus stiffness as a function of mechanical parameters in experimental rat fracture healing studies—A numerical study. *PLoS ONE* **2014**, *9*, e115695, [[CrossRef](#)]
343. Tsafnat, N.; Wroe, S. An experimentally validated micromechanical model of a rat vertebra under compressive loading. *J. Anat.* **2011**, *218*, 40–46. [[CrossRef](#)] [[PubMed](#)]
344. Newham, E.; Kague, E.; Aggleton, J.A.; Fernee, C.; Brown, K.R.; Hammond, C.L. Finite element and deformation analyses predict pattern of bone failure in loaded zebrafish spines. *J. R. Soc. Interface* **2019**, *16*, 20190430. [[CrossRef](#)] [[PubMed](#)]
345. Rothstock, S.; Kowaleski, M.; Boudrieau, R.; Beale, B.; Piras, A.; Ryan, M.; Bouré, L.; Brianza, S. Biomechanical and computational evaluation of two loading transfer concepts for pancarpal arthrodesis in dogs. *Am. J. Vet. Res.* **2012**, *73*, 1687–1695. [[CrossRef](#)] [[PubMed](#)]
346. Arias-Moreno, A.; Ito, K.; van Rietbergen, B. Micro-Finite Element analysis will overestimate the compressive stiffness of fractured cancellous bone. *J. Biomech.* **2016**, *49*, 2613–2618. [[CrossRef](#)]
347. Bright, J.; Gröning, F. Strain accommodation in the zygomatic arch of the pig: A validation study using digital speckle pattern interferometry and finite element analysis. *J. Morphol.* **2011**, *272*, 1388–1398. [[CrossRef](#)]
348. Lei, T.; Xie, L.; Tu, W.; Chen, Y.; Tan, Y. Development of a finite element model for blast injuries to the pig mandible and a preliminary biomechanical analysis. *J. Trauma Acute Care Surg.* **2012**, *73*, 902–907. [[CrossRef](#)]
349. Li, S.; Abdel-Wahab, A.; Demirci, E.; Silberschmidt, V. Penetration of cutting tool into cortical bone: Experimental and numerical investigation of anisotropic mechanical behaviour. *J. Biomech.* **2014**, *47*, 1117–1126. [[CrossRef](#)]
350. Qi, L.; Wang, X.; Meng, M. 3D finite element modeling and analysis of dynamic force in bone drilling for orthopedic surgery. *Int. J. Numer. Methods Biomed. Eng.* **2014**, *30*, 845–856. [[CrossRef](#)]
351. Sabet, F.; Jin, O.; Koric, S.; Jasiuk, I. Nonlinear micro-CT based FE modeling of trabecular bone Sensitivity of apparent response to tissue constitutive law and bone volume fraction. *Int. J. Numer. Methods Biomed. Eng.* **2018**, *34*, e2941, [[CrossRef](#)]

352. Stricker, A.; Widmer, D.; Gueorguiev, B.; Wahl, D.; Varga, P.; Duttonhoefer, F. Finite element analysis and biomechanical testing to analyze fracture displacement of alveolar ridge splitting. *BioMed Res. Int.* **2018**, *2018*, [CrossRef]
353. Avery, C.; Bujtár, P.; Simonovics, J.; Dézsi, T.; Váradi, K.; Sándor, G.; Pan, J. A finite element analysis of bone plates available for prophylactic internal fixation of the radial osteocutaneous donor site using the sheep tibia model. *Med. Eng. Phys.* **2013**, *35*, 1421–1430. [CrossRef] [PubMed]
354. Müller, R.; Henss, A.; Kampschulte, M.; Rohnke, M.; Langheinrich, A.; Heiss, C.; Janek, J.; Voigt, A.; Wilke, H.; Ignatius, A.; et al. Analysis of microscopic bone properties in an osteoporotic sheep model: A combined biomechanics, FE and ToF-SIMS study. *J. R. Soc. Interface* **2019**, *16*, 20180793. [CrossRef] [PubMed]
355. Rehman, S.; Garner, P.; Aaron, J.; Wilcox, R. The use of preserved tissue in finite element modelling of fresh ovine vertebral behaviour. *Comput. Methods Biomech. Biomed. Eng.* **2013**, *16*, 1163–1169. [CrossRef] [PubMed]
356. Guilleau, T.; Zhang, Q.H.; Tozzi, G.; Ohrndorf, A.; Christ, H.J.; Tong, J. Compressive behaviour of bovine cancellous bone and bone analogous materials, microCT characterisation and FE analysis. *J. Mech. Behav. Biomed.* **2011**, *4*, 1452–1461. [CrossRef] [PubMed]
357. Jungmann, R.; Szabo, M.; Schitter, G.; Yue-Sing Tang, R.; Vashishth, D.; Hansma, P.; Thurner, P. Local strain and damage mapping in single trabeculae during three-point bending tests. *J. Mech. Behav. Biomed.* **2011**, *4*, 523–534. [CrossRef] [PubMed]
358. Ng, T.; R. Koloor, S.; Djuansjah, J.; Abdul Kadir, M. Assessment of compressive failure process of cortical bone materials using damage-based model. *J. Mech. Behav. Biomed.* **2017**, *66*, 1–11. [CrossRef]
359. Ridha, H.; Thurner, P. Finite element prediction with experimental validation of damage distribution in single trabeculae during three-point bending tests. *J. Mech. Behav. Biomed.* **2013**, *27*, 94–106. [CrossRef]
360. Tozzi, G.; Zhang, Q.H.; Tong, J. 3D real-time micromechanical compressive behaviour of bone-cement interface: Experimental and finite element studies. *J. Biomech.* **2012**, *45*, 356–363. [CrossRef]
361. Zhang, G.; Xu, S.; Yang, J.; Guan, F.; Cao, L.; Mao, H. Combining specimen-specific finite-element models and optimization in cortical-bone material characterization improves prediction accuracy in three-point bending tests. *J. Biomech.* **2018**, *76*, 103–111. [CrossRef]
362. Zhang, G.J.; Yang, J.; Guan, F.J.; Chen, D.; Li, N.; Cao, L.; Mao, H. Quantifying the Effects of Formalin Fixation on the Mechanical Properties of Cortical Bone Using Beam Theory and Optimization Methodology with Specimen-Specific Finite Element Models. *J. Biomech. Eng.* **2016**, *138*, 094502. [CrossRef]
363. Zhang, M.; Gao, J.; Huang, X.; Gong, H.; Zhang, M.; Liu, B. Effects of scan resolutions and element sizes on bovine vertebral mechanical parameters from quantitative computed tomography-based finite element analysis. *J. Healthc. Eng.* **2017**, *2017*, [CrossRef] [PubMed]
364. Harrison, S.; Chris Whitton, R.; Kawcak, C.; Stover, S.; Pandey, M. Evaluation of a subject-specific finite-element model of the equine metacarpophalangeal joint under physiological load. *J. Biomech.* **2014**, *47*, 65–73. [CrossRef] [PubMed]
365. Huynh Nguyen, N.; Pahr, D.; Gross, T.; Skinner, M.; Kivell, T. Micro-finite element ( $\mu$ FE) modeling of the siamang (*Symphalangus syndactylus*) third proximal phalanx: The functional role of curvature and the flexor sheath ridge. *J. Hum. Evol.* **2014**, *67*, 60–75. [CrossRef] [PubMed]
366. Cox, P.; Fagan, M.; Rayfield, E.; Jeffery, N. Finite element modelling of squirrel, guinea pig and rat skulls: Using geometric morphometrics to assess sensitivity. *J. Anat.* **2011**, *219*, 696–709. [CrossRef] [PubMed]
367. Liu, J.; Shi, J.; Fitton, L.; Phillips, R.; O'Higgins, P.; Fagan, M. The application of muscle wrapping to voxel-based finite element models of skeletal structures. *Biomech. Model. Mechanobiol.* **2012**, *11*, 35–47. [CrossRef] [PubMed]
368. Strazic Geljic, I.; Melis, N.; Boukhechba, F.; Schaub, S.; Mellier, C.; Janvier, P.; Laugier, J.P.; Bouler, J.M.; Verron, E.; Scimeca, J.C. Gallium enhances reconstructive properties of a calcium phosphate bone biomaterial. *J. Tissue Eng. Regen. Med.* **2018**, *12*, e854–e866, [CrossRef] [PubMed]
369. Mengoni, M.; Voide, R.; de Bien, C.; Freichels, H.; Jérôme, C.; Leonard, A.; Toye, D.; Müller, R.; van Lenthe, G.; Ponthot, J. A non-linear homogeneous model for bone-like materials under compressive load. *Int. J. Numer. Methods Biomed. Eng.* **2012**, *28*, 334–348. [CrossRef]
370. Pramudita, J.; Kamiya, S.; Ujihashi, S.; Choi, H.Y.; Ito, M.; Watanabe, R.; Crandall, J.; Kent, R. Estimation of conditions evoking fracture in finger bones under pinch loading based on finite element analysis. *Comput. Methods Biomech. Biomed. Eng.* **2017**, *20*, 35–44. [CrossRef]

371. Chen, J.; He, Y.; Keilig, L.; Reimann, S.; Hasan, I.; Weinhold, J.; Radlanski, R.; Bourauel, C. Numerical investigations of bone remodelling around the mouse mandibular molar primordia. *Ann. Anat.* **2019**, *222*, 146–152. [\[CrossRef\]](#)
372. Doostmohammadi, A.; Karimzadeh Esfahani, Z.; Ardeshiryajimi, A.; Rahmati Dehkordi, Z. Zirconium modified calcium-silicate-based nanoceramics: An in vivo evaluation in a rabbit tibial defect model. *Int. J. Appl. Ceram. Technol.* **2019**, *16*, 431–437. [\[CrossRef\]](#)
373. Ren, L.M.; Arahira, T.; Todo, M.; Yoshikawa, H.; Myoui, A. Biomechanical evaluation of porous bioactive ceramics after implantation: Micro CT-based three-dimensional finite element analysis. *J. Mater. Sci. Mater. Med.* **2012**, *23*, 463–472. [\[CrossRef\]](#) [\[PubMed\]](#)
374. Karunratanakul, K.; Kerckhofs, G.; Lammens, J.; Vanlauwe, J.; Schrooten, J.; Van Oosterwyck, H. Validation of a finite element model of a unilateral external fixator in a rabbit tibia defect model. *Med. Eng. Phys.* **2013**, *35*, 1037–1043. [\[CrossRef\]](#) [\[PubMed\]](#)
375. Ni, Y.; Wang, L.; Liu, X.; Zhang, H.; Lin, C.Y.; Fan, Y. Micro-mechanical properties of different sites on woodpecker's skull. *Comput. Methods Biomech. Biomed. Eng.* **2017**, *20*, 1483–1493. [\[CrossRef\]](#) [\[PubMed\]](#)
376. McCartney, W.; MacDonald, B.; Ober, C.; Lostado-Lorza, R.; Gómez, F. Pelvic modelling and the comparison between plate position for double pelvic osteotomy using artificial cancellous bone and finite element analysis. *BMC Vet. Res.* **2018**, *14*, 100. [\[CrossRef\]](#) [\[PubMed\]](#)
377. Weiner, S.; Traub, W. Bone structure: From angstroms to microns. *FASEB J.* **1992**, *6*, 879–885. [\[CrossRef\]](#) [\[PubMed\]](#)
378. Rho, J.Y.; Kuhn-Spearing, L.; Zioupos, P. Mechanical properties and the hierarchical structure of bone. *Med. Eng. Phys.* **1998**, *20*, 92–102. [\[CrossRef\]](#)
379. Keaveny, T.M.; Morgan, E.F.; Yeh, O.C. *Standard Handbook Of Biomedical Engineering And Design*; Chapter Bone Mechanics; McGraw-Hill: New York, NY, USA, 2003.
380. Schwarcz, H.P. The ultrastructure of bone as revealed in electron microscopy of ion-milled sections. *Semin. Cell Dev. Biol.* **2015**, *46*, 44–50. [\[CrossRef\]](#)
381. Fratzl, P.; Weinkamer, R. Hierarchical Structure and Repair of Bone: Deformation, Remodelling, Healing. In *Self Healing Materials: An Alternative Approach to 20 Centuries of Materials Science*; van der Zwaag, S., Ed.; Springer: Dordrecht, The Netherlands, 2007; pp. 323–335. [\[CrossRef\]](#)
382. McNally, E.A.; Schwarcz, H.P.; Botton, G.A.; Arsenaault, A.L. A Model for the Ultrastructure of Bone Based on Electron Microscopy of Ion-Milled Sections. *PLoS ONE* **2012**, *7*, e29258. [\[CrossRef\]](#)
383. Schwarcz, H.P.; McNally, E.A.; Botton, G.A. Dark-field transmission electron microscopy of cortical bone reveals details of extrafibrillar crystals. *J. Struct. Biol.* **2014**, *188*, 240–248. [\[CrossRef\]](#)
384. Kuhn, L. Bone Mineralization. In *Encyclopedia of Materials: Science and Technology*; Buschow, K.J., Cahn, R.W., Flemings, M.C., Ilshner, B., Kramer, E.J., Mahajan, S., Veyssièrè, P., Eds.; Elsevier: Oxford, UK, 2001; pp. 787–794. [\[CrossRef\]](#)
385. Hellmich, C.; Ulm, F.J.; Dormieux, L. Can the diverse elastic properties of trabecular and cortical bone be attributed to only a few tissue-independent phase properties and their interactions? *Biomech. Model Mechanobiol.* **2004**, *2*, 219–238. [\[CrossRef\]](#)
386. Buehler, M.J. Nature designs tough collagen: Explaining the nanostructure of collagen fibrils. *Proc. Natl. Acad. Sci. USA* **2006**, *103*, 12285–12290. [\[CrossRef\]](#) [\[PubMed\]](#)
387. Parenteau-Bareil, R.; Gauvin, R.; Berthod, F. Collagen-Based Biomaterials for Tissue Engineering Applications. *Materials* **2010**, *3*, 1863–1887. [\[CrossRef\]](#)
388. Shoulders, M.D.; Raines, R.T. Collagen Structure and Stability. *Annu. Rev. Biochem.* **2009**, *78*, 929–958. [\[CrossRef\]](#) [\[PubMed\]](#)
389. Hodge, A.J.; Petruska, J.A. Recent studies with the electron microscope on ordered aggregates of the tropocollagen macromolecule. In *Aspects of Protein Structure*; Ramachandran, G.N., Ed.; Academic Press: New York, NY, USA, 1963; pp. 289–300.
390. Orgel, J.P.R.O.; Irving, T.C.; Miller, A.; Wess, T.J. Microfibrillar structure of type I collagen in situ. *Proc. Natl. Acad. Sci. USA* **2006**, *103*, 9001–9005. [\[CrossRef\]](#) [\[PubMed\]](#)
391. Lees, S.; Prostack, K.S.; Ingle, K.; Kjoller, K. The loci of mineral in turkey leg tendon as seen by atomic force microscope and electron microscopy. *Calcif. Tissue Int.* **1994**, *55*, 180–189. [\[CrossRef\]](#) [\[PubMed\]](#)
392. Lees, S.; Bonar, L.C.; Mook, H.A. A study of dense mineralized tissue by neutron diffraction. *Int. J. Biol. Macromol.* **1984**, *6*, 321–326. [\[CrossRef\]](#)

393. Bonar, L.C.; Lees, S.; Mook, H. Neutron diffraction studies of collagen in fully mineralized bone. *J. Mol. Biol.* **1985**, *181*, 265–270. [[CrossRef](#)]
394. Lees, S.; Probst, K.S. The locus of mineral crystallites in bone. *Connect. Tissue Res.* **1988**, *18*, 41–54. [[CrossRef](#)]
395. Lees, S.; Probst, K.S. Visualization of crystal-matrix structure. In situ demineralization of mineralized turkey leg tendon and bone. *Calcif. Tissue Int.* **1996**, *59*, 474–479. [[CrossRef](#)]
396. Sasaki, N.; Tagami, A.; Goto, T.; Taniguchi, M.; Nakata, M.; Hikichi, K. Atomic force microscopic studies on the structure of bovine femoral cortical bone at the collagen fibril-mineral level. *J. Mater. Sci. Mater. Med.* **2002**, *13*, 333–337. [[CrossRef](#)]
397. Pidaparti, R.; Chandran, A.; Takano, Y.; Turner, C. Bone mineral lies mainly outside collagen fibrils: Predictions of a composite model for osteonal bone. *J. Biomech.* **1996**, *29*, 909–916. [[CrossRef](#)]
398. Hellmich, C.; Ulm, F.J. Micromechanical Model for Ultrastructural Stiffness of Mineralized Tissues. *J. Eng. Mech.* **2002**, *128*, 898–908. [[CrossRef](#)]
399. Kurfürst, A.; Henits, P.; Morin, C.; Abdalrahman, T.; Hellmich, C. Bone Ultrastructure as Composite of Aligned Mineralized Collagen Fibrils Embedded Into a Porous Polycrystalline Matrix: Confirmation by Computational Electrodynamics. *Front. Phys.* **2018**, *6*, 125. [[CrossRef](#)]
400. Weiner, S.; Wagner, H.D. The Material Bone: Structure-Mechanical Function Relations. *Annu. Rev. Mater. Sci.* **1998**, *28*, 271–298. [[CrossRef](#)]
401. Craig, A.S.; Birtles, M.J.; Conway, J.F.; Parry, D.A. An Estimate of the Mean Length of Collagen Fibrils in Rat Tail-Tendon as a Function of age. *Connect. Tissue Res.* **1989**, *19*, 51–62. [[CrossRef](#)]
402. Reznikov, N.; Shahar, R.; Weiner, S. Bone hierarchical structure in three dimensions. *Acta Biomater.* **2014**, *10*, 3815–3826. [[CrossRef](#)]
403. Birk, D.E.; Nurminskaya, M.V.; Zycband, E.I. Collagen fibrillogenesis in situ: Fibril segments undergo post-depositional modifications resulting in linear and lateral growth during matrix development. *Dev. Dyn.* **1995**, *202*, 229–243. [[CrossRef](#)]
404. Lai, Z.B.; Yan, C. Mechanical behaviour of staggered array of mineralised collagen fibrils in protein matrix: Effects of fibril dimensions and failure energy in protein matrix. *J. Mech. Behav. Biomed.* **2017**, *65*, 236–247. [[CrossRef](#)]
405. Wang, Y.; Ural, A. Effect of modifications in mineralized collagen fibril and extra-fibrillar matrix material properties on submicroscale mechanical behavior of cortical bone. *J. Mech. Behav. Biomed.* **2018**, *82*, 18–26. [[CrossRef](#)]
406. Reznikov, N.; Chase, H.; Brumfeld, V.; Shahar, R.; Weiner, S. The 3D structure of the collagen fibril network in human trabecular bone: Relation to trabecular organization. *Bone* **2015**, *71*, 189–195. [[CrossRef](#)]
407. Fish, J. *Practical Multiscale*, 1st ed.; John Wiley & Sons Inc.: Hoboken, NJ, USA, 2014.
408. Tomasz Sadowski, P.T.E. *Multiscale Modeling of Complex Materials: Phenomenological, Theoretical and Computational Aspects*, 1st ed.; CISM International Centre for Mechanical Sciences 556; Springer: Wien, Austria, 2014; Volume 556. [[CrossRef](#)]
409. Ostojca-Starzewski, M. *Microstructural Randomness and Scaling in Mechanics of Materials*; Modern Mechanics and Mathematics; CRC Press: Boca Raton, FL, USA, 2007.
410. Feldesman, M.R.; Kleckner, J.G.; Lundy, J.K. Femur/stature ratio and estimates of stature in mid- and late-pleistocene fossil hominids. *Am. J. Phys. Anthropol.* **1990**, *83*, 359–372. [[CrossRef](#)]
411. Åwengen, D.F.; Kurokawa, H.; Nishihara, S.; Goode, R.L. Measurements of the Stapes Superstructure. *Ann. Otol. Rhinol. Laryngol.* **1995**, *104*, 311–316. [[CrossRef](#)] [[PubMed](#)]
412. Wei, S.; Siegal, G.P. *Atlas of Bone Pathology*, 1st ed.; Atlas of Anatomic Pathology; Springer: New York, NY, USA, 2013.
413. Almora-Barrios, N.; De Leeuw, N.H. Molecular Dynamics Simulation of the Early Stages of Nucleation of Hydroxyapatite at a Collagen Template. *Cryst. Growth Des.* **2012**, *12*, 756–763. [[CrossRef](#)]
414. Zhou, Z.; Qian, D.; Minary-Jolandan, M. Clustering of hydroxyapatite on a super-twisted collagen microfibril under mechanical tension. *J. Mater. Chem. B* **2017**, *5*, 2235–2244. [[CrossRef](#)]
415. Barrios, N.A. A Computational Investigation of the Interaction of the Collagen Molecule with Hydroxyapatite. Ph.D. Thesis, University College London, London, UK, 2010.
416. Peter Fratzl, P.F. *Collagen: Structure and Mechanics*, 1st ed.; Springer: Berlin, Germany, 2008.
417. Liu, Y.; Luo, D.; Wang, T. Hierarchical Structures of Bone and Bioinspired Bone Tissue Engineering. *Small* **2016**, *12*, 4611–4632. [[CrossRef](#)] [[PubMed](#)]

418. Budarapu, P.R.; Rabczuk, T. Multiscale Methods for Fracture: A Review. *J. Ind. Sci.* **2017**, *97*, 339–376. [[CrossRef](#)]
419. Nair, A.K.; Gautieri, A.; Chang, S.W.; Buehler, M.J. Molecular mechanics of mineralized collagen fibrils in bone. *Nat. Commun.* **2013**, *4*, 1724. [[CrossRef](#)]
420. Nair, A.K.; Gautieri, A.; Buehler, M.J. Role of Intrafibrillar Collagen Mineralization in Defining the Compressive Properties of Nascent Bone. *Biomacromolecules* **2014**, *15*, 2494–2500. [[CrossRef](#)]
421. Kanouté, P.; Boso, D.P.; Chaboche, J.L.; Schrefler, B.A. Multiscale Methods for Composites: A Review. *Arch. Comput. Methods Eng.* **2009**, *16*, 31–75. [[CrossRef](#)]
422. Benedetti, I.; Aliabadi, M. Multiscale modeling of polycrystalline materials: A boundary element approach to material degradation and fracture. *Comput. Meth. Appl. Mech. Eng.* **2015**, *289*, 429–453. [[CrossRef](#)]
423. Ostoja-Starzewski, M. Material spatial randomness: From statistical to representative volume element. *Probab. Eng. Mech.* **2006**, *21*, 112–132. [[CrossRef](#)]
424. Nguyen, V.P.; Stroeven, M.; Sluys, L.J. Multiscale Continuous and Discontinuous Modeling of Heterogeneous Materials: A Review on Recent Developments. *J. Multiscale Modell. (JMM)* **2011**, *3*, 229–270. [[CrossRef](#)]
425. Mesarovic, S.D.; Padbidri, J. Minimal kinematic boundary conditions for simulations of disordered microstructures. *Philos. Mag.* **2005**, *85*, 65–78. [[CrossRef](#)]
426. Joseph, G.; Jörg, B.; Volker, U. On boundary conditions for homogenization of volume elements undergoing localization. *Int. J. Numer. Methods Eng.* **2017**, *113*, 1–21. [[CrossRef](#)]
427. Ricardez-Sandoval, L.A. Current challenges in the design and control of multiscale systems. *Can. J. Chem. Eng.* **2011**, *89*, 1324–1341. [[CrossRef](#)]
428. Qu, T.; Verma, D.; Shahidi, M.; Pichler, B.; Hellmich, C.; Tomar, V. Mechanics of organic-inorganic biointerfaces—Implications for strength and creep properties. *MRS Bull.* **2015**, *40*, 349–358. [[CrossRef](#)]
429. Bhowmik, R.; Katti, K.S.; Katti, D.R. Mechanics of molecular collagen is influenced by hydroxyapatite in natural bone. *J. Mater. Sci.* **2007**, *42*, 8795–8803. [[CrossRef](#)]
430. Chandra, N.; Namilae, S.; Srinivasan, A. Linking Atomistic and Continuum Mechanics Using Multiscale Models. *AIP Conf. Proc.* **2004**, *712*, 1571–1576. [[CrossRef](#)]
431. Raffi-Tabar, H.; Hua, L.; Cross, M. A multi-scale atomistic-continuum modelling of crack propagation in a two-dimensional macroscopic plate. *J. Condens. Matter Phys.* **1998**, *10*, 2375–2387. [[CrossRef](#)]
432. Guin, L.; Raphanel, J.L.; Kysar, J.W. Atomistically derived cohesive zone model of intergranular fracture in polycrystalline graphene. *J. Appl. Phys.* **2016**, *119*, 245107. [[CrossRef](#)]
433. Enayatpour, S.; van Oort, E.; Patzek, T. Thermal shale fracturing simulation using the Cohesive Zone Method (CZM). *J. Nat. Gas Sci. Eng.* **2018**, *55*, 476–494. [[CrossRef](#)]
434. Lawrimore, W.; Paliwal, B.; Chandler, M.; Johnson, K.; Horstemeyer, M. Hierarchical multiscale modeling of Polyvinyl Alcohol/Montmorillonite nanocomposites. *Polymer* **2016**, *99*, 386–398. [[CrossRef](#)]
435. Paggi, M.; Wriggers, P. A nonlocal cohesive zone model for finite thickness interfaces—Part I: Mathematical formulation and validation with molecular dynamics. *Comput. Mater. Sci.* **2011**, *50*, 1625–1633. [[CrossRef](#)]
436. Plimpton, S. Fast Parallel Algorithms for Short-Range Molecular Dynamics. *J. Comput. Phys.* **1995**, *117*, 1–19. [[CrossRef](#)]
437. De Leeuw, N.H. A computer modelling study of the uptake and segregation of fluoride ions at the hydrated hydroxyapatite (0001) surface: Introducing a  $\text{Ca}_{10}(\text{PO}_4)_6(\text{OH})_2$  potential model. *Phys. Chem. Chem. Phys.* **2004**, *6*, 1860–1866. [[CrossRef](#)]
438. Yeo, J.; Jung, G.; Tarakanova, A.; Martín-Martínez, F.J.; Qin, Z.; Cheng, Y.; Zhang, Y.W.; Buehler, M.J. Multiscale modeling of keratin, collagen, elastin and related human diseases: Perspectives from atomistic to coarse-grained molecular dynamics simulations. *Extreme Mech Lett.* **2018**, *20*, 112–124. [[CrossRef](#)]
439. Cornell, W.D.; Cieplak, P.; Bayly, C.I.; Gould, I.R.; Merz, K.M.; Ferguson, D.M.; Spellmeyer, D.C.; Fox, T.; Caldwell, J.W.; et al. A Second Generation Force Field for the Simulation of Proteins, Nucleic Acids, and Organic Molecules. *J. Am. Chem. Soc.* **1995**, *117*, 5179–5197. [[CrossRef](#)]
440. Griebel, M.; Knapek, S.; Zumbusch, G. Numerical Simulation in Molecular Dynamics. In *Numerics, Algorithms, Parallelization, Applications*; Volume 5 of Texts in Computational Science and Engineering; Springer: Berlin/Heidelberg, Germany, 2007.
441. Hirschfelder, J.O.; Curtiss, C.F.; Bird, R.B. *Molecular Theory of Gases and Liquids*; Wiley: New York, NY, USA, 1964.

442. Rabone, J.A.L.; De Leeuw, N.H. Interatomic potential models for natural apatite Crystals: Incorporating strontium and the lanthanides. *J. Comput. Chem.* **2006**, *27*, 253–266. [[CrossRef](#)]
443. Hauptmann, S.; Dufner, H.; Brickmann, J.; Kast, S.M.; Berry, R.S. Potential energy function for apatites. *Phys. Chem. Chem. Phys.* **2003**, *5*, 635–639. [[CrossRef](#)]
444. Walser, R.; Hünenberger, P.H.; van Gunsteren, W.F. Comparison of different schemes to treat long-range electrostatic interactions in molecular dynamics simulations of a protein crystal. *Proteins* **2001**, *43*, 509–519. [[CrossRef](#)]
445. Scheiner, S.; Pivonka, P.; Hellmich, C. Coupling systems biology with multiscale mechanics, for computer simulations of bone remodeling. *Comput. Meth. Appl. Mech. Eng.* **2013**, *254*, 181–196. [[CrossRef](#)]
446. Scheiner, S.; Pivonka, P.; Hellmich, C. Poromicromechanics reveals that physiological bone strains induce osteocyte-stimulating lacunar pressure. *Biomech. Model. Mechanobiol.* **2016**, *15*, 9–28. [[CrossRef](#)] [[PubMed](#)]
447. Pastrama, M.L.; Scheiner, S.; Pivonka, P.; Hellmich, C. A mathematical multiscale model of bone remodeling, accounting for pore space-specific mechanosensation. *Bone* **2018**, *107*, 208–221. [[CrossRef](#)] [[PubMed](#)]
448. Klein-Nulend, J.; van der Plas, A.; Semeins, C.M.; Ajubi, N.E.; Frangos, J.A.; Nijweide, P.J.; Burger, E.H. Sensitivity of osteocytes to biomechanical stress in vitro. *FASEB J.* **1995**, *9*, 441–445. [[CrossRef](#)] [[PubMed](#)]
449. Colloca, M.; Blanchard, R.; Hellmich, C.; Ito, K.; van Rietbergen, B. A multiscale analytical approach for bone remodeling simulations: Linking scales from collagen to trabeculae. *Bone* **2014**, *64*, 303–313. [[CrossRef](#)]
450. Mirzaali, M.J.; Schwiedrzik, J.J.; Thaiwichai, S.; Best, J.P.; Michler, J.; Zysset, P.K.; Wolfram, U. Mechanical properties of cortical bone and their relationships with age, gender, composition and microindentation properties in the elderly. *Bone* **2016**, *93*, 196–211. [[CrossRef](#)]
451. Zimmermann, E.A.; Launey, M.E.; Ritchie, R.O. The significance of crack-resistance curves to the mixed-mode fracture toughness of human cortical bone. *Biomaterials* **2010**, *31*, 5297–5305. [[CrossRef](#)]
452. Zimmermann, E.A.; Gludovatz, B.; Schaible, E.; Busse, B.; Ritchie, R.O. Fracture resistance of human cortical bone across multiple length-scales at physiological strain rates. *Biomaterials* **2014**, *35*, 5472–5481. [[CrossRef](#)]
453. Chandran, M. Fracture Risk Assessment in Clinical Practice: Why Do It? What to Do It with? *J. Clin. Densitom.* **2017**, *20*, 274–279. [[CrossRef](#)]
454. Kanis, J.A.; Johnell, O.; De Laet, C.; Jonsson, B.; Oden, A.; Ogelsby, A.K. International Variations in Hip Fracture Probabilities: Implications for Risk Assessment. *J. Bone Miner. Res.* **2002**, *17*, 1237–1244. [[CrossRef](#)]
455. Curtis, E.M.; Moon, R.J.; Harvey, N.C.; Cooper, C. The impact of fragility fracture and approaches to osteoporosis risk assessment worldwide. *Bone* **2017**, *104*, 29–38. [[CrossRef](#)] [[PubMed](#)]
456. Pothuaud, L.; Carceller, P.; Hans, D. Correlations between grey-level variations in 2D projection images (TBS) and 3D microarchitecture: Applications in the study of human trabecular bone microarchitecture. *Bone* **2008**, *42*, 775–787. [[CrossRef](#)] [[PubMed](#)]
457. Bousson, V.; Bergot, C.; Sutter, B.; Levitz, P.; Cortet, B.; The Scientific Committee of the GRIO (Groupe de Recherche et d'Information sur les Ostéoporoses). Trabecular bone score (TBS): available knowledge, clinical relevance, and future prospects. *Osteoporos. Int.* **2012**, *23*, 1489–1501. [[CrossRef](#)] [[PubMed](#)]
458. Shevroja, E.; Lamy, O.; Kohlmeier, L.; Koromani, F.; Rivadeneira, F.; Hans, D. Use of Trabecular Bone Score (TBS) as a Complementary Approach to Dual-energy X-ray Absorptiometry (DXA) for Fracture Risk Assessment in Clinical Practice. *J. Clin. Densitom.* **2017**, *20*, 334–345. [[CrossRef](#)]
459. Mirzaei, A.; Jahed, S.A.; Nojomi, M.; Rajaei, A.; Zabihyeganeh, M. A study of the value of trabecular bone score in fracture risk assessment of postmenopausal women. *Taiwan J. Obstet. Gynecol.* **2018**, *57*, 389–393. [[CrossRef](#)]
460. Martineau, P.; Leslie, W. Trabecular bone score (TBS): Method and applications. *Bone* **2017**, *104*, 66–72. [[CrossRef](#)]
461. Bousson, V.; Bergot, C.; Sutter, B.; Thomas, T.; Bendavid, S.; Benhamou, C.L.; Blain, H.; Brazier, M.; Breuil, V.; Briot, K.; et al. Trabecular Bone Score: Where are we now? *Jt. Bone Spine* **2015**, *82*, 320–325. [[CrossRef](#)]
462. Harvey, N.; Glüer, C.; Binkley, N.; McCloskey, E.; Brandi, M.L.; Cooper, C.; Kendler, D.; Lamy, O.; Laslop, A.; Camargos, B.; et al. Trabecular bone score (TBS) as a new complementary approach for osteoporosis evaluation in clinical practice. *Bone* **2015**, *78*, 216–224. [[CrossRef](#)]
463. Parfitt, A. Misconceptions (2): Turnover is always higher in cancellous than in cortical bone. *Bone* **2002**, *30*, 807–809. [[CrossRef](#)]
464. Sahana, S.; Nitin, K.; Joseph, B.; Nihal, T.; Thomas, P. Bone turnover markers: Emerging tool in the management of osteoporosis. *Ind. J. Endocrinol. Metab.* **2016**, *20*, 846–852. [[CrossRef](#)]

465. Vasikaran, S.; Eastell, R.; Bruyère, O.; Foldes, A.J.; Garnero, P.; Griesmacher, A.; McClung, M.; Morris, H.A.; Silverman, S.; Trenti, T.; et al. Markers of bone turnover for the prediction of fracture risk and monitoring of osteoporosis treatment: a need for international reference standards. *Osteoporos. Int.* **2011**, *22*, 391–420. [[CrossRef](#)] [[PubMed](#)]
466. Swaminathan, R. Biochemical markers of bone turnover. *Clin. Chim. Acta* **2001**, *313*, 95–105. [[CrossRef](#)]
467. Afsarimanesh, N.; Mukhopadhyay, S.; Kruger, M. Sensing technologies for monitoring of bone-health: A review. *Sens. Actuators A Phys.* **2018**, *274*, 165–178. [[CrossRef](#)]
468. Afsarimanesh, N.; Mukhopadhyay, S.; Kruger, M. State-of-the-art of sensing technologies for monitoring of bone-health. *Smart Sens. Measur. Instrum.* **2019**, *30*, 7–31. [[CrossRef](#)]
469. Kanis, J.A.; Johnell, O.; Oden, A.; Johansson, H.; McCloskey, E. FRAX™ and the assessment of fracture probability in men and women from the UK. *Osteoporos. Int.* **2008**, *19*, 385–397. [[CrossRef](#)]
470. Kanis, J.A.; Harvey, N.C.; Johansson, H.; Odén, A.; Leslie, W.D.; McCloskey, E.V. FRAX Update. *J. Clin. Densitom.* **2017**, *20*, 360–367. [[CrossRef](#)]
471. Edwards, B.J. Osteoporosis Risk Calculators. *J. Clin. Densitom.* **2017**, *20*, 379–388. [[CrossRef](#)]
472. Fuleihan, G.E.H.; Chakhtoura, M.; Cauley, J.A.; Chamoun, N. Worldwide Fracture Prediction. *J. Clin. Densitom.* **2017**, *20*, 397–424. [[CrossRef](#)]
473. Dimai, H.P. Use of dual-energy X-ray absorptiometry (DXA) for diagnosis and fracture risk assessment; WHO-criteria, T- and Z-score, and reference databases. *Bone* **2017**, *104*, 39–43. [[CrossRef](#)]
474. Donaldson, M.G.; Palermo, L.; Schousboe, J.T.; Ensrud, K.E.; Hochberg, M.C.; Cummings, S.R. FRAX and Risk of Vertebral Fractures: The Fracture Intervention Trial. *J. Bone Miner. Res.* **2009**, *24*, 1793–1799. [[CrossRef](#)]
475. Okazaki, N.; Burghardt, A.J.; Chiba, K.; Schafer, A.L.; Majumdar, S. Bone microstructure in men assessed by HR-pQCT: Associations with risk factors and differences between men with normal, low, and osteoporosis-range areal BMD. *Bone Rep.* **2016**, *5*, 312–319. [[CrossRef](#)] [[PubMed](#)]
476. Hippisley-Cox, J.; Coupland, C. Predicting risk of osteoporotic fracture in men and women in England and Wales: Prospective derivation and validation of QFractureScores. *BMJ* **2009**, *339*, b4229, [[CrossRef](#)] [[PubMed](#)]
477. Hippisley-Cox, J.; Coupland, C. Derivation and validation of updated QFracture algorithm to predict risk of osteoporotic fracture in primary care in the United Kingdom: prospective open cohort study. *BMJ* **2012**, *344*, e3427, [[CrossRef](#)] [[PubMed](#)]
478. Nguyen, N.D.; Frost, S.A.; Center, J.R.; Eisman, J.A.; Nguyen, T.V. Development of a nomogram for individualizing hip fracture risk in men and women. *Osteoporos. Int.* **2007**, *18*, 1109–1117. [[CrossRef](#)]
479. Nguyen, N.D.; Frost, S.A.; Center, J.R.; Eisman, J.A.; Nguyen, T.V. Development of prognostic nomograms for individualizing 5-year and 10-year fracture risks. *Osteoporos. Int.* **2008**, *19*, 1431–1444. [[CrossRef](#)]
480. Nguyen, N.D.; Pongchaiyakul, C.; Center, J.R.; Eisman, J.A.; Nguyen, T.V. Identification of High-Risk Individuals for Hip Fracture: A 14-Year Prospective Study. *J. Bone Miner. Res.* **2005**, *20*, 1921–1928. [[CrossRef](#)]
481. Nguyen, T.V.; Eisman, J.A. Fracture Risk Assessment: From Population to Individual. *J. Clin. Densitom.* **2017**, *20*, 368–378. [[CrossRef](#)]
482. Curtis, E.M.; Moon, R.J.; Harvey, N.C.; Cooper, C. Reprint of: The impact of fragility fracture and approaches to osteoporosis risk assessment worldwide. *Int. J. Orthop. Trauma Nurs.* **2017**, *26*, 7–17. [[CrossRef](#)]
483. Kanis, J.A.; Harvey, N.C.; Johansson, H.; Odén, A.; McCloskey, E.V.; Leslie, W.D. Overview of Fracture Prediction Tools. *J. Clin. Densitom.* **2017**, *20*, 444–450. [[CrossRef](#)]
484. Leslie, W.D.; Lix, L.M. Comparison between various fracture risk assessment tools. *Osteoporos. Int.* **2014**, *25*, 1–21. [[CrossRef](#)]
485. Nguyen, T.V. Individualized Assessment of Fracture Risk: Contribution of “Osteogenomic Profile”. *J. Clin. Densitom.* **2017**, *20*, 353–359. [[CrossRef](#)] [[PubMed](#)]
486. Forgetta, V.; Keller-Baruch, J.; Forest, M.; Durand, A.; Bhatnagar, S.; Kemp, J.; Morris, J.A.; Kanis, J.A.; Kiel, D.P.; McCloskey, E.V.; et al. Machine Learning to Predict Osteoporotic Fracture Risk from Genotypes. *bioRxiv* **2018**, 413716. [[CrossRef](#)]

487. DVO-Leitlinie. Methodenreport der DVO-Leitlinie 2014 zur Prophylaxe, Diagnostik und Therapie der Osteoporose bei Männern ab dem 60. Lebensjahr und bei postmenopausalen Frauen. 2014. Available online: <http://www.dv-osteologie.org/uploads/Leitlinie%202014/DVO-Leitlinie%20Osteoporose%202014%20Kurzfassung%20und%20Langfassung%20Version%201a%2012%2001%202016.pdf> (accessed on 12 December 2019).
488. Thomasius, F.; Baum, E.; Bernecker, P.; Böcker, W.; Brabant, T.; Clarenz, P.; Demary, W.; Dimai, H.P.; Engelbrecht, M.; Engelke, K.; et al. DVO Leitlinie 2017 zur Prophylaxe, Diagnostik und Therapie der Osteoporose bei postmenopausalen Frauen und Männern / S-3 DVO Guidelines 2017 in prophylaxis, diagnosis and therapy of osteoporosis in postmenopausal women und men. *Osteologie* **2018**, *27*, 154–160. [[CrossRef](#)]
489. Reber, K.C.; König, H.H.; Becker, C.; Rapp, K.; Büchele, G.; Mächler, S.; Lindlbauer, I. Development of a risk assessment tool for osteoporotic fracture prevention: A claims data approach. *Bone* **2018**, *110*, 170–176. [[CrossRef](#)]
490. Black, D.; Steinbuch, M.; Palermo, L.; Dargent-Molina, P.; Lindsay, R.; Hoseyni, M.; Johnell, O. An assessment tool for predicting fracture risk in postmenopausal women. *Osteoporos. Int.* **2001**, *12*, 519–528. [[CrossRef](#)]
491. Järvinen, T.L.; Michaëlsson, K.; Jokihaara, J.; Collins, G.S.; Perry, T.L.; Mintzes, B.; Musini, V.; Erviti, J.; Gorricho, J.; Wright, J.M.; et al. Overdiagnosis of bone fragility in the quest to prevent hip fracture. *BMJ* **2015**, *350*, h2088, [[CrossRef](#)]
492. Hamdy, R.C. Osteoporosis—Assessing Fracture Risk. *J. Clin. Densitom.* **2017**, *20*, 271. [[CrossRef](#)]
493. Baim, S. The Future of Fracture Risk Assessment in the Management of Osteoporosis. *J. Clin. Densitom.* **2017**, *20*, 451–457. [[CrossRef](#)]
494. Gurtin, M.; Fried, E.; Anand, L. *The Mechanics and Thermodynamics of Continua*; Cambridge University Press: Cambridge, UK, 2010.
495. Carathéodory, C. *Vorlesungen über Reelle Funktionen*, 2nd ed.; Springer: Berlin, Germany, 1927.
496. Motteler, Z.; Miranda, C. *Partial Differential Equations of Elliptic Type*; Ergebnisse der Mathematik und ihrer Grenzgebiete. 2. Folge; Springer: Berlin/Heidelberg, Germany, 2012.
497. Willard, S. *General Topology*; Addison-Wesley series in mathematics; Dover Publications: Mineola, NY, USA, 2004.
498. Henry, D.; Hale, J.; Pereira, A. *Perturbation of the Boundary in Boundary-Value Problems of Partial Differential Equations*; London Mathematical Society Lecture Note Series; Cambridge University Press: Cambridge, UK, 2005.
499. Ogden, R. *Non-Linear Elastic Deformations*; Dover Civil and Mechanical Engineering; Dover Publications: Mineola, NY, USA, 1997.
500. Chaboche, J. A review of some plasticity and viscoplasticity constitutive theories. *Int. J. Plast.* **2008**, *24*, 1642–1693. [[CrossRef](#)]
501. Malvern, L. *Introduction to the Mechanics of a Continuous Medium*; Prentice-Hall series in engineering of the physical sciences; Prentice-Hall: Upper Saddle River, NJ, USA, 1969.
502. Truesdell, C.; Noll, W. *The Non-Linear Field Theories of Mechanics*, 3rd ed.; Springer: Berlin/Heidelberg, Germany, 2004; [[CrossRef](#)]
503. Smith, D.R. *An Introduction to Continuum Mechanics—After Truesdell and Noll*; Springer: Dordrecht, The Netherlands, 1993; [[CrossRef](#)]
504. Truesdell, C. *A First Course in Rational Continuum Mechanics*; Academic Press Inc.: Cambridge, MA, USA, 1991; Volume 1.
505. Lai, W.M.; Rubin, D.; Krempl, E. *Introduction to Continuum Mechanics*, 4th ed.; Butterworth-Heinemann: Boston, MA, USA, 2010; [[CrossRef](#)]
506. Fung, Y. *Foundations of Solid Mechanics*; International series in dynamics; Prentice-Hall: Upper Saddle River, NJ, USA, 1965.
507. Lubliner, J. *Plasticity Theory*; Dover books on engineering; Dover Publications: Mineola, NY, USA, 2008.
508. Coussy, O. *Poromechanics*, 2nd ed.; Wiley: Hoboken, NJ, USA, 2004.
509. Kachanov, L. *Introduction to Continuum Damage Mechanics*, 1st ed.; Mechanics of Elastic Stability; Springer: Berlin, Germany, 2010.
510. Murakami, S. *Continuum Damage Mechanics: A Continuum Mechanics Approach to the Analysis of Damage and Fracture*, 1st ed.; Solid Mechanics and Its Applications 185; Springer: Dordrecht, The Netherlands, 2012.

511. Krajcinovic, D.; Lemaitre, J. *Continuum Damage Mechanics Theory and Application*; CISM International Centre for Mechanical Sciences; Springer: Vienna, Austria, 2014.
512. Wohua Zhang, Y.C. *Continuum Damage Mechanics and Numerical Applications*; Jointly published with zhejiang university press, 2011 ed.; Advanced Topics in Science and Technology in China; Springer: Berlin/Heidelberg, Germany, 2010.
513. Truesdell, C. *The Elements of Continuum Mechanics*; Springer: Berlin/Heidelberg, Germany, 1984; [CrossRef]
514. Lekhnitskik, S.G. *Theory of Elasticity of an Anisotropic Elastic Body*; Holden-Day: Toronto, ON, Canada, 1963.
515. Gamelin, T.; Greene, R. *Introduction to Topology*, 2nd ed.; Dover Books on Mathematics, Dover Publications: Mineola, NY, USA, 2013.
516. Cowin, S.C. Bone Stress Adaptation Models. *J. Biomech. Eng.* **1993**, *115*, 528–533. [CrossRef]



© 2019 by the authors. Licensee MDPI, Basel, Switzerland. This article is an open access article distributed under the terms and conditions of the Creative Commons Attribution (CC BY) license (<http://creativecommons.org/licenses/by/4.0/>).

### 3 DEVISING BONE MOLECULAR MODELS AT THE NANOSCALE

As discussed in Chapter 1, the improvement of bone fracture prediction and diagnosis currently requires a comprehensive understanding of the mechanical behavior of bones at the nanoscale, i.e., (1.), which requires elaborate and computer expensive all-atom molecular models. There is only limited information in the literature providing clear and thorough instructions on how to model bone at the nanoscale. Furthermore, no molecular model presented in the literature exhibited mineralization in the extrafibrillar volume, nor the extrafibrillar region itself.

The following paper provides a detailed prescription on how to devise all-atom bone molecular models that include mineral both in the intra- and extrafibrillar volumes. To our knowledge, it was the first molecular model presented in the literature to take into account this important element of the biology, chemistry, and mechanics of fibers in bones. Our models unfold a new alternative to study the nanoscale mechanics of bones, and together with the information provided in this paper, can be used as the foundation of future studies regarding the modeling and mechanical properties of bone at the nanoscale.

The advancement of the field requires more and more people collaborating towards the investigation of the nanomechanics of bones. Yet, devising all-atom bone molecular models is far from trivial, especially when it displays an extrafibrillar volume. To facilitate and accelerate dissemination of our models and findings, we provided all used scripts and files together with detailed modeling instructions.

Article

# Devising Bone Molecular Models at the Nanoscale: From Usual Mineralized Collagen Fibrils to the First Bone Fibers Including Hydroxyapatite in the Extra-Fibrillar Volume

Amadeus C. S. Alcântara <sup>1,2</sup> , Levi C. Felix <sup>2,3</sup> , Douglas S. Galvão <sup>2,3</sup> , Paulo Sollero <sup>1,2</sup>   
and Munir S. Skaf <sup>2,4,\*</sup> 

- <sup>1</sup> Department of Computational Mechanics, School of Mechanical Engineering, University of Campinas—UNICAMP, Campinas 13083-860, SP, Brazil; amadeus.alcantara@fem.unicamp.br (A.C.S.A.); sollero@fem.unicamp.br (P.S.)
- <sup>2</sup> Center for Computing in Engineering & Sciences, CCES, University of Campinas—UNICAMP, Campinas 13083-861, SP, Brazil; felixce@ifi.unicamp.br (L.C.F.); galvao@ifi.unicamp.br (D.S.G.)
- <sup>3</sup> Department of Applied Physics, Gleb Wataghin Institute of Physics, University of Campinas—UNICAMP, Campinas 13083-859, SP, Brazil
- <sup>4</sup> Institute of Chemistry, University of Campinas—UNICAMP, Campinas 13083-970, SP, Brazil
- \* Correspondence: skaf@unicamp.br



**Citation:** Alcântara, A.C.S.; Felix, L.C.; Galvão, D.S.; Sollero, P.; Skaf, M.S. Devising Bone Molecular Models at the Nanoscale: From Usual Mineralized Collagen Fibrils to the First Fibers Including Hydroxyapatite in the Extra-Fibrillar Volume. *Materials* **2022**, *15*, 2274. <https://doi.org/10.3390/ma15062274>

Academic Editors: Bin Wang and Arash Soleiman-Fallah

Received: 31 January 2022

Accepted: 17 March 2022

Published: 19 March 2022

**Publisher's Note:** MDPI stays neutral with regard to jurisdictional claims in published maps and institutional affiliations.



**Copyright:** © 2022 by the authors. Licensee MDPI, Basel, Switzerland. This article is an open access article distributed under the terms and conditions of the Creative Commons Attribution (CC BY) license (<https://creativecommons.org/licenses/by/4.0/>).

**Abstract:** At the molecular scale, bone is mainly constituted of type-I collagen, hydroxyapatite, and water. Different fractions of these constituents compose different composite materials that exhibit different mechanical properties at the nanoscale, where the bone is characterized as a fiber, i.e., a bundle of mineralized collagen fibrils surrounded by water and hydroxyapatite in the extra-fibrillar volume. The literature presents only models that resemble mineralized collagen fibrils, including hydroxyapatite in the intra-fibrillar volume only, and lacks a detailed prescription on how to devise such models. Here, we present all-atom bone molecular models at the nanoscale, which, differently from previous bone models, include hydroxyapatite both in the intra-fibrillar volume and in the extra-fibrillar volume, resembling fibers in bones. Our main goal is to provide a detailed prescription on how to devise such models with different fractions of the constituents, and for that reason, we have made step-by-step scripts and files for reproducing these models available. To validate the models, we assessed their elastic properties by performing molecular dynamics simulations that resemble tensile tests, and compared the computed values against the literature (both experimental and computational results). Our results corroborate previous findings, as Young's Modulus values increase with higher fractions of hydroxyapatite, revealing all-atom bone models that include hydroxyapatite in both the intra-fibrillar volume and in the extra-fibrillar volume as a path towards realistic bone modeling at the nanoscale.

**Keywords:** bone nanoscale model; mineralized collagen fibril; collagen fiber; hydroxyapatite; extra-fibrillar volume; molecular dynamics; bone elastic properties

## 1. Introduction

If current preventive diagnosis techniques remain unimproved, aging-related bone diseases, such as osteoporosis and their subsequent bone fractures are expected to overload health care systems worldwide [1]. Understanding the mechanical properties of bones at each length scale is essential to improving such techniques. Computer simulations allow the investigation of mechanical properties at all length scales by combining mathematical, physical, engineering, and biological concepts [2]. Furthermore, the more realistic they are, the more reliable such preventive diagnosis techniques become.

Bones are patient-specific and exhibit a multiscale structure [2–4]. This means that a bone fragment from a given individual exhibits a complex network of different physical structures and mechanical properties down to the molecular scale, where fracture ultimately

originates. Thus, the best-achievable simulations must seek to: (1) consider bones as patient-specific by devising different models with different fractions of the constituents, testing several specimens of a statistical population, or by extracting geometry and mechanical properties directly from the targeted bone, e.g., from computed tomography; (2) consider the multiscale nature of bone by modeling and coupling several length scales, or by devising models that directly include information from other length scales.

Several works performing molecular dynamics (MD) simulations of the bone structure have tried to comply with these two points, as shown by recent reviews [2,3,5]. Especially after Ref. [6] made available the first fibrillar structure of type I collagen, i.e., the structure of bone at the sub-nanoscale [2], MD simulations were carried out to study the heterogeneous nature of collagen [7,8], the orientation and chemical processes of its structure [9,10], and its mechanical properties [11]. Subsequently, hydroxyapatite crystals were included in the models based on the fibrillar structure provided by Ref. [6] for further investigations, especially for the mechanical properties [12–17]. To date, hydroxyapatite has been included solely within fibrils, in the intra-fibrillar volume (IFV). Yet, as several experiments have shown, higher concentrations of hydroxyapatite are indeed found surrounding the fibrils in the extra-fibrillar volume (EFV) [18–23], which is also labeled as the extra-fibrillar matrix.

Understanding the mechanical properties of bones and the molecular aspects that underlie their behavior at small non-continuous length scales constitutes an open field of research and requires substantial further endeavors. This work aims to contribute to the field by: (1) detailing the process of modeling all-atom bone collagen fibrils (subnanoscale [2]) and, for the first time, fibers (nanoscale [2]); (2) investigating the mechanical properties of bone at the nanoscale to validate the model. This paper details how all-atom models that resemble the structure of fibers in bones can be devised, and how they can be subjected to nanoscale traction tests to assess their Young's Modulus values. The models consist of a bundle of mineralized collagen fibrils surrounded by hydroxyapatite in the EFV, similar to the experiments presented in Ref. [20] Figure 4 (reproduced in Ref. [24] Figure 1), and Ref. [18] Figure 8. All files and scripts used to devise the described models are available in the Supplementary Materials.

### 1.1. Reading This Paper—Textual Organization and Notation

This paper covers a multidisciplinary topic, which may attract the attention of researchers from different fields, including biology, medicine, physics, chemistry, and engineering. Thus, inspired by Ref. [2], four extra text environments were used to increase the paper readability:

**Definition:** Non-mathematical definitions that may be differently understood by specialists from different fields;

**Highlight:** A statement that plays a major role in the interpretations and discussions of the results;

**Open Issue:** Issues and problems not clearly defined or not yet completely solved within the surveyed literature;

**Remark:** Relevant notes.

The appendices contain detailed information about the modeling process. Readers seeking to reproduce the models are advised to read the main text along with the appendices.

### 1.2. The Multiscale Structure of Bone: From the Molecular Scale to the Nanoscale

At the molecular scale, bone is a unique and complex composite material mainly composed of type I collagen (CLG), hydroxyapatite (HA)  $\text{Ca}_{10}(\text{PO}_4)_6(\text{OH})_2$ , and water ( $\text{H}_2\text{O}$ ) [2,25–28]. Different fractions of these constituents lead to different mechanical properties of the material; bones with a lower concentration of HA usually display lower stiffness, and vice versa [12,29].

- Reference values for their volume fractions are: 33–43% mineral material (mainly HA), 32–44% organic material (mainly CLG), and 15–25% H<sub>2</sub>O [23,30].
- Reference values for their mass fractions are: 60–65% mineral material (mainly HA), 25–30% organic material (mainly CLG), and 10% H<sub>2</sub>O [22,30–32].

A single CLG molecule, i.e., a tropocollagen, is a helical structure consisting of three (two alpha-1 and one alpha-2) left-handed polypeptide chains coiled around each other to form a right-handed superhelix; see Figure 1. A polypeptide chain consists of a sequence of amino acids covalently linked by peptide bonds. An alpha-amino acid (labeled here as simply amino acid) is an organic compound that contains an amino group (NH<sub>2</sub>), a carboxyl group (COOH), and an R group, and is also known as a *side chain*. A peptide bond is the CO–NH chemical covalent bond formed between two molecules when the C of the carboxyl group of one molecule reacts with the N of the amino group of the other molecule, releasing a molecule of H<sub>2</sub>O.

The amino and carboxyl groups are standard parts of amino acids. The R group can vary among amino acids. Thus, it is the R group that defines the type of amino acid. Type I CLG displays polypeptide chains that consist mostly of GLY–X–Y. This means that one in three amino acids is a *glycine*. The most common amino acids present in the X and Y positions are *proline* (PRO) and *hydroxyproline* (HYP), respectively. Prolines at the third position of the tripeptide repeating unit GLY–X–Y tend to be hydroxylated, turning into hydroxyproline.

At the sub-nanoscale, a collection of axially connected CLG molecules arranged side by side forms a collagen fibril (CLGf); see Figure 1. A CLGf is labeled a mineralized collagen fibril (mCLGf) when there are HA crystals between the CLG molecules, mostly in their gap zones. Although denser than gap zones, mCLGf overlap zones can also exhibit HA molecules. In short, an mCLGf is a CLG fibril filled with HA in the IFV, the IFV being composed of CLG fibrils, gap zones, and overlap zones. Furthermore, a bundle of fibrils forms a fiber. At the nanoscale, bone can be described as a fiber built by a combination of wet CLGfs and mCLGfs with surrounding H<sub>2</sub>O and HA crystals in the EFV.

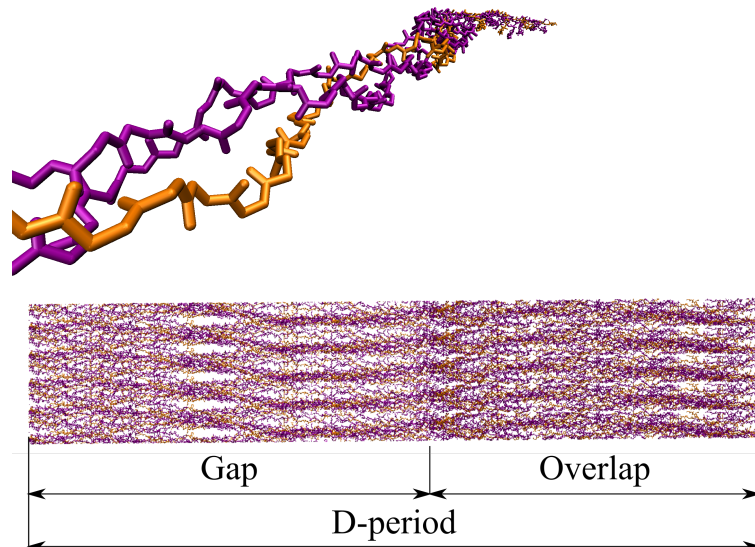


**Figure 1.** Structural representation of the backbone of a single molecule (**top**) and fibril (**bottom**) of the type I CLG. Chains A and C (alpha-1) are indicated in the purple color, and Chain B (alpha-2) in orange one.

**Remark 1** (Bone Length Scales). *The multiple length scales of bone are not equally structured and represented in the literature. The structure presented by Ref. [2], Figure 4, Section 13 is adopted here. For further reading regarding bone multiscale characteristics, see Refs. [2,4,30,33].*

In brief, from the molecular scale up to the nanoscale, bone is composed of a large number of interacting molecules. Each molecule comprises several atoms participating in interatomic bonds. Assuming that modeling each atom as a solid particle and each bond as an elastic spring is accurate enough, the molecular/nanoscale domain is defined as a gathering of discrete particles, i.e., a non-continuum, which is mostly studied through MD simulations.

## 2. Materials and Methods: Devising Bone at the Nanoscale

### 2.1. Devising the Simulation Box

Here, a step-by-step description is given of how models that resemble fibers in bones can be devised.

First, starting from the sequence of amino acids and an available fibrillar structure, the CLG Fibril model was devised through homology modeling. Then, a structure of the CLG fibril that requires Periodic Boundary Conditions (PBCs) only along the z direction was extracted and labeled CLG NanoFiber. When the latter is replicated along the x and y directions, surrounded by an EFV, and subjected to PBCs in the x, y, and z directions, the newly devised model is labeled CLG Fiber. Finally, adding H<sub>2</sub>O and HA both in the EFV and IFV of the CLG Fiber gives origin to the Bone Fiber model. See Figure 2 for a schematic view of this modeling process, described in detail throughout this section.

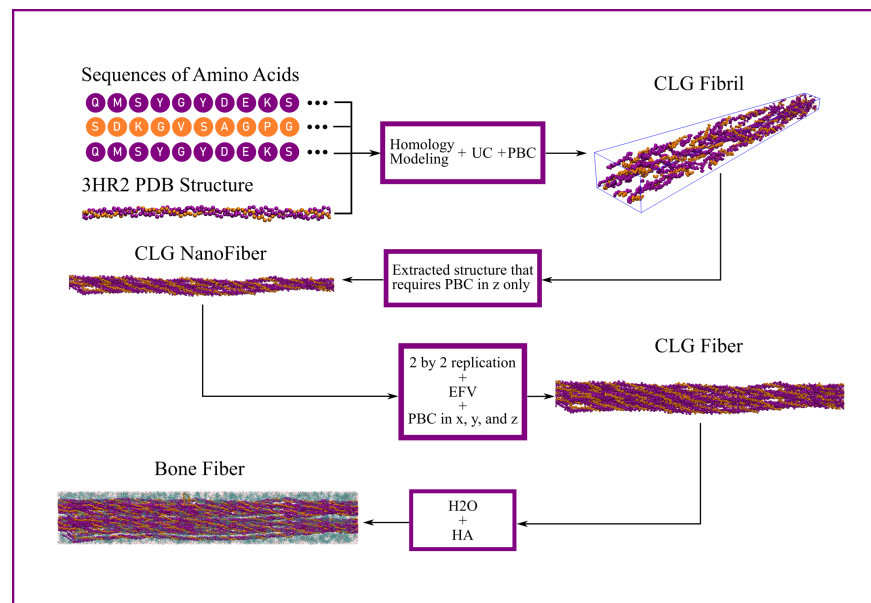


**Figure 2.** Schematic view of the modeling of a structure that resembles fibers in bones.

#### 2.1.1. CLG Fibril

Different from most proteins, CLG is not found isolated and fully solvated in bones, and it does not completely fold to perform a specific function. It is the association of CLGs under *physiological conditions* into fibrils and, consequently, fibers, which confer CLG-based tissues with their remarkable macroscale mechanical properties, such as high tensile strength. Thus, it is crucial to reproduce the fibrillar and fiber structure in MD simulations when studying the CLG mechanical properties.

**Definition 1** (Physiological Conditions). *In biochemistry, reactions are usually studied under physiological conditions, that is, an electrically neutral aqueous solution at 1 atm pressure, ~ 37 °C temperature, 0.16 mol/L salt concentration (Na<sup>+</sup> and Cl<sup>-</sup> ions), "enantiomer specific", and a specific pH.*

To date, only the amino acid sequence, i.e., the primary protein structure, of human type I CLG has been fully determined. This can be found at the Universal Protein Resource (UniProt) website [34] under the codes COL1A1\_human (P02452) and COL1A2\_human (P08123) for the alpha-1 and alpha-2 chains, respectively. However, to perform MD simulations, the spatial position of every atom, i.e., at least the tertiary protein structure, is required. Several high-resolution structures such as 1WZB [35], which periodically reproduces a common amino acid pattern of the CLG, can be found in the Protein Data Bank (PDB) [36] and can be used as approximations of the type I CLG human structure. However, as mentioned before, it is crucial to reproduce the fibrillar and fiber structure, i.e., the quaternary protein structure, when studying the CLG mechanical properties.

**Definition 2** (High-Resolution and Low-Resolution Protein Structures). *Low-resolution structures usually contain only the position of the alpha carbons (CA). All other atomic positions, e.g., side-chain atoms, must be inferred. High-resolution structures usually contain the position of every non-hydrogen atom.*

Unfortunately, there is no experimentally determined molecular structure of the quaternary protein structure of the human type I CLG available in the PDB. An alternative for modeling the human type I CLG structure is *homology modeling*.

**Definition 3** (Homology Modeling). *Also labeled comparative modeling of protein 3D structures, homology modeling is a procedure that produces a previously unknown 3D protein structure by associating an amino acid sequence (labeled the target) with a known experimentally determined 3D atomic-resolution structure (labeled the template) of a homologous sequence. Two amino acid sequences are considered homologous when they are very similar, e.g., they display a high sequence identity value, meaning that they share a common evolutionary ancestry. Homologous sequences display similar structures and, frequently, similar functions [37].*

The PDB structure 3HR2 [6], an experimentally determined low-resolution crystal structure for type I CLG of rat tail tendons, is, to our knowledge, the only structure available in the PDB that encompasses the fibrillar structure of type I CLG. It reproduces the fibrillar structure as a crystal, with a unit cell (UC) that is periodically replicated along the x, y, and z directions.

When aligned, the type I CLG amino acid sequences of the human—Uniprot P02452 and P08123—and rat—PDB 3HR2—exhibit sequence identity above 90%, indicating that they are highly homologous. Hence, they are appropriate for comparative structural modeling. If the 3HR2 structure were a high-resolution structure, it could be directly used for the MD simulations proposed here. However, since it contains only the positions of the CA atoms of the amino acids, the position of the non-CA atoms must be inferred. Homology modeling allows the inference of the positions of the non-CA atoms.

MODELLER 9.25 [38] was used to build a homology model that correlates the human amino acids sequences—Uniprot P02452 and P08123—with the rat fibrillar CLG structure—PDB 3HR2. In Appendix A, the necessary steps to build this model are described. All the necessary files and scripts for its reproduction together with further details are also provided in the Supplementary Materials.

When compressed in the crystal-like triclinic UC determined by Ref. [6] ( $a = 39.970 \text{ \AA}$ ;  $b = 26.950 \text{ \AA}$ ;  $c = 677.900 \text{ \AA}$ ;  $\alpha = 89.24^\circ$ ;  $\beta = 94.59^\circ$ ;  $\gamma = 105.58^\circ$ ; see Figure 3), and periodically replicated in space through periodic boundary conditions (PBCs) (see Figure 4), the built homology model reproduces the type I CLG fibrillar structure experimentally determined by Ref. [6]. This new model is labeled CLG Fibril throughout this paper. It can be devised by performing three steps:

1. Importing the homology model, built as described in Appendix A, into VMD [39,40] (<http://www.ks.uiuc.edu/Research/vmd/>, accessed on 30 January 2022). The H atoms can be kept or not. The models built here did not keep the H atoms, since they

can be added later using the VMD software when generating a PSF file, as described in Appendix C;

2. Setting triclinic UC dimensions using the “`pbcs set {39.970 26.950 677.900 89.24 94.59 105.58}`” command of the VMD PBCTools Plugin in the VMD TkConsole;
3. Wrapping all atoms into the defined UC using the “`pbcs wrap`” command of the VMD PBC Tools Plugin in the VMD TkConsole.

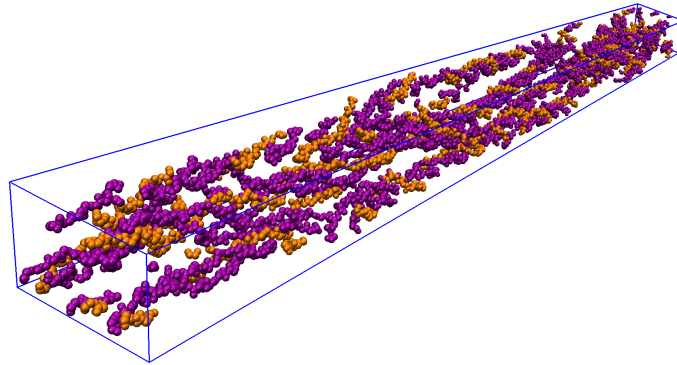


**Figure 3.** CLG Fibril within UC; snapshot from VMD viewer.

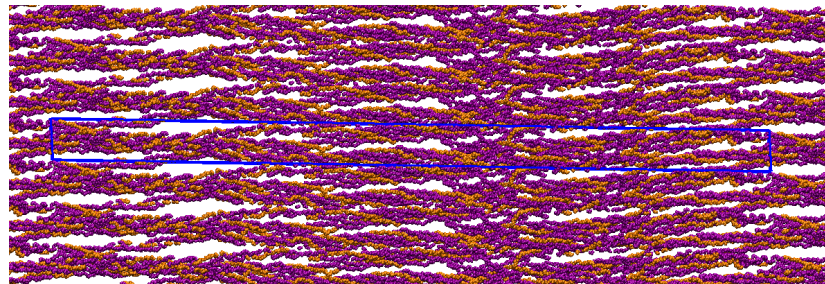


**Figure 4.** CLG Fibril periodically replicated in space; snapshot from VMD viewer.

Models such as the CLG Fibril, which combine the human amino acids sequences with the rat fibrillar CLG structure, have been previously reported; see Refs. [8–13,17,41,42]. Ref. [11], followed by Refs. [12–15,17], also performed homology modeling using *MODELLER* and provided a structural framework used in this work.

**Highlight 1** (Devising more realistic models). *As described in Sections 2.1.2 and 2.1.3, the CLG Fibril model was improved into Bone Fiber, which is a better representation of the experimentally determined nanostructure of bone presented in Refs. [18,20,22].*

**Remark 2** (D-period). *The CLG Fibril, which is derived from the 3HR2 PDB from Ref. [6], exhibits the D-period of the CLG structure along the direction of its principal axis (z) [8], Figure 1. This means that at least one gap and one overlap zone are present in the CLG Fibril’s UC, and consequently in the CLG Fiber and Bone Fiber models described next.*

### 2.1.2. CLG Fiber

As previously mentioned, the deposition of HA in the IFV yields the mCLGf. However, as shown in Refs. [18–20,22,23], it is important to emphasize that most of the HA is found not in the IFV, but between and around fibrils, in the EFV. The results of Refs. [18,19] corroborate estimations exhibited in Ref. [21]; for cortical bone, about 70–80% of the HA content is situated in the EFV in a plate-like shape.

To the best of our knowledge, there are, as of yet, no available studies reporting MD simulations of the bone structure while taking into consideration the HA content in the EFV. There are probably two main reasons for this:

- (a) The 3HR2 structure (and others derived from it, such as the presented CLG Fibril model) does not directly allow the deposition of HA in the EFV, but only within the fibril. That is because the UC defined by [6] possesses CLG covalent bonds that require PBCs in all directions. There is no room left for molecules in the EFV, and if the UC is expanded along the x and y directions to make space for such molecules, these would block the path of the CLG covalent bonds that require PBCs in the radial directions (x and y);
- (b) Including HA in the EFV means devising a very large system (much larger than the UC of the 3HR2 structure), which implies computationally more expensive simulations.

Refs. [12,14,15], for example, do include HA in their models, but only in the IFV; i.e., the mCLGf is modeled by inserting HA crystals to the UC of a homology model similar to the CLG Fibril described here.

**Open Issue 1** (Coarse-Grained Models). *An alternative to simulate the CLG fiber structure without requiring a prohibitively large number of atoms is to use coarse-grained models where an entire group (typically from three up to five atoms) is treated as a single interacting entity [7,8,43,44]. Reference [43] presents a coarse-grained model of CLG molecules (including the non-standard amino acid HYP) using an extended version of the MARTINI force field [45]. Coarse-grained models combining CLG, H<sub>2</sub>O, and HA are still an open field of research.*

The first step to create a model that resembles the structure of the fibers present in bone is to extract from the CLG Fibril a structure that requires no PBCs along the x and y direction, labeled here as CLG NanoFiber, as shown in Figure 2. After that, the desired model is obtained by replicating the latter along the x and y directions and inserting it into an EFV, i.e., a volume large enough to contain extra-fibrillar H<sub>2</sub>O and HA, the boundaries of which are subjected to PBCs. In Appendix B, a description is given on how to devise this structure, labeled as CLG Fiber.

### 2.1.3. Bone Fiber

When H<sub>2</sub>O and HA molecules are added to the CLG Fiber model described in Section 2.1.2, which contains an EFV, the newly devised model is labeled Bone Fiber.

**Remark 3** (CLG Fiber vs. Bone Fiber models). *A bundle of axially aligned CLGfs and mCLGfs surrounded by H<sub>2</sub>O and HA characterizes bone at the nanoscale. The literature usually refers to this bundle as a CLG fiber. Throughout this paper, to avoid misunderstanding and to facilitate the understanding of the modeling process, a CLG Fiber model refers to a bundle of CLGfs (without H<sub>2</sub>O and HA). A Bone Fiber model refers to a bundle of hydrated mCLGf surrounded by H<sub>2</sub>O and HA in the EFV. Thus, here a Bone Fiber model refers to the CLG Fiber model plus H<sub>2</sub>O and HA, i.e., a composite material composed of fibers (CLG, H<sub>2</sub>O, and HA) and a matrix (H<sub>2</sub>O and HA).*

The mechanical properties of bones at the nanoscale are affected by the relative fractions of their constituents. All models presented here consider bone to be constituted of CLG, HA, and H<sub>2</sub>O only; i.e., they consider the whole organic phase to be CLG and the whole inorganic phase to be HA. Four models were devised, each with a specific percentage of mass based on the reference values in Section 1.2 [22,30–32], as shown in Table 1.

**Table 1.** Devised Bone Fiber models, the mass percentages of the bone constituents, and their total number of atoms.

| Model Name    | HA % | CLG % | H <sub>2</sub> O % | Number of Atoms |
|---------------|------|-------|--------------------|-----------------|
| Bone Fiber 55 | 55   | 35    | 10                 | 299136          |
| Bone Fiber 60 | 60   | 30    | 10                 | 331797          |
| Bone Fiber 65 | 65   | 25    | 10                 | 377486          |
| Bone Fiber 70 | 70   | 20    | 10                 | 446018          |

**Open Issue 2 (Even More Realistic Bone Models).** *The presented models consider bone to be constituted of CLG, HA, and H<sub>2</sub>O only. However, about 10% of the bone organic phase exhibits an association of other collagen types (III and VI), and non-collagenous proteins (NCPs) [2]. Furthermore, parts of the mineral phase may exhibit some deficiencies in hydroxyl, and also substitutes for hydroxyl which leads to the formation of other types of minerals, not only what is commonly labeled hydroxyapatite [4,46]. Both these variations may not represent a large fraction of the total organic and mineral phase and they are not simple to model, but they might affect the computed mechanical properties. Recently, Ref. [47] reported the implications of extra-fibrillar NCPs on the bone mechanical properties.*

Packmol, a package distributed as free software for building initial configurations for MD simulations [48], was used to add HA and H<sub>2</sub>O molecules to the CLG Fiber model, obeying the percentages of mass shown in Table 1. Note that the devised Bone Fiber models were labeled based on their HA concentration. Details on how to devise these models, and on how to compute the number of molecules of each constituent to be added to the simulation box are provided in Appendices C and D.

In all devised models, the total number of HA molecules was added to the simulation box such that 80% belong to the EFV, and only 20% to the IFV, as Refs. [18–23] point out. Packmol allows the creation of different geometries, including parallelepiped, sphere, cylinder, and other geometric shapes within which the new molecules will be inserted. The IFV was defined as a parallelepiped region within the larger simulation box, where CLG fibrils are mostly inside.

Figures 5 and 6 show the boxes that define the IFV and EFV.

The devised IFV displays the x, y, and z dimensions  $60 \times 86 \times 678 \text{ \AA}$ , and the simulation box dimensions  $88 \times 142 \times 679 \text{ \AA}$ . This indicates that the length of the simulated fibers is  $679 \text{ \AA}$ .

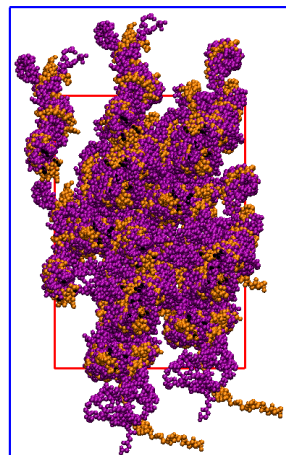


**Figure 5.** Bone Fiber view of the xy-plane (VMD). The simulation box (blue) defines the external boundary of the EFV. The IFV box (red) defines the external boundary of the IFV and the internal boundary of the EFV. Only CLG backbone molecules are shown.

Note that 20% of the HA molecules were added into the IFV box, and the remaining 80% were outside the IFV, but inside the simulation box. The EFV is defined as the volume of the simulation box subtracted from the volume of the IFV box.

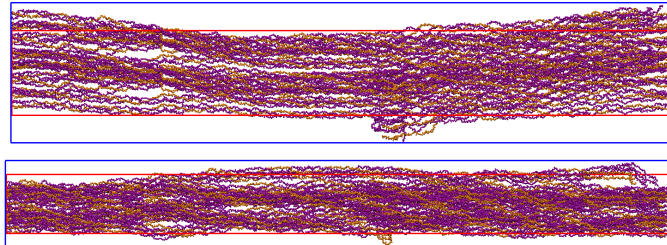


**Figure 6.** Bone Fiber view (VMD) of yz-plane (**top**) and xz-plane (**bottom**). The simulation box (blue) defines the external boundary of the EFV. The IFV box (red) defines the external boundary of the IFV and the internal boundary of the EFV. Only CLG backbone molecules are shown.

**Open Issue 3 (EFV vs. IFV).** *By visually identifying the volume mostly occupied by the CLG fibrils, two different boxes were created that define the IFV and EFV. However, there may be more accurate ways to define the IFV and EFV for MD simulations. This paper presents a realistic model of a bone fiber (not fibril), i.e., the first model to reproduce fibrils and to insert HA molecules both in the IFV and in the EFV. However, modeling both the IFV and EFV can be considered an open issue.*

All the devised models display a salt concentration of 0.16 mol/L. This was assured by adding a total of 132 chloride ions and 0 sodium ions to the models (these 132 atoms are already included in the number of atoms shown in Table 1).

Figures 7 and 8 show a devised Bone Fiber model, i.e., mCLGfs immersed in water and surrounded by HA inside the EFV. HA molecules from the INTERFACE force field (IFF) [49] database were used. Appendix E provides more detail about the used HA PDB file.

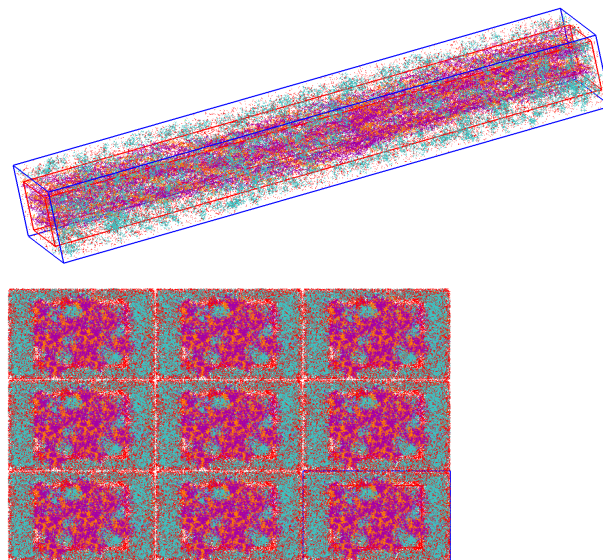


**Figure 7.** Simulation box of a Bone Fiber model, and a view of a 3-by-3 periodic replication of its xy-cross-section (VMD). HA, H<sub>2</sub>O, and CLG molecules are shown in cyan, red, and purple (alpha-1 chains) and orange colors (alpha-2 chains), respectively.

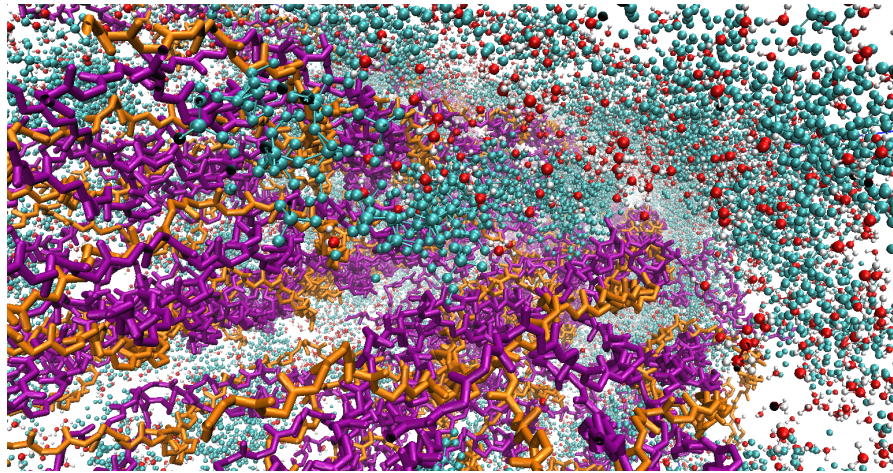


**Figure 8.** Zoomed view of a bone fiber in VMD. HA, H<sub>2</sub>O, and CLG molecules are shown in cyan, red, and purple (alpha-1 chains) and orange colors (alpha-2 chains), respectively.

Notice that Ref. [42], Figure 1c, and Ref. [50], Figure 1d also extracted a CLG NanoFiber from the 3HR2 PDB structure provided by Ref. [6]; see Appendix B, Step 2. However, they do not further develop the model into a bone fiber structure, i.e., into a model such as the presented CLG Fiber or Bone Fiber.

## 2.2. Force Fields

Force fields (FFs) can significantly affect MD simulation results. It is thus paramount to select FFs that are appropriate for the specific goal of the simulation [51].

CHARMM36m [52–55], a well-known and tested FF especially developed for proteins, lipids, and carbohydrates, was selected. The files:

- *top\_all36\_prot.rtf*, *par\_all36m\_prot.prm* for proteins;
- *toppar\_all36\_prot\_modify\_res.rtf* for modified residues, i.e., HYP;
- *toppar\_water\_ions.prm* for water and ions;

were used for the simulations described in this article, and included in the MODELLER 9.25 library during the homology modeling process, as described previously in Section 2.1.1 and Appendix A.

It is important to mention that the files *par\_all36\_lipid.prm*, *par\_all36\_carb.prm*, *par\_all36\_na.prm*, *par\_all36\_cgennf.prm*, and *par\_HA.prm*, though not containing parameters for the atoms of the presented models, were also loaded in the NAMD configuration files, since CHARMM files contain NBFIX, and CHARMM commands specifically written for the CHARMM program, not for NAMD. Reading all these files avoids errors in NAMD.

For the HA species, parameters from the IFF [49], which operates as an extension of CHARMM, were used. The parameters of the triclinic UC for HA are:  $a = 9.417 \text{ \AA}$ ;  $b = 9.417 \text{ \AA}$ ;  $c = 6.875 \text{ \AA}$ ;  $\alpha = 90^\circ$ ;  $\beta = 90^\circ$ ;  $\gamma = 120^\circ$ . See Appendix E for further details.

## 2.3. Minimization and Equilibration

Once devised, the Bone Fiber structure went through minimization steps and equilibration runs in NAMD before starting the production run; see Definition 4.

**Definition 4 (Production Run).** *There is a subtle difference between equilibration or thermalization and production runs. Both basically consist in running MD simulations (solving Newton's Second Law for each atom in the system). However, data is only collected in the production run, since the computed properties should correspond to a system in thermodynamic equilibrium.*

MD simulations consist in solving Newton's 2nd Law of Motion at a material molecular scale whose spatial domain contains  $a$  atoms interacting with up to  $n$  neighbor atoms:

$$m_a \frac{d^2 \mathbf{r}_a(t)}{dt^2} = \sum_{n_1=1}^n f_2(\mathbf{r}_a(t), \mathbf{r}_{n_1}(t)) + \cdots + \sum_{n_1=1}^n \sum_{\substack{n_2=1 \\ n_2 \neq n_1}}^n \cdots \sum_{\substack{n_k=1 \\ n_k \neq n_1, n_2, \dots}}^n f_n(\mathbf{r}_a(t), \mathbf{r}_{n_1}(t), \dots, \mathbf{r}_{n_k}(t)) \quad (1)$$

where, for each  $a$ -th atom:  $m_a$  is the mass,  $\mathbf{r}_a$  is the position vector, and  $f_2$  is a force vector function that describes pairwise atomic interactions; similarly,  $f_n$  describes  $n$ -atom interactions. Each  $f_n$  is the spatial-derivative of a potential energy function that accounts for up to  $n$ -body and quantum interactions. The total energy of the  $a$ -th atom is a function of an  $a$ -th atom's position  $\mathbf{r}_a(t)$  and its  $n$  neighbors' positions  $\mathbf{r}_1(t), \dots, \mathbf{r}_n(t) \in \mathbb{R}^3$ .

Details of the minimization and equilibration performed in NAMD and their parameters are shown in Table 2. Further information on the parameters can be found in the NAMD user guide.

**Table 2.** Parameters of MD simulation for minimization and equilibration in NAMD.

| Parameter Name                       | Parameter Value             |
|--------------------------------------|-----------------------------|
| Minimization Algorithm               | Conjugate Gradient          |
| Equilibration Time                   | 100 ns                      |
| Equilibration Time Step              | 2.0 fs                      |
| Equilibration Ensemble               | NPT                         |
| Cutoff                               | 12.0 Å                      |
| Switch distance                      | 10.0 Å                      |
| Pair list distance                   | 14.0 Å                      |
| Particle-Mesh Ewald Sum Grid Spacing | 1.0 Å                       |
| Temperature Control Algorithm        | Langevin Dynamics           |
| Constant Temperature                 | 310 K                       |
| Pressure Control Algorithm           | Nosé–Hoover Langevin Piston |
| Constant Pressure                    | 1.01325 bar                 |

Structural convergence was ensured by analysis of the root mean squared deviation (RMSD), a numerical measure of the difference between two structures, of the CA atoms. The slope of the RMSD with respect to time approached zero short before 100 ns of equilibration. Figure 9 displays the computed RMSD for the devised Bone Fiber model.

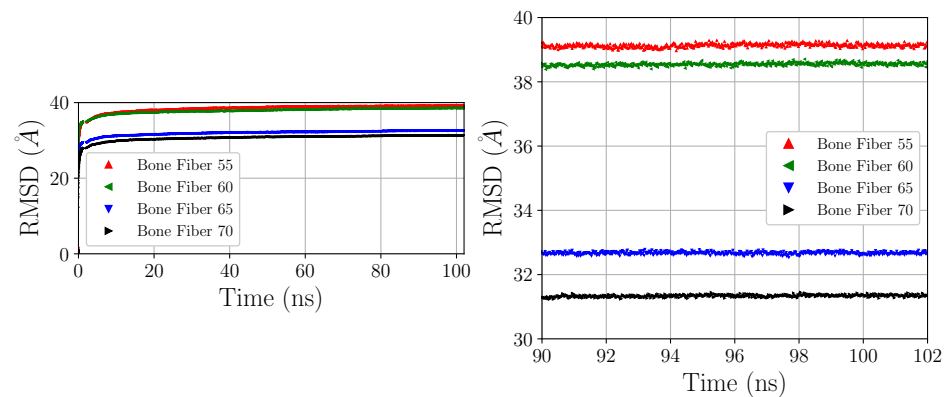


**Figure 9.** RMSD of Bone Fiber models (with respect to devised models, frame 0).

**Remark 4** (Volume Contraction). *During equilibration, a volume contraction varying from 30 to 50% with respect to the devised models was noticed. The volume contraction reflects a structural*

relaxation that is made possible by simulating in the NPT ensemble, which keeps the number of particles, pressure, and temperature constant, allowing the volume to adapt. Moreover, differently from other works that fully solvated the CLG molecule in water, here, a pre-defined number of water molecules was set to guarantee the relative composition of the nanomaterial, as shown in Table 1.

LAMMPS, an open-source code with a focus on materials modeling and science [56–63], is among the most suitable code to study elastic properties of molecular models, including soft matter such as polymers and biomolecules such as CLG. As described in Section 2.4, LAMMPS was used for the computation of the Young's Modulus of the devised models. A short additional equilibration using LAMMPS was also needed prior to the calculation of the elastic properties. The structurally stable (or simply relaxed) Bone Fiber structures were converted to LAMMPS using *charmm2lammmps.pl* from LAMMPS tool. The LAMMPS equilibration consisted of: 1 ns equilibration with time step 1 fs and neighbor skin 1.0, followed by an additional 5 ns equilibration with a time step of 2 fs, as indicated in Table 3. Further information on the parameters can be found in the LAMMPS user guide.

**Table 3.** Parameters of MD simulation for minimization and equilibration in LAMMPS.

| Parameter Name                                 | Parameter Value    |
|--|--------------------|
| Equilibration Time                             | 5 ns               |
| Equilibration Time Step                        | 2 fs               |
| Equilibration Ensemble                         | NPT                |
| Inner Cutoff                                   | 12.0 Å             |
| Outer Cutoff                                   | 14 Å               |
| Neighbor Skin                                  | 2.0 Å              |
| Particle-Particle Particle-Mesh Solver Desired |                    |
| Relative Error in Forces                       | $1 \times 10^{-6}$ |
| Temperature Control Algorithm                  | Langevin Dynamics  |
| Constant Temperature                           | 310 K              |
| Pressure Control Algorithm                     | Nosé–Hoover        |
| Constant Pressure                              | 1.0 atm            |

PBCs were applied in all directions and during all steps.

#### 2.4. Elastic Properties

Assessing elastic properties using MD simulations is sometimes difficult [64,65], especially for biological systems, including proteins such as CLG. Nevertheless, a series of studies have been reported describing different techniques to address this problem [14–17]. Here, LAMMPS scripts were written which deform the simulation box in a manner that mimics uniaxial tensile tests.

A uniaxial deformation along the z-axis was imposed by gradually increasing the z-length value of the simulation box, i.e., of the domain. Taking advantage of the continuum mechanics and strength of materials, the engineering strain along the z direction can be defined as:

$$\varepsilon_{zz}(t) = \frac{L_z(t) - L_z(t_0)}{L_z(t_0)} = \frac{L_z(t) - L_{z0}}{L_{z0}} \quad (2)$$

where  $L_z(t_0) = L_{z0}$  is the initial ( $t = 0$  s) length of the box along the z direction, and  $L_z(t)$  is the length of the box along the z direction at time t. The engineering strain rate can be written as:

$$\dot{\varepsilon}_{zz}(t) = \frac{d\varepsilon_{zz}(t)}{dt} = \frac{d}{dt} \left( \frac{L_z(t) - L_{z0}}{L_{z0}} \right) = \frac{dL_z}{dt} \frac{1}{L_{z0}} = \frac{v_z(t)}{L_{z0}} \quad (3)$$

where  $v_z(t)$  is the velocity with which the box  $z$  length changes over time. The LAMMPS *fix deform* command deforms the box by extending the box length  $L_z$ , at each time step  $t$ , following:

$$L_z(t) = L_{z0}(\dot{\epsilon}_{zz}(t) \cdot t + 1) = v_z(t) \cdot t + L_{z0}. \quad (4)$$

LAMMPS allows the user to decide whether to input the strain rate  $\dot{\epsilon}_{zz}(t)$  or velocity  $v_z(t)$ . Here, a constant strain rate of  $10^{-5}[1/\text{fs}]$  was set. Since a box extension of 30%,  $L(t_{\text{final}}) = 1,3L_0 = L_0(10^{-5} \cdot t + 1)$ , is more than sufficient to assess the elastic properties of such a system through MD simulations, a total deformation run time of 30 ps was used. Table 4 shows the main parameters used for the tensile test simulations.

**Table 4.** Parameters of MD simulation for tensile tests in LAMMPS.

| Parameter Name                                 | Parameter Value                        |
|--|--|
| Deformation Time                               | 30 ps                                  |
| Deformation Time Step                          | 2 fs                                   |
| Deformation Direction                          | $z$                                    |
| Strain Rate                                    | $1 \times 10^{-5} \frac{1}{\text{fs}}$ |
| Equilibration Ensemble                         | NPT                                    |
| Inner Cutoff                                   | $12.0 \text{ \AA}$                     |
| Outer Cutoff                                   | $14 \text{ \AA}$                       |
| Neighbor Skin                                  | $2.0 \text{ \AA}$                      |
| Particle-Particle Particle-Mesh Solver Desired |  |
| Relative Error in Forces                       | $1 \times 10^{-6}$                     |
| Temperature Control Algorithm                  | Langevin Dynamics                      |
| Constant Temperature                           | 310 K                                  |
| Pressure Control Algorithm (in $x$ and $y$ )   | Nosé–Hoover                            |
| Constant Pressure                              | 1.0 atm                                |

PBCs were applied in all directions and during all steps of the production run. While the box was deformed along the  $z$  direction, an NPT ensemble was used for the  $x$  and  $y$  ones. Figure 10 shows the UC of the Bone Fiber 55 model before and after being uniaxially deformed by 30%.

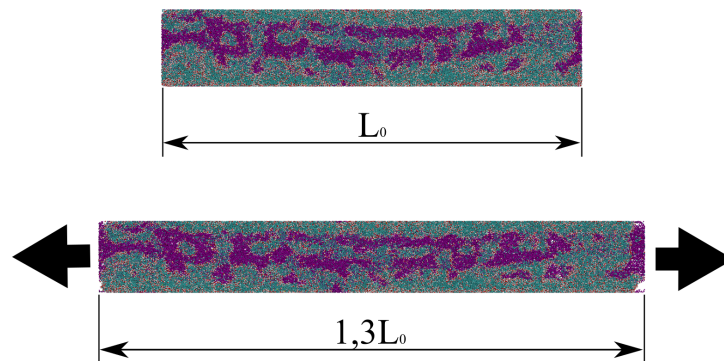


**Figure 10.** Bone Fiber 55 UC before (**top**) and after (**bottom**) the tensile test; snapshots from OVITO [66]. The arrows indicate the stretching directions.

Assuming bone as a Cauchy-Linear-Elastic (CLE) material [2] complying with Hooke's Law, a tensile test allows the estimation of the Young's Modulus  $E$  through the following stress-strain relationship:

$$\sigma_{zz} = E\epsilon_{zz} \quad (5)$$

The LAMMPS default *compute pressure* command computes the elements of the symmetric pressure tensor at the molecular scale by adding components of the kinetic energy tensor and of the virial tensor:

$$P_{ij} = \frac{\sum_{k=1}^N m_k v_{ki} v_{kj}}{V} + \frac{\sum_{k=1}^{N'} r_{ki} f_{kj}}{V} \quad (6)$$

where  $N$  is the number of atoms ( $N'$  includes atoms from neighboring sub-domains, labeled ghost atoms),  $m_k$  is the mass of the  $k$ -th atom,  $v_{ki}$  the  $i$ -th component of the velocity of the  $k$ -th atom,  $r_{ki}$  the  $i$ -th component of the position of the  $k$ -th atom, and  $f_{ki}$  the  $i$ -th component of the resultant force applied on the  $k$ -th atom. Here, pressure can be interpreted as stress; i.e.,  $P_{ij} = \sigma_{ij}$ .

### 3. Results and Discussion

During the MD tensile tests simulations, stress and strain were frequently outputted and later plotted to strain–stress curves. Figure 11 shows the stress–strain curves obtained from MD simulation using the LAMMPS *fix deform* command and the respective linear fitting of the elastic region.

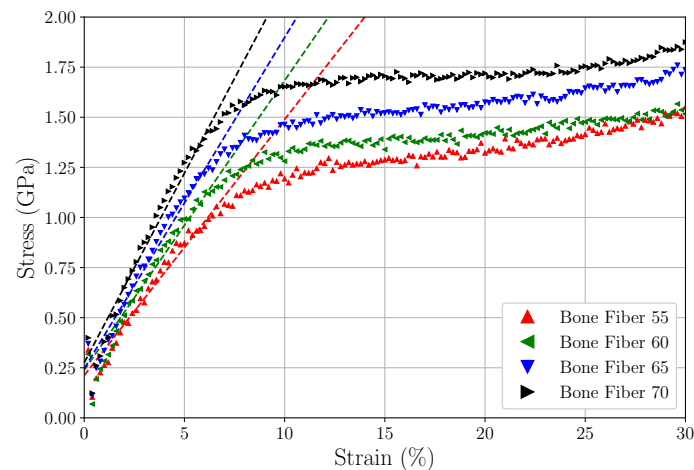


**Figure 11.** Stress–strain curves computed for the devised models, and their respective linear regression.

A simple linear regression based on least squares using *scipy.optimize.curve\_fit* [67] was used to compute the lines that fit the elastic region of the models (adopted as the region between 1 and 7% of strain), and consequently the estimatives of Young’s Modulus values, defined as the slope of the lines. Table 5 displays the estimated Young’s Modulus values for the devised Fiber models.

**Table 5.** Computed Young’s Modulus values for devised Bone Fiber models.

| Model Name    | Young’s Modulus [GPa] |
|---------------|-----------------------|
| Bone Fiber 55 | 12.77                 |
| Bone Fiber 60 | 14.45                 |
| Bone Fiber 65 | 16.52                 |
| Bone Fiber 70 | 18.90                 |

Here, bone was considered a CLE material complying with Hooke’s Law. No plastic, viscoelastic, or non-linear behavior was considered. The Young’s Modulus values shown

in Table 5 were compared with those presented in the literature. A discussion on how they can be interpreted is provided below.

Ref. [4] compares Young's Modulus values calculated for CLG at different length scales applying different methods. They presented Young's Modulus values ranging between 0.35 and 12 GPa for their classification of the molecular scale, between 0.2 and 38 GPa for their classification of the microfibrillar/fibrillar scale, and between 0.03 and 1.57 GPa for their classification of fiber scale. The large range and difference between the presented Young's Modulus values can be explained by the different applied methodologies (molecular dynamics, X-ray diffraction, atomic force microscope, and others).

Ref. [14] performed MD simulations to compute Young's Modulus values for mCLGf models with different concentrations of HA and H<sub>2</sub>O, obtaining values ranging from 0.2 to 1.9 GPa. Furthermore, Ref. [14] displays a compilation of Young's Modulus values ranging from 0.2 to 2.8 GPa for mCLGfs computed using both experimental and computational methods. Reference [15] also displays a compilation of Young's Modulus values, this time compressive, ranging from 0.03 to 22.11 (13.87 + 8.24) GPa for mCLGfs computed using both experimental and computational methods.

Refs. [68,69] devised continuum multiscale models and obtained homogenized stiffness tensors for nanoscale models (see [68] Appendix B), which also agrees with the presented literature, and thus with our results.

As shown above and also discussed by ref. [70,71], there is no standard value for the Young's Modulus of CLGf, mCLGf, and CLG fibers. The literature presents values that differ more than 100% from each other and also do not precisely classify the applied length scale. What one reference classifies as microfibril, is sometimes classified as fibril by another reference; see Remark 1.

As discussed in Appendix B, Open Issue A1, the model labeled Bone Fiber possesses too few CLG molecules when compared to a real CLG fiber. However, it is the most realistic model that has, to our knowledge, been devised to date. It displays 20 CLG single molecules (tropocollagens), in the overlap region, 16 in the gap region, and includes HA molecules both in the IFV and in the EFV. A rigorous classification places the devised Bone Fiber models somewhere between mCLGfs and CLG fibers, so the computed Young's Modulus should lay in the range between these two; i.e., any value between 0.03 to ~20 GPa can be considered reasonable.

Nevertheless, the presented approach allows the modeling of larger, and even more realistic bone nanoscale fiber model. Unfortunately, the almost prohibitive computational cost of these models precludes its large use, since this would require millions, and even billions, of atoms.

#### 4. Conclusions

Although earlier experiments showed that fibers in bone exhibit most of their HA in the EFV [18,20], no molecular model regarding this feature has been presented in the literature. We present for the first time all-atom bone models that include HA both in the IFV and in the EFV, i.e., more elaborate bone nanoscale models from a biological point of view. Our purpose is to provide a detailed prescription on how to devise such models with different fractions of their basic constituents. Thus, we provide all used scripts as well as the PDB and PSF files of the equilibrated structures (~100 ns) in the Supplementary Materials.

We performed simple tensile tests using LAMMPS in order to assess the Young's Modulus values of the devised models. Our results are in good agreement with the literature, although the data reported by different groups for bone-like nanostructures fall over a broad range of values. Future computational and experimental studies could provide additional validation.

By including HA in the EFV, the present Bone Fiber models take into account an important element of the biology and chemistry of fibers in bones, and can be easily modified to model larger and even more human-like bone fibers. The models unfold a new alternative to study the nanoscale mechanics of bones, and together with the information

provided in this work, can be used as the foundation of future studies regarding the modeling and mechanical properties of bone at the nanoscale.

**Supplementary Materials:** The following supporting information can be downloaded at: <https://www.mdpi.com/article/10.3390/ma15062274/s1>, **(0-COL1\_Modeller.)**—files and scripts used to perform homology modeling using MODELLER 9.25; **(1-CLG\_Fibril.)**—files and scripts used to devise the CLG Fibril model; **(2-CLG\_Fiber.)**—files and scripts used to devise the CLG NanoFiber and CLG Fiber models; **(3-Bone\_Fiber.)**—files and scripts used to devise CLG Bone Fiber models and equilibrate it. In the latter, we also provide PDB and PSF files of the equilibrated Bone Fiber models.

**Author Contributions:** Conceptualization, A.C.S.A., P.S. and M.S.S.; methodology, A.C.S.A., P.S. and M.S.S.; software, A.C.S.A. and L.C.F.; validation, A.C.S.A., L.C.F., P.S., D.S.G. and M.S.S.; formal analysis, A.C.S.A.; investigation, A.C.S.A.; resources, P.S. and M.S.S.; data curation, A.C.S.A.; writing—original draft preparation, A.C.S.A.; writing—review and editing, A.C.S.A., L.C.F., P.S., D.S.G. and M.S.S.; visualization, A.C.S.A. and L.C.F.; supervision, P.S. and M.S.S.; project administration, P.S. and M.S.S.; funding acquisition, A.C.S.A., P.S. and M.S.S. All authors have read and agreed to the published version of the manuscript.

**Funding:** This research was funded by the São Paulo Research Foundation (FAPESP) grant #2018/18503-2, the Center for Computing in Engineering & Sciences (CCES/UNICAMP) grant #2013/08293-7, and the Coordenação de Aperfeiçoamento de Pessoal de Nível Superior–Brasil (CAPES).

**Data Availability Statement:** The data presented in this study are available in the Supplementary Materials.

**Acknowledgments:** This work used resources of the “Centro Nacional de Processamento de Alto Desempenho em São Paulo” (CENAPAD-SP), and CCES grant #2013/08293-7.

**Conflicts of Interest:** The authors declare no conflict of interest.

## Abbreviations

The following abbreviations are used in this manuscript:

|         |   |
|---------|---|
| CA      | Alpha Carbon  |
| CHARMM  | Chemistry at HARvard Macromolecular Mechanics             |
| CLE     | Cauchy-Linear-Elastic                                     |
| CLG     | CoLlaGen  |
| CLGf    | CoLlaGen fibril   |
| mCLGf   | mineralized CoLlaGen fibril                               |
| EFV     | Extra-Fibrillar Volume                                    |
| FF      | Force Field   |
| GLY     | GLYcine   |
| HA      | HydroxyApatite  |
| HPC     | High Performance Computing                                |
| HYP     | HYdroxyProlyne  |
| IFF     | Interface Force Field                                     |
| IFV     | Intra-Fibrillar Volume                                    |
| LAMMPS  | Large-scale Atomic/Molecular Massively Parallel Simulator |
| NAMD    | NAnoscale Molecular Dynamics                              |
| NCP     | Non-Collagenous Protein                                   |
| OVITO   | Open VI-sualization TOol                                  |
| PBC     | Periodic Boundary Condition                               |
| PDB     | Protein Data Bank (also a file format)                    |
| PRO     | PROline   |
| PSF     | Protein Structure File (a file format)                    |
| RMSD    | Root Mean Squared Deviation                               |
| UC      | Unit Cell   |
| UniProt | Universal Protein resource                                |
| VMD     | Visual Molecular Dynamics                                 |

## Appendix A. Building Homology Models of Human Type-I Collagen Using MODELLER 9.25

There are five main steps:

1. Select *target* sequences and properly prepare the data;
2. Select *template* structures and properly prepare the data;
3. Align *target* and *template* sequences;
4. Build models;
5. Check the models.

All used files and scripts are available in the Supplementary Materials.

### Appendix A.1. Selecting Target Sequence and Preparing Its Data

The COL1A1\_human (P02452) and COL1A2\_human (P08123) amino acid sequences were selected as targets. As mentioned before, they can be found on the UniProt website. Since only the CLG chains need to be modeled, i.e., without signal peptide and propeptide, only the residues in positions 162 to 1218 (feature identifier PRO\_0000005720) are needed for COL1A1, and residues 80 to 1119 (feature identifier PRO\_0000005805) for COL1A2. Furthermore, these sequences also contain modified residues, i.e., non-standard amino acids such as HYP. Although UniProt indicates the position of each non-standard amino acid, it exports the sequence with the respective unmodified residue in the FASTA format. Specific PROs located at the third position of the tripeptide repeating unit GLY-X-Y were manually substituted with HYPs. This was done by replacing the specific letter P with the letter O.

Finally, the modified human CLG sequence was converted to the PIR format (MODELLER'S preferred format for comparative modeling) for later alignment with the rat sequence.

### Appendix A.2. Selecting Template Structure and Preparing Its Data

The rat CLG structure (3HR2) was selected as the template. As mentioned before, it can be found in the PDB. The 3HR2 structure contains two non-standard amino acids: HYP (4-Hydroxyproline) and LYZ (5-Hydroxylysine). To include them in the final model, their topology and force field parameters files must be included in MODELLER's library. Since LYZ appears only a few times in the structure and is not paramount to the fibrillar structure, the 3HR2.pdb file was manually edited by substituting all LYZ by LYS (Lysine), a standard amino acid. HYP, on the other hand, was not removed because it is very abundant in the CLG and plays an important role in the formation of the fibrillar structure. However, MODELLER does not automatically identify the non-standard amino acids (HETATM) when reading the sequence of a PDB file. It is possible only by appropriately editing MODELLER's scripts, and the library file *restyp.lib*. See the available README.txt files in the Supplementary Materials for details.

A MODELLER script was used to extract the sequence in the PIR format from the template structure. This sequence was then added to an input alignment file (.ali) containing the target sequence as well.

### Appendix A.3. Aligning Target and Template Sequences

In MODELLER 9.25, there are two types of alignment (\*.ali) files. There is an *input alignment file* containing the non-aligned sequences of both target and template and an *output alignment file* containing the aligned sequences of both target and template. An alignment script performs the alignment of the input alignment file into an output alignment file.

In the input alignment file containing the non-aligned target and template sequences, several "-" were manually added to the template sequences of the rat CLG so that they could exhibit the same lengths as the target human sequences (1057–1040–1057 for chains A, B, and C, respectively). This input alignment file was used as input for the alignment of the sequences, which is described next.

**Remark A1** (Human sequence length vs. Rat sequence length). To devise models with the length of the target *Homo sapiens* (Human) sequence, "-" was manually included in the template sequences. To devise models with the length of the template *Rattus Norvegicus* (Brown Rat) sequence, a few residues from the target sequences were manually deleted. The latter were discarded since the goal was to devise models as close to the human type-I collagen as possible. We believe that models with the original human sequence length are a better representation of the real human collagen.

Further details can be found in the scripts available in the Supplementary Materials.

#### Appendix A.4. Building Models

Output align files become the input files for scripts that build homology models. Twenty models were built, ten using the *automodel* function and ten using the *allhmodel* function. It takes much longer to build models using *allhmodel* (it includes H atoms); however, since the used HYP topology and force field parameters (CHARMM36m) include H atoms, models with *allhmodel* were also built. Figure A1 shows the best model built with the *allhmodel* function. A comparison between the models built with each function and how the best model was chosen is described in the next step.



**Figure A1.** Model of human triple-helix CLG structure devised by homology modeling using MODELLER and shown in VMD with drawing and coloring methods Quicksurf and Chain, respectively.

Force field parameters and topology files for HYP were added by editing MODELLER's library files *par.lib*, *top\_heav.lib/top\_allh.lib*, *radii.lib*, *radii14.lib*, and *solv.lib*. The same CHARMM36m parameters and topology for HYP used here were later used for the MD simulations.

#### Appendix A.5. Checking the Models

MODELLER provides some *assessment functions* so the user can assess the quality of the model. GA341 and DOPE are two examples of them. GA341 is recommended for single-chain proteins and a GA341 score below 0.7 indicates a "bad" model. DOPE is the most reliable at separating native-like models from decoys. DOPE score is calculated based on energy, meaning that smaller values are better.

However, the best model among the models built by MODELLER does not necessarily mean a "good" model. It is also important to compute the RMSD between the built model and template structure and to visualize and compare both using external software. Figure A2 shows chains A of both the built model and the 3HR2 template structure.

The RMSD between the CA atoms of the template structure, and the models built with both *automodel* and *allhmodel* were computed chain-by-chain. For the lowest DOPE model built using *automodel*, an average RMSD value of 5.5 Å was obtained. For the lowest DOPE model built using *allhmodel*, on the other hand, an average RMSD value of 4.5 Å. Hence, the lowest DOPE model built using *allhmodel* was selected. The likely reason being that the CHARMM36m force field topology for HYP is added to the MODELLER's library. It includes hydrogen atoms and, therefore, MODELLER builds better models when this information is added. To create models using *automodel*, i.e., with no hydrogen atoms, the hydrogen lines from the topology file for HYP had to be manually commented out.

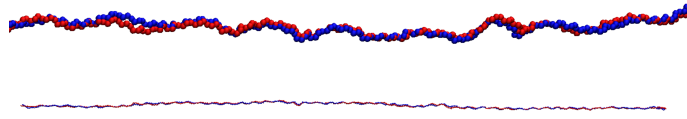


**Figure A2.** Chains A of the lowest DOPE model built with *allmodel* (blue) and 3HR2 (red) are shown in VMD as VDW. Zoomed (**top**) and distant (**bottom**) views.

### Appendix B. CLG Fiber

The CLG Fiber model consists of a bundle of CLG Fibril models surrounded by H<sub>2</sub>O and HA along the x and y directions. However, simply doing this is not possible. The atoms of the CLG Fibril covalently bonded through the PBCs of the UC would be far apart from each other. Their covalent bonds would clash with H<sub>2</sub>O and HA. This issue can be solved by exploiting the *minimum-image convention*. Below, a three-step description is given of how the CLG Fiber was devised starting from the CLG Fibril:

1. Replicate the CLG Fibril in the x and y directions.

To use the minimum-image convention, images of the UC must be generated. Thus, the CLG Fibril's UC was replicated along the x and y directions using the script *replicateCrystal.tcl* with a few subtle modifications. The original script belongs to the Bionanotechnology Tutorial available on the NAMD website [72,73] (<http://www.ks.uiuc.edu/Research/namd/> accessed on 30 January 2022). The UC was replicated seven times along the x and y directions, thus creating a so-called supercell of 49 UC images that guarantees enough molecules to extract the desired structure. It can be seen from Figure 3C of Ref. [6] that a single CLG molecule goes through seven UCs along the x direction (represented there by the letter a). For example, trying to do the same with a three-by-three reproduction of the CLG Fibril did not yield a final model that requires no PBC along the x and y directions.

2. Extract the CLG NanoFiber, a structure that requires PBCs along the z direction only.

A Matlab script was written which, starting from the middle UC image (located at the center of the seven-by-seven UCs), selects the first atom of each chain and searches for the next nearest atom in the chain among its possible 49 images. The pseudocode shown in Algorithm A1 details the main core of this Matlab script [74].

Figure A3 shows the extracted structure in cyan color, labeled CLG NanoFiber, among the seven-by-seven replication of the CLG Fibril.



**Figure A3.** Extraction of CLG NanoFiber (blue) from the seven-by-seven periodic replication (orange transparent) of the CLG Fibril (red). View of xz-plane (**left**) and yz-plane (**right**) in VMD.

**Algorithm A1** Extracting CLG NanoFiber from super cell of 49 CLG Fibril replications

---

```

▷ % For desired number of central box (cb), i.e., a UC located in center of the 49 images %
for j ← 1 : ncb do
▷ % From the 2nd to the last atom of the cb %
  for j ← 2 : natomcb do
    cb_index ← converts local index of cb (j) to cb global index
    if cb_index-th atom belongs to same chain as (cb_index-1)-th atom then
      index_set(1,49) ← set of atoms in the j-th position in each of the 49 images
      xy_set(49,2) ← (x,y) coordinates of atoms of the set index_set
      xy_ref(1,2) ← (x,y) coordinates of (cb_index-1)-th atom (reference atom)
      ▷ % compute distance between atoms of the set index_set and the reference atom %
      rset ← sqrt((xyset(:,1) - xyref(1,1)).2 + (xyset(:,2) - xyref(1,2)).2)
      ▷ % get minimum distance %
      [minval, minindex] ← min(rset)
      ▷ % if nearest atom not already in cb %
      if index_set(1, minindex) ≠ cb_index then
        Replace atom of the cb by nearest atom (from other UC) !
      end if
    else
      ▷ % do nothing %
      ▷ % cb_index-th atom is 1st atom of chain and reference for (cb_index+1)-th atom %
    end if
  end for
end for

```

---

The CLG NanoFiber is a structure that requires PBCs along the z direction only. This means that, differently from the CLG Fibril, H<sub>2</sub>O and HA molecules can be added around the CLG molecules in the EFV without clashing CLG covalent bonds.

3. Replicate the CLG NanoFiber along the x and y directions to produce the CLG Fiber.

Finally, using the same modified *replicateCrystal.tcl* script, the CLG NanoFiber was replicated two times along the x and y directions by a distance apart equivalent to the CLG Fibril's UC, mentioned in Section 2.1.1. The final goal is to devise a model similar to the fiber structure described in Refs. [2,18,20,22], which can be regarded as a bundle of mCLG fibrils immersed in an EFV filled with H<sub>2</sub>O and HA. The inclusion of H<sub>2</sub>O and HA is described in Section 2.1.3 and detailed in Appendix C.

**Remark A2** (Skipping Step 3). *An alternative way to devise the same CLG Fiber model, but without performing Step 3 described above, is to adapt Algorithm A1 to extract not only one central box, but four boxes in the central area of the 49 images, i.e., n<sub>cb</sub> = 4. This way it directly provides a two-by-two replication of the CLG NanoFiber model. This adaptation is straightforward and provided in the Supplementary Materials. However, Algorithm A1 was not carefully optimized to run fast and, for instance, if a five-by-five replication is desired, we recommend replicating, as Step 3 shows, an extracted single central box, n<sub>cb</sub> = 1, instead of using Algorithm A1 to extract 25 boxes.*

The devised CLG Fiber (see Figures A4 and A5) displays 20 CLG molecules in the overlap zone and 16 in the gap zone, since the CLG Fibril (derived from the PDB 3HR2 structure) displays five and four, respectively.



**Figure A4.** CLG Fiber (blue): a two-by-two replication of CLG NanoFiber, seen among the seven-by-seven periodic replication of the CLG Fibril's UC (orange transparent). View of xz-plane (**left**) and yz-plane (**right**) in VMD.

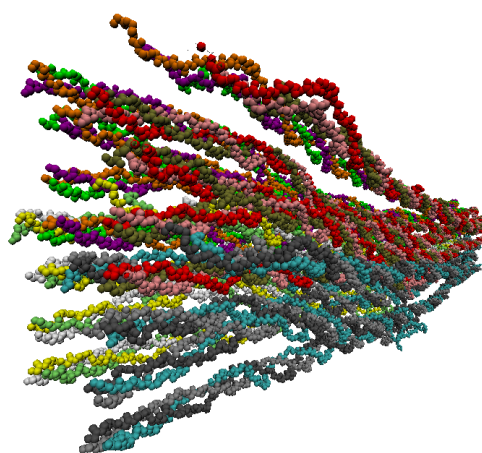


**Figure A5.** Devised CLG Fiber shown in VMD. The CLG chains (three chains each in one color) of a previous specific CLG NanoFiber are all represented five times (in the overlap zone) by the same three colors, e.g., five CLG molecules with their three chains in gray, cyan, and black. The different replications of the previous CLG NanoFiber can be identified by the colors cyan, red, yellow, and orange.

**Open Issue A1** (Larger and more realistic Fibers). *A real CLG fiber possesses far more than just 20 CLG molecules. However, too many CLG molecules imply a very large UC and an elevated number of H<sub>2</sub>O and HA molecules. This is computationally expensive and demands time-consuming simulations, even when taking advantage of high-performance computing (HPC). However, a much larger bundle of CLG molecules that better represents the fiber structure of CLG can be easily produced following the procedures (and files) provided in the Supplementary Materials. The final CLG Fiber could be a three-by-three, five-by-five, or even ten-by-ten (500 CLG molecules in the overlap zone and 400 in the gap zone) replication of the CLG NanoFiber. The computer performance of the MD simulations is the main limitation. Note that no replication along the z direction is required. The PBC along the z direction and the CLG Fibril, which derives from the 3HR2 PDB, guarantee the D-period of the CLG; i.e., at least one gap and one overlap zone are included in the simulation box (see Remark 2).*

### Appendix C. Bone Fiber

Using the CLG Fiber model described in Section 2.1.2 and Appendix B, the following steps were performed to devise the Bone Fiber model.

1. Aligning the principal axes of the model to the x, y, and z directions.

This was done following instructions provided on [https://www.ks.uiuc.edu/Research/vmd/script\\_library/scripts/orient/](https://www.ks.uiuc.edu/Research/vmd/script_library/scripts/orient/) (accessed on 30 January 2022);

2. Translating the center of the model to the origin of the Cartesian system.

This step is not mandatory, but working with the center of the simulation box positioned at the center of the Cartesian system, i.e.,  $(x_{\text{center}}, y_{\text{center}}, z_{\text{center}}) = (0, 0, 0)$ , is a common procedure in MD simulations that facilitates some future computation and analysis;

3. Adding H atoms.

Though, as described in Appendix A, a homology model containing H atoms was selected (built with the *allhmodel* function), the H atoms were removed, as described in Section 2.1.1. Here, H atoms are added to the model through a script for the VMD psfgen plugin to generate a PSF and a new PDB file.

**Remark A3** (Bad contacts). *After adding H atoms to the aligned and translated CLG Fiber model, a few minimization and equilibration steps (MD simulation runs) were performed in NAMD to assure that the model runs stably, and is suitable for further modifications. Here, a few bad contacts were found in the model. After a careful search, it was found that:*

- (1) *Bad contacts between residues LEU2470 and HYP2708 appeared earlier in the CLG Fibril model after wrapping all atoms into the CLG Fibril's UC, at Section 2.1.1, Step 3. A possible reason is the position of the side chains and H atoms determined by the homology modeling and the VMD psfgen plugin. By including the side chain and H atoms in a very dense UC, it is probable that the newly included atoms were positioned too close or even crossed other molecules. They do not necessarily avoid the crossing of different molecules (entangling);*
- (2) *Bad contacts also appeared after replicating the CLG NanoFiber by distances equivalent to the CLG Fibril's UC (or by directly extracting the CLG Fiber from the 49 images). After adding H atoms to the CLG Fiber model, a small number of molecules crossed the pentagonal structure of other molecules. The size of the CLG Fibril's UC seems too short for the extracted NanoFiber structure accounting for the side chains and H atoms added by MODELLER and the VMD psfgen plugin, respectively.*

*All bad contacts were manually removed using the VMD shortcut 5.*

4. Adding H<sub>2</sub>O and HA using PACKMOL.

Packmol was used to add H<sub>2</sub>O and HA molecules to the aligned and translated CLG Fiber model so that predefined fractions of molecular mass are kept constant. A detailed description is given in Appendices C and D of how the number of water ( $n_{\text{H}_2\text{O}}$ ) and hydroxyapatite ( $n_{\text{HA}}$ ) molecules to be added to the CLG Fiber model was calculated. Models with different mass percentages of CLG, HA, and H<sub>2</sub>O were devised, as shown in Table 1.

In all devised models the total number of HA molecules was added to the box such that 80% belongs to the EFV, and only 20% to the IFV. Figures 5 and 6 visually differentiate the EFV and IFV.

Once the correct number of H<sub>2</sub>O and HA molecules were added to the simulation box, the newly devised model was labeled Bone Fiber. Again, the VMD psfgen plugin was used to generate a PSF and a new PDB file for the Bone Fiber model.

#### Appendix D. Mass Fraction Calculation

$$\text{Units: Volume (V) } [\text{\AA}^3]; \text{ Mass (m) [g]; Molar mass (mm) } \left[ \frac{\text{g}}{\text{mol}} \right]; \text{ Density } (\rho) \left[ \frac{\text{g}}{\text{ml}} \right] = \left[ \frac{\text{g}}{\text{cm}^3} \right] = \left[ \frac{\text{g}}{10^{24} \text{\AA}^3} \right].$$

$$\text{Avogadro constant: } N_A = 6.022 \cdot 10^{23} \left[ \frac{1}{\text{mol}} \right]$$

Basic equations of micromechanics:

Mass conservation (m)

$$\begin{aligned} m_{\text{sys}} &= m_{\text{CLG}} + m_{\text{HA}} + m_{\text{H}_2\text{O}}, \\ \rho_{\text{sys}} \cdot V_{\text{sys}} &= \rho_{\text{CLG}} \cdot V_{\text{CLG}} + \rho_{\text{HA}} \cdot V_{\text{HA}} + \rho_{\text{H}_2\text{O}} \cdot V_{\text{H}_2\text{O}}, \\ \rho_{\text{sys}} &= \rho_{\text{CLG}} \cdot V_{\text{fCLG}} + \rho_{\text{HA}} \cdot V_{\text{fHA}} + \rho_{\text{H}_2\text{O}} \cdot V_{\text{fH}_2\text{O}}. \end{aligned} \quad (\text{A1})$$

Volume conservation (V)

$$\begin{aligned} V_{\text{sys}} &= V_{\text{CLG}} + V_{\text{HA}} + V_{\text{H}_2\text{O}}, \\ \frac{m_{\text{sys}}}{\rho_{\text{sys}}} &= \frac{m_{\text{CLG}}}{\rho_{\text{CLG}}} + \frac{m_{\text{HA}}}{\rho_{\text{HA}}} + \frac{m_{\text{H}_2\text{O}}}{\rho_{\text{H}_2\text{O}}}, \\ \frac{1}{\rho_{\text{sys}}} &= \frac{M_{\text{fCLG}}}{\rho_{\text{CLG}}} + \frac{M_{\text{fHA}}}{\rho_{\text{HA}}} + \frac{M_{\text{fH}_2\text{O}}}{\rho_{\text{H}_2\text{O}}}. \end{aligned} \quad (\text{A2})$$

Mass fraction (Mf)

$$M_{\text{fCLG}} = \frac{m_{\text{CLG}}}{m_{\text{sys}}}, \quad (\text{A3})$$

Volume fraction (Vf)

$$M_{\text{fCLG}} + M_{\text{fHA}} + M_{\text{fH}_2\text{O}} = 1. \quad (\text{A4})$$

The main goal is to add H<sub>2</sub>O and HA molecules to a molecular domain, i.e., the simulation box, previously with collagen molecules in vacuum only, so that predefined percentages of the constituent's molecular masses are kept constant. For this, Packmol was used. Below a description is provided of how the number of water (n<sub>H<sub>2</sub>O</sub>) and hydroxyapatite (n<sub>HA</sub>) molecules was calculated. The inputs are predefined mass fractions of the constituents, their molar mass, and their initial density.

Desired mass fractions of bone constituents:

$$M_{\text{fCLG}} \quad M_{\text{fHA}} \quad M_{\text{fH}_2\text{O}}. \quad (\text{A5})$$

Values for the desired mass fraction were selected based on the literature [22,30–32], see Section 1.2. The selected values are shown in Table 1.

$$\text{Density of constituents } \left[ \frac{\text{g}}{\text{ml}} \right] = \left[ \frac{\text{g}}{\text{cm}^3} \right] = \left[ \frac{\text{g}}{10^{24} \text{\AA}^3} \right]$$

$$\rho_{\text{CLG}} = 1.43, \quad \rho_{\text{HA}} = 3, \quad \rho_{\text{H}_2\text{O}} = 1. \quad (\text{A6})$$

These density values were taken from Ref. [75], apud [76], and [77], apud [21,78].

Molar mass of constituents [g/mol]

$$mm_{\text{CLG}} = 1222226.78 \left[ \frac{\text{g}}{\text{mol}} \right], mm_{\text{HAunit}} = 1004.62 \left[ \frac{\text{g}}{\text{mol}} \right], mm_{\text{H}_2\text{Ounit}} = 18.01 \left[ \frac{\text{g}}{\text{mol}} \right]. \quad (\text{A7})$$

Values for mm<sub>CLG</sub> and mm<sub>HAunit</sub> were computed using the script solvate.tcl from Packmol's utilities (<http://leandro.iqm.unicamp.br/m3g/packmol/utilities.shtml>, accessed on 30 January 2022).

Note that the mass of the constituents in [g] can be calculated by:

$$m_{\text{CLG}} = \frac{mm_{\text{CLG}}}{N_A}, \quad m_{\text{HA}} = \frac{mm_{\text{HAunit}} \cdot n_{\text{HA}}}{N_A}, \quad m_{\text{H}_2\text{O}} = \frac{mm_{\text{H}_2\text{Ounit}} \cdot n_{\text{H}_2\text{O}}}{N_A}. \quad (\text{A8})$$

From Equation (A2), the density of the system ( $\rho_{\text{sys}}$ ) is obtained.

$$\rho_{\text{sys}} = \left( \frac{M_{\text{fCLG}}}{\rho_{\text{CLG}}} + \frac{M_{\text{fHA}}}{\rho_{\text{HA}}} + \frac{M_{\text{fH}_2\text{O}}}{\rho_{\text{H}_2\text{O}}} \right)^{-1} \quad (\text{A9})$$

From Equations (A4) and (A3), the volume fractions of the constituents are obtained.

$$M_{\text{fCLG}} = \frac{m_{\text{CLG}}}{m_{\text{sys}}} = \frac{\rho_{\text{CLG}} V_{\text{CLG}}}{\rho_{\text{sys}} V_{\text{sys}}} = \frac{\rho_{\text{CLG}} V_{\text{fCLG}}}{\rho_{\text{sys}}}, \quad V_{\text{fHA}} = \frac{\rho_{\text{sys}} M_{\text{fHA}}}{\rho_{\text{HA}}}, \quad V_{\text{fH}_2\text{O}} = \frac{\rho_{\text{sys}} M_{\text{fH}_2\text{O}}}{\rho_{\text{H}_2\text{O}}}. \quad (\text{A10})$$

From Equation (A3), the total mass of the system and consequently, of HA and H<sub>2</sub>O, is obtained.

$$m_{\text{sys}} = \frac{m_{\text{CLG}}}{M_{\text{fCLG}}} = \frac{m_{\text{mCLG}}}{M_{\text{fCLG}} \cdot N_{\text{A}}}, \quad m_{\text{HA}} = M_{\text{fHA}} \cdot m_{\text{sys}}, \quad m_{\text{H}_2\text{O}} = M_{\text{fH}_2\text{O}} \cdot m_{\text{sys}}. \quad (\text{A11})$$

Thus, from Equation (A8), the desired number of H<sub>2</sub>O and HA molecules are:

$$n_{\text{HA}} = \frac{m_{\text{HA}} \cdot N_{\text{A}}}{m_{\text{mHAunit}}} = \frac{m_{\text{mHA}}}{m_{\text{mHAunit}}}, \quad n_{\text{H}_2\text{O}} = \frac{m_{\text{H}_2\text{O}} \cdot N_{\text{A}}}{m_{\text{mH}_2\text{Ounit}}} = \frac{m_{\text{mH}_2\text{O}}}{m_{\text{mH}_2\text{Ounit}}} \quad (\text{A12})$$

The fraction of the volume occupied by H<sub>2</sub>O is used for the computations of the number of ions of each type (chloride and sodium). This can be determined in two different ways:

$$V_{\text{H}_2\text{O}} = V_{\text{fH}_2\text{O}} \cdot V \quad \text{or} \quad V_{\text{H}_2\text{O}} = \frac{m_{\text{mH}_2\text{Ounit}} \cdot n_{\text{H}_2\text{O}}}{\rho_{\text{H}_2\text{O}} \cdot N_{\text{A}}} \cdot 10^{24}. \quad (\text{A13})$$

A total of 132 chloride ions and 0 sodium ions (accounted for in Table 1) were added to all the devised models. They were calculated such that the system exhibits a salt concentration of 0.16 mol/L.

## Appendix E. HA Structure and FF Files

The IFF contains in its database Material Studios .car and .mdf files for HA. However, to use Packmol and NAMD to devise and simulate the Bone Fiber model, files in the PDB and PSF format are required.

The msi2namd tool, a modification of msi2lmp Version 3.9.6 developed at the Heinz laboratory from IFF [49], was used to convert the *hap\_unit\_cell.car* and *hap\_unit\_cell.mdf* files from the IFF model database to the PDB and PSF formats.

Note that if only one HA UC, i.e., one HA molecule, is needed, the PSF file created with msi2namd would be useful for further simulations. However, since the goal was to add several HA and H<sub>2</sub>O molecules to a box with CLG molecules, i.e., to devise the Bone Fiber, a CHARMM topology file was required so that the VMD psfgen plugin can be used to generate a PSF file for models with several HA UCs, i.e., several HA molecules. The CHARMM topology file for HA was manually created and tested against the PSF file generated using msi2namd. The CHARMM parameter file for HA was taken from the IFF database.

The used HA structure and FF files are available in the Supplementary Materials.

## References

1. Odén, A.; McCloskey, E.; Kanis, J.; Harvey, N.C.; Johansson, H. Burden of high fracture probability worldwide: secular increases 2010–2040. *Osteoporos. Int.* **2015**, *26*, 2243–2248. [[CrossRef](#)] [[PubMed](#)]
2. Alcantara, A.C.S.; Assis, I.; Prada, D.; Mehle, K.; Schwan, S.; Costa-Paiva, L.; Skaf, M.S.; Wrobel, L.C.; Sollero, P. Patient-Specific Bone Multiscale Modelling, Fracture Simulation and Risk Analysis—A Survey. *Materials* **2020**, *13*, 106. [[CrossRef](#)] [[PubMed](#)]
3. Sabet, F.A.; Raeisi Najafi, A.; Hamed, E.; Jasiuk, I. Modelling of bone fracture and strength at different length scales: A review. *Interface Focus*. **2016**, *6*, 20150055. [[CrossRef](#)] [[PubMed](#)]
4. Sherman, V.R.; Yang, W.; Meyers, M.A. The materials science of collagen. *J. Mech. Behav. Biomed. Mater.* **2015**, *52*, 22–50. [[CrossRef](#)] [[PubMed](#)]

5. Mohammad, M.-G.; Wang, X.Z. Nanomechanics and Ultrastructure of Bone: A Review. *Comput. Model. Eng. Sci.* **2020**, *125*, 1–32. [[CrossRef](#)]
6. Orgel, J.P.R.O.; Irving, T.C.; Miller, A.; Wess, T.J. Microfibrillar structure of type I collagen in situ. *Proc. Natl. Acad. Sci. USA* **2006**, *103*, 9001–9005. [[CrossRef](#)]
7. Tang, M.; Li, T.; Gandhi, N.S.; Burrage, K.; Gu, Y. Heterogeneous nanomechanical properties of type I collagen in longitudinal direction. *Biomech. Model. Mechanobiol.* **2017**, *16*, 1023–1033. [[CrossRef](#)]
8. Zhou, Z.; Majid, M.-J. A simulation study on the significant nanomechanical heterogeneous properties of collagen. *Biomech. Model. Mechanobiol.* **2015**, *14*, 445–457. [[CrossRef](#)]
9. Collier, T.A.; Nash, A.; Birch, H.L.; de Leeuw, N.H. Relative orientation of collagen molecules within a fibril: A homology model for homo sapiens type I collagen. *J. Biomol. Struct. Dyn.* **2019**, *37*, 537–549. [[CrossRef](#)]
10. Streeter, I.; de Leeuw, N.H. Atomistic Modeling of Collagen Proteins in Their Fibrillar Environment. *J. Phys. Chem. B* **2010**, *114*, 13263–13270. [[CrossRef](#)]
11. Gautieri, A.; Vesentini, S.; Redaelli, A.; Buehler, M.J. Hierarchical Structure and Nanomechanics of Collagen Microfibrils from the Atomistic Scale Up. *Nano Lett.* **2011**, *11*, 757–766. [[CrossRef](#)] [[PubMed](#)]
12. Nair, A.K.; Gautieri, A.; Chang, S.W.; Buehler, M.J. Molecular mechanics of mineralized collagen fibrils in bone. *Nat. Commun.* **2013**, *4*, 1724. [[CrossRef](#)] [[PubMed](#)]
13. Nair, A.K.; Gautieri, A.; Buehler, M.J. Role of Intrafibrillar Collagen Mineralization in Defining the Compressive Properties of Nascent Bone. *Biomacromolecules.* **2014**, *15*, 2494–2500. [[CrossRef](#)]
14. Fielder, M.; Nair, A.K. Effects of hydration and mineralization on the deformation mechanisms of collagen fibrils in bone at the nanoscale. *Biomech. Model. Mechanobiol.* **2019**, *18*, 57–68. [[CrossRef](#)]
15. Fielder, M.; Nair, A.K. A computational study of mechanical properties of collagen-based bio-composites. *Int. Biomech.* **2020**, *7*, 76–87. [[CrossRef](#)] [[PubMed](#)]
16. Milazzo, M.; Jung, G.S.; Danti, S.; Buehler, M.J. Mechanics of Mineralized Collagen Fibrils upon Transient Loads. *ACS Nano* **2020**, *14*, 8307–8316. [[CrossRef](#)]
17. Milazzo, M.; David, A.; Jung, G.S.; Danti, S.; Buehler, M.J. Molecular origin of viscoelasticity in mineralized collagen fibrils. *Biomater. Sci.* **2021**. [[CrossRef](#)]
18. McNally, E.A.; Schwarcz, H.P.; Botton, G.A.; Arsenaault, A.L. A Model for the Ultrastructure of Bone Based on Electron Microscopy of Ion-Milled Sections. *PLoS ONE* **2012**, *7*, e29258. [[CrossRef](#)]
19. McNally, E.; Nan, F.; Botton, G.A.; Schwarcz, H.P. Scanning transmission electron microscopic tomography of cortical bone using Z-contrast imaging. *Micron* **2013**, *49*, 46–53. [[CrossRef](#)]
20. Schwarcz, H.P.; McNally, E.A.; Botton, G.A. Dark-field transmission electron microscopy of cortical bone reveals details of extrafibrillar crystals. *J. Struct. Biol.* **2014**, *188*, 240–248. [[CrossRef](#)]
21. Lees, S. Considerations Regarding the Structure of the Mammalian Mineralized Osteoid from Viewpoint of the Generalized Packing Model. *Connect. Tissue Res.* **1987**, *16*, 281–303. [[CrossRef](#)] [[PubMed](#)]
22. Schwarcz, H.P. The ultrastructure of bone as revealed in electron microscopy of ion-milled sections. *Semin. Cell Dev. Biol.* **2015**, *46*, 44–50. [[CrossRef](#)] [[PubMed](#)]
23. Schwarcz, H.P.; Abueidda, D.; Jasiuk, I. The Ultrastructure of Bone and Its Relevance to Mechanical Properties. *Front. Phys.* **2017**, *5*, 39. [[CrossRef](#)]
24. Pang, S.; Schwarcz, H.P.; Jasiuk, I. Interfacial bonding between mineral platelets in bone and its effect on mechanical properties of bone. *J. Mech. Behav. Biomed. Mater.* **2021**, *113*, 104132. [[CrossRef](#)] [[PubMed](#)]
25. Shoulders, M.D.; Raines, R.T. Collagen Structure and Stability. *Annu. Rev. Biochem.* **2009**, *78*, 929–958. [[CrossRef](#)] [[PubMed](#)]
26. Makareeva, E.; Leikin, S. Chapter 7-Collagen Structure, Folding and Function. In *Osteogenesis Imperfecta*; Shapiro, J.R., Byers, P.H., Glorieux, F.H., Sponseller, P.D., Eds.; Academic Press: San Diego, CA, USA, 2014; pp. 71–84. [[CrossRef](#)]
27. Bodian, D.L.; Radmer, R.J.; Holbert, S.; Klein, T.E. Molecular dynamics simulations of the full triple helical region of collagen type I provide an atomic scale view of the protein's regional heterogeneity. *Biocomputing* **2011**, 193–204. [[CrossRef](#)]
28. Fratzl, P. *Collagen—Structure and Mechanics*; Springer: Berlin, Germany, 2008. [[CrossRef](#)]
29. Vass, V.; Morin, C.; Scheiner, S.; Hellmich, C. Review of “Universal” Rules Governing Bone Composition, Organization, and Elasticity Across Organizational Hierarchies. In *Multiscale Mechanobiology of Bone Remodeling and Adaptation*; Pivonka, P., Ed.; Springer International Publishing: Berlin, Germany, 2018; pp. 175–229. [[CrossRef](#)]
30. Olszta, M.J.; Cheng, X.; Jee, S.S.; Kumar, R.; Kim, Y.Y.; Kaufman, M.J.; Douglas, E.P.; Gower, L.B. Bone structure and formation: A new perspective. *Mater. Sci. Eng. R Rep.* **2007**, *58*, 77–116. [[CrossRef](#)]
31. Keaveny, T.M.; Morgan, E.F.; Yeh, O.C. *Standard Handbook Of Biomedical Engineering And Design*; McGraw-Hill: New York, NY, USA, 2003.
32. Gong, J.K.; Arnold, J.S.; Cohn, S.H. Composition of trabecular and cortical bone. *Anat. Rec.* **1964**, *149*, 325–331. [[CrossRef](#)]
33. Launey, M.E.; Buehler, M.J.; Ritchie, R.O. On the Mechanistic Origins of Toughness in Bone. *Annu. Rev. Mater. Res.* **2010**, *40*, 25–53. [[CrossRef](#)]
34. The UniProt Consortium. UniProt: the universal protein knowledgebase in 2021. *Nucleic Acids Res.* **2020**, *49*, D480–D489. [[CrossRef](#)]

35. Kawahara, K.; Nishi, Y.; Nakamura, S.; Uchiyama, S.; Nishiuchi, Y.; Nakazawa, T.; Ohkubo, T.; Kobayashi, Y. Effect of Hydration on the Stability of the Collagen-like Triple-Helical Structure of [4(R)-Hydroxyprolyl-4(R)-hydroxyprolylglycine]<sub>10</sub>. *Biochemistry* **2005**, *44*, 15812–15822. [[CrossRef](#)] [[PubMed](#)]
36. Berman, H.M.; Westbrook, J.; Feng, Z.; Gilliland, G.; Bhat, T.N.; Weissig, H.; Shindyalov, I.N.; Bourne, P.E. The Protein Data Bank. *Nucleic Acids Res.* **2000**, *28*, 235–242. [[CrossRef](#)] [[PubMed](#)]
37. Pearson, W.R. An Introduction to Sequence Similarity (“Homology”) Searching. *Curr. Protoc. Bioinform.* **2013**, *42*, 3.1.1–3.1.8. [[CrossRef](#)] [[PubMed](#)]
38. Sali, A. Comparative protein modeling by satisfaction of spatial restraints. *Mol. Med. Today* **1995**, *1*, 270–277. [[CrossRef](#)]
39. Humphrey, W.; Dalke, A.; Schulten, K. VMD—Visual Molecular Dynamics. *J. Mol. Graph.* **1996**, *14*, 33–38. [[CrossRef](#)]
40. Stone, J. An Efficient Library for Parallel Ray Tracing and Animation. Master’s Thesis, Computer Science Department, University of Missouri-Rolla, Rolla, MI, USA, 1998.
41. Streeter, I.; de Leeuw, N.H. A molecular dynamics study of the interprotein interactions in collagen fibrils. *Soft Matter* **2011**, *7*, 3373–3382. [[CrossRef](#)]
42. Zhou, Z.; Qian, D.; Minary-Jolandan, M. Molecular Mechanism of Polarization and Piezoelectric Effect in Super-Twisted Collagen. *ACS Biomater. Sci. Eng.* **2016**, *2*, 929–936. [[CrossRef](#)]
43. Gautieri, A.; Russo, A.; Vesentini, S.; Redaelli, A.; Buehler, M.J. Coarse-Grained Model of Collagen Molecules Using an Extended MARTINI Force Field. *J. Chem. Theory Comput.* **2010**, *6*, 1210–1218. [[CrossRef](#)]
44. Depalle, B.; Qin, Z.; Shefelbine, S.J.; Buehler, M.J. Influence of cross-link structure, density and mechanical properties in the mesoscale deformation mechanisms of collagen fibrils. *J. Mech. Behav. Biomed. Mater.* **2015**, *52*, 1–13. [[CrossRef](#)]
45. Marrink, S.J.; Risselada, H.J.; Yefimov, S.; Tieleman, D.P.; de Vries, A.H. The MARTINI Force Field: Coarse Grained Model for Biomolecular Simulations. *J. Phys. Chem. B* **2007**, *111*, 7812–7824. [[CrossRef](#)]
46. Cho, G.; Wu, Y.; Ackerman, J.L. Detection of Hydroxyl Ions in Bone Mineral by Solid-State NMR Spectroscopy. *Science* **2003**, *300*, 1123–1127. [[CrossRef](#)] [[PubMed](#)]
47. Wang, Y.; Morsali, R.; Dai, Z.; Minary-Jolandan, M.; Qian, D. Computational Nanomechanics of Noncollagenous Interfibrillar Interface in Bone. *ACS Appl. Mater. Interfaces* **2020**, *12*, 25363–25373. [[CrossRef](#)] [[PubMed](#)]
48. Martínez, L.; Andrade, R.; Birgin, E.G.; Martínez, J.M. PACKMOL: A package for building initial configurations for molecular dynamics simulations. *J. Comput. Chem.* **2009**, *30*, 2157–2164. [[CrossRef](#)] [[PubMed](#)]
49. Heinz, H.; Lin, T.J.; Kishore Mishra, R.; Emami, F.S. Thermodynamically Consistent Force Fields for the Assembly of Inorganic, Organic, and Biological Nanostructures: The INTERFACE Force Field. *Langmuir* **2013**, *29*, 1754–1765. [[CrossRef](#)]
50. Zhou, Z.; Qian, D.; Minary-Jolandan, M. Clustering of hydroxyapatite on a super-twisted collagen microfibril under mechanical tension. *J. Mater. Chem. B* **2017**, *5*, 2235–2244. [[CrossRef](#)]
51. Becker, C.A.; Tavazza, F.; Trautt, Z.T.; de Macedo, R.A.B. Considerations for choosing and using force fields and interatomic potentials in materials science and engineering. *Curr. Opin. Solid State Mater. Sci.* **2013**, *17*, 277–283. [[CrossRef](#)]
52. MacKerell, A.D.; Bashford, D.; Bellott, M.; Dunbrack, R.L.; Evanseck, J.D.; Field, M.J.; Fischer, S.; Gao, J.; Guo, H.; Ha, S.; et al. All-Atom Empirical Potential for Molecular Modeling and Dynamics Studies of Proteins. *J. Phys. Chem. B* **1998**, *102*, 3586–3616. [[CrossRef](#)]
53. MacKerell, A.D.; Feig, M.; Brooks, C.L. Improved Treatment of the Protein Backbone in Empirical Force Fields. *J. Am. Chem. Soc.* **2004**, *126*, 698–699. [[CrossRef](#)]
54. Best, R.B.; Zhu, X.; Shim, J.; Lopes, P.E.M.; Mittal, J.; Feig, M.; MacKerell, A.D. Optimization of the Additive CHARMM All-Atom Protein Force Field Targeting Improved Sampling of the Backbone  $\phi$ ,  $\psi$  and Side-Chain  $\chi_1$  and  $\chi_2$  Dihedral Angles. *J. Chem. Theory Comput.* **2012**, *8*, 3257–3273. [[CrossRef](#)]
55. Huang, J.; Rauscher, S.; Nawrocki, G.; Ran, T.; Feig, M.; de Groot, B.L.; Grubmüller, H.; MacKerell, A.D. CHARMM36m: An improved force field for folded and intrinsically disordered proteins. *Nat. Methods* **2017**, *14*, 71–73. doi: [[CrossRef](#)]
56. Thompson, A.P.; Aktulga, H.M.; Berger, R.; Bolintineanu, D.S.; Brown, W.M.; Crozier, P.S.; in ’t Veld, P.J.; Kohlmeyer, A.; Moore, S.G.; Nguyen, T.D.; et al. LAMMPS—A flexible simulation tool for particle-based materials modeling at the atomic, meso, and continuum scales. *Comput. Phys. Comm.* **2022**, *271*, 108171. [[CrossRef](#)]
57. Plimpton, S. Fast Parallel Algorithms for Short-Range Molecular Dynamics. *J. Comput. Phys.* **1995**, *117*, 1–19. [[CrossRef](#)]
58. Brown, W.M.; Wang, P. Implementing Molecular Dynamics on Hybrid High Performance Computers—Short Range Forces. *Comp. Phys. Comm.* **2011**, *182*, 898–911. [[CrossRef](#)]
59. Brown, W.M.; Kohlmeyer, A. Implementing Molecular Dynamics on Hybrid High Performance Computers—Particle-Particle Particle-Mesh. *Comp. Phys. Comm.* **2012**, *183*, 449–459. [[CrossRef](#)]
60. Brown, W.M. Implementing Molecular Dynamics on Hybrid High Performance Computers—Three-Body Potentials. *Comp. Phys. Comm.* **2013**, *184*, 2785–2793. [[CrossRef](#)]
61. Nguyen, T.D. Accelerating dissipative particle dynamics simulations for soft matter systems. *Comput. Mater. Sci.* **2015**, *100*, 173–180. [[CrossRef](#)]
62. Nguyen, T.D. GPU-accelerated Tersoff potentials for massively parallel Molecular Dynamics simulations. *Comp. Phys. Comm.* **2017**, *212*, 113–122. [[CrossRef](#)]
63. Nikolskiy, V.S. GPU acceleration of four-site water models in LAMMPS. In Proceedings of the International Conference on Parallel Computing (ParCo 2019), Prague, Czech Republic, 10–13 September 2019.

64. Cranford, S.W.; Buehler, M.J. *Biomateriomics*, 1st ed.; Springer: Berlin, Germany, 2012. [[CrossRef](#)]
65. Clavier, G.; Desbiens, N.; Bourasseau, E.; Lachet, V.; Brusselle-Dupend, N.; Rousseau, B. Computation of elastic constants of solids using molecular simulation: Comparison of constant volume and constant pressure ensemble methods. *Mol. Simul.* **2017**, *43*, 1413–1422. [[CrossRef](#)]
66. Stukowski, A. Visualization and analysis of atomistic simulation data with OVITO—the Open Visualization Tool. *Model. Simul. Mater. Sci. Eng.* **2010**, *18*. [[CrossRef](#)]
67. Virtanen, P.; Gommers, R.; Oliphant, T.E.; Haberland, M.; Reddy, T.; Cournapeau, D.; Burovski, E.; Peterson, P.; Weckesser, W.; Bright, J.; et al. SciPy 1.0: Fundamental Algorithms for Scientific Computing in Python. *Nat. Methods* **2020**, *17*, 261–272. [[CrossRef](#)]
68. Prada, D.M. Multiscale Anisotropic Elastostatic Homogenization of Healthy and Osteoporotic Bone Tissue Using 3D BEM. Master Dissertation, Universidade Estadual de Campinas, Campinas, Brazil, 2019.
69. Prada, D.M.; Galvis, A.F.; Alcântara, A.C.S.; Soller, P. 3D Boundary element meshing for multiscale bone anisotropic analysis. *Eur. J. Comput. Mech.* **2018**, *27*, 425–442. [[CrossRef](#)]
70. Collins, C.J.; Andriotis, O.G.; Nedelkovski, V.; Frank, M.; Katsamenis, O.L.; Thurner, P.J. Bone Micro- and Nanomechanics. In *Encyclopedia of Biomedical Engineering*; Narayan, R., Ed.; Elsevier: Oxford, UK, 2019; pp. 22–44. [[CrossRef](#)]
71. Andriotis, O.G.; Desissaire, S.; Thurner, P.J. Collagen Fibrils: Nature’s Highly Tunable Nonlinear Springs. *ACS Nano* **2018**, *12*, 3671–3680. [[CrossRef](#)]
72. Phillips, J.C.; Hardy, D.J.; Maia, J.D.C.; Stone, J.E.; Ribeiro, J.V.; Bernardi, R.C.; Buch, R.; Fiorin, G.; Hénin, J.; Jiang, W.; et al. Scalable molecular dynamics on CPU and GPU architectures with NAMD. *J. Chem. Phys.* **2020**, *153*, 044130. [[CrossRef](#)] [[PubMed](#)]
73. Lu, D.; Aksimentiev, A.; Shih, A.Y.; Cruz-Chu, E.; Freddolino, P.L.; Arkhipov, A.; Schulten, K. The role of molecular modeling in bionanotechnology. *Phys. Biol.* **2006**, *3*, S40–S53. [[CrossRef](#)]
74. MATLAB. 9.6.0.1072779 (R2019a); The MathWorks Inc.: Natick, MA, USA, 2019.
75. Hasslinger, P.; Vass, V.; Dejacó, A.; Blanchard, R.; Örylgsson, G.; Gargiulo, P.; Hellmich, C. Coupling multiscale X-ray physics and micromechanics for bone tissue composition and elasticity determination from micro-CT data, by example of femora from OVX and sham rats. *Int. J. Comput. Methods Eng. Sci. Mech.* **2016**, *17*, 222–244. [[CrossRef](#)]
76. Harley, R.; James, D.; Miller, A.; White, J. Phonons and the elastic moduli of collagen and muscle. *Nature* **1977**, *267*, 285–287. [[CrossRef](#)]
77. Fritsch, A.; Hellmich, C. ‘Universal’ microstructural patterns in cortical and trabecular, extracellular and extravascular bone materials: Micromechanics-based prediction of anisotropic elasticity. *J. Theor. Biol.* **2007**, *244*, 597–620. [[CrossRef](#)]
78. Katz, E.P.; Li, S.T. Structure and function of bone collagen fibrils. *J. Mol. Biol.* **1973**, *80*, 1–15. [[CrossRef](#)]

## 4 INVESTIGATING MECHANICAL PROPERTIES OF BONE MOLECULAR MODELS

Using the methodology provided in Chapter 3, we investigated structural and mechanical properties of all-atom bone molecular models composed of type-I collagen, hydroxyapatite, and water, by means of fully atomistic MD simulations. In terms of structure, we found that mineral components are hydrated and lose the initial crystal-like order with which they were placed into the simulation box during model construction. Moreover, water, present in limited quantities in the confining environment of the models, strongly coordinates HA calcium and phosphate ions and loses the typical tetrahedral local order that characterizes the bulk liquid. The structural features of water (more similar to that of nonpolar liquids) are similar in the extra- and intrafibrillar volumes.

We subjected our models to tensile loads and analyzed their mechanical responses. Our results show that high mineral content renders stiffer bones, which is well-known (Nair *et al.*, 2013; Fielder; Nair, 2019; Fielder; Nair, 2020; Prada *et al.*, 2022). The mineral tends to accumulate higher stress values, supporting most of the loads. Furthermore, an analysis of the stress distribution showed that the extrafibrillar region plays a crucial role in the mechanical response of the bone nanoscale models. Both HA and water molecules accumulate higher stresses when located in this region. Our results are also consistent with recent studies from continuum level models showing that mineralization of the intrafibrillar volume provides only a modest contribution to bone stiffness (Alijani; Vaughan, 2022), and that the extrafibrillar volume plays a major role in the mechanical properties of bones (Lin *et al.*, 2017). The minerals located in the extrafibrillar volume dominate the load-bearing response in bones.

Together with Chapter 3, this Chapter constitutes a novel, and crucial, contribution for the improvement of (1.).

Additionally, using the methodology by both the paper presented here and in Chapter 3, we have been investigating interface between bone and tendon by performing MD simulations of nonmineralized (tendon), partially mineralized (enthesis), and fully mineralized collagen fibrils (bone) to gain insight on the mechanisms that makes the interface so unique, see Figure 4.1.

It is well known that the mismatch between mechanical properties at the interface between soft and hard materials is one of the main challenges in engineering design. The

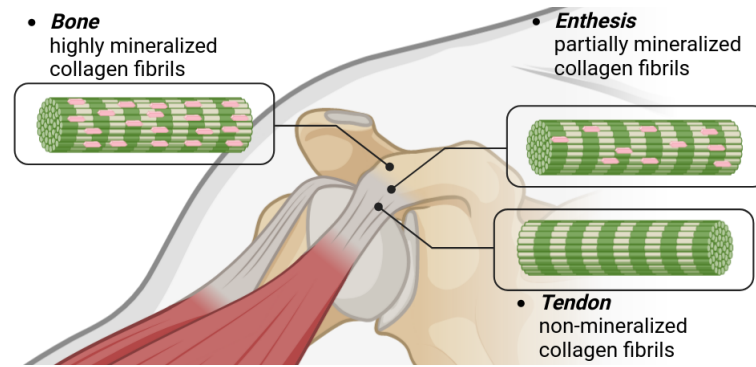


Figure 4.1 – Schematic visualization of the structure of Enthesis, Bone and Tendon. Created with BioRender.com.

enthesion, i.e., the interface between bones and tendons, seems to be a nature solution for this problem. However, fundamental understanding of the enthesion at the molecular level is still limited.

Our results related to the enthesion investigations are out of the scope of this thesis. We want to highlight that the methodology developed for devising bone molecular models can be further exploited to other materials.

# The Role of the Extrafibrillar Volume on the Mechanical Properties of Molecular Models of Mineralized Bone Microfibrils

Amadeus C. S. de Alcântara, Levi C. Felix, Douglas S. Galvão, Paulo Sollero, and Munir S. Skaf\*

**Cite This:** *ACS Biomater. Sci. Eng.* 2023, 9, 230–245

**Read Online**

ACCESS |

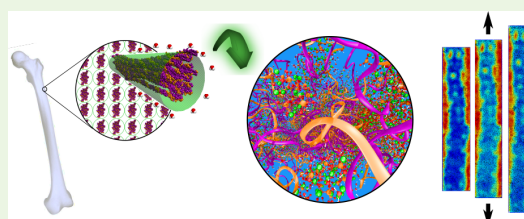
 Metrics & More

 Article Recommendations

 Supporting Information

**ABSTRACT:** Bones are responsible for body support, structure, motion, and several other functions that enable and facilitate life for many different animal species. They exhibit a complex network of distinct physical structures and mechanical properties, which ultimately depend on the fraction of their primary constituents at the molecular scale. However, the relationship between structure and mechanical properties in bones are still not fully understood. Here, we investigate structural and mechanical properties of all-atom bone molecular models composed of type-I collagen, hydroxyapatite (HA), and water by means of fully atomistic molecular dynamics simulations. Our models encompass an extrafibrillar volume (EFV) and consider mineral content in both the EFV and intrafibrillar volume (IFV), consistent with experimental observations. We investigate solvation structures and elastic properties of bone microfibril models with different degrees of mineralization, ranging from highly mineralized to weakly mineralized and nonmineralized models. We find that the local tetrahedral order of water is lost in similar ways in the EFV and IFV regions for all HA containing models, as calcium and phosphate ions are strongly coordinated with water molecules. We also subject our models to tensile loads and analyze the spatial stress distribution over the nanostructure of the material. Our results show that both mineral and water contents accumulate significantly higher stress levels, most notably in the EFV, thus revealing that this region, which has been only recently incorporated in all-atom molecular models, is fundamental for studying the mechanical properties of bones at the nanoscale. Furthermore, our results corroborate the well-established finding that high mineral content makes bone stiffer.

**KEYWORDS:** microfibrils, mineralized collagen fibril, collagen fiber, extrafibrillar volume, molecular dynamics, bone nanomechanics



## INTRODUCTION

Following the increasing average life expectancy in the last decades,<sup>1,2</sup> bone diseases are becoming commonplace among the elderly population.<sup>3</sup> Bone diseases, such as osteoporosis, induce bone fragility fractures and are a major health concern to health care systems worldwide.<sup>4–6</sup> Practitioners and researchers from different fields are looking to improve current predictive diagnosis techniques to minimize the social and financial impacts of disease-induced bone fractures.<sup>7</sup> Digital diagnosis techniques, however, often require a deeper understanding of the bone structure and their mechanical properties, which can be achieved, for instance, by considering the multiscale and patient-specific nature of the bone tissue.<sup>7–11</sup>

Bones typically constitute an organic phase, an inorganic (or mineral) phase, and water.<sup>7,12</sup> The organic phase is mainly composed of type-I collagen (CLG). The inorganic phase is composed of minerals containing phosphate and calcium ions, but the exact morphology of these minerals is still not fully understood. The literature refers to minerals in bone in different ways: apatite, hydroxyapatite (HA), biological apatite, carbonate-substituted hydroxyapatite, and calcium phosphate.<sup>13</sup> Different morphologies have been attributed to bone minerals: plate-like, needle-like (acicular), and stacks of different shapes.

However, none of them is comprehensively characterized. There are numerous variations of minerals in bones, which also differ among biological species.<sup>13,14</sup> Furthermore, it has been found that most minerals in bones may not be crystalline.<sup>15–17</sup>

The constituents of bone combine into a fiber-like nanocomposite material, whose mechanical properties depend on the relative fractions of these constituents.<sup>7,12,18–27</sup> Altered compositions of bone constituents might be related to bone diseases and bone fractures. For example, calcium deficiency makes bone more susceptible to fragility fractures,<sup>28,29</sup> and increased Ca intake is recommended to prevent bone loss as a treatment for osteoporosis,<sup>30,31</sup> which is characterized by low bone mineral density. Also, the dietary intake of direct forms of HA,  $\text{Ca}_{10}(\text{PO}_4)_6(\text{OH})_2$ , is used to prevent bone loss<sup>29</sup> and indicates the key role played by the mineral phase in fragility fractures.

**Received:** June 28, 2022

**Accepted:** November 23, 2022

**Published:** December 9, 2022



Shortly after the first CLG fibrillar structure was made available in the Protein Data Bank (PDB)<sup>32</sup> by Orgel et al.,<sup>33</sup> molecular dynamics (MD) studies of bone at the subnanoscale appeared in the literature.<sup>34,35</sup> Subsequently, several other studies included water and HA within the CLG fibrillar structure, i.e., in the intrafibrillar volume (IFV), to also address how the degree of mineralization influences bone mechanical properties.<sup>36–41</sup>

Recently, we presented nanoscale models of mineralized bone microfibrils that include HA in the extrafibrillar volume (EFV), and not solely in the IFV as in subnanoscale models.<sup>42</sup> These are, to our knowledge, the only all-atom molecular models to date that resemble simplified fibers in bones, as experimentally determined.<sup>26,43–45</sup> For further details on the inspiration for our models, see Schwarcz et al.<sup>45</sup> Figure 4 (reproduced in Figure 1 by Pang<sup>43</sup>) and McNally et al.<sup>44</sup> Figure 8. Mineralization of the EFV has been considered before only in models with continuous media.<sup>46–48</sup> Consideration of the EFV is of fundamental importance to understand the mechanical properties of bones at the nanoscale, and even to be able to create advanced biocompatible scaffolds.<sup>16</sup> Indeed, experiments have shown that most of the mineral content in bone, about 70% to 80%, is found in the EFV.<sup>23,26,44,45,49,50</sup> The remaining part is found in the IFV, distributed among the gap and overlap zones. Recently, by employing correlative bright field and dark-field transmission electron microscopy of ion milled bovine bone, Schwarcz et al.<sup>15</sup> have shown that calcium and phosphorus can be found in the IFV, not necessarily as HA crystals, but as amorphous calcium phosphate. The material inside the gap zone is either crystallites of apatite too small to Bragg-scatter electrons, or amorphous calcium phosphate. Yet, amorphous Ca phosphate usually rapidly crystallizes into apatite form.<sup>15</sup>

Here, we present fiber-like all-atom molecular models of mineralized bone microfibrils that include mineral content in both the IFV and EFV and conduct a systematic study of the their structural and mechanical properties at the nanoscale. Applying the detailed modeling process presented in our recent work,<sup>42</sup> we also considered less mineralized models. After equilibrating the proposed models, we investigated some of their structural properties. We then performed MD simulations that mimic tensile tests and analyzed their mechanical behavior. Fully atomistic MD simulations can provide valuable information on some essential elements of the biology and chemistry of fibers, fibrils, and microfibrils in bones, allowing us to better understand the deformation, and even failure, of bone at such length scales.

We first investigated the structural features of the mineralized aqueous environments in the EFV and IFV regions of models covering a wide range of mineralization degrees and, subsequently, studied the effects of mineralization on the elastic properties. In particular, we obtain the tridimensional spatial distribution of the von Mises stress within the nanomaterial.<sup>51–55</sup>

## METHODS

**Molecular Models.** Starting from the rat CLG structure available in the PDB (PDB ID: 3HR2),<sup>33</sup> and the human amino acid sequences COL1A1\_human (P02452) and COL1A2\_human (P08123) from the Universal Protein Resource (UniProt) Web site,<sup>56</sup> we performed homology modeling to build a model of the fibrillar structure of the human type-I CLG<sup>42</sup> displaying five CLG molecules, also labeled tropocollagen, in the overlap zone. Similar subnanoscale models have been presented in the literature.<sup>34–36,40,41,57–60</sup>

It is known that several CLG molecules group to form fibrils and that fibrils filled with Ca-based minerals in the IFV are labeled mineralized CLG fibrils. Yet, fibers in bone (also known as CLG fibers) are actually formed when minerals are placed around bundles of mineralized CLG fibrils, i.e., in the EFV, and immersed in water.<sup>26,43–45</sup> Except for the models presented in our recent work,<sup>42</sup> no other all-atom molecular model included HA, or any other Ca-based mineral content, in both, the IFV and EFV.

To include HA also in the EFV, we first extracted from the CLG fibril a structure that requires periodic boundary conditions along the *z*-direction and large enough to allow an EFV. Then, we replicated this new structure along the *x*- and *y*-directions, creating a 2 × 2 supercell with fibrils side by side (thus, the model has 20 CLG molecules in the IFV). Lastly, we used the Packmol code<sup>61</sup> to include HA and water molecules in both, the IFV and EFV. The IFV was defined as a parallelepiped inside the new simulation box.<sup>42</sup> The EFV consists of the volume of the simulation box subtracted from IFV. The models were inspired by Figure 4 of Schwarcz et al.<sup>45</sup> The final structures are labeled extrafibrillar models (EFMs). HA was added to the system in a way that 80% of the mineral mass belonged to the EFV and the remaining 20% to the IFV, consistent with the experimental data.<sup>23,26,44,45,49,50</sup>

Since the CLG molecules are derived from the 3HR2 PDB structure, the models maintain a quasi-hexagonal lateral packing, as shown in Figure S8 in the Supporting Information (SI). Hydroxylation of proline (PRO) into 4-hydroxyproline (HYP) is also considered in the EFMs. However, we do not consider hydroxylation of lysine residues. We use the standard form of lysine instead. There are two main reasons for that. First, there are only 15 lysine residues (versus 297 prolines) in the 3HR2 structure. Second, there are no interaction potentials available in CHARMM for hydroxylated lysine residues, and this could also affect the homology modeling.

Here, we use HA to represent the entire bone mineral phase. Schwarcz et al.<sup>15</sup> pointed out that instead of HA, amorphous Ca phosphate is more likely to be found in the IFV. In their work, they also mention the possibility of amorphous Ca phosphate crystallizing to apatite, and that small crystals would not have been identified by Bragg-scatter electrons. The exact structure of the mineral phase in bone, that is, whether it is present as crystals or amorphous fragments or combinations thereof, is still not well-established.<sup>13,14</sup> Most of the mineral in bone may actually be amorphous and not crystalline, but many of them certainly mineralize at some point.<sup>15–17</sup> The mineralization process in bone is too complex to be fully and reliably incorporated in MD simulations, as pointed out by Nair et al.,<sup>40</sup> especially of such large atomistic models. We assume that by filling IFV and EFV with HA we replicate the final stage of the mineralization process in bone and also that using only HA as the mineral content is not likely to strongly influence the mechanical properties of the material. We would like to emphasize two aspects: First, most mineral content in bone is found in the EFV and our EFMs consider this attribute,<sup>42</sup> and second, any other mineral content can be used in place of HA when creating such models, as previously reported.<sup>42</sup>

Reference values for the mass fractions of the bone constituents are 60–65% mineral material, 25–30% organic material, and 10% water.<sup>12,24–26</sup> We created fiber resembling bone models, which correspond to these compositions, as well as to other degrees of mineralization. Table 1 summarizes the compositions of the EFMs considered here.

A schematic representation of the EFMs is depicted in Figure 1 providing a perception of length scale.

Further details on the modeling process of these structures are described elsewhere.<sup>42</sup>

**Equilibration.** Before investigating the mechanical properties of the EFMs, we ran MD simulations using NAMD<sup>65</sup> and the CHARMM36m force field,<sup>66–69</sup> including parameters from the INTERFACE force field (IFF)<sup>70,71</sup> for HA. To equilibrate the structures, we started by running energy minimization steps with the conjugate gradient method. Then, we performed an NPT equilibration at 310 K and 1 atm for about 100 ns. We used a cutoff distance of 12 Å, and a smooth switch distance of 10 Å for the van der Waals interactions and the short-range part of the Coulomb interactions. The particle mesh Ewald method was used for

**Table 1. Mass Percentages of the Constituents, and the Corresponding Total Number of Atoms of the Extrafibrillar Models**

| model name | HA % | CLG % | water % | number of atoms |
|------------|------|-------|---------|-----------------|
| EFM00–00   | 00   | 100   | 00      | 156,856         |
| EFM00–25   | 00   | 75    | 25      | 164,707         |
| EFM15      | 15   | 75    | 10      | 194,730         |
| EFM30      | 30   | 60    | 10      | 217,576         |
| EFM45      | 45   | 45    | 10      | 255,635         |
| EFM55      | 55   | 35    | 10      | 299,136         |
| EFM60      | 60   | 30    | 10      | 331,797         |
| EFM65      | 65   | 25    | 10      | 377,486         |
| EFM70      | 70   | 20    | 10      | 446,018         |

handling the electrostatic forces<sup>72</sup> in simulations with NAMD.<sup>65</sup> The closely related particle–particle–mesh technique was used for the tensile stress simulations with LAMMPS<sup>73,74</sup> (see more details below). Furthermore, we constrained the hydrogen covalent bonds using the SHAKE algorithm to allow an integration time step of 2 fs. Further details on the parameters of the equilibration are described elsewhere.<sup>42</sup>

We ensured structural convergence by analyzing the root mean squared deviation (RMSD) of the protein backbone, as well as the time evolution of the pressure, D-band length (or D-period), CLG end-to-end distances, collagen widths, and box dimensions. See Figure S1–S7 in the Supporting Information (SI). Our simulations preserve the signature D-band structure of the collagen bundle under nonisochoric conditions. At the beginning of the NPT simulation the box shrinks very rapidly, but starts stabilizing after 20 ns or so and, as shown in the SI, the computed variables remain almost constant after 60 ns through the end of the equilibration. The D-band shrinks considerably by 16.6% for the EFM00–25 and 19% for the EFM60, but gap/overlap ratios (initially ~42–58% of the repeating unit for our EFMs) remained nearly constant, see SI Table S1. About 100 ns equilibration was required to ensure that the structure was stable. We made available the PDB and PSF files of the equilibrated EFMs at the link provided in the SI. Our analysis showed similar behavior, both quantitatively and qualitatively, to those of Varma et al.<sup>75</sup>

**Structural Characterization.** An important aspect of the atomistic behavior is related to how water and HA organize themselves in the presence of CLG fibrils. The rearrangement of water has been

previously addressed in mineralized microfibril models.<sup>76</sup> A structural analysis of our EFMs can provide further understanding regarding the role of mineralization in the structural and mechanical properties of more elaborate fibers resembling bone molecular models.

**Pair Distribution Functions.** The structure of liquids and amorphous materials can be described in terms of the radial pair-distribution functions (RDF), given by

$$g_{\alpha\beta}(r) = \frac{N_{\alpha\beta}(r)}{4\pi r^2 \Delta r \rho_{\beta}} \quad (1)$$

where  $N_{\alpha\beta}(r)$  is the average number of  $\beta$  atoms located in a shell of thickness  $\Delta r$  centered at a distance  $r$  of a reference  $\alpha$  atom,  $\rho_{\beta} = N_{\beta}/V$  is the average bulk density over the simulation box volume  $V$ . Amorphous materials with the same atomic composition and similar  $g(r)$  should possess similar properties, even though their atomic positions may differ. In other words,  $g(r)$  functions and the composition are the minimum information necessary to characterize a material.

From the last five nanoseconds of the equilibration simulations performed with NAMD (before the tensile test simulation with LAMMPS), we used the OVITO<sup>64</sup> code to compute the  $g(r)$  for different atomic pairs by averaging over five different snapshots separated by 1 ns. RDFs were also computed for the time window 80–85 ns of the trajectories.

To obtain additional structural information, we computed the coordination number that corresponds to the first-neighbor shell:

$$N_{\alpha\beta}^1 = 4\pi\rho_{\beta} \int_0^{r_1'} g_{\alpha\beta}(r)r^2 dr \quad (2)$$

where  $r_1'$  is the position of the first minimum in the  $g_{\alpha\beta}$  after the first peak at  $r_1$ . The integral above gives the average number of  $\beta$  atoms surrounding the  $\alpha$  ones.

**NAMD to LAMMPS.** Although NAMD is a well established MD code, especially for biomolecules, it currently lacks a more straightforward approach to deal with deformation and atomic stress calculations (especially beyond the linear regime) that are necessary to study the mechanical properties of materials. Thus, we converted the structures equilibrated in the NAMD to the LAMMPS software,<sup>73,74,77–83</sup> in order to perform the tensile tests described below. The conversion was performed using *charmm2lammps.pl* from the LAMMPS tool. Two remarks worth mentioning here: (1) All force field topology and parameter files must be grouped (and properly enumerated) into a single topology and one parameter file, respectively,

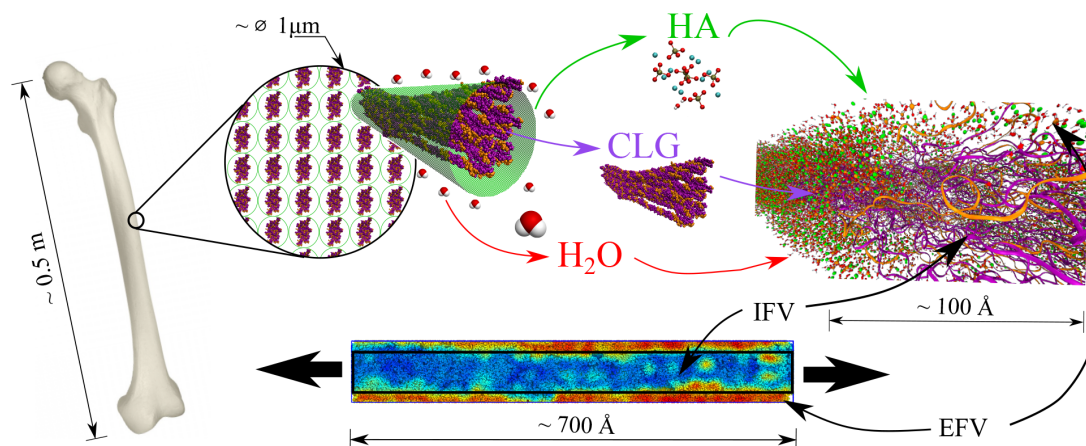


**Figure 1.** Graphical representation of the extrafibrillar model. A zoomed view at the nanoscale of a femur shows aligned fibers, which are basically bundles of mineralized collagen fibrils surrounded by hydroxyapatite crystals and immersed in water (similar in structure to our EFMs, but EFMs contain 20 CLG molecules, whereas fibers in bones contain many more CLG molecules). Rightmost, a VMD<sup>62,63</sup> view of an MD snapshot of the EFM45. At the bottom, a von Mises stress distribution on an EFM subjected to tensile loads shown with OVITO.<sup>64</sup> The EFMs are composed of both mineralized EFV and IFV. This figure also discerns both.

and (2) TER cards/records must be added after the last line of a chain in the PDB file. Both these issues were circumvented, either manually or using Matlab scripts.<sup>84</sup> Further details and all scripts necessary for this conversion are available at the link provided in the SI.

Further equilibration steps prior to the tensile MD run were performed with LAMMPS to avoid problems with any residual stress. The first equilibration step lasted 1 ns using a time step of 1 fs, and the second lasted 5 ns with a time step of 2 fs. We used a Langevin thermostat<sup>85</sup> and a Nosé–Hoover barostat,<sup>86–89</sup> under LAMMPS commands *fix langevin* and *fix nph*. The scripts used for the equilibration with LAMMPS are available at the link provided in the SI.

**Tensile Tests.** We used LAMMPS *fix deform* command to increase the box length  $L_z$  at each time step, while computing the symmetric pressure tensor using LAMMPS *compute pressure* command.

LAMMPS *fix deform* command updates the length of the box along the  $z$ -direction following

$$L_z(t) = L_{z0}(\dot{\epsilon}_{zz}(t) \cdot t + 1) \quad (3)$$

where  $L_{z0}$  is the length of the box at the beginning of the simulation, and  $\dot{\epsilon}_{zz}(t)$  is the engineering strain rate along the  $z$ -direction.

We used LAMMPS *compute pressure* command to compute the elements of the symmetric pressure tensor  $P_{ij}$  given by

$$P_{ij} = \sum_{k=1}^N m_k v_{ki} v_{kj} / V + \sum_{k=1}^{N'} r_{ki} f_{kj} / V \quad (4)$$

$P_{ij}$  adds components of the kinetic energy tensor and of the virial tensor where  $m_k$  is the mass of the  $k$ -th atom,  $v_{ki}$  is the  $i$ -th component of the velocity of the  $k$ -th atom,  $r_{ki}$  is the  $i$ -th component of the position of the  $k$ -th atom,  $f_{ki}$  is the  $i$ -th component of the resultant force applied on the  $k$ -th atom,  $V$  is the system volume, and  $N$  is the number of atoms ( $N'$  includes atoms from neighboring subdomains, labeled ghost atoms). The virial component includes the sum of pair, bond, angle, dihedral, improper, kspace (long-range), and fix contributions to the force on each atom.

The parameters used during the tensile test simulations are shown in Table 2. Besides periodic boundary conditions for all directions, we

**Table 2. Parameters of MD Simulation for Tensile Tests with LAMMPS**

| parameter name  | parameter value   |
|---|-------------------|
| Deformation Time  | 30 ps             |
| Deformation Timestep  | 2 fs              |
| Deformation Direction   | $z$               |
| Strain Rate   | $10^{-5}$ 1/fs    |
| Equilibration Ensemble  | NPT               |
| Inner Cutoff  | 12.0 Å            |
| Outer Cutoff  | 14 Å              |
| Neighbor Skin   | 2.0 Å             |
| Particle–Particle Particle–Mesh Solver Desired Relative Error in Forces | $10^{-6}$         |
| Temperature Control Algorithm   | Langevin Dynamics |
| Target Temperature  | 310 K             |
| Pressure Control Algorithm (in $x$ and $y$ )                            | Nosé–Hoover       |
| Target Pressure   | 1.0 atm           |

implemented an NPT ensemble along the  $x$ - and  $y$ -directions, while a constant engineering strain rate deformed the box along the  $z$ -axis up to 30% strain.

**Computing Young's Modulus.** We estimated Young's modulus values  $E$  during the uniaxial tensile tests along the  $z$ -direction, by relating stress and strain through  $\sigma_{zz} = E\epsilon_{zz}$ , as described elsewhere.<sup>42</sup> The per-atom pressure is actually the negative of the per-atom stress, i.e.,  $\sigma_{zz} = -P_{zz}$ , see eq 6. We assumed bone, and thus the EFMs, complies with Hooke's law. In this work, we are mainly interested in the elastic regime of the models.

There are other ways of computing mechanical properties from MD simulations. Free energy calculations, for example, provide a thermodynamically proper and more consistent way of computing Young's Modulus than tensile test simulations.<sup>90</sup> However, computing potential of mean force for large systems, like those considered here, is prohibitively costly, even for computational resources much superior than the ones we have available.

**Computing the Equivalent von Mises Stress.** The von Mises failure criterion also called the maximum distortion energy theory, predicts, for isotropic ductile materials, that yielding occurs when the maximum deformation energy equals the distortion energy at yielding in a uniaxial tensile test. It was initially developed by Richard von Mises and later refined by others; it is also known as the Maxwell–Huber–Hencky–von Mises theory.<sup>51</sup>

This theory defines the equivalent von Mises stress (or simply von Mises stress), which comprises the elements of the Cauchy stress tensor into a scalar value, and is independent of the hydrostatic stresses (depends only on the effects of the deviatoric stresses). Although defined for continuous materials, the theory can also be applied at discrete scales.<sup>52–55</sup> During the tensile test simulations carried out with LAMMPS, we computed the equivalent von Mises stress  $\sigma_v$  for each atom following:

$$\sigma_v^k = \sqrt{\frac{1}{2} \sum_{i < j} (\sigma_{ij}^k - \sigma_{ji}^k)^2 - 6(\sigma_{ii}^k)^2} \quad (5)$$

where  $i = x, y, z$  and  $\sigma_{ij}^k$  is an element of the stress tensor of the  $k$ -th atom, which, in turn, is computed using LAMMPS *compute stress/atom* command through

$$\sigma_{ij}^k = -m_k v_{ki} v_{kj} - W_{ij}^k \quad (6)$$

$W_{ij}^k$  is the virial contribution of the stress computed by eq 7, by adding pairwise, bond, angle, dihedral, improper, and also  $k$ -space contribution from long-range Coulombic interactions, as well as contributions from an applied *fix shake* command:

$$\begin{aligned} W_{ij}^k = & \frac{1}{2} \sum_{n=1}^{N_p} (r_{1i} F_{1j} + r_{2i} F_{2j}) + \frac{1}{2} \sum_{n=1}^{N_j} (r_{1i} F_{1j} + r_{2i} F_{2j}) \\ & + \frac{1}{3} \sum_{n=1}^{N_i} (r_{1i} F_{1j} + r_{2i} F_{2j} + r_{3i} F_{3j}) \\ & + \frac{1}{4} \sum_{n=1}^{N_j} (r_{1i} F_{1j} + r_{2i} F_{2j} + r_{3i} F_{3j} + r_{4i} F_{4j}) \\ & + \frac{1}{4} \sum_{n=1}^{N_i} (r_{1i} F_{1j} + r_{2i} F_{2j} + r_{3i} F_{3j} + r_{4i} F_{4j}) + \text{Kspace}(r_{ki}, F_{kj}) \\ & + \sum_{n=1}^{N_j} r_{ki} F_{kj} \end{aligned} \quad (7)$$

Notice that eq 6 exhibits a kinetic contribution  $m_k v_{ki} v_{kj}$  and a virial contribution  $W_{ij}^k$  due to intra- and intermolecular interactions, just as eq 4 does, and hence  $\sigma_{ij} = -P_{ij}$ .

The LAMMPS *compute stress/atom* command computes  $\sigma_{ij}^k$  in units of pressure  $\times$  volume. Therefore, we must divide the final computed  $\sigma_v^k$  by the per-atom volume in order to compute the per-atom von Mises stress in pressure units. We divided the computed  $\sigma_v^k$  by the total volume of the simulation box just to adjust the units. If a more precise quantitative value for the per-atom von Mises stress is needed, LAMMPS *compute voronoi/atom* command can estimate a per-atom volume. Since our systems are mostly completely filled with atoms that are homogeneously distributed in the simulation box, we can multiply the computed von Mises values by the number of atoms in the system in order to estimate more realistic stress values. However, the exact value of the per-atom von Mises stress is not of particular interest here.

It is important to emphasize that caution is required when computing the von Mises stress for intrinsically anisotropic systems and biological fibrous materials, such as CLG fibrils and fibers. As discussed by

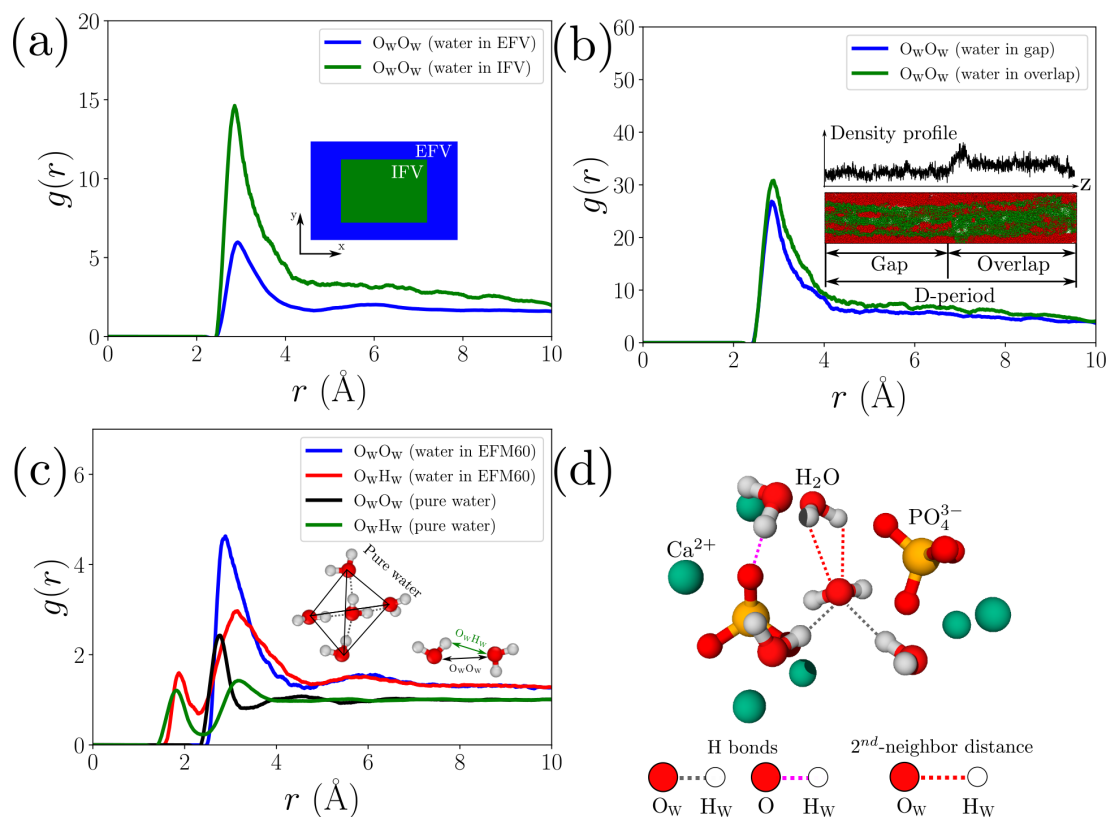


**Figure 2.** Structural analysis of water in EFM60. (a)  $g_{O_wO_w}$  corresponds to EFV and IFV with a schematic on the inset illustrating their definitions. (b)  $g_{O_wO_w}$  in the gap and overlap region inside the EFMs. The inset shows the atomic density profile used to define gap and overlap regions within the EFM. (c) RDFs for  $O_wO_w$  and  $O_wH_w$  pairs for the EFM60 and pure water. (d) MD snapshot showing a few H-bonds to illustrate the behavior of the radial distributions shown in (c). H-bonds are defined in the legend.

Korenczuk et al.,<sup>91</sup> the von Mises stress values may be inadequate to assess the risk of structural failure for anisotropic materials, particularly biological fibrous tissues. Here, we are not interested in quantifying the material failure in the proper sense, but rather, we compute the von Mises stress distribution across the structures as a means of gaining qualitative insights regarding the most fracture susceptible regions of the bone models, as well as which bone constituents accumulate more stresses.

## RESULTS AND DISCUSSION

**Structural Analysis. Local Structure of Water.** When creating the EFMs, the IFV was defined as a rectangular box inside the whole simulation box with dimensions of  $[60 \text{ \AA}, 86 \text{ \AA}, L_z]$ , where  $L_z$  is the length of the simulation box along the  $z$ -axis. The EFV was defined as the region outside the IFV with outer dimensions of  $[88 \text{ \AA}, 142 \text{ \AA}, L_z = 679 \text{ \AA}]$ . The inset of Figure 2(a) illustrates a cross-section of the simulation box highlighting EFV and IFV. During the MD simulations, the IFV dimensions were updated by keeping the same ratio between EFV and IFV dimensions, as defined before equilibration. The radial density profiles of water oxygen atoms ( $O_w$ ), phosphorus, calcium, and CLG  $C_\alpha$  atoms with respect to the main axis ( $z$ -axis) centered along the length of the structures show that water and HA are similarly distributed and mostly surrounding the CLG triple helices (see SI Figures S9–S11).

The pair distribution functions for water oxygen atoms ( $O_w$ ) in both the IFV and EFV of the EFM60 are shown in Figure 2. All structural analysis results presented in this section refer to the EFM60, since all models containing HA show very similar features (see SI Figures S12–S17). Water molecules in the IFV and EFV are similarly arranged with two pronounced coordination shells peaked at around  $r \approx 2.86$  and  $5.96 \text{ \AA}$ . A large percentage of water molecules in the IFV is presumed to interact with the CLG fibril, especially when compared to water molecules in the EFV. Nevertheless, the principal and secondary peaks of the water–water RDFs appear at very similar positions for both EFV and IFV regions. The difference in peak intensities between the two cases is a consequence of different normalization factors due to  $\rho_\beta$ . There are fewer water molecules in IFV resulting in a lower average density and larger values of  $g(r)$ .

It is also interesting to analyze the organization of water molecules in an even more confining environment, such as the gap and overlap regions. Following previous studies,<sup>40,41</sup> we identify the gap and overlap regions by looking at the CLG density profile, as shown in the inset of Figure 2(b). One gap and one overlap zone, a D-period, are present in the simulation box. As shown in Figure 2(b), both gap and overlap RDFs present similar shapes and peak intensities.

In Figure 2(c), we compare water–water RDFs computed for the EFM60 (cf. Table 1) and for pure water at 310 K and 1 atm, obtained from a 10 ns simulation with 2880 TIP3P molecules.

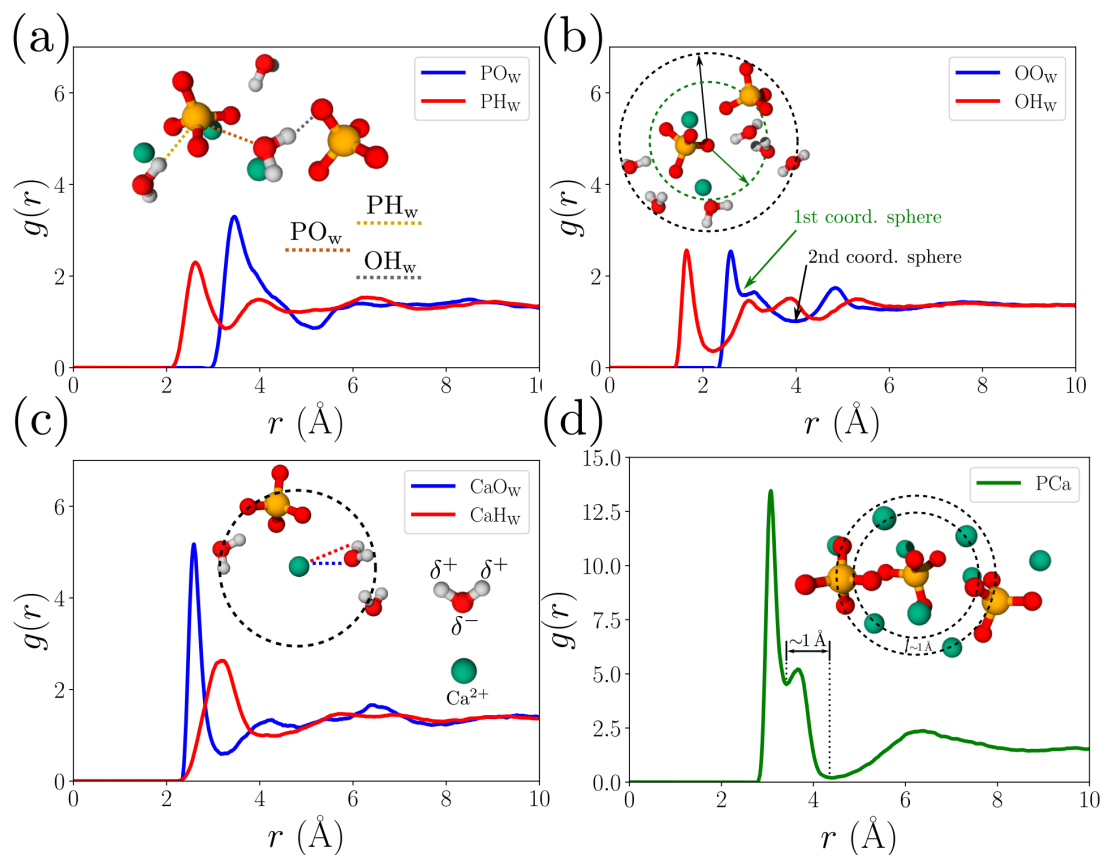


**Figure 3.** RDF between HA components and HA-water pairs in the EFM60 corresponding to (a)  $\text{PO}_w$  and  $\text{PH}_w$ , (b)  $\text{OO}_w$  and  $\text{OH}_w$ , (c)  $\text{CaO}_w$  and  $\text{CaH}_w$ , and (d) PCa. Sketches in the insets are taken from MD simulation snapshots.

For pure water, the first two peaks, centered at  $r_1 = 2.76 \text{ \AA}$  and  $r_2 = 4.54 \text{ \AA}$ , respectively, exhibit a well-defined tetrahedral relation<sup>92,93</sup>,  $r_2 = 2(2/3)^{1/2}r_1$  (black curve in Figure 2(c)). However, this is not the case for water in the bone environment. Remarkably, the locations of the first and second peaks in  $g_{\text{O}_w\text{O}_w}$  reveal that water in the bone confining environment no longer exhibits the characteristic local tetrahedral order of the liquid. The interaction between water and the other components of the bone models significantly changes the water local structure as its coordination shells peak at different radial distances. This is observed in the blue curve (Figure 2(c)), where  $r_1 = 2.88 \text{ \AA}$  and  $r_2 = 6.04 \text{ \AA}$  ( $\approx 2r_1$ ), are considerably different from the case of pure water. The coordination number  $N_{\text{O}_w\text{O}_w}^1$  for  $\text{O}_w\text{O}_w$  in pure water and in the EFMs is approximately 4. The presence of HA components, such as phosphates ( $\text{PO}_4^{3-}$ ) and  $\text{Ca}^{2+}$  ions, breaks the tetrahedral structure of pure water by modifying the environment with their strong ionic electrostatic fields. Similar features are found in less mineralized models (see SI Figures S12–S14).

The hydrogen bonding in water can be examined from  $g_{\text{O}_w\text{H}_w}$ , shown in Figure 2(c). In both EFV and IFV environments, we find the H-bond bond-length values close to that of pure water (1.82 and 1.87  $\text{ \AA}$ , respectively). The average number of H-bonds, however, drops from  $\approx 4$  in pure water (inset of Figure 2(c)) to  $\approx 2$  in the bone environment due to the presence of phosphate O atoms, which are strong H-bond acceptors, see

Figure 2(d). In the EFM, the nearest water molecules involved in the H-bond formation with the central molecule shown in Figure 2(d) are distant from their second H atom a little further from the origin and, thus, are part of the second peak in  $g_{\text{O}_w\text{H}_w}$ . Additionally, unlike in pure water, the second nearest neighbor water molecules can be oriented in such a way that both H atoms point to the  $\text{O}_w$  atoms of the reference molecule as a result of interaction with its negatively charged site. These distances are also within the second peak. These two different water molecular arrangements above-mentioned explain why the second peak of both  $g_{\text{O}_w\text{H}_w}$  has a larger intensity than that of the first one.

**HA Structure.** HA constituents may rearrange themselves in many different ways, such as small crystallite fragments or as an amorphous phase surrounded by water. We analyzed the hydration structures surrounding  $\text{PO}_4^{3-}$  and  $\text{Ca}^{2+}$  ions in the EFM. Figure 3(a) shows the  $\text{PO}_w$  and  $\text{PH}_w$  RDFs in the EFM environment (which consists of EFV + IFV). Due to their negative charges, phosphates tend to attract H atoms, which results in  $g_{\text{PH}_w}$  having its first peak ( $r_1 \approx 2.62 \text{ \AA}$ ) situated at a smaller radial distance than in  $g_{\text{PO}_w}$  ( $r_1 \approx 3.46 \text{ \AA}$ ). Nevertheless, the coordination number for  $\text{PH}_w$  pairs is only  $\approx 2$ . Water molecules are found mostly bridging among phosphate anions and  $\text{Ca}^{2+}$ , as shown in the inset of Figure 3(a). The red dashed line on the same inset depicts a  $\text{PO}_w$  pair involving a water molecule that is H-bonded to an O atom of another phosphate,

represented by the gray dashed line. This also contributes to the first coordination shell. Thus, we have two configurations of water molecules with similar  $PO_w$  distances from the reference P, which explains why the first peak in the blue curve looks like two peaks coalesced into a single one.

The O sites in phosphates play an important role in redistributing H-bonds from surrounding water molecules. Figure 3(b) shows that  $O_w$  distribution around a phosphate O atom has two overlapping peaks in the first coordination shell. The first peak comes from molecules with the only H-bond with the reference O atom, as its corresponding coordination number is less than 1. The second layer comes from other water molecules that are coordinated by other nearby phosphates and, thus, contribute to a more intense peak, as can be inferred from the snapshot in Figure 3 (b). The first coordination sphere shown in the inset yields an average number of 1.5 and the second one 4.5, which implies two compact coordination shells that have on average of 6 water molecules around a phosphate O atom.

The hydration structure around  $Ca^{2+}$  ions reflected in the RDFs is shown in Figure 3(c). The  $g_{CaO_w}$  pair distribution exhibits a sharp peak at 2.58 Å, indicating that the  $Ca^{2+}$  ions are well-coordinated by water molecules. The solvation shell around  $Ca^{2+}$  also contains phosphate anions due to their strong electrostatic attraction. The first peak of  $g_{CaH_w}$  is centered at a larger distance than that of  $g_{CaO_w}$  as  $H_w$  atoms tend to point away from the line segment joining  $Ca^{2+}$  and  $O_w$ . Moreover,  $H_w$  atoms are highly attracted to the H-bond of the  $PO_4^{3-}$  anions.

To conclude our structural analysis, we show the arrangement between  $PO_4^{3-}$  and  $Ca^{2+}$  ions from HA after equilibration, illustrated by the results shown in Figure 3(d). The HA components introduced into the system during assembly of the simulation box are crystalline in the sense that their initial atomic positions are given by the unit cell coordinates. In this case the  $g_{PCa}(r)$  RDF would show a series of sharp peaks centered at distances corresponding to first, second, third neighbors, and so on. However, after the EFM equilibration, a sharp and broader double-peak is found centered at  $r_1 = 3.22$  Å and  $r_2 = 5.69$  Å (see Figure 3(c)). Each of these peaks contributes  $\approx 3$   $Ca^{2+}$  cations to the neighborhood of a central P phosphate, whereas the contribution of the less intense shoulder peak comes from  $Ca^{2+}$  ions coordinated by nearby phosphates, as shown in the inset of Figure 3(d). The presence of broader peaks beyond 4 Å indicates that the crystallinity of a pure HA mineral is broken by the presence of water and CLG molecules. This result corroborates previous studies reporting that the mineral content in bone is mainly found in noncrystalline forms.<sup>15,16,23,26,45</sup>

From the last five nanoseconds of the equilibration simulations performed with NAMD (before the tensile test simulation with LAMMPS), we used the OVITO<sup>64</sup> code to compute the  $g(r)$  for different atomic pairs by averaging over five different snapshots separated by 1 ns.

The peaks positions and coordination numbers for the computed RDFs are summarized in Table 3.

We have also calculated RDFs using the 80–85 ns window of the trajectories in order to verify that molecular conformations of the protein backbone and solvent plus mineral distributions were sufficiently sampled. The results are identical to the ones obtained from the 95–100 ns segment of the trajectories (see SI Figures S18–S19).

**Young's Modulus.** The stress and strain tensors computed during the tensile tests were plotted as stress–strain curves in Figure 4(a). Less mineralized EFMs (15 wt % and lower) exhibit

**Table 3. Position of the Peaks and Coordination Numbers for the Presented RDFs. We Chose to Present Only the Coordination Numbers That Were Used in Our Discussions**

| pair ( $\alpha\beta$ ) | $r_1$ [Å] | $r_2$ [Å] | $N_{\alpha\beta}^1$ | $N_{\alpha\beta}^2$ |
|------------------------|-----------|-----------|---------------------|---------------------|
| $O_wO_w$ (pure water)  | 2.76      | 4.54      | 4                   |                     |
| $O_wH_w$ (pure water)  | 1.82      | 3.16      | 4                   |                     |
| $O_wO_w$ (EFM60)       | 2.88      | 6.04      | 4                   |                     |
| $O_wH_w$ (EFM60)       | 1.87      | 3.14      | 2                   |                     |
| $PO_w$                 | 3.46      | 6.20      | 2                   | 3                   |
| $PH_w$                 | 2.62      | 3.96      | 2                   |                     |
| $OO_w$                 | 2.60      | 3.10      | 0                   | 1                   |
| $OH_w$                 | 1.65      | 2.97      | 0                   |                     |
| $CaO_w$                | 2.58      | 4.25      | 1                   |                     |
| $CaH_w$                | 3.22      | 5.69      | 5                   |                     |
| PCa                    | 3.07      | 3.65      | 3                   | 3                   |

different stress–strain curves when compared to the more mineralized models. The shortage of HA results in poorly mineralized models that do not show a saturation (for the values shown in the Figure) in the stress–strain response curves after reaching an apparent yield strength or elastic limit. However, these results have to be analyzed taking into consideration that CHARMM36m<sup>66–69</sup> is a nonreactive force field, and can not reliably describe deformations for very large strain values. In this sense, there will be no structural failure during tensile tests. If the deformation continues to very large strain values, the covalent bonds of the CLG molecules would be stretched indefinitely. The stress–strain responses do not exhibit a fracture or an ultimate strength region. Thus, here we only consider the low-strain values of the tensile test (between 1% and 7% strain) to estimate Young's modulus values.

We estimated Young's modulus values from the slope of the low-strain region of the stress–strain curves by linear regression. The results are displayed in Figure 4(b). Details of the computation of Young's modulus, as well as the values for the EFM55, EFM60, EFM65, and EFM70, can be found in our previous work.<sup>42</sup>

Figure 4(b) shows that the estimated Young's modulus values are directly proportional to the HA content for models with an HA weight fraction of 15% and higher. This proportionality and the estimated values are in agreement with the literature.<sup>11,38,39</sup> Yet, as discussed by previous works,<sup>42,94,95</sup> there is no standard value for Young's modulus of CLG fibrils, mineralized CLG fibrils, and fiber resembling models like the ones considered here. However, the computed values are not far from the experimental literature. For example, in his book,<sup>96</sup> Currey reports Young's Modulus values ranging from  $\sim 10$  to 20 GPa for tension tests in human haversians (cortical bone).<sup>97</sup> Our curves are also qualitatively similar to experimental works.<sup>98</sup> Furthermore, our results also indicate that the water fraction does not significantly affect the values. A water mass fraction increase of 25% resulted in a Young's modulus increase of just  $\approx 0.23$  GPa, i.e., less than 4%, as shown for the EFM00–00 and 00–25 in Table 1 and Figure 4(b).

Before discussing the stress distribution, we make a brief note on the applied strain rate. A relatively high strain rate, maybe unrealistic in terms of experimental work, was applied for our tensile test simulations, see Table 2. It is known that a lower strain rate can lead to lower values of Young's Modulus. To investigate its effect, we performed tensile test simulations with a strain rate of  $10^{-7}$  1/fs, i.e., 100 times smaller than the previous one. Results for Young's Modulus values obtained with different

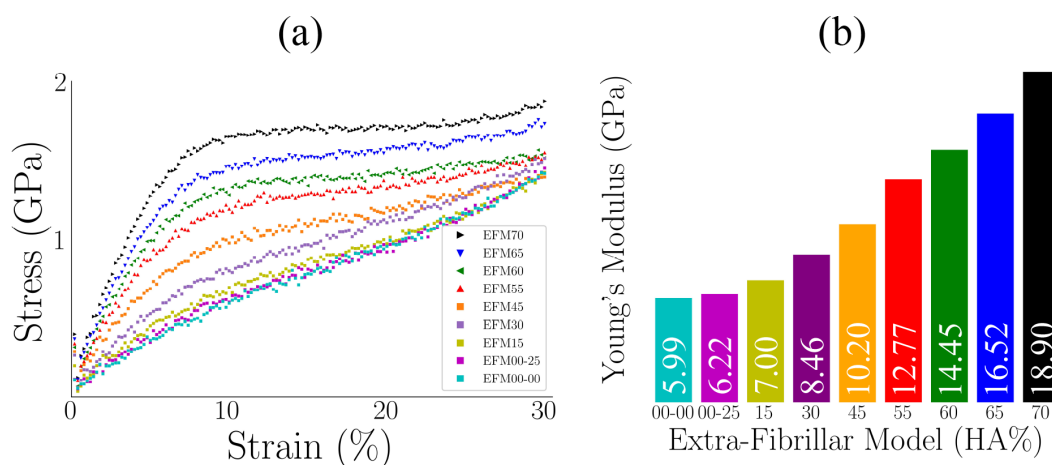


**Figure 4.** (a) Stress–strain response curves computed for the EFM, and (b) the corresponding Young's modulus values.

strain rate values are shown in Table 4. A 100-fold slower strain rate resulted in just  $\sim 10\%$  smaller Young's Modulus values. The

**Table 4. Computed Young's Modulus (YM) Values for Simulations Performed with Different Strain Rate (st) Values**

| model name | YM with st of $10^{-5}$ 1/fs | YM with st of $10^{-7}$ 1/fs | difference in % |
|------------|------------------------------|------------------------------|-----------------|
| EFM00-25   | 6.22                         | 5.65                         | 9.2             |
| EFM15      | 7.00                         | 6.12                         | 12.6            |
| EFM45      | 10.20                        | 9.30                         | 8.8             |
| EFM60      | 14.45                        | 14.01                        | 3.0             |

stress–strain curves and their respective linear regression are displayed in Figure S20 of the SI.

**von Mises Stress Distribution.** For the described MD simulations of the uniaxial tensile tests, the von Mises stress is

approximately equal to  $\sigma_{zz}$ . However, since it does not depend on the direction of the applied load, the von Mises stress is a more general form of displaying a stress distribution, regardless of the type of test performed on the material. Below, we discuss the von Mises stress distribution during the tensile tests. In general continuum von Mises stress analysis, areas with high stress values indicate higher risk of yielding. In our case, for classical MD simulations, areas with high stress values (indicated in red in the scale) serve only to indicate regions accumulating high stress values.

**CLG  $\times$  Water  $\times$  HA.** First, we analyzed the EFM00-00. This model is just for reference since it contains neither HA nor water molecules. Figure 5(a) shows a per-atom distribution of the von Mises stress in the EFM00-00 for strains ranging from 0 to 30%. Figure 5(b) shows the corresponding normalized histograms containing the distribution of the von Mises stress. A total of 100 histogram bins were used in OVITO<sup>64</sup> to generate the data for

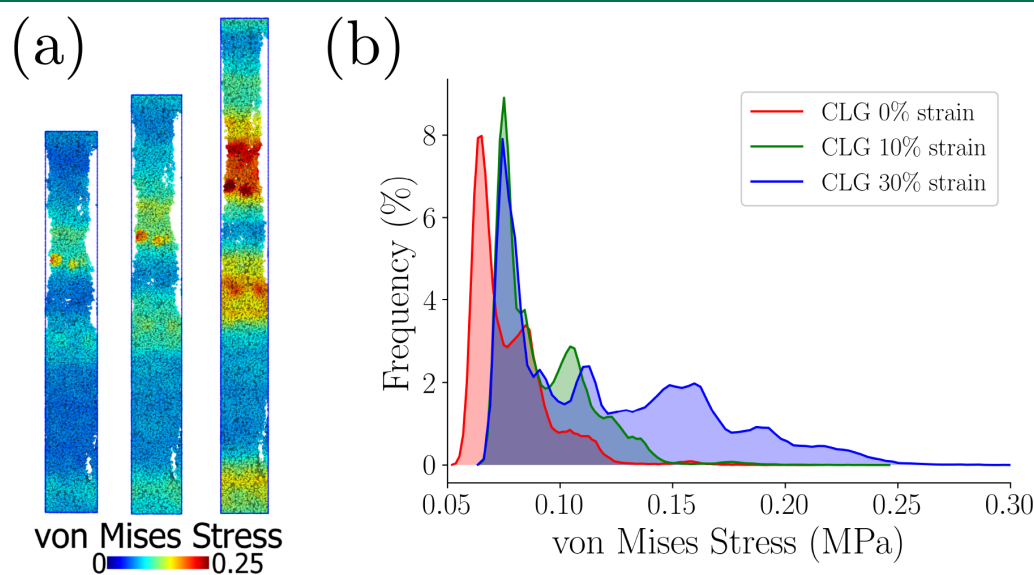


**Figure 5.** EFM00-00: (a) per-atom visualization of von Mises stress [MPa] at 0, 10, and 30% strain; (b) normalized distribution of stress at 0, 10, and 30% strain.

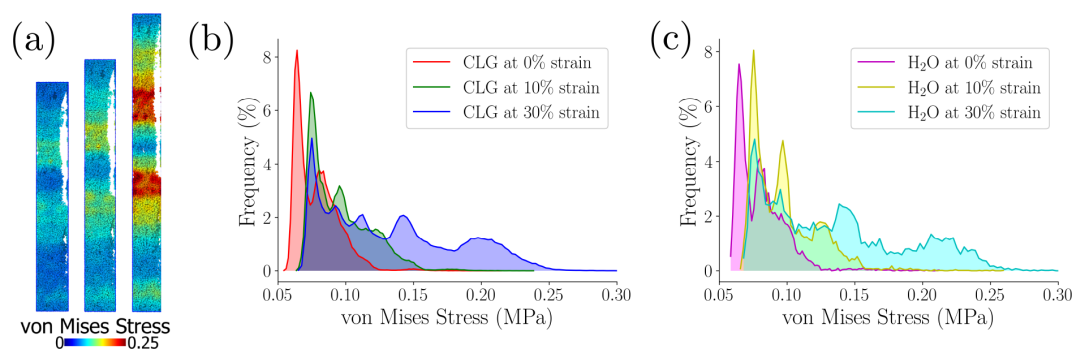


**Figure 6.** EFM00–25: (a) per-atom visualization of von Mises stress [MPa] at 0, 10, and 30% strain; (b) normalized distribution of stress on CLG at 0, 10, and 30% strain; (c) normalized distribution of stress on water at 0, 10, and 30% strain.

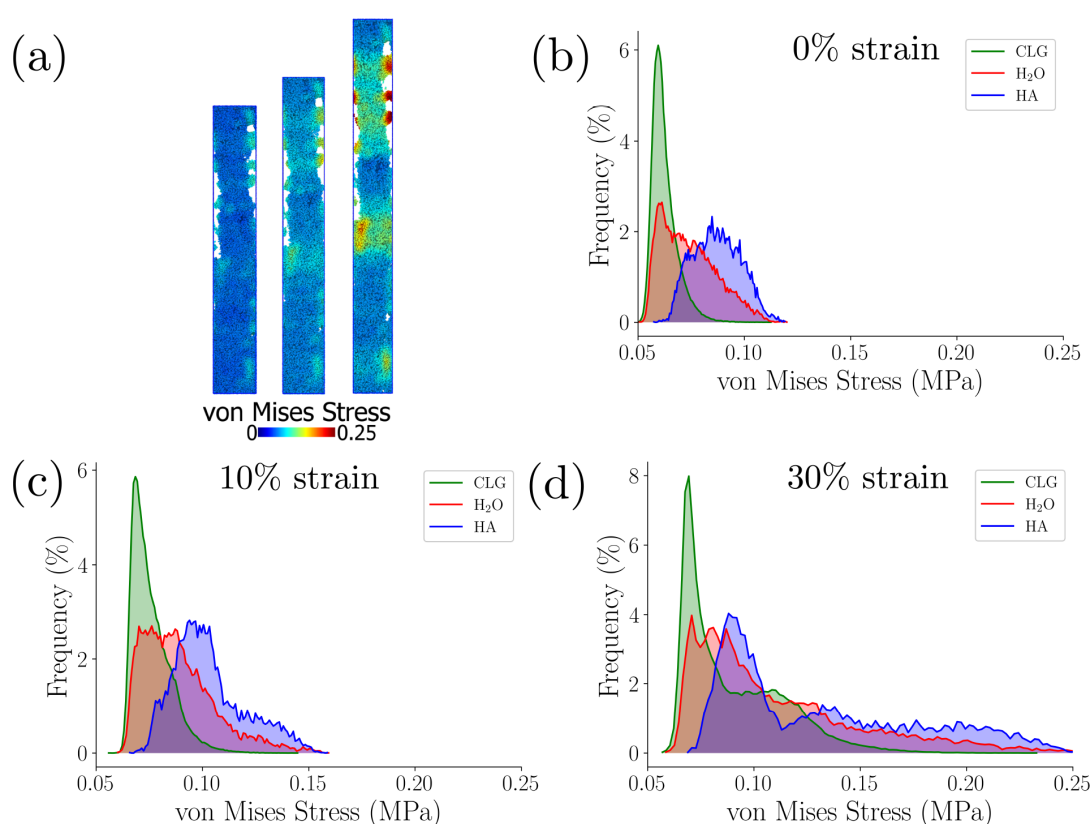


**Figure 7.** EFM15: (a) per-atom visualization of von Mises stress [MPa] at 0, 10, and 30% strain; (b–d) normalized distribution of stress at 0, 10, and 30% strain, respectively.

all the histograms presented below. Normalization was performed by dividing the atom count for each bin (stress value) by the total atom count of an atom's group (i.e., for CLG, HA, and water). It is evident that increasing strain leads to increasing stress. At 30% strain (blue area in Figure 5(b)), there are much more atoms under high stresses (in red in Figure 5(a)) than at 10% or 0% strain. It is worth mentioning that a strain of 30% is way beyond experimental values and typical yield strain in bones. We show these values as an extreme case.

For the EFM00–25, which contains water, but no HA, Figure 6(a) shows a per-atom distribution of the von Mises stress along

the structure, and Figure 6 panels b and c show the corresponding normalized histograms containing the distribution of the von Mises stress taking into consideration, respectively, CLG and water atoms. As expected, these results indicate that a greater fraction of the particles will experience higher stress values the higher the strain level. This feature is equally apparent for CLG and water.

Figure 7(a) shows a per-atom distribution of the von Mises stress in the EFM15. Interestingly, most atoms displaying high-stress values (in red) are now located on the edges of the box, in the EFV, as opposed to the models without HA, which shows

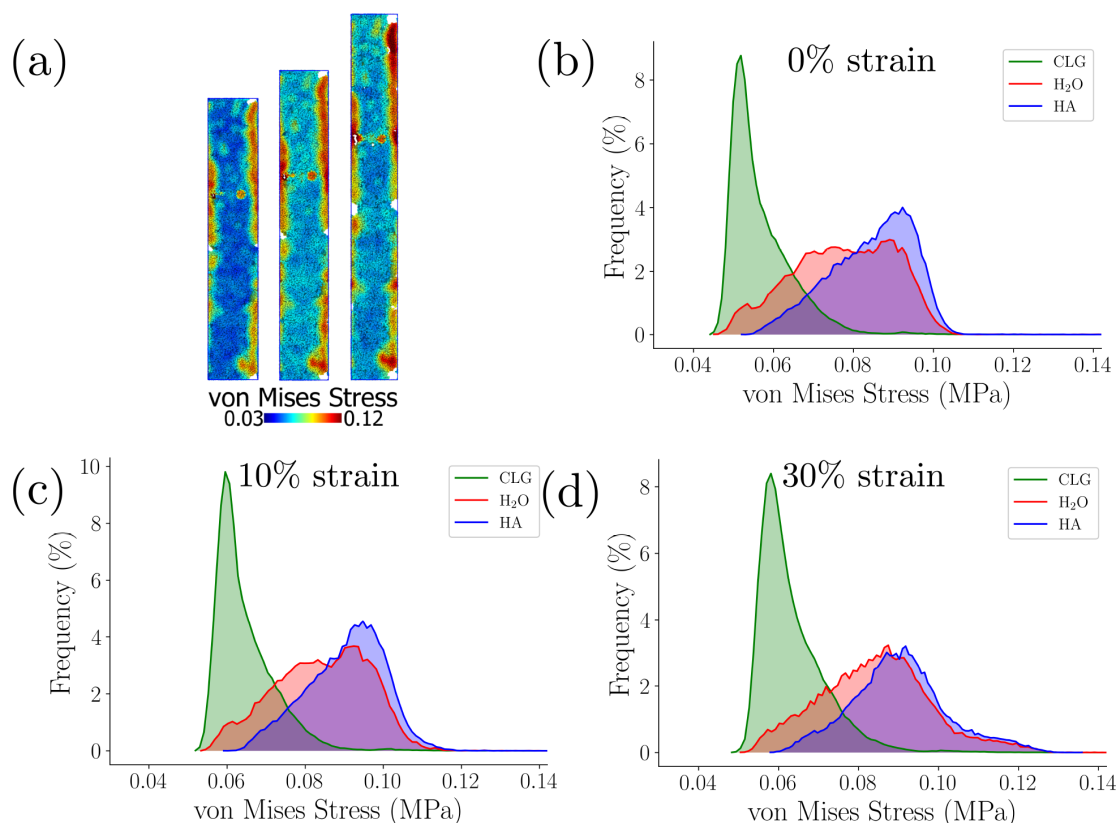


**Figure 8.** EFM45: (a) per-atom visualization of von Mises stress [MPa] at 0, 10, and 30% strain; (b–d) normalized distribution of stress at 0, 10, and 30% strain, respectively.

that the high stress (red) regions are mostly on CLG in the IFV (Figures 5(a) and 6(a)). Figure 7 panels b–d show per-atom normalized histograms of the von Mises stress distribution in the EFM15 for CLG, water, and HA separately at specific strains in each panel. The data show that the atomic constituents of HA and water, although present in lesser numbers than CLG atoms, are under higher stress values, thus suggesting that HA and water are actually supporting most of the load.

Figure 8(a) shows a per-atom distribution of the von Mises stress in the EFM45, in which most red regions also appear at the lateral edges of the simulation box. Notice, however, that the range of the stress color scale is nearly half of the EFM15 (Figure 7(a)). Moreover, highly stressed regions appear even at 0% strain. This is because particles are more tightly packed in the same initial volume, even before the tensile test, when HA is added. Here too, the nonorganic components, HA and water, exhibit much higher stress values.

As the mineralization level increases in the EFM60, the depicted stress scale decreases by roughly 30% from the previous case and the differences between the von Mises stress distribution among CLG (blue) and a combination of HA and water (red) become more pronounced (Figure 9(a)). The distribution of the von Mises stress per atom under different strains (Figure 9(b–d)) clearly indicates that the nonorganic moieties support most of the high-stress components, with HA (blue curves) playing a particularly relevant role providing the stiffness of EFMs, and possibly of bone, at the nanoscale.

*IFV × EFV.* Our EFMs have the unique feature of displaying HA atoms both in the IFV and EFV. Thus, it is also important to investigate the influence of the EFV atoms on their mechanical behavior. We start investigating the role played by HA molecules.

It should be stressed that the EFMs contain 80% of HA in the EFV, and 20% in the IFV. Thus, it might be expected that the HA atoms in the EFV will be a majority both for high and low stress values simply because HA atoms are more numerous in the EFV. However, since the IFV is a denser region we could also expect that the HA atoms in the IFV will exhibit higher stress values. The gap zones provide some space where HA molecules can be found, but there are very narrow regions for HA atoms in the overlap zone and generally among the CLG molecules, i.e., in the IFV.

Figure 10 shows normalized histograms containing the distribution of the von Mises stress on the HA atoms of the EFM15, EFM45, and EFM60. There are differences for the HA atoms in the IFV and in the EFV at different strain values. The results show that HA components in the EFV display, on average, higher stress values. The feature is more evident in more mineralized models. Our results show that HA components in the EFV, when compared to HA in the IFV, support most of the loads during the simulated uniaxial tensile tests.

When creating the models,<sup>42</sup> the water molecules were equally distributed throughout the simulation box, subjected only to avoiding steric repulsions. The mass fraction of water molecules in the whole simulation box was set without distinguishing IFV

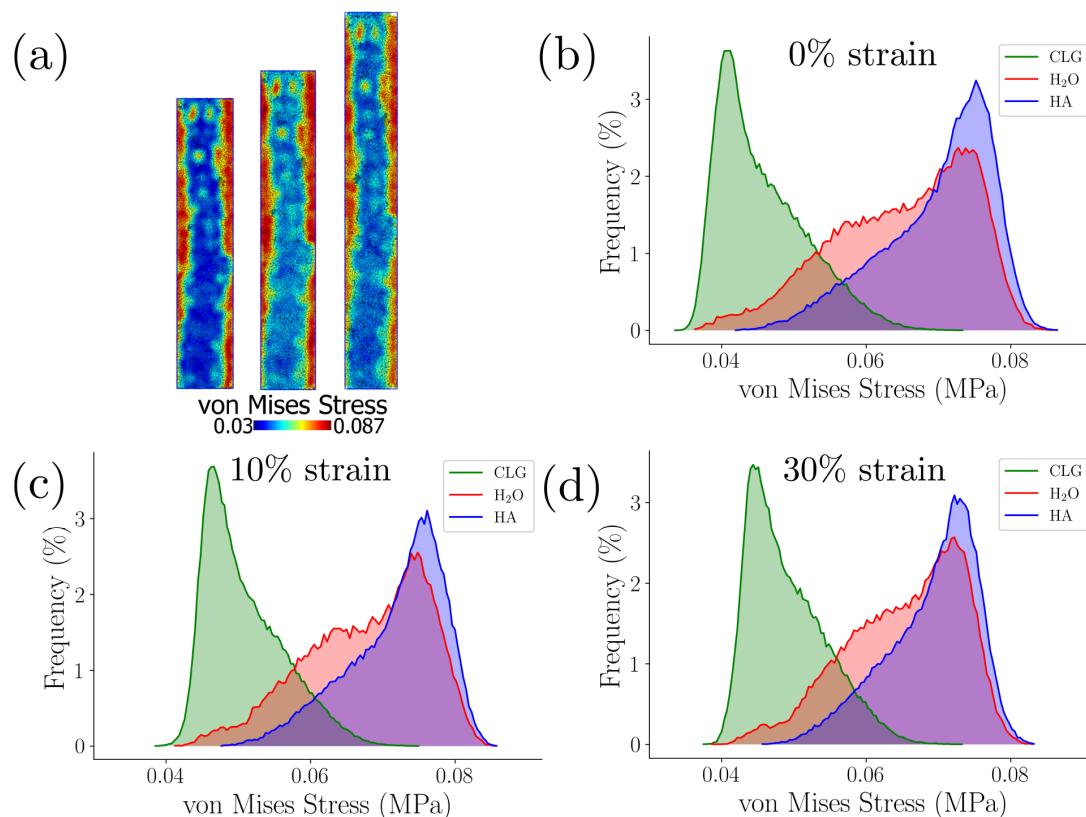


**Figure 9.** EFM60: (a) per-atom visualization of von Mises stress [MPa] at 0, 10, and 30% strain; (b) distribution of stress at 0% strain; (c) distribution of stress at 10% strain; (d) distribution of stress at 30% strain.

from EFV regions, unlike HA, for which 80% was bound to the EFV and 20% to the IFV.

Figure 11 presents the distribution of von Mises stress over water molecules in the IFV and EFV regions for three models, at low (15%), medium (45%), and high (60%) mineralization levels under different strain loads. Similar to the mineral moiety, water in the EFV region also appears to support higher stress loads than it does in the IFV. This behavior is shared by all models considered here.

## CONCLUSION

In this study, we investigated the structural properties and mechanical responses of atomistic bone models to applied tensile loads. Our EFMs encompass an EFV and exhibit mineral content in both the IFV and EFV regions, consistent with experiments and observations showing that most of the mineral content in the nanostructure of bones is actually in the EFV structure.<sup>14,15,23,26,44,45,49,50</sup>

In terms of structure, we found that HA components are hydrated and lose the initial crystal-like order with which they were placed into the simulation box during model construction. Moreover, water, present in limited quantities in the confining environment of the EFMs, strongly coordinates HA calcium and phosphate ions and loses the typical tetrahedral local order that characterizes the bulk liquid. The structural features of water (more similar to that of nonpolar liquids) are similar in the EFV and IFV (both in the gap and overlap regions).

The EFMs were subjected to tensile loads and their mechanical responses were analyzed. Our results show that at the molecular level high mineral content renders stiffer bones, which is well-known.<sup>38–40,48</sup> We found that the mineral tends to accumulate higher stress values, supporting most of the loads. Furthermore, an analysis of the stress distribution showed that the EFV plays a crucial role in the mechanical response of the EFMs. Both HA and water molecules accumulate higher stresses when located in the EFV. Our results are also consistent with recent studies from continuum level models showing that mineralization of the IFV provides only a modest contribution to bone stiffness,<sup>99</sup> and that the EFV plays a major role in the mechanical properties of bones.<sup>100</sup> The minerals located in the EFV dominate the load-bearing response in bones.

The EFV has been only recently incorporated in all-atom models.<sup>42</sup> Since it accommodates most of the mineral content and has shown to support higher loads in comparison to the IFV, further investigation of the EFV role in the mechanical behavior of bone could lead to a better understanding of bone diseases like osteoporosis. A discussion on the experimental deformation of mineral in the EFV is provided by Poundarik et al.<sup>27</sup> However, their main focus is the interaction between mineral and noncollagenous proteins in the EFV.

MD simulations of our EFMs account for essential elements of the biology and chemistry of bones from fundamental physical principles. Our study revealed the EFV as crucial when studying the mechanical properties of bone-related fibrils at the molecular level. Further development and investigations of such

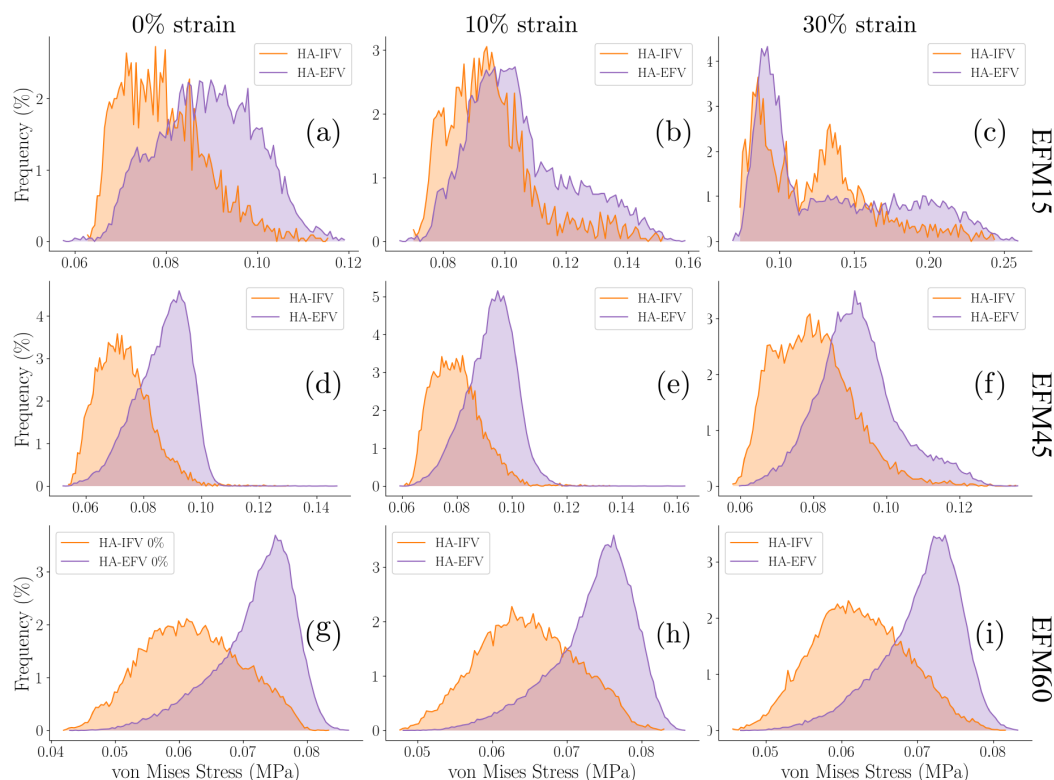


**Figure 10.** Normalized distribution of stress among the HA atoms in the IFV and EFV for EFM15, EFM45, and EFM60 at 0, 10, and 30% strain. Panels a–c correspond to EFM15, panels d–f to EFM45, and panels g–i to EFM60. Each column represents a strain value in an increasing order from left to right.

atomistic models can produce state-of-the-art knowledge on bone deformation and failure processes, enabling the improvement of predictive diagnosis techniques by meticulously addressing bone diseases and subsequent fractures. Further investigations comparing IFV and EFV, their mineralization, and additional refinements of the model can lead to a better understanding of the bone mechanical behavior and new insights regarding other properties. We conclude this article by mentioning some limitations of our models and highlighting key biological considerations that could improve bone molecular modeling and the estimation of its nanoscale properties:

- Defining IFV and EFV. The IFV, and consequently the EFV (= simulation box - IFV), are manually defined in our models as the volume mostly occupied by the CLG fibrils. There may be more accurate and automated ways to define the IFV and EFV. Studies comparing different shapes and sizes of IFV and EFV might lead to a new understanding of their influence on bone mechanics.
- Organic phase. The organic phase in bone is 90% constituted of type-I CLG and 10% of a combination of other CLG types (III and VI) plus noncollagenous proteins,<sup>7,12</sup> including specific proteins that hold bone minerals together.<sup>43</sup> We assumed the whole organic phase in our models to be composed of type I collagen. Consideration of other CLG types and noncollagenous proteins might provide new insights.<sup>101,102</sup> Furthermore, if considered in the model, noncollagenous proteins should be placed in the EFV.
- Inorganic phase. In the EFMs, we regard the inorganic phase as HA only. However, it has been shown that different kinds of minerals, including amorphous Ca phosphate, can be found in bones.<sup>13–17</sup> Including other types of inorganic minerals into the models require only moderate efforts, as discussed elsewhere.<sup>42</sup>
- Fiber's size. When creating the EFM, we assumed a  $2 \times 2$  reproduction of the CLG unit cell model as sufficient to mimic a fiber.<sup>42</sup> However, the EFM displays few CLG molecules ( $4 \times 5 = 20$ ) if compared to real fibers in bones. Models with more CLG molecules would also result in smaller Young's modulus values. Creating EFMs with more CLG molecules (fibers with a larger diameter) may not be that difficult, as we recently reported.<sup>42</sup> For instance, by keeping the same fractions of the constituents and increasing the number of CLG molecules from 20 ( $2 \times 2$  reproduction of CLG unit cell) to 125 ( $5 \times 5$  reproduction of CLG unit cell). However, it greatly increases the number of atoms and thus the simulation time.
- CLG cross-links. At the end of CLG molecules, intermolecular covalent cross-links are formed along the D-period.<sup>11,103</sup> Varying cross-link densities have been shown to alter the mechanical properties of CLG fibril structures.<sup>104</sup>
- Additional analysis. Further studies exploring the mechanical properties of such elaborate models under different loads (e.g., compression, bending, torsion,

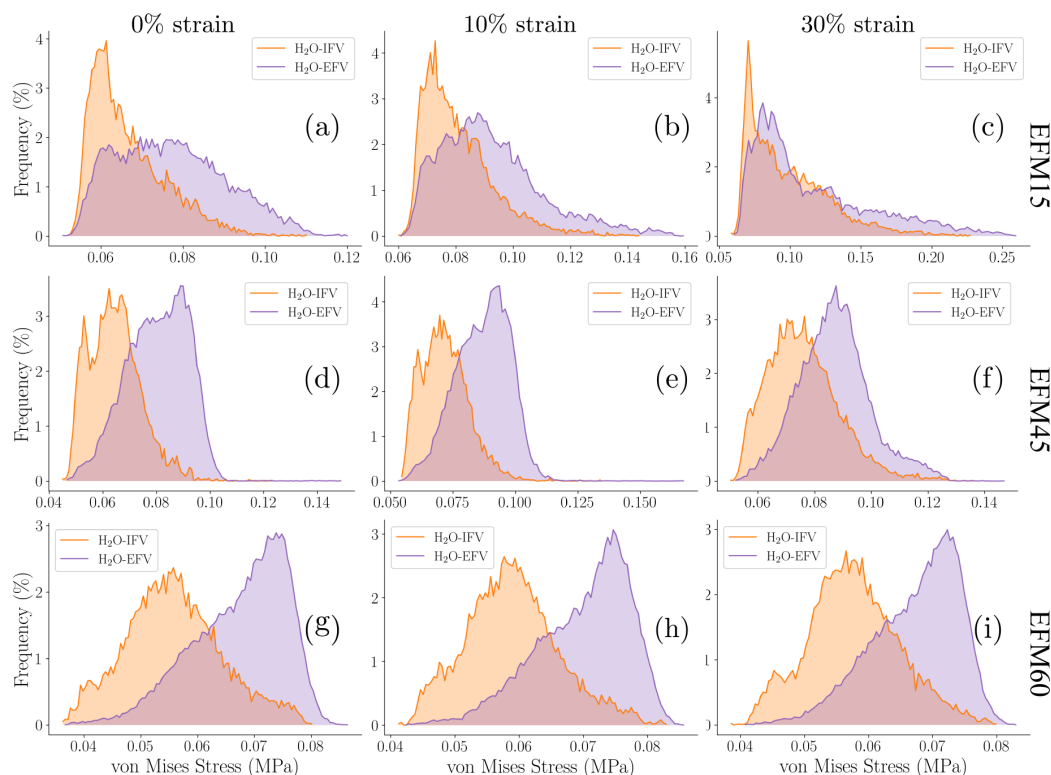


**Figure 11.** Normalized distribution of stress among the water atoms in the IFV and EFV for EFM15, EFM45, and EFM60 at 0, 10, and 30% strain. Panels a–c correspond to EFM15, panels d–f to EFM45, and panels g–i to EFM60. Each column represents a strain value in an increasing order from left to right.

shearing), computing the elements of the stiffness tensor, and estimating fracture parameters (e.g., using a reactive force field like Reaxff<sup>105,106</sup>) may help advance the state of the art of bone nanomechanics.

## ■ ASSOCIATED CONTENT

### Supporting Information

The Supporting Information is available free of charge at <https://pubs.acs.org/doi/10.1021/acsbomaterials.2c00728>.

Time evolution of RMSD, D-band length (simulation box length), molecular end-to-end distances, overlap region length, collagen widths, and pressure; figures showing the cross-sectional quasi-hexagonal packing of collagen molecules; radial density profiles of  $O_w$ , P, Ca, and  $CLG C_\alpha$  atoms with respect to the  $z$ -axis centered along the length of the EFM15, EFM45, and EFM60; radial pair distributions for water in EFM15, EFM45, and EFM70; RDF between HA components and HA–water pairs in the EFM15, EFM45, and EFM70; stress–strain curves and their respective linear regression; links to PDB and PSF files for EFM15, EFM45, and EFM70; LAMMPS files and scripts to transfer/convert EFM15, EFM45, and EFM70 PDB and PSF files (from NAMD/CHARMM) to LAMMPS, files and scripts to run short equilibration in LAMMPS, and files and scripts to run tensile tests in LAMMPS (PDF)

## ■ AUTHOR INFORMATION

### Corresponding Author

Munir S. Skaf – Institute of Chemistry, University of Campinas, Campinas 13083-970 SP, Brazil; Center for Computing in Engineering & Sciences, CCES, University of Campinas, Campinas 13083-861 SP, Brazil; [orcid.org/0000-0001-7485-1228](https://orcid.org/0000-0001-7485-1228); Email: [skaf@unicamp.br](mailto:skaf@unicamp.br)

### Authors

Amadeus C. S. de Alcântara – Department of Computational Mechanics, School of Mechanical Engineering, University of Campinas, Campinas 13083-860 SP, Brazil; Center for Computing in Engineering & Sciences, CCES, University of Campinas, Campinas 13083-861 SP, Brazil

Levi C. Felix – Department of Applied Physics, Gleb Wataghin Institute of Physics, University of Campinas, Campinas 13083-859 SP, Brazil; Center for Computing in Engineering & Sciences, CCES, University of Campinas, Campinas 13083-861 SP, Brazil; [orcid.org/0000-0001-5928-0885](https://orcid.org/0000-0001-5928-0885)

Douglas S. Galvão – Department of Applied Physics, Gleb Wataghin Institute of Physics, University of Campinas, Campinas 13083-859 SP, Brazil; Center for Computing in Engineering & Sciences, CCES, University of Campinas, Campinas 13083-861 SP, Brazil

Paulo Sollero – Department of Computational Mechanics, School of Mechanical Engineering, University of Campinas, Campinas 13083-860 SP, Brazil; Center for Computing in Engineering & Sciences, CCES, University of Campinas, Campinas 13083-861 SP, Brazil

Complete contact information is available at:  
<https://pubs.acs.org/10.1021/acsbomaterials.2c00728>

### Funding

This study was financed in part by the São Paulo Research Foundation (Fapesp) grants #2018/18503-2 and #2018/11352-9, the Center for Computing in Engineering & Sciences (CCES/UNICAMP) Fapesp grant #2013/08293-7, and the Coordenação de Aperfeiçoamento de Pessoal de Nível Superior – Brasil (CAPES). This work used resources of the “Centro Nacional de Processamento de Alto Desempenho em São Paulo” (CENAPAD-SP).

### Notes

The authors declare no competing financial interest.

### ACKNOWLEDGMENTS

The authors thank CENAPAD for their assistance with computer clusters, and the VMD/NAMD, LAMMPS, and MODELLER community for the valuable information and assistance provided both in their guides/manuals and through their respective mailing lists. The authors thank Fapesp for funding this work.

### REFERENCES

- (1) World Health Organization, World Health Organization, World health statistics 2016: monitoring health for the SDGs, sustainable development goals. 2016, Available online: [https://www.who.int/gho/publications/world\\_health\\_statistics/2016/en/](https://www.who.int/gho/publications/world_health_statistics/2016/en/) (last accessed on 02/12/2019).
- (2) United Nations World Population Ageing 2017 Highlights; Statistical Papers - United Nations (Ser. A), Population and Vital Statistics Report; United Nations: New York, 2018; pp 42.
- (3) Osterhoff, G.; Morgan, E. F.; Shefelbine, S. J.; Karim, L.; McNamara, L. M.; Augat, P. Bone mechanical properties and changes with osteoporosis. *Injury* **2016**, *47*, S11–S20.
- (4) Odén, A.; McCloskey, E.; Kanis, J.; Harvey, N. C.; Johansson, H. Burden of high fracture probability worldwide: secular increases 2010–2040. *Osteoporosis Int.* **2015**, *26*, 2243–2248.
- (5) Kling, J. M.; Clarke, B. L.; Sandhu, N. P. Osteoporosis Prevention, Screening, and Treatment: A Review. *J. Women's Health* **2014**, *23*, 563–572.
- (6) Holzer, L. A.; Leithner, A.; Holzer, G. The Most Cited Papers in Osteoporosis and Related Research. *J. Osteoporos.* **2015**, *2015*, 12.
- (7) Alcantara, A. C. S.; Assis, I.; Prada, D.; Mehle, K.; Schwan, S.; Costa-Paiva, L.; Skaf, M. S.; Wrobel, L. C.; Sollero, P. Patient-Specific Bone Multiscale Modelling, Fracture Simulation and Risk Analysis—A Survey. *Materials* **2020**, *13*, 106.
- (8) Chin-yun Shen, S.; Peña Fernández, M.; Tozzi, G.; Buehler, M. J. Deep learning approach to assess damage mechanics of bone tissue. *J. Mech Behav Biomed* **2021**, *123*, 104761.
- (9) Maghsoudi-Ganjeh, M.; Wang, X.; Zeng, X. Nanomechanics and Ultrastructure of Bone: A Review. *Cmes-Comp Model Eng.* **2020**, *125*, 1–32.
- (10) Sabet, F. A.; Raeisi Najafi, A.; Hamed, E.; Jasiuk, I. Modelling of bone fracture and strength at different length scales: a review. *Interface Focus.* **2016**, *6*, 20150055.
- (11) Sherman, V. R.; Yang, W.; Meyers, M. A. The materials science of collagen. *J. Mech Behav Biomed* **2015**, *52*, 22–50.
- (12) Keaveny, T. M.; Morgan, E. F.; Yeh, O. C. *Standard Handbook Of Biomedical Engineering And Design*; McGraw-Hill: New York, 2003; Chapter Bone Mechanics.
- (13) Kono, T.; Sakae, T.; Nakada, H.; Kaneda, T.; Okada, H. Confusion between Carbonate Apatite and Biological Apatite (Carbonated Hydroxyapatite) in Bone and Teeth. *Minerals* **2022**, *12*, 170.

- (14) Reznikov, N.; Bilton, M.; Lari, L.; Stevens, M. M.; Kröger, R. Fractal-like hierarchical organization of bone begins at the nanoscale. *Science* **2018**, *360*, eaao2189.
- (15) Schwarcz, H.; Binkley, D.; Luo, L.; Grandfield, K. A search for apatite crystals in the gap zone of collagen fibrils in bone using dark-field illumination. *Bone* **2020**, *135*, 115304.
- (16) Tertuliano, O. A.; Greer, J. R. The nanocomposite nature of bone drives its strength and damage resistance. *Nat. Mater.* **2016**, *15*, 1195–1202.
- (17) Chen, H.; et al. Surface Stability and Morphology of Calcium Phosphate Tuned by pH Values and Lactic Acid Additives: Theoretical and Experimental Study. *ACS Appl. Mater. Inter* **2022**, *14*, 4836–4851.
- (18) Vass, V.; Morin, C.; Scheiner, S.; Hellmich, C. In *Multiscale Mechanobiology of Bone Remodeling and Adaptation*; Pivonka, P., Ed.; Springer International Publishing: Cham, 2018; pp 175–229.
- (19) Shoulders, M. D.; Raines, R. T. Collagen Structure and Stability. *Annu. Rev. Biochem.* **2009**, *78*, 929–958.
- (20) Makareeva, E.; Leikin, S. In *Osteogenesis Imperfecta*; Shapiro, J. R., Byers, P. H., Glorieux, F. H., Sponseller, P. D., Eds.; Academic Press: San Diego, 2014; pp 71–84.
- (21) Bodian, D. L.; Radmer, R. J.; Holbert, S.; Klein, T. E. Molecular dynamics simulations of the full triple helical region of collagen type I provide an atomic scale view of the protein's regional heterogeneity. *Pac Symp. Biocomput* **2010**, 193–204.
- (22) Fratzl, P., Ed. *Collagen - Structure and Mechanics*; Springer: US, 2008.
- (23) Schwarcz, H. P.; Abueidda, D.; Jasiuk, I. The Ultrastructure of Bone and Its Relevance to Mechanical Properties. *Front Phys.* **2017**, *5*, 39.
- (24) Gong, J. K.; Arnold, J. S.; Cohn, S. H. Composition of trabecular and cortical bone. *Anat Rec* **1964**, *149*, 325–331.
- (25) Olszta, M. J.; Cheng, X.; Jee, S. S.; Kumar, R.; Kim, Y.-Y.; Kaufman, M. J.; Douglas, E. P.; Gower, L. B. Bone structure and formation: A new perspective. *Mater. Sci. Eng. R Rep* **2007**, *58*, 77–116.
- (26) Schwarcz, H. P. The ultrastructure of bone as revealed in electron microscopy of ion-milled sections. *Semin Cell Dev Biol.* **2015**, *46*, 44–50.
- (27) Poundarik, A. A.; Diab, T.; Sroga, G. E.; Ural, A.; Boskey, A. L.; Gundberg, C. M.; Vashishth, D. Dilatational band formation in bone. *Proc. Natl. Acad. Sci. U.S.A.* **2012**, *109*, 19178–19183.
- (28) Balk, E. M.; Adam, G. P.; Langberg, V. N.; Earley, A.; Clark, P.; Ebeling, P. R.; Mithal, A.; Rizzoli, R.; Zerbin, C. A. F.; Pierroz, D. D.; Dawson-Hughes, B. for the International Osteoporosis Foundation Calcium Steering Committee, Global dietary calcium intake among adults: a systematic review. *Osteoporosis Int.* **2017**, *28*, 3315–3324.
- (29) Castelo-Branco, C.; Hidalgo, M. J. C.; Palacios, S.; Ciria-Recasens, M.; Fernández-Pareja, A.; Carbonell-Abella, C.; Manasanch, J.; Haya-Palazuelos, J. Efficacy and safety of ossein-hydroxyapatite complex versus calcium carbonate to prevent bone loss. *Climacteric* **2020**, *23*, 252–258.
- (30) Compston, J.; Cooper, A.; Cooper, C.; Gittoes, N.; Gregson, C.; Harvey, N.; Hope, S.; Kanis, J. A.; McCloskey, E. V.; Poole, K. E. S.; Reid, D. M.; Selby, P.; Thompson, F.; Thurston, A.; Vine, N. UK clinical guideline for the prevention and treatment of osteoporosis. *Arch Osteoporos* **2017**, *12*, 43.
- (31) Eastell, R.; Rosen, C. J.; Black, D. M.; Cheung, A. M.; Murad, M. H.; Shoback, D. Pharmacological Management of Osteoporosis in Postmenopausal Women: An Endocrine Society\*Clinical Practice Guideline. *J. Clin Endocrinol Metab* **2019**, *104*, 1595–1622.
- (32) Berman, H. M.; Westbrook, J.; Feng, Z.; Gilliland, G.; Bhat, T. N.; Weissig, H.; Shindyalov, I. N.; Bourne, P. E. The Protein Data Bank. *Nucleic Acids Res.* **2000**, *28*, 235–242.
- (33) Orgel, J. P. R. O.; Irving, T. C.; Miller, A.; Wess, T. J. Microfibrillar structure of type I collagen in situ. *Proc. Natl. Acad. Sci. U.S.A.* **2006**, *103*, 9001–9005.
- (34) Gautieri, A.; Vesentini, S.; Redaelli, A.; Buehler, M. J. Hierarchical Structure and Nanomechanics of Collagen Microfibrils from the Atomistic Scale Up. *Nano Lett.* **2011**, *11*, 757–766.

- (35) Streeter, I.; de Leeuw, N. H. Atomistic Modeling of Collagen Proteins in Their Fibrillar Environment. *J. Phys. Chem. B* **2010**, *114*, 13263–13270.
- (36) Milazzo, M.; David, A.; Jung, G. S.; Danti, S.; Buehler, M. J. Molecular origin of viscoelasticity in mineralized collagen fibrils. *Biomater. Sci.* **2021**, *9*, 3390–3400.
- (37) Milazzo, M.; Jung, G. S.; Danti, S.; Buehler, M. J. Mechanics of Mineralized Collagen Fibrils upon Transient Loads. *ACS Nano* **2020**, *14*, 8307–8316.
- (38) Fielder, M.; Nair, A. K. A computational study of mechanical properties of collagen-based bio-composites. *Int. Biomech* **2020**, *7*, 76–87.
- (39) Fielder, M.; Nair, A. K. Effects of hydration and mineralization on the deformation mechanisms of collagen fibrils in bone at the nanoscale. *Biomech Model Mechanobiol* **2019**, *18*, 57–68.
- (40) Nair, A. K.; Gautieri, A.; Chang, S.-W.; Buehler, M. J. Molecular mechanics of mineralized collagen fibrils in bone. *Nat. Commun.* **2013**, *4*, 1724.
- (41) Nair, A. K.; Gautieri, A.; Buehler, M. J. Role of Intrafibrillar Collagen Mineralization in Defining the Compressive Properties of Nascent Bone. *Biomacromolecules* **2014**, *15*, 2494–2500.
- (42) Alcântara, A. C. S.; Felix, L. C.; Galvão, D. S.; Sollero, P.; Skaf, M. S. Devising Bone Molecular Models at the Nanoscale: From Usual Mineralized Collagen Fibrils to the First Bone Fibers Including Hydroxyapatite in the Extra-Fibrillar Volume. *Materials* **2022**, *15*, 2274.
- (43) Pang, S.; Schwarcz, H. P.; Jasiuk, I. Interfacial bonding between mineral platelets in bone and its effect on mechanical properties of bone. *J. Mech Behav Biomed* **2021**, *113*, 104132.
- (44) McNally, E. A.; Schwarcz, H. P.; Botton, G. A.; Arsenault, A. L. A Model for the Ultrastructure of Bone Based on Electron Microscopy of Ion-Milled Sections. *PLoS One* **2012**, *7*, 1–12.
- (45) Schwarcz, H. P.; McNally, E. A.; Botton, G. A. Dark-field transmission electron microscopy of cortical bone reveals details of extrafibrillar crystals. *J. Struct Biol.* **2014**, *188*, 240–248.
- (46) Alexander, B.; Daulton, T. L.; Genin, G. M.; Lipner, J.; Pasteris, J. D.; Wopenka, B.; Thomopoulos, S. The nanometre-scale physiology of bone: steric modelling and scanning transmission electron microscopy of collagen and mineral structure. *J. R Soc. Interface* **2012**, *9*, 1774–1786.
- (47) Liu, Y.; Thomopoulos, S.; Chen, C.; Birman, V.; Buehler, M. J.; Genin, G. M. Modelling the mechanics of partially mineralized collagen fibrils, fibres and tissue. *J. R Soc. Interface* **2014**, *11*, 20130835.
- (48) Prada, D. M.; Galvis, A. F.; Miller, J.; Foster, J. M.; Zavgaglia, C. Multiscale stiffness characterisation of both healthy and osteoporotic bone tissue using subject-specific data. *J. Mech Behav Biomed Mater.* **2022**, *135*, 105431.
- (49) McNally, E.; Nan, F.; Botton, G. A.; Schwarcz, H. P. Scanning transmission electron microscopic tomography of cortical bone using Z-contrast imaging. *Micron* **2013**, *49*, 46–53.
- (50) Lees, S. Considerations Regarding the Structure of the Mammalian Mineralized Osteoid from Viewpoint of the Generalized Packing Model. *Connect Tissue Res.* **1987**, *16*, 281–303.
- (51) von Mises, R. Mechanik der festen Körper im plastisch-deformablen Zustand. *Nachrichten von der Gesellschaft der Wissenschaften zu Göttingen, Mathematisch-Physikalische Klasse* **1913**, *1*, 582–592.
- (52) Clavier, G.; Desbiens, N.; Bourasseau, E.; Lachet, V.; Brusselle-Dupend, N.; Rousseau, B. Computation of elastic constants of solids using molecular simulation: comparison of constant volume and constant pressure ensemble methods. *Mol. Simul* **2017**, *43*, 1413–1422.
- (53) Zhou, M. A new look at the atomic level virial stress: on continuum-molecular system equivalence. *Proc. Math Phys. Eng. Sci.* **2003**, *459*, 2347–2392.
- (54) Subramanian, A. K.; Sun, C. Continuum interpretation of virial stress in molecular simulations. *Int. J. Solids Struct* **2008**, *45*, 4340–4346.
- (55) Tsai, D. H. The virial theorem and stress calculation in molecular dynamics. *J. Chem. Phys.* **1979**, *70*, 1375–1382.
- (56) Consortium, T. U. UniProt: the universal protein knowledgebase in 2021. *Nucleic Acids Res.* **2021**, *49*, D480–D489.
- (57) Streeter, I.; de Leeuw, N. H. A molecular dynamics study of the interprotein interactions in collagen fibrils. *Soft Matter* **2011**, *7*, 3373–3382.
- (58) Collier, T. A.; Nash, A.; Birch, H. L.; de Leeuw, N. H. Relative orientation of collagen molecules within a fibril: a homology model for homo sapiens type I collagen. *J. Biomol Struct Dyn* **2019**, *37*, S37–S49.
- (59) Zhou, Z.; Minary-Jolandan, M.; Qian, D. A simulation study on the significant nanomechanical heterogeneous properties of collagen. *Biomech Model Mechanobiol* **2015**, *14*, 445–457.
- (60) Zhou, Z.; Qian, D.; Minary-Jolandan, M. Molecular Mechanism of Polarization and Piezoelectric Effect in Super-Twisted Collagen. *ACS Biomater Sci. Eng.* **2016**, *2*, 929–936.
- (61) Martínez, L.; Andrade, R.; Birgin, E. G.; Martínez, J. M. PACKMOL: A package for building initial configurations for molecular dynamics simulations. *J. Comput. Chem.* **2009**, *30*, 2157–2164.
- (62) Humphrey, W.; Dalke, A.; Schulten, K. VMD - Visual Molecular Dynamics. *J. Mol. Graph* **1996**, *14*, 33–38.
- (63) Stone, J. An Efficient Library for Parallel Ray Tracing and Animation. M.Sc. Thesis, Computer Science Department, University of Missouri-Rolla, 1998.
- (64) Stukowski, A. Visualization and analysis of atomistic simulation data with OVITO-the Open Visualization Tool. *Model Simul Mater. Sci. Eng.* **2010**, *18*, 015012.
- (65) Phillips, J. C.; et al. Scalable molecular dynamics on CPU and GPU architectures with NAMD. *J. Chem. Phys.* **2020**, *153*, 044130.
- (66) MacKerell, A. D.; et al. All-Atom Empirical Potential for Molecular Modeling and Dynamics Studies of Proteins. *J. Phys. Chem. B* **1998**, *102*, 3586–3616.
- (67) MacKerell, A. D.; Feig, M.; Brooks, C. L. Improved Treatment of the Protein Backbone in Empirical Force Fields. *J. Am. Chem. Soc.* **2004**, *126*, 698–699.
- (68) Best, R. B.; Zhu, X.; Shim, J.; Lopes, P. E. M.; Mittal, J.; Feig, M.; MacKerell, A. D. Optimization of the Additive CHARMM All-Atom Protein Force Field Targeting Improved Sampling of the Backbone  $\phi$ ,  $\psi$  and Side-Chain  $\chi_1$  and  $\chi_2$  Dihedral Angles. *J. Chem. Theory Comput* **2012**, *8*, 3257–3273.
- (69) Huang, J.; Rauscher, S.; Nawrocki, G.; Ran, T.; Feig, M.; de Groot, B. L.; Grubmüller, H.; MacKerell, A. D. CHARMM36m: an improved force field for folded and intrinsically disordered proteins. *Nat. Methods* **2017**, *14*, 71–73.
- (70) Heinz, H.; Lin, T.-J.; Kishore Mishra, R.; Emami, F. S. Thermodynamically Consistent Force Fields for the Assembly of Inorganic, Organic, and Biological Nanostructures: The INTERFACE Force Field. *Langmuir* **2013**, *29*, 1754–1765.
- (71) Lin, T.-J.; Heinz, H. Accurate Force Field Parameters and pH Resolved Surface Models for Hydroxyapatite to Understand Structure, Mechanics, Hydration, and Biological Interfaces. *J. Phys. Chem. C* **2016**, *120*, 4975–4992.
- (72) Darden, T.; York, D.; Pedersen, L. Particle mesh Ewald: An  $N \log(N)$  method for Ewald sums in large systems. *J. Chem. Phys.* **1993**, *98*, 10089–10092.
- (73) Thompson, A. P.; Aktulga, H. M.; Berger, R.; Bolintineanu, D. S.; Brown, W. M.; Crozier, P. S.; in 't Veld, P. J.; Kohlmeyer, A.; Moore, S. G.; Nguyen, T. D.; Shan, R.; Stevens, M. J.; Tranchida, J.; Trott, C.; Plimpton, S. J. LAMMPS - a flexible simulation tool for particle-based materials modeling at the atomic, meso, and continuum scales. *Comput. Phys. Commun.* **2022**, *271*, 108171.
- (74) Thompson, A. P.; Aktulga, H. M.; Berger, R.; Bolintineanu, D. S.; Brown, W. M.; Crozier, P. S.; in 't Veld, P. J.; Kohlmeyer, A.; Moore, S. G.; Nguyen, T. D.; Shan, R.; Stevens, M. J.; Tranchida, J.; Trott, C.; Plimpton, S. J. LAMMPS - a flexible simulation tool for particle-based materials modeling at the atomic, meso, and continuum scales. *Comput. Phys. Commun.* **2022**, *271*, 108171.
- (75) Varma, S.; Botlani, M.; Hammond, J. R.; Scott, H. L.; Orgel, J. P. R. O.; Schieber, J. D. Effect of intrinsic and extrinsic factors on the simulated D-band length of type I collagen. *Proteins* **2015**, *83*, 1800–1812.

- (76) Zhou, Z.; Qian, D.; Minary-Jolandan, M. Clustering of hydroxyapatite on a super-twisted collagen microfibril under mechanical tension. *J. Mater. Chem. B* **2017**, *5*, 2235–2244.
- (77) Plimpton, S. Fast Parallel Algorithms for Short-Range Molecular Dynamics. *J. Comput. Phys.* **1995**, *117*, 1–19.
- (78) Brown, W. M.; Wang, P.; Plimpton, S. J.; Tharrington, A. N. Implementing Molecular Dynamics on Hybrid High Performance Computers - Short Range Forces. *Comput. Phys. Commun.* **2011**, *182*, 898–911.
- (79) Brown, W. M.; Kohlmeyer, A.; Plimpton, S. J.; Tharrington, A. N. Implementing Molecular Dynamics on Hybrid High Performance Computers - Particle-Particle Particle-Mesh. *Comput. Phys. Commun.* **2012**, *183*, 449–459.
- (80) Brown, W. M.; Yamada, M. Implementing Molecular Dynamics on Hybrid High Performance Computers - Three-Body Potentials. *Comput. Phys. Commun.* **2013**, *184*, 2785–2793.
- (81) Nguyen, T. D.; Plimpton, S. J. Accelerating dissipative particle dynamics simulations for soft matter systems. *Comput. Mater. Sci.* **2015**, *100*, 173–180.
- (82) Nguyen, T. D. GPU-accelerated Tersoff potentials for massively parallel Molecular Dynamics simulations. *Comput. Phys. Commun.* **2017**, *212*, 113–122.
- (83) Nikolskiy, V.; Stegailov, V. GPU acceleration of four-site water models in LAMMPS. *Parallel Comput.: Technol. Trends* **2020**, 565.
- (84) *Matlab*, ver. 9.6.0.1072779 (R2019b); The MathWorks Inc.: Natick, MA, 2019.
- (85) Schneider, T.; Stoll, E. Molecular-dynamics study of a three-dimensional one-component model for distortive phase transitions. *Phys. Rev. B* **1978**, *17*, 1302–1322.
- (86) Shinoda, W.; Shiga, M.; Mikami, M. Rapid estimation of elastic constants by molecular dynamics simulation under constant stress. *Phys. Rev. B* **2004**, *69*, 134103.
- (87) Tuckerman, M. E.; Alejandre, J.; López-Rendón, R.; Jochim, A. L.; Martyna, G. J. A Liouville-operator derived measure-preserving integrator for molecular dynamics simulations in the isothermal–isobaric ensemble. *J. Phys. A Math Gen* **2006**, *39*, S629–S651.
- (88) Martyna, G. J.; Tobias, D. J.; Klein, M. L. Constant pressure molecular dynamics algorithms. *J. Chem. Phys.* **1994**, *101*, 4177–4189.
- (89) Parrinello, M.; Rahman, A. Polymorphic transitions in single crystals: A new molecular dynamics method. *J. Appl. Phys.* **1981**, *52*, 7182–7190.
- (90) Varma, S.; Orgel, J.; Schieber, J. Nanomechanics of Type I Collagen. *Biophys. J.* **2016**, *111*, 50–56.
- (91) Korenczuk, C. E.; Votava, L. E.; Dhume, R. Y.; Kizilski, S. B.; Brown, G. E.; Narain, R.; Barocas, V. H. Isotropic Failure Criteria Are Not Appropriate for Anisotropic Fibrous Biological Tissues. *J. Biomech Eng.* **2017**, *139*, 071008.
- (92) Ladanyi, B. M.; Skaf, M. S. Computer Simulation of Hydrogen-Bonding Liquids. *Annu. Rev. Phys. Chem.* **1993**, *44*, 335–368.
- (93) Clark, G. N.; Cappa, C. D.; Smith, J. D.; Saykally, R. J.; Head-Gordon, T. The structure of ambient water. *Mol. Phys.* **2010**, *108*, 1415–1433.
- (94) Collins, C. J.; Andriotis, O. G.; Nedelkovski, V.; Frank, M.; Katsamenis, O. L.; Thurner, P. *J. In Encyclopedia of Biomedical Engineering*; Narayan, R., Ed.; Elsevier: Oxford, 2019; pp 22–44.
- (95) Andriotis, O. G.; Desissaire, S.; Thurner, P. J. Collagen Fibrils: Nature's Highly Tunable Nonlinear Springs. *ACS Nano* **2018**, *12*, 3671–3680.
- (96) Currey, J. D. *Bones: Structure and Mechanics*; Princeton University Press, 2002; pp 54–123.
- (97) Reilly, D. T.; Burstein, A. H. The elastic and ultimate properties of compact bone tissue. *J. Biomech* **1975**, *8*, 393–405.
- (98) Hang, F.; Barber, A. H. Nano-mechanical properties of individual mineralized collagen fibrils from bone tissue. *J. R. Soc. Interface* **2011**, *8*, 500–505.
- (99) Alijani, H.; Vaughan, T. J. A multiscale finite element investigation on the role of intra- and extra-fibrillar mineralisation on the elastic properties of bone tissue. *J. Mech Behav Biomed* **2022**, *129*, 105139.

- (100) Lin, L.; Samuel, J.; Zeng, X.; Wang, X. Contribution of extrafibrillar matrix to the mechanical behavior of bone using a novel cohesive finite element model. *J. Mech Behav Biomed Mater.* **2017**, *65*, 224–235.
- (101) Sroga, G. E.; Vashishth, D. Effects of Bone Matrix Proteins on Fracture and Fragility in Osteoporosis. *Curr. Osteoporos Rep* **2012**, *10*, 141–150.
- (102) Wang, Y.; Morsali, R.; Dai, Z.; Minary-Jolandan, M.; Qian, D. Computational Nanomechanics of Noncollagenous Interfibrillar Interface in Bone. *ACS Appl. Mater. Inter* **2020**, *12*, 25363–25373.
- (103) Domene, C.; Jorgensen, C.; Abbasi, S. W. A perspective on structural and computational work on collagen. *Phys. Chem. Chem. Phys.* **2016**, *18*, 24802–24811.
- (104) Buehler, M. J. Nanomechanics of collagen fibrils under varying cross-link densities: Atomistic and continuum studies. *J. Mech Behav Biomed* **2008**, *1*, 59–67.
- (105) van Duin, A. C. T.; Dasgupta, S.; Lorant, F.; Goddard, W. A. ReaxFF: A Reactive Force Field for Hydrocarbons. *J. Phys. Chem. B* **2001**, *105*, 9396–9409.
- (106) Chenoweth, K.; van Duin, A. C. T.; Goddard, W. A. ReaxFF Reactive Force Field for Molecular Dynamics Simulations of Hydrocarbon Oxidation. *J. Phys. Chem. A* **2008**, *112*, 1040–1053.

## Recommended by ACS

### Introduction: Self-Healing in Chemical Systems

Vassiliki-Alexandra Glezakou, Tong Lin, *et al.*

JANUARY 25, 2023  
CHEMICAL REVIEWS

READ 

### 3D Printing of a Biocompatible Nanoink Derived from Waste Animal Bones

Manojit Das, Chandra Sekhar Tiwary, *et al.*

MARCH 22, 2023  
ACS APPLIED BIO MATERIALS

READ 

### Unraveling Water-Mediated <sup>31</sup>P Relaxation in Bone Mineral

Navneet Dwivedi, Neeraj Sinha, *et al.*

MAY 02, 2022  
ACS OMEGA

READ 

### Insight on the Role of Poly(acrylic acid) for Directing Calcium Phosphate Mineralization of Synthetic Polymer Bone Scaffolds

Sarah E. Gleeson, Christopher Y. Li, *et al.*

AUGUST 31, 2022  
ACS APPLIED BIO MATERIALS

READ 

Get More Suggestions >

## 5 A ROAD MAP FOR FUTURE RESEARCH ON BONE MULTI-SCALE MODELING

As mentioned in Chapter 2, our literature survey hints at a framework for devising realistic patient-specific bone fracture simulations. It is presented in Section 5.1 as an approach to the early diagnosis and prediction of fracture in bones. The details and the clear directions provided by this approach serve as a road map for future research on the field, contributing to (2.).

The complexity of its implementation demands huge collaborative research and enough time to test and validate each step. Thus, its implementation is out of the scope of this thesis. The investigations of the mechanical properties of bones at the nanoscale presented in Chapters 3 and 4 relate to Step VI, a crucial step of this approach. Together with the nano-micro and micro-nano transitions, they are likely the most challenging steps. Further development and implementation of this approach constitutes one of my future endeavors and research goals.

### 5.1 An Approach to the early Diagnosis and Prediction of Fracture in Bones

The approach can be divided into **9** steps:

- I. From Computed Tomography (CT) data, define a continuum homogeneous **macro** domain at the most fracture-susceptible **macroscale** sub-region of cortical bone, defining the **macroscale**. Impose, at the **macro** domain contour, Boundary Conditions (BCs) representative of common physical trauma among the elderly.
- II. Using the Boundary Element Method (BEM), compute displacement and traction fields at predefined points within the most fracture-susceptible **macroscale** sub-region of cortical bone at the **macroscale**.
- III. To each predefined point at the **macroscale**, an associated continuum non-homogeneous cube-shaped **micro** domain is defined. The union set of all **micro** domains defines the **microscale**. The side of each **micro** domain cube is, in length, orders of magnitude greater than the average osteon diameter.
- IV. The **micro** domain BCs are modeled as a function of the **macroscale** displacement and traction fields.

- V. The bone failure/cracking process is initiated at the most fracture-susceptible **macroscale** sub-region of cortical bone by imposing the **micro** domain BCs to the **micro** domains. A Cohesive Zone Model (CZM), described by a Traction-Separation Law (TSL), governs the crack propagation in the cohesive failure zone, which sits along the path of minimal energy release rate.
- VI. The TSL, introduced at Step V, is computed by numerical experiments at the **molecular scale** using an MD approach. MD simulation is conducted using the LAMMPS software package. Inter- and intramolecular potentials of hydroxyapatite (HA), collagen (CLG) and water, the basic constituents of bone tissue, are selected according to their adequacy in modeling bone mechanical behavior. A sequence of MD simulations provides the TSL (Guin *et al.*, 2016).
- VII. Back to the **microscale**, a space-time average of the TSL provided at Step VI gives the crack propagation parameters of each isolated **microfracture** at the current time step.
- VIII. As the simulation time progresses, all the **microfractures** coalesce into a disruption of the the continuum at the **macroscale**; this disruption is the **macrofracture**.
- IX. A correlation between simulation results and fracture predictive diagnosis is established towards the construction of an osteoporitic bone fracture diagnosis methodology that includes patient-specific quantitative information based on multiscale fracture mechanics.

Algorithm 1 shows the sequence of our approach's methodology.

---

#### Algorithm 1 Methodology Flow

---

```

1: for (healthy hip bone tissue) and (osteoporotic hip bone tissue) do
2:   Step I  $\longrightarrow$  Step III  $\longrightarrow$  Step II  $\longrightarrow$  Step IV;
3:   for each molecular scale time step do
4:     (Step VI  $\rightarrow$  Step V)  $\longrightarrow$  (Step VII  $\rightarrow$  Step V);
5:   end for
6:   for each macroscale time step do
7:     Step VII  $\longrightarrow$  Step VIII;
8:   end for
9: end for
10: do Step IX

```

---

Each step of the present methodology is described in further details below.

#### 5.1.1 Step I – Defining macro domain geometry and mechanical properties from medical imaging and imposing realistic BCs

As shown in Algorithm 1, the first Steps are performed once for a healthy hip bone and a second time for an osteoporotic hip bone, since hip fractures are the most com-

mon osteoporotic-induced fractures among the elderly (Morales-Torres; Gutiérrez-Ureña, 2004; Marinho *et al.*, 2014; Lewiecki *et al.*, 2018; Ritchie; Hansma, 2009). At the macroscale, hip bone tissue is either cortical or trabecular, see Chapter 2. Trabecular bone consists of a porous network of rod-like trabeculae filled with bone marrow and fills the inside of many bones. Cortical bone, the most dense bone tissue, forms most of the outer shell of the bone. We focus on the fracture analysis of cortical bone for mainly two reasons: **(1.)** The osteon, a primary component of cortical bone at the microscale, is the main structural feature that controls toughness (measure of energy absorption capacity up to failure (F. A. Sabet, A. R. Najafi, E. Hamed and I. Jasiuk, 2016)) in bone (Ritchie; Hansma, 2009); **(2.)** The cortical bone has a greater contribution to bone strength (resistance to failure (F. A. Sabet, A. R. Najafi, E. Hamed and I. Jasiuk, 2016)) (Holzer *et al.*, 2009). Furthermore, cortical bone is more brittle. For these reasons, it is assumed that cortical bone failure implies general bone failure.

To devise macroscopic computational bone geometry models, medical imaging data is required. Computed Tomography (CT) is argued to be the most accurate medical imaging techniques capable of reconstructing 3D-geometry bone models. It is a non destructive technique capable of providing bone geometry and material properties (Alcântara *et al.*, 2020). CT data is stored in *DICOM* (Digital Imaging and Communications in Medicine) (*DICOM...*, 2015) files, which contain information on the patient (*e.g.*, age, sex, health condition) in addition to sets of CT images.

Completion of the following steps **(A.)**  $\rightarrow$  **(E.)** constitute bone 3D geometry modeling, discretization and attribution of material properties:

**(A.)** From *DICOM* files, obtain an *.STL* (STereoLithography) file, describing only the surface geometry of the 3D object (*ie.*, the hip bone), by using either the InVesalius (Amorim *et al.*, 2015) or a similar software packages.

**(B.)** Using a CAD software, the *.STL* file is converted into a *.STEP* (STandard for the Exchange of Product model data) file, which provides a readily-modifiable 3D solid model of the hip bone.

**(C.)** A 3D mesh with  $n$  nodes and  $e$  elements is created in an appropriated mesh edition environment using the *.STEP* file. The mesh is described by a node matrix, which contains the coordinates of each  $n$ -th node, and an incidence matrix, which relates  $n$  nodes to  $e$  elements.

**(D.)** Material properties (*e.g.*, Young's Modulus  $E$ , density  $\rho$ ) are assigned to each

mesh-element using a material mapping routine (Alcantara, 2017; Zannoni *et al.*, 1999; Taddei *et al.*, 2004; Taddei *et al.*, 2007).

(E.) Boundary conditions representative of common physical trauma among the elderly are imposed at the hip bone contour (*e.g.*, a zero displacement condition at the contact zone between the hip bone and the *sacrum* and the application of a load, representative of the human gait, at the contact zone between the hip bone and the femoral head).

**Step I needs:** CT data (*DICOM* files).

**Step I provides:** Spatial **macro** domain geometry, material properties, boundary conditions and mesh-nodes coordinates.

### 5.1.2 Step II – Macroscale: Computing the traction and displacement fields

The Boundary Element Method has been extensively applied to simulate crack initiation and dynamic propagation (Gamez *et al.*, 2010; Aliabadi, 1997; Cruse, 2012; Liu *et al.*, 2017). The BEM is particularly recommended for fracture mechanics problems due to the following features: (1.) The BEM provides accurate solutions to problems featuring stress concentration and fracture (major phenomenons in bone cracking) (Brebbia; Dominguez, 1994; Brebbia, 1982); (2.) The BEM only requires discretization of the boundary domain rather than of the whole domain as required by the most famous Finite Element Method (FEM) (Brebbia; Dominguez, 1994). Thus, the BEM formulation requires less degrees of freedom than the FEM formulation; this reduction highly increases the feasibility of the computationally-expensive multiscale modeling procedure (Sfantos; Aliabadi, 2007a); (3.) Applying the BEM readily provides the domain boundary displacement and traction fields (Aliabadi, 2002). These traction and displacement fields are used by the Cohezive Zone Model (CZM) (at Step V) to provide the local crack opening displacement at the crack dynamic propagation simulation initial time step.

Despite the above-mentioned features, few works using the BEM are available, when compared to the number of works using the Finite Element Method (FEM). Exploration of the three above-mentioned features in simulating bone crack initiation and propagation constitute an open field of research. Recently, former lab colleagues (Galvis *et al.*, 2021; Prada *et al.*, 2018; Prada *et al.*, 2022) presented a methodology based on homogenisation for predicting the anisotropic stiffness tensor of bone given the porosity and mineral fraction. They used the BEM to model micro- and macroscales and transition between them in a upscaling manner. This is an analogous way, but yet different, to perform steps I, II, IV, and VII.

The mathematical models presented by (Taesun You, Yong-Rak Kim and Taehyo Park, 2016; Liu *et al.*, 2017; Benedetti; Aliabadi, 2015; Gamez *et al.*, 2010; Aliabadi, 1997) consider that general fracture, of which bone fracture is a particular case, under impact loading occurs at static equilibrium. Therefore, crack initiation and propagation is assumed to occur under static equilibrium; it is also assumed that an eventual accelerated rigid body bone motion conveys no relevant contribution to bone fracture. High damping in bone tissue is a cause of static equilibrium consideration.

Equação 5.1 represents the static equilibrium condition, with acceleration term equal to zero, for any linear elastic continuum spatial domain:

$$\frac{\partial T_{kj}(x_1, x_2, x_3)}{\partial x_j} + b_k(x_1, x_2, x_3) = 0 \in \Omega \text{ with } j = 1, 2, 3 \text{ and } k = 1, 2, 3 \quad (5.1)$$

where  $T_{kj} [N/m^2]$  is an element of the Cauchy stress tensor  $\mathbf{T} \in \mathbb{R}^{3 \times 3}$ ,  $b_k [N/m^3]$  is an element of the body force vector  $\mathbf{b} \in \mathbb{R}^3$  and  $x_j [m]$  is the  $j$ -th spatial coordinate (Lai *et al.*, 2010). Applying the weighted residuals method and integrating Equação 5.1 by parts, one arrives at the elastostatics governing integral equation (Brebbia; Dominguez, 1994; Kane, 1994) known as Somigliana's Identity, with  $\mathbf{x} = [x_1 \ x_2 \ x_3]^\top$ ,  $\mathbf{d}_i = [d_1^i \ d_2^i \ d_3^i]^\top$ ,  $l = 1, 2, 3$  and  $i = 1, 2, \dots, n$ :

$$c_{lk}(\mathbf{d}_i)u_l(\mathbf{d}_i) = \int_{\Gamma} t_k(\mathbf{x})u_{lk}^*(\mathbf{x}, \mathbf{d}_i)d\Gamma - \int_{\Gamma} u_k(\mathbf{x})t_{lk}^*(\mathbf{x}, \mathbf{d}_i)d\Gamma + \int_{\Omega} u_{lk}^*(\mathbf{x}, \mathbf{d}_i)b_k(\mathbf{x})d\Omega \quad (5.2)$$

Equação 5.2 provides  $u_l(\mathbf{d}_i)$ , which is the  $l$ -th component of the displacement vector  $\mathbf{u}(\mathbf{d}_i)$  at the  $i$ -th point  $\mathbf{d}$  of application of the load, in terms of the boundary  $\Gamma$  values of displacement  $u_k(\mathbf{x})$  and traction  $t_k(\mathbf{x})$  ( $t_k(\mathbf{x}) = T_{kj}(\mathbf{x})n_j$ );  $c_{lk}(\mathbf{d}_i)$  depends on the position of the  $i$ -th source-point  $\mathbf{d}$  (also referred to as load-point);  $b_k(\mathbf{x})$  represents the body forces throughout the spatial domain  $\Omega$ ;  $u_{lk}^*(\mathbf{x}, \mathbf{d}_i)$  and  $t_{lk}^*(\mathbf{x}, \mathbf{d}_i)$  represent the known fundamental solutions, which are the  $k$ -th vector components of displacement and tractions due to a unit-valued point load in the  $l$  direction. The 3D elastostatic fundamental solution for anisotropic media based on double Fourier series proposed by (Tan *et al.*, 2013) and used by (Galvis *et al.*, 2018b) is applied. To minimize computational costs,  $n$  is chosen as a prescribed number of points in the most fracture-susceptible macroscale sub-region of cortical bone. This sub-region is referred to as the Region Of Interest (ROI). The set of  $n$  points is partitioned into subsets of 8 node-points. Each node-point represents the vertex of a cube-shaped microscale domain (see Step III).

The traction field is obtained from Hooke's Law:  $T_{kj} = C_{kjlm}\epsilon_{lm}$  where  $C_{kjlm} \in \mathbb{R}^{3 \times 3 \times 3 \times 3}$  is the stiffness tensor;  $\epsilon_{lm}$  is a component of the strain tensor

$$\epsilon_{3 \times 3} = \frac{1}{2} \left( [\nabla \mathbf{u}(\mathbf{d}_i)]_{3 \times 3} + [\nabla \mathbf{u}(\mathbf{d}_i)]_{3 \times 3}^T \right) \text{ and } m = 1, 2, 3.$$

A BEM-based code for computing the three-dimensional traction-displacement fields has already been implemented in Fortran 90 using the GNU compiler *gfortran* and validated by Sollero's group (Galvis *et al.*, 2018b; Galvis *et al.*, 2018a; Galvis *et al.*, 2021; Prada *et al.*, 2022). Displacement and traction values of prescribed points among the  $n$  mesh-nodes of Step I (C.) is computed.

**Step II needs:** Spatial **macro** domain (ROI) geometry, material properties, boundary conditions and mesh-nodes coordinates.

**Step II provides:** Displacement and traction values of prescribed points throughout the spatial **macro** domain (ROI) geometry.

### 5.1.3 Step III – Transitioning from the macro- to the microscale

The proposed multiscale-bone-fracture model comprises the macro (whole bone), micro (osteon level) and the atomistic (atoms arranged in molecules) length scales of bone tissue. Between atomic and micro levels bone basically consists of fiber structures. A group of mineralized collagen fibrils builds a fiber. A group of layers, each layer containing an arrangement of unidirectional fibers, is called *lamellae*. Different assemblies of *lamellae* give origin to two different types of bone: cortical and trabecular. The molecular scale simulation domain is large enough to comprise mineralized collagen fibrils. It is assumed that the mere layering of several mineralized collagen fibrils does not change the TSL that governs microscale crack propagation.

As argued in Step I only cortical bone is modeled at the microscale. The majority of computational micro cortical bone geometry models in the literature (F. A. Sabet, A. R. Najafi, E. Hamed and I. Jasiuk, 2016; Taesun You, Yong-Rak Kim and Taehyo Park, 2016; Gamez *et al.*, 2010) consist on drawing contours over images of osteons immersed in interstitial *lamellae*; these images are either acquired from dead tissue microscopy or randomly created microscale geometry and properties. A novel way of creating cortical bone microscale models is proposed: The  $\mu$ CT-based discretization of cortical bone.

Identification of the cortical bone zone is made by selecting the mesh-elements (created at Step 1, sub-step (C.)) which are located at the close-to-the-bone-external-boundary region. As argued in Step II, the BEM is only applied to the  $n$  points in the most fracture-susceptible macroscale sub-region of cortical bone, which is the Region of Interest. The ROI

features the smallest spatially-local average of Hounsfield Unit (HU) values (numerical values proportional to elastic and mass density properties (Alcantara, 2017; Alcântara *et al.*, 2020), see Step I).

The osteon, a primary component of cortical bone at the microscale, ranges between 100-300 $\mu\text{m}$  in diameter. Standard CT resolution is approximately 500 $\mu\text{m}$  and thus not refined enough to provide bone microscale geometry. Human bone microscale geometry can be imaged using  $\mu\text{CT}$  (Landis; Keane, 2010), which is presently limited to peripheral skeletal regions (wrist and tibia (Burghardt *et al.*, 2011)), at a resolution of 82  $\mu\text{m}$ . In order to create a multiscale patient-specific computer geometry model combining the advantages of CT and  $\mu\text{CT}$ , the bone macroscale geometry and BCs must be taken from CT-data (see Step I) and the bone microscale geometry and material properties are taken from  $\mu\text{CT}$ -data.

Consider, for the sake of argument, that each mesh-element (see Step 1, sub-step (C.)) is created with volume  $\sim 10$  times smaller than the average volume of an osteon. Since conventional CT spatial resolution does not comprise osteon-length-scale geometry and properties, creating osteon subdivisions from CT is unfruitful overmeshing. The coupling between CT- and  $\mu\text{CT}$ -information allows the construction of a macroscale bone geometry model enhanced by *in vivo* osteon-length-scale material properties. All cortical bone tissue is constituted of osteons immersed in interstitial *lamellae*. Thus, it is assumed that the microscale geometry of two cortical bone samples is the same independently of skeletal site, if these two sites feature the same spatially-local average of the HU numerical values.

Assuming CT resolution 500 $\mu\text{m}$ ,  $\mu\text{CT}$  resolution 100 $\mu\text{m}$  and osteon diameter 200 $\mu\text{m}$ , the CT- $\mu\text{CT}$ -model-coupling consists in executing the following steps: **(1.)** The hip-bone-CT-model is discretized into cube-shaped elements (of edge length  $\sim 600\mu\text{m}$ ) containing  $\approx 9$  osteons. These cube-shaped elements are the *Representative Micro Volume Elements* (RMVEs). **(2.)** The peripheral-bone- $\mu\text{CT}$ -model is discretized into cube-shaped elements (of edge length  $\sim 100\mu\text{m}$ ), the volumes of which are  $\approx 19$  orders of magnitude smaller than the average volume of an osteon. These elements are the *grains*. From these assumptions,  $\sim 216$  grains fit into an RMVE. **(3.)** Each CT-RMVE is filled up with  $\sim 216$   $\mu\text{CT}$ -grains whose spatially-local average of the HU numerical value is similar. Thus, mechanical properties from the peripheral-bone- $\mu\text{CT}$ -model are incorporated into the hip-bone-CT-model. Each CT-RMVE turns into a cube of periodically-arranged  $\mu\text{CT}$ -grains. This approach to microscale cortical bone modeling is similar to the approach consolidated to polycrystalline materials (Benedetti; Aliabadi, 2015; Galvis

*et al.*, 2018b; Galvis *et al.*, 2018a), where the RMVE is an arrangement of smaller homogeneous grains.

This methodology, however, does not randomly attributes material properties as done by (Benedetti; Aliabadi, 2015; Sfantos; Aliabadi, 2007b; Galvis *et al.*, 2018b; Galvis *et al.*, 2018a), but instead, relies on the HU numerical values from the  $\mu$ CT to provide realistic patient-specific microscale material properties.

Figura 5.1 displays an overview of the multiscale approach presented here:

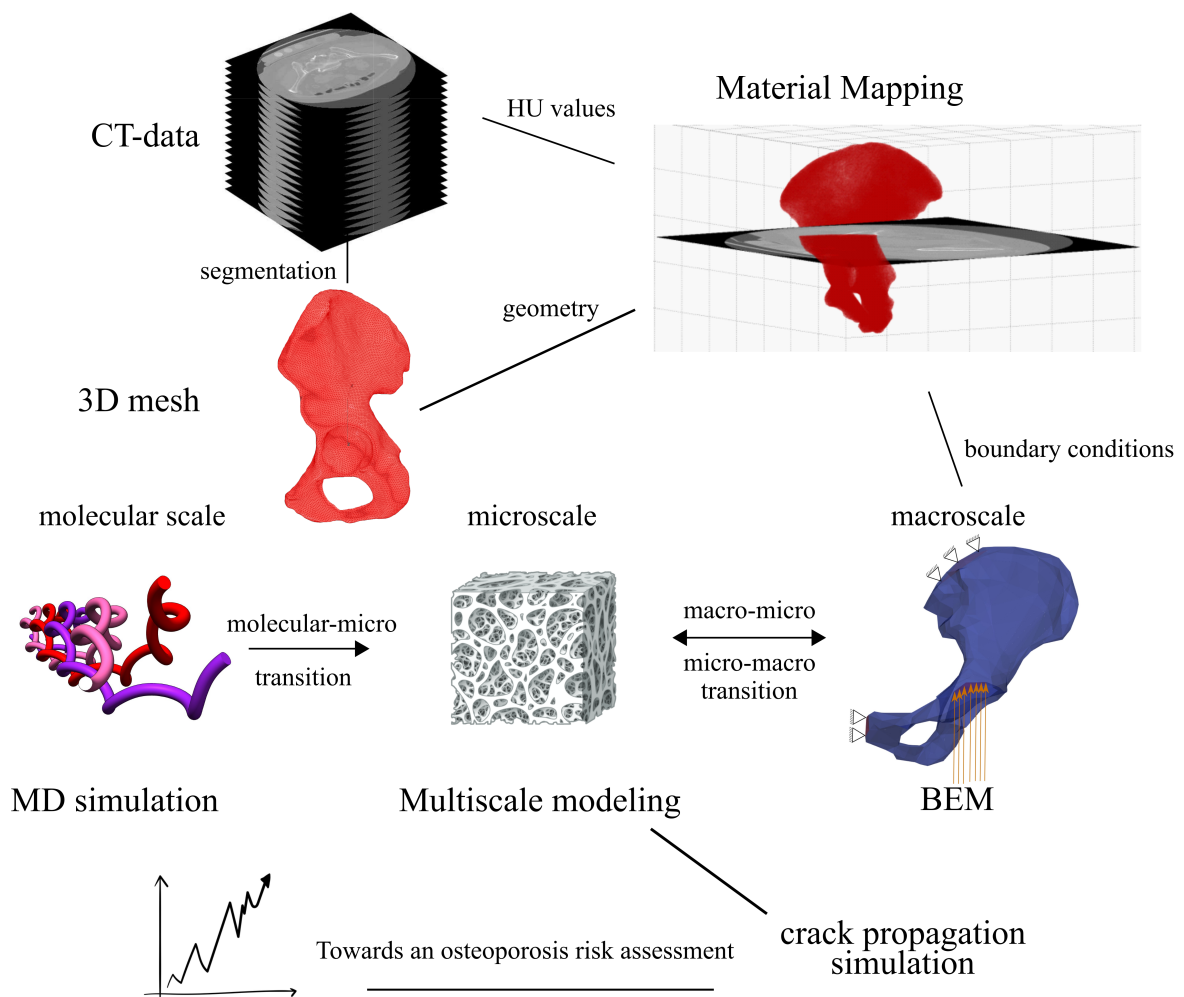


Figure 5.1 – Overview of our multiscale approach (The representation of the microscale was created with BioRender.com).

CT data provides the macroscale-**bone** geometry. Only a *Region of Interest (ROI)* of the cortical bone is used for in-domain traction-displacement computations (see Step II). The selected ROI is subdivided into several cube-shaped *Representative Micro Volume Elements*

(**RMVEs**). Each RMVE is filled up with  $\mu$ CT-**grains**. Between two *Grain Boundaries* (**GBs**) there is a *Cohesive Zone Volume Element* (**CZVE**) (see Step VII). Each CZVE is orders of magnitude greater than the *Representative Atomistic Volume Element* (**RAVE**) (see Step VI).

**Step III needs:** Displacement and traction values of prescribed points throughout the spatial **macro** domain (ROI) geometry.

**Step III provides:** Patient-specific spatial RMVE geometry and material properties.

#### 5.1.4 Step IV – Determining micro domain BCs

The transitioning from the macro- to the microscale is attained when the macro displacements and traction fields are transferred as suitable boundary conditions to each prescribed RMVE boundary (Benedetti; Aliabadi, 2015; Ostoja-Starzewski, 2006; NGUYEN *et al.*, 2011; †; Padbidri, 2005; Joseph *et al.*, 2017).

The nodes of the 3D mesh generated in Step I (C.) are used for the creation of cube-shaped RMVEs. To each  $n$ -th prescribed point in the macro domain (ROI) interior, a macro traction  $\mathbf{t}$  and a displacement  $\mathbf{u}$  vector (computed in Step II) is associated. The macro strain tensor  $[\epsilon]_{3 \times 3}$  is evaluated from vector  $\mathbf{u}$  (see Step II) to be then interpolated as a boundary condition imposed on the external boundary  $\Gamma_\mu = \partial\Omega_\mu$  (cube surface) of the cube-shaped RMVE  $\Omega_\mu$ . The macro stress tensor  $[\mathbf{T}]_{3 \times 3}$  is not directly calculated from  $\epsilon_{3 \times 3}$  at the current Step IV, but calculated at Step VIII.

Three classes of BCs, from several possible, are selected for further analysis:

| Class of BC          | (1.) PBC   | (2.) MKBC  | (3.) TBC                      |
|----------------------|--|--|-------------------------------|
| Bibliographical Ref. | (Benedetti; Aliabadi, 2015; NGUYEN <i>et al.</i> , 2011) | (†; Padbidri, 2005; NGUYEN <i>et al.</i> , 2011) | (Joseph <i>et al.</i> , 2017) |

(1.) Periodic Boundary Conditions (PBCs) are the most used BCs for spatial macro-micro transitioning. As an upside, they provide the fastest convergence of the macro physical and mechanical properties. As a downside, the fact that they restrict the deformation to obey the micro-structure periodicity frame imposes unphysical deformation constraints over localization zones (*ie.*, regions of relative extremely high deformation gradient where micro-cracks occur). (2.) Minimal Kinematic Boundary Conditions (MKBCs) ensure effective deformation shear strain but overestimate the amount of localization zones near the domain boundary. (3.) Tesselation Boundary Conditions (TBCs) maintain the point-to-point conditions imposed by PBCs, but shifting the periodicity frame to correspond to the developing localization zone. For bio-

materials (eg., bone) TBCs have been proved to give the least-error estimation of macroscopic stresses and strains (Joseph *et al.*, 2017). Thus the main priority at this step is to implement TBCs throughout all micro domains (RMVEs).

**Step IV needs:** Patient-specific spatial RMVE geometry and material properties.

**Step IV provides:** RMVE-length-scaled BCs.

### 5.1.5 Step V – Transitioning from the micro to the molecular scale: Modeling the bone cracking process

The micro domain BCs provided by Step IV drive the micro domain material to rupture, initiating the cracking process. The cracking process is described by a Cohesive Zone Model (CZM), which is governed by a Traction-Separation Law (TSL).

Linear Elastic Fracture Mechanics (LEFM) is the classical cracking process mathematical model. A CZM approach, based on considering fracture separation occurring at an extended zone ahead of the crack tip (also called “cohesive zone”), was proposed by (Barenblatt, 1962; Dugdale, 1960). Despite bone being modeled as an anisotropic linear elastic continuum at the microscale, two reasons make the CZM superior to LEFM for bone crack analysis: (1.) Bone fracture experimental data analysis performed by (Cox; Yang, 2007) demonstrated the need of a nonlinear model considering a spatial stress distribution at the fracture zone. (2.) Unlike with LEFM, the CZM can remove stress singularities ahead of the crack tip; *ie.*, ahead of the furthest extent of damage (Taesun You, Yong-Rak Kim and Taehyo Park, 2016).

The CZM considers a narrow region where the local opening displacement  $\delta$  vanishes into the undamaged material. In this region, two opposite sides are subjected to resistive cohesive force pairs  $t$  parallel to the crack local opening displacement, as shown in Figure 5.2(a). Interactions at the molecular scale, considered at Step IV, originate these cohesive traction force pairs.

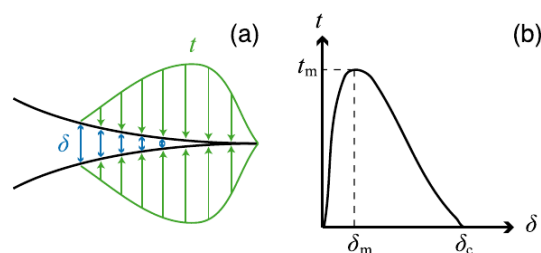


Figure 5.2 – (a) Representation of a cohesive zone; (b) Typical representation of a TSL. Reprinted from (Guin *et al.*, 2016), with the permission of AIP Publishing.

The TSL describes the distribution of resistive force pairs  $t$  along the cohesive zone. Figura 5.2(b) depicts a typical TSL, which relates the displacement vector  $\delta$  to the traction force vector  $t$  along the cohesive zone. From Figura 5.2(b), observe that the displacement grows with increasing traction force up to a maximum traction force value  $t_m$  and maximum separation displacement  $\delta_m$ . When  $t_m$  is reached, fracture is irreversible. The crack opening displacement  $\delta$  continues to grow with decreasing traction force  $t$  value. When the traction force  $t$  goes to zero, the local crack is fully open, and the crack opening displacement reaches the critical value  $\delta_c$ . The bilinear TSL proposed by (Geubelle; Baylor, 1998) is defined by three parameters: the peak traction  $t_m$ , the corresponding separation  $\delta_m$  for the ascending part, and the critical separation  $\delta_c$  at which the traction goes to zero for the decreasing part. Extending the relationship between the traction vector  $\mathbf{t} = [t_n \ t_{t_1} \ t_{t_2}]^\top$  and the displacement jump vector  $\delta = [\delta_n \ \delta_{t_1} \ \delta_{t_2}]^\top$  to the 3D case using (Ural; Mischinski, 2013; M.; A., 1999; Park; Paulino, 2013):

$$\begin{aligned} t_n &= \frac{s}{1-s} \tilde{\delta}_n t_{n,\max} & t_{t_1} &= \frac{s}{1-s} \tilde{\delta}_{t_1} t_{t_1,\max} & t_{t_2} &= \frac{s}{1-s} \tilde{\delta}_{t_2} t_{t_2,\max} \\ \tilde{\delta}_n &= \frac{\delta_n}{\delta_{nc}} = \frac{\delta_n t_{n,\max} s_{\text{initial}}}{2G_{Ic}} & \tilde{\delta}_{t_1} &= \frac{\delta_{t_1}}{\delta_{t_1c}} = \frac{\delta_{t_1} t_{t_1,\max} s_{\text{initial}}}{2G_{IIc}} & \tilde{\delta}_{t_2} &= \frac{\delta_{t_2}}{\delta_{t_2c}} = \frac{\delta_{t_2} t_{t_2,\max} s_{\text{initial}}}{2G_{IIIc}} \end{aligned} \quad (5.3)$$

where  $s = \min \left( s_{\min}, \max \left( 0, 1 - \|\tilde{\delta}\|_2 \right) \right)$  with  $\|\tilde{\delta}\|_2$  being the 2-norm of the non-dimensionalized displacement jump vector  $\tilde{\delta} = [\tilde{\delta}_n \ \tilde{\delta}_{t_1} \ \tilde{\delta}_{t_2}]^\top$ ;  $\delta_{nc,t_1c,t_2c} = 2G_{Ic,IIc,IIIc} (t_{(n,t_1,t_2),\max} s_{\text{initial}})^{-1}$  the critical displacement discontinuities, in which  $a$  represents one of the directions  $n$ ,  $t_1$  or  $t_2$  and  $G_{ac}$  being  $G_{Ic}$ ,  $G_{IIc}$  or  $G_{IIIc}$ , which are, respectively, the critical energy release rates of fracture modes I, II and III;  $s_{\min}$  and  $s_{\text{initial}}$  are, respectively, the minimum and the initial values of the so-called ‘‘internal residual strength variable’’  $s = 1 - \|\tilde{\delta}\|_2$ ;  $t_{n,\max}$  is the critical value of the tensile cohesive stress;  $t_{t_1,\max}$  is the critical value of the shear cohesive stress at direction  $t_1$ , which is perpendicular to direction  $t_2$ . The parameters of the TSL are extracted from MD simulations, described at Step VI. Bilinear approximations provide a continuous function for the traction-displacement relationship from the discrete traction-displacement values obtained at Step VII.

**Step V needs:** Micro domain BCs provided by Step IV and the TSL provided by Steps VI and VII.

**Step V provides:** Bilinear approximations to TSL at the molecular and macro length scales.

### 5.1.6 Step VI – Computing the TSL through an MD approach

At the molecular scale, bone tissue is composed of three components: water, an organic phase and an inorganic phase. *Water* ( $H_2O$ ) represents approximately 10% of total bone mass. The organic phase represents 30% of total bone mass and is constituted of *type I CoLLa-Gen* (90%) (*CLG*) and a combination of other collagen types (III and VI) plus noncollagenous proteins (10%). The inorganic phase of bone is a ceramic crystalline-type mineral referred to as *hydroxyapatite* (*HA*):  $Ca_{10}(PO_4)_6(OH)_2$  (Keaveny *et al.*, 2003) and represents 60% of total bone mass.

The herein proposed MD approach assumes bone tissue to be constituted of  $H_2O$ , *HA* and *CLG* at specific percentages for healthy and osteoporotic bone;  $H_2O$ , *CLG* and *HA* percentages are used to create a molecular scale spatial domain using a Monte Carlo (Nair *et al.*, 2013) approach.

The MD approach, as proposed by (Plimpton, 1995), consists in solving Newton's equation of motion at the atomic level of a material whose spatial domain contains  $i$  atoms interacting with their  $n$  closest neighbours;  $t$  refers to time:

$$m_i \frac{d^2 \mathbf{r}_i(t)}{dt^2} = \sum_{j_1=1}^n \mathbf{F}_2(\mathbf{r}_i(t), \mathbf{r}_{j_1}(t)) + \sum_{j_1=1}^n \sum_{j_2=1}^n \mathbf{F}_3(\mathbf{r}_i(t), \mathbf{r}_{j_1}(t), \mathbf{r}_{j_2}(t)) + \dots + \sum_{j_1=1}^n \dots \sum_{j_n=1}^n \mathbf{F}_n(\mathbf{r}_i(t), \mathbf{r}_{j_1}(t), \dots, \mathbf{r}_{j_n}(t)) \quad (5.4)$$

where, for each  $i$ -th atom:  $\mathbf{r}_i$  is the position vector;  $m_i$  is the mass,  $\mathbf{F}_2$  is a force vector function describing pairwise atomic interactions up to  $\mathbf{F}_n$ , which describes  $n$ -atom interactions. Each  $\mathbf{F}_n$  is the time-derivative of an energy function considering  $n$ -body and quantum interactions; the  $i$ -th atom's energy is a function of the  $i$ -th atom's position  $\mathbf{r}_i(t)$  and of its  $n$  neighbors' positions  $\mathbf{r}_{j_1}(t), \dots, \mathbf{r}_{j_n}(t)$ .

For each molecule in each **inter**- and **intra**-molecular interaction there is a specific energy function whose expressions are found in the literature and in so called force fields (Brooks *et al.*, 1983; Best *et al.*, 2012; Huang *et al.*, 2017; MacKerell *et al.*, 1998; MacKerell *et al.*, 2004; Heinz *et al.*, 2013).

The inputs of MD simulation are the atoms initial positions  $\mathbf{r}(0)$  and velocities  $\dot{\mathbf{r}}(0)$  and the set of force field parameters. The outputs of MD simulations are the position  $\mathbf{r}_i(t)$  and velocity  $\dot{\mathbf{r}}_i(t)$  of every  $i$ -th atom in the molecular spatial domain at each time step. The accuracy of MD simulation results depends strongly on the interatomic (also inter- and intra-molecular) potential's validity. Therefore, force field parameters must be selected according

to their accuracy in modeling bone mechanics at the molecular scale (Almora-Barrios; Leeuw, 2012; Zhou *et al.*, 2017). Interatomic force function vectors  $\mathbf{f}^{ab}(t) = \mathbf{F}_2(t)$  are implicit to the molecular potentials provided by the force field.

The atomic stress tensor  $S_{ij}^a$  for each  $a$ -th atom are computed based on the Virial Theorem (Guin *et al.*, 2016):

$$S_{ij}^a(t) = -\frac{1}{\Omega^a} \left( m^a \dot{r}_i^a(t) \dot{r}_j^a(t) + \frac{1}{2} \sum_{b=1}^{B(a)} r_i^{ab}(t) f_j^{ab}(t) \right) \quad \sigma_{ij}^k(t) = \frac{1}{N_\tau \Omega^k} \sum_{t=1}^{N_\tau} \sum_{a=1}^{A^k(a)} \Omega^a S_{ij}^a(t) \quad (5.5)$$

where  $i = 1, 2, 3$  and  $j = 1, 2, 3$  are the Cartesian directions,  $m^a$  denotes the  $a$ -th mass atom and  $\dot{\mathbf{r}}^a(t)$  its velocity vector;  $\Omega^a$  is the volume of  $a$ -th atom;  $\mathbf{r}^{ab}(t) = \mathbf{r}^a(t) - \mathbf{r}^b(t)$  is the displacement vector between atom  $a$  and atom  $b$ ;  $f_j^{ab}(t)$  is the interatomic force exerted on atom  $a$  by atom  $b$  in the  $j$ -th direction;  $B(a)$  is the number of neighboring atoms  $b_1, \dots, b_{B(a)}$  that interact with atom  $a$ ;  $\sigma_{ij}^k(t)$  is an space-time averaged 3D stress tensor associated to the  $k$ -th Representative Atomistic Volume Element (RAVE), a cuboid whose volume  $\Omega^k$  is orders of magnitude greater than  $\Omega^a$ ;  $N_\tau$  is the number of time steps  $t$  in the interval  $\tau$  over which the time-average is calculated and  $A^k(a)$  is the number of atoms  $a$  contained in the  $k$ -th RAVE.

MD simulation is conducted using the LAMMPS (Plimpton, 1995) software package in order to provide the TSL for Step VII (Yamakov *et al.*, 2006; Guin *et al.*, 2016). Following steps must be done for the calculation of a RAVE-length-scaled TSL from MD: **(1.)** To obtain a RAVE-length-scaled value corresponding to the normal traction  $t_n$  of Step V, a numerical tension test on the RAVE must be performed. For this purpose, a positive traction force proportional to  $\dot{r}_i(t)$  is applied to the atoms lying on two opposite RAVE-faces; **(2.)** The motion of the atoms on these two opposite RAVE-faces in the  $i$ -th direction imply the motion of neighbor-atoms due to the interatomic forces, triggering a chain of RAVE-wide atomic motion governed by Equação 5.4; **(3.)** At each simulation time instant, associated values of  $S_{ii}^a(t)$ ,  $\sigma_{ii}^k(t)$  (Equação 5.5) and of the RAVE elongation  $\delta$  (see Step V) in the  $i$ -th direction are obtained; **(4.)** Thus, for each  $\delta$  a  $\sigma_{ii}^k(t)$  is associated, where  $\sigma_{ii}^k(t)$  corresponds to a RAVE-length-scaled  $t_n$  (Equação 5.3). Consecutive calculations of the RAVE-length-scaled  $t_n$  by incrementing  $\delta$  provides the RAVE-length-scaled TSL in the normal direction. Similarly, by applying a shear force proportional to  $\dot{r}_i(t)$ , correspondent RAVE-length-scaled TSL's are computed for  $t_{i1}$  and  $t_{i2}$ .

**Step VI needs:** Inter-molecular potentials for *HA*, *CLG* and *H<sub>2</sub>O* and their associated possible interactions.

**Step VI provides:** RAVE-length-scaled TSLs.

### 5.1.7 Step VII – Transitioning from the molecular to the microscale

Re-capping Step III, the microscale spatial domain is a periodic structure composed of RMVE's. The results from MD simulations provide RAVE-length-scaled normal and tangential TSLs. The current Step VII provides an averaged continuum Grain Boundary (GB) length-scaled TSL (distinct from the RAVE-length-scaled TSL provided at Step VI) accounting for all pairwise grain interface interactions occurring inside every RMVE.

When the sequence of microdomain-scale quasi-static simulations starts, before cracks are nucleated inside each RMVE, a two-layered surface of 3D rectangular volume elements called “Cohesive Zone Volume Elements” (CZVEs) is defined to cover the geometric locus formed by the union of all GB interfaces inside the RMVE.

Cracks start nucleating when the RVME BCs impose a hydrostatic load capable of disrupting the cohesive forces at one or more GBs (Glaessgen *et al.*, 2006). RMVE BCs are interpolated at Step IV from the  $n$  prescribed points' tractions and displacements computed at Step II.

Each CZVE along a GB interface displays individualized behavior, depending on its own structural irregularities at the atomic level. The relationships between the GB-length-scaled and the RAVE-length-scaled TSL's are:

$$\begin{aligned} t_n(\delta_i) &= \frac{1}{(2m+1)} \sum_{j=-m}^m \sigma_{yy}^k(\delta_{i+j}); \\ t_{t1}(\delta_i) &= \frac{1}{(2m+1)} \sum_{j=-m}^m \sigma_{yx}^k(\delta_{i+j}); \\ t_{t2}(\delta_i) &= \frac{1}{(2m+1)} \sum_{j=-m}^m \sigma_{yz}^k(\delta_{i+j}); \end{aligned} \quad (5.6)$$

where  $\sigma_{yz}^k(\delta_{i+j})$  are the stresses acting along direction  $z$  on the plane perpendicular to direction  $y$  associated to the  $k$ -th RAVE-length-scaled TSL and located at the CZVE whose opening displacement is  $\delta_{i+j}$ ;  $\mathbf{t} = [t_n \ t_{t1} \ t_{t2}]^T$  is the traction vector associated to the GB-length-scaled TSL (see Equação 5.3 at Step V); each GB-length-scale comes from a RAVE-length-scale TSL averaged over  $m$  CZVE's before and  $m$  CZVE's after the  $i$ -th CZVE along one GB interface;  $\delta_i$  is the opening displacement at the  $i$ -th CZVE along one GB interface.

A sequence of CZVE de-cohesion states leads to the formation of a dominant microcrack (Yamakov *et al.*, 2006).

As the simulation time progresses, the increasing boundary strains applied to the RMVE dictate the location at which a dominant crack begins to form based on the minimal energy release rate required for separation at the cohesive zone. When boundary strains applied to the RMVE reach a critical value, the local coalescence of GB openings form a dominant micro-crack that cuts through an entire RMVE (Glaessgen *et al.*, 2006). With further increasing boundary strain values applied to the RMVE, a succession of neighboring failed RMVE's will characterize fracture at the macro-scale at the next Step VIII.

An option to creating CZVEs is to convert the RMVE-length-scale TSL into BCs at all grain interfaces. These BCs fulfill the same role as the CZVE.

**Step VII needs:** RAVE-length-scaled TSL and BCs.

**Step VII provides:** RMVE-length-scale fracture.

#### 5.1.8 Step VIII – Transitioning from the micro- to the macroscale

The micro-macro transition is done when micro displacement and traction vectors are averaged to macro displacement and traction vectors through homogenization averaging theorems (Benedetti; Aliabadi, 2015; Ostoja-Starzewski, 2006; NGUYEN *et al.*, 2011).

The macro stress  $\mathbf{T}$  and strain  $\epsilon$  tensors of a point  $\mathbf{x} \in \Omega_\mu$ , localized inside the RMVE, at any instant  $t$  are defined as the volume average of the micro stress  $\mathbf{T}^\mu$  and strain  $\epsilon^\mu$  tensors at the same point  $\mathbf{x}$  at any instant  $t$ , respectively (Benedetti; Aliabadi, 2015; NGUYEN *et al.*, 2011):

$$\begin{aligned} T_{ij}(\mathbf{x}, t) &= \langle T_{ij}^\mu(\mathbf{x}, t) \rangle = \frac{1}{|\Omega_\mu|} \int_{\Omega_\mu} T_{ij}^\mu(\mathbf{x}, t) d\Omega_\mu \\ \epsilon_{ij}(\mathbf{x}, t) &= \langle \epsilon_{ij}^\mu(\mathbf{x}, t) \rangle = \frac{1}{|\Omega_\mu|} \int_{\Omega_\mu} \epsilon_{ij}^\mu(\mathbf{x}, t) d\Omega_\mu \end{aligned} \quad (5.7)$$

where  $|\Omega_\mu|$  denotes the absolute value of the micro domain volume;  $i, j = 1, 2, 3$ .

After interpolating the macro strain tensor  $\epsilon_n = [\epsilon_{ij}(\mathbf{x}, t)]_n$  at the  $n$ -th prescribed point as suitable boundary conditions to the RMVE boundary at Step IV, and proceeding all the way to Step VII, Equação 5.7 is used at the current Step VIII to evaluate the homogenized macro stresses  $T_{ij}(\mathbf{x}, t)$  that, for a generic RMVE, fulfill the relationship (Benedetti; Aliabadi, 2015):

$$T_{ij}(\mathbf{x}, t) = T_{ij}^{el}(\mathbf{x}, t) - T_{ij}^D(\mathbf{x}, t) \quad (5.8)$$

where  $\mathbf{T}^{el}$  is the elastic stress tensor that corresponds to the macro strain tensor  $\epsilon_n$  in the case of *absence of damage* at the microscale, *i.e.* in case the RMVE remains in pristine condition;

$\mathbf{T}^{el}$  can be computed by either averaging the micro stresses  $T_{ij}^{\mu}$  in the pristine RMVE at each macroscale time instant or by using the relationship  $T_{ij}^{el} = C_{ijkl}\epsilon_{lk}$ , where  $C_{ijkl} \in \mathbb{R}^{3 \times 3 \times 3 \times 3}$  is the macro stiffness tensor evaluated for the RMVE vertexes at Step II;  $\mathbf{T}^D$  is the decremental macro stress calculated as  $T_{ij}^D = D_{ij}T_{ij}^{el}$ , no summation is implied, and  $0 \leq D_{ij} \leq 1$  is the macro-damage coefficient.  $D_{ij} = 0, \forall i, j$ , implies a pristine RMVE, and the absence of micro-damage;  $D_{ij} = 1$  implies a completely fractured RMVE, and entails the introduction of a macroscale-crack, accomplished with the removal of the failed RMVE. As the simulation time progresses, these removed RMVEs coalesce into a macro-length-scale (ROI-length-scale) fracture.

**Step VIII needs:** RMVE-length-scale fracture.

**Step VIII provides:** ROI-length-scale fracture.

#### 5.1.9 Step IX – Towards an osteoporosis diagnosis

Bone porosity increases the strain energy concentration, implying that osteoporotic bone requires less energy to fracture when compared to normal bone, assuming both must support equal loading conditions (Osterhoff *et al.*, 2016; Rachner *et al.*, 2011; Reber *et al.*, 2018).

The proposed methodology does not intend to create a new osteoporosis risk assessment tool from scratch, but instead, to give already existent osteoporosis risk assessment tools (Black *et al.*, 2001; Kanis, 2002; Reber *et al.*, 2018) its contribution by adding diagnostic quantitative information based on multiscale continuum mechanics. Current osteoporosis risk assessment tools are fundamentally based on qualitative medical variables (*e.g.*, sex, age, weight, patient's case history (Black *et al.*, 2001; Kanis, 2002; Reber *et al.*, 2018)). Adding, from CT-data-based computer models, patient-specific quantitative fracture mechanics-based variables to these tools is crucial to the improvement of current fracture risk assessment, being the next step towards an improved fracture-predictive diagnosis.

**Step IX needs:** A simulation-based prediction of the ROI-length-scale fracture.

**Step IX provides:** A correlation between simulation results and fracture predictive diagnosis.

#### Concluding remarks

There are three main items that highlight the importance of this work, which are:

(1.) Linking CT and  $\mu$ CT data in order to devise bone models with patient-specific macro geom-

etry, microstructure and material properties; (2.) Deriving bone fracture information from the atomic and molecular structures; (3.) Adding quantitative fracture mechanics-based variables into an osteoporosis risk analysis.

The execution of these items together with the connection among Steps I through to IX constitute the main contribution and novelty of this research approach. Its outcomes may increase the sensibility of current bone fracture risk assessments. They play a relevant role in the public health context.

## 5.2 Future Directions

It is important to mention that the methodology present in Section 5.1 was suggested during the first years of my graduate studies. Since then, we identified minor flaws and better ways of doing some of the steps. The modeling of the nanoscale itself was much more laborious than we expected. Also, deriving a TSL from MD simulations may be a common practice for simple crystal structures, but is much more complex (if doable) for biomolecules like mineralized collagen fibrils. The implementation of this methodology, especially finding possibilities to transition from the nano- to the microscale, is now one of my future research goals.

Some of other steps of this approach have been started and partially developed. During my Bachelor degree, I have worked on material mapping for patient-specific macroscopic models (Alcantara, 2017). Furthermore, open source softwares like Bonemat allow a readily implementation of step I (Zannoni *et al.*, 1999; Taddei *et al.*, 2004; Taddei *et al.*, 2007; Schileo *et al.*, 2020).

Methodologies for steps II, V, VII and VIII have been, in a parallel context and in a different approach, explored by former lab colleagues that I met at the beginning of my graduate studies. They developed BESLE (Boundary Element Software for 3D Linear Elasticity), a parallel open-source code to analyse the mechanical behaviour of heterogeneous materials using the BEM in 3D and in both an elastostatic and elastodynamic settings (Galvis *et al.*, 2021). They also developed BEM models capable of propagating cracks using the CZM and presented a methodology, based on homogenisation, for predicting the anisotropic stiffness tensor of bone given the porosity and mineral fraction (Galvis *et al.*, 2018b; Galvis *et al.*, 2018a; Galvis *et al.*, 2021; Prada *et al.*, 2018; Prada *et al.*, 2022). They used the BEM to model micro- and macroscales and transition between them in an upscaling manner. I got involved in one of the initial steps of this project (Prada *et al.*, 2018) before focusing on all-atom molecular models.

## 6 OTHER WORKS I HAVE BEEN INVOLVED WITH DURING MY PHD

During my PhD, I was able to participate and get involved in other projects, especially with the skills and knowledge gained modeling bone at the nanoscale. I describe a few of them below.

### 6.1 3D Boundary Element Meshing for Multiscale Bone Anisotropic Analysis

“In this work, a multi-scale BEM mesh model of bone tissue ranging from the nanoscale to the mesoscale is sought. A new nanoscale design which considers the hydroxyapatite crystals inside, and outside the fibrils is developed. Furthermore, the fibrils are modelled with reported elliptical cross sections. Additionally, a procedure to develop the BEM meshes using multimedia software is proposed, based upon the similarities between them. Finally, several meshes were created using triangular continuous elements(Prada *et al.*, 2018).”

This work was part of Daniel Prada’s Master, an later PhD, thesis.

I highlight here that before focusing on the all-atom models for MD simulations, I worked on the modeling of bone at the macroscale using the boundary element method.

### 6.2 Coarse-Grain Modeling of Polymer Hydrogels

“Reversible crosslinkers can enable several desirable mechanical properties, such as improved toughness and self-healing, when incorporated in polymer networks for bioengineering and structural applications. In this work, we performed coarse-grained molecular dynamics to investigate the effect of the energy landscape of reversible crosslinkers on the dynamic mechanical properties of crosslinked polymer network hydrogels.(Khare *et al.*, 2024)”

In this work, I had my first contact with coarse-grain modeling, which is a simplified version of MD simulations that allow the modeling of larger systems . This is important for my future endeavors with multiscale modeling.

This work was part of Eesha Khare’s PhD thesis. Eesha is a dear friend, whom I had the pleasure to work with while at MIT.

### 6.3 Mechanical Properties of Plant Cell Walls

Plant cell walls (PCWs) is a biocomposite constituted usually of cellulose, hemicellulose, lignin and water. It is responsible for the structural integrity of many plants and trees, and gives wood its superior mechanical properties. We investigated the mechanical behavior of PCWs at the nanoscale by performing MD simulations that resemble tensile and compression tests, similar to those described in Chapters 3 and 4 for bones.

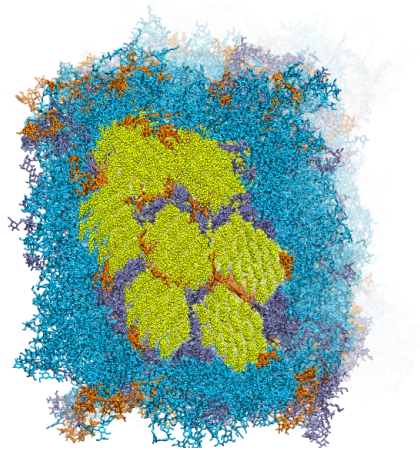


Figure 6.1 – Schematic visualization of the plant cell wall molecular model.

This work is part of Lucas N. Trentin's PhD thesis, one of Prof. Skaf's PhD students.

## BIBLIOGRAPHY

- Alcantara, A. C. S. Implementierung verschiedener Algorithmen zur automatisierten Berechnung und Zuweisung von Materialgesetzen von CT-Daten auf FE-Netze. **Bachelor thesis - Hochschule Merseburg**, 2017, <<http://dx.doi.org/10.25673/6272>>.
- Alcântara, A. C. S.; Assis, I.; Prada, D.; Mehle, K.; Schwan, S.; Costa-Paiva, L.; Skaf, M. S.; Wrobel, L. C.; Sollero, P. Patient-Specific Bone Multiscale Modelling, Fracture Simulation and Risk Analysis—A Survey. **Materials**, v. 13, 2020.
- Alcântara, A. C. S.; Felix, L. C.; Galvão, D. S.; Sollero, P.; Skaf, M. S. Devising bone molecular models at the nanoscale: From usual mineralized collagen fibrils to the first bone fibers including hydroxyapatite in the extra-fibrillar volume. **Materials**, v. 15, p. 2274, 2022.
- Alcântara, A. C. S. de; Felix, L. C.; Galvão, D. S.; Sollero, P.; Skaf, M. S. The role of the extrafibrillar volume on the mechanical properties of molecular models of mineralized bone microfibrils. **ACS Biomaterials Science & Engineering**, v. 9, n. 1, p. 230–245, 2023, PMID: 36484626.
- Aliabadi, M. Boundary element formulations in fracture mechanics. **Applied Mechanics Reviews**, v. 50, p. 83–96, 1997.
- Aliabadi, M. **The boundary element method. Volume 2, Applications in solids and structures**. [S.l.]: Wiley, 2002.
- Alijani, H.; Vaughan, T. J. A multiscale finite element investigation on the role of intra- and extra-fibrillar mineralisation on the elastic properties of bone tissue. **J Mech Behav Biomed**, v. 129, p. 105139, 2022.
- Almora-Barrios, N.; De Leeuw, N. H. Molecular dynamics simulation of the early stages of nucleation of hydroxyapatite at a collagen template. **Crystal Growth & Design**, v. 12, n. 2, p. 756–763, 2012.
- Amorim, P.; Moraes, T.; Silva, J.; Pedrini, H. Invesalio: An interactive rendering framework for health care support. In: Bebis, G.; Boyle, R.; Parvin, B.; Koracin, D.; Pavlidis, I.; Feris, R.; McGraw, T.; Elendt, M.; Kopper, R.; Ragan, E.; Ye, Z.; Weber, G. (Ed.). **Advances in Visual Computing**. Cham: Springer International Publishing, 2015. p. 45–54. ISBN 978-3-319-27857-5.
- Barenblatt, G. The mathematical theory of equilibrium cracks in brittle fracture. In: Dryden, H.; Kármán, T. von; Kuerti, G.; Dungen, F. van den; Howarth, L. (Ed.). Elsevier, 1962, (Advances in Applied Mechanics, v. 7). p. 55 – 129. Disponível em: <<http://www.sciencedirect.com/science/article/pii/S0065215608701212>>.
- Benedetti, I.; Aliabadi, M. Multiscale modeling of polycrystalline materials: A boundary element approach to material degradation and fracture. **Computer Methods in Applied Mechanics and Engineering**, v. 289, p. 429 – 453, 2015.
- Best, R. B.; Zhu, X.; Shim, J.; Lopes, P. E. M.; Mittal, J.; Feig, M.; MacKerell, A. D. Optimization of the additive charmm all-atom protein force field targeting improved sampling

of the backbone  $\phi$ ,  $\psi$  and side-chain  $\chi_1$  and  $\chi_2$  dihedral angles. **Journal of Chemical Theory and Computation**, v. 8, n. 9, p. 3257–3273, 2012, PMID: 23341755.

Black, D.; Steinbuch, M.; Palermo, L.; Dargent-Molina, P.; Lindsay, R.; Hoseyni, M.; Johnell, O. An assessment tool for predicting fracture risk in postmenopausal women. **Osteoporosis International**, v. 12, n. 7, p. 519–528, 2001.

Brebbia, C. **Boundary element methods in engineering**. [S.l.]: Springer New York, NY, USA:, 1982.

Brebbia, C. A.; Dominguez, J. **Boundary elements: an introductory course**. [S.l.]: WIT press, 1994.

Brooks, B. R.; Bruccoleri, R. E.; Olafson, B. D.; States, D. J.; Swaminathan, S.; Karplus, M. Charmm: A program for macromolecular energy, minimization, and dynamics calculations. **Journal of Computational Chemistry**, v. 4, n. 2, p. 187–217, 1983.

Burghardt, A. J.; Link, T. M.; Majumdar, S. High-resolution computed tomography for clinical imaging of bone microarchitecture. **Clinical Orthopaedics and Related Research**, 2011.

Cox, B. N.; Yang, Q. Cohesive zone models of localization and fracture in bone. **Engineering Fracture Mechanics**, v. 74, n. 7, p. 1079 – 1092, 2007.

Cruse, T. A. **Boundary element analysis in computational fracture mechanics**. [S.l.]: Springer Science & Business Media, 2012. v. 1.

DICOM: Digital Imaging and Communications in Medicine. <http://dicom.nema.org/>. 2015. Disponível em: <<http://dicom.nema.org/>>.

Dugdale, D. Yielding of steel sheets containing slits. **Journal of the Mechanics and Physics of Solids**, v. 8, n. 2, p. 100 – 104, 1960.

F. A. Sabet, A. R. Najafi, E. Hamed and I. Jasiuk. Modelling of bone fracture and strength at different length scales: a review. **Interface Focus**, 2016.

Fielder, M.; Nair, A. K. Effects of hydration and mineralization on the deformation mechanisms of collagen fibrils in bone at the nanoscale. **Biomechanics and Modeling in Mechanobiology**, v. 18, n. 1, p. 57–68, 2019, PMID: 33998387.

Fielder, M.; Nair, A. K. A computational study of mechanical properties of collagen-based bio-composites. **International Biomechanics**, v. 7, n. 1, p. 76–87, 2020, PMID: 33998387.

Galvis, A. F.; Prada, D. M.; Moura, L. S.; Zavaglia, C.; Foster, J. M.; Sollero, P.; Wrobel, L. C. Besle: Boundary element software for 3d linear elasticity. **Computer Physics Communications**, v. 265, p. 108009, 2021.

Galvis, A. F.; Rodríguez, R. Q.; Sollero, P. Analysis of three-dimensional hexagonal and cubic polycrystals. using the boundary element method. **Mech Mater.**, v. 117, p. 58 – 72, 2018.

Galvis, A. F.; Rodríguez, R. Q.; Sollero, P. Dynamic analysis of three-dimensional polycrystalline materials using the boundary element method. **Comput Struct.**, v. 200, p. 11 – 20, 2018.

Gamez, B.; Divo, E.; Kassab, A.; Cerrolaza, M. Evaluation of fatigue crack growing in cortical bone using the bem. **International Journal of Healthcare Technology and Management**, v. 11, n. 3, p. 202–221, 2010.

Geubelle, P. H.; Baylor, J. S. Impact-induced delamination of composites: a 2d simulation. **Composites Part B: Engineering**, v. 29, n. 5, p. 589 – 602, 1998.

Glaessgen, E.; Saether, E.; Phillips, D.; Yamakov, V. Multiscale modeling of grain-boundary fracture: Cohesive zone models parameterized from atomistic simulations. **47th AIAA/ASME/ASCE/AHS/ASC Structures, Structural Dynamics, and Materials Conference**, 2006.

Guin, L.; Raphanel, J. L.; Kysar, J. W. Atomistically derived cohesive zone model of intergranular fracture in polycrystalline graphene. **Journal of Applied Physics**, v. 119, n. 24, p. 245107, 2016.

Heinz, H.; Lin, T.-J.; Kishore Mishra, R.; Emami, F. S. Thermodynamically consistent force fields for the assembly of inorganic, organic, and biological nanostructures: The interface force field. **Langmuir**, v. 29, n. 6, p. 1754–1765, 2013, PMID: 23276161.

Holzer, G.; Skrbensky, G. von; Holzer, L. A.; Pichl, W. Hip fractures and the contribution of cortical versus trabecular bone to femoral neck strength. **Journal of Bone and Mineral Research**, v. 24, n. 3, p. 468–474, 2009.

Huang, J.; Rauscher, S.; Nawrocki, G.; Ran, T.; Feig, M.; Groot, B. L. de; Grubmüller, H.; MacKerell, A. D. Charmm36m: an improved force field for folded and intrinsically disordered proteins. **Nature Methods**, v. 14, n. 1, p. 71–73, 2017.

Joseph, G.; Jörg, B.; Volker, U. On boundary conditions for homogenization of volume elements undergoing localization. **International Journal for Numerical Methods in Engineering**, v. 113, n. 1, p. 1–21, 2017.

Kane, J. H. **Boundary Element Analysis in Engineering Continuum Mechanics**. [S.l.]: Prentice Hall, 1994.

Kanis, J. A. Diagnosis of osteoporosis and assessment of fracture risk. **THE LANCET**, v. 359, p. 1929–2936, 2002.

Keaveny, T. M.; Morgan, E. F.; Yeh, O. C. Standard handbook of biomedical engineering and design. In: \_\_\_\_\_. [S.l.]: New York: McGraw-Hill, 2003. cap. Bone Mechanics.

Khare, E.; Alcântara, A. C. S. de; Lee, N.; Skaf, M. S.; Buehler, M. J. Crosslinker energy landscape effects on dynamic mechanical properties of ideal polymer hydrogels. **Mater. Adv.**, p. –, 2024.

Lai, W. M.; Rubin, D.; Krempl, E. **Introduction to Continuum Mechanics**. 4. ed. Boston: Butterworth-Heinemann, 2010. ISBN 978-0-7506-8560-3.

Landis, E. N.; Keane, D. T. X-ray microtomography. **Elsevier**, 2010.

Michael Lewiecki, E.; Wright, N. C.; Curtis, J. R.; Siris, E.; Gagel, R. F.; Saag, K. G.; Singer, A. J.; Steven, P. M.; Adler, R. A. Hip fracture trends in the united states, 2002 to 2015. **Osteoporosis International**, v. 29, n. 3, p. 717–722, Mar 2018.

Lin, L.; Samuel, J.; Zeng, X.; Wang, X. Contribution of extrafibrillar matrix to the mechanical behavior of bone using a novel cohesive finite element model. **J Mech Behav Biomed Mater**, v. 65, p. 224–235, 2017.

Liu, Y.; Li, Y.; Xie, W. Modeling of multiple crack propagation in 2-d elastic solids by the fast multipole boundary element method. **Engineering Fracture Mechanics**, v. 172, p. 1–16, 2017.

M., O.; A., P. Finite-deformation irreversible cohesive elements for three-dimensional crack-propagation analysis. **International Journal for Numerical Methods in Engineering**, v. 44, n. 9, p. 1267–1282, 1999.

MacKerell, A. D.; Bashford, D.; Bellott, M.; Dunbrack, R. L.; Evanseck, J. D.; Field, M. J.; Fischer, S.; Gao, J.; Guo, H.; Ha, S.; Joseph-McCarthy, D.; Kuchnir, L.; Kuczera, K.; Lau, F. T. K.; Mattos, C.; Michnick, S.; Ngo, T.; Nguyen, D. T.; Prodhom, B.; Reiher, W. E.; Roux, B.; Schlenkrich, M.; Smith, J. C.; Stote, R.; Straub, J.; Watanabe, M.; Wiórkiewicz-Kuczera, J.; Yin, D.; Karplus, M. All-atom empirical potential for molecular modeling and dynamics studies of proteins. **The Journal of Physical Chemistry B**, v. 102, n. 18, p. 3586–3616, 1998, pMID: 24889800.

MacKerell, A. D.; Feig, M.; Brooks, C. L. Improved treatment of the protein backbone in empirical force fields. **Journal of the American Chemical Society**, v. 126, n. 3, p. 698–699, 2004, pMID: 14733527.

Marinho, B. C. G. A.; Guerra, L. P.; Drummond, J. B.; Silva, B. C.; Soares, M. M. S. The burden of osteoporosis in Brazil. **Arquivos Brasileiros de Endocrinologia & Metabologia**, v. 58, p. 434 – 443, 07 2014.

Morales-Torres, J.; Gutiérrez-Ureña, S. The burden of osteoporosis in Latin America. **Osteoporosis International**, v. 15, n. 8, p. 625–632, Aug 2004.

Nair, A. K.; Gautieri, A.; Chang, S.-W.; Buehler, M. J. Molecular mechanics of mineralized collagen fibrils in bone. **Nat Commun.**, v. 4, p. 1724, 2013.

NGUYEN, V. P.; STROEVEN, M.; SLUYS, L. J. Multiscale continuous and discontinuous modeling of heterogeneous materials: A review on recent developments. **Journal of Multiscale Modelling**, v. 03, n. 04, p. 229–270, 2011.

Osterhoff, G.; Morgan, E. F.; Shefelbine, S. J.; Karim, L.; McNamara, L. M.; Augat, P. Bone mechanical properties and changes with osteoporosis. **Injury**, v. 47, p. S11–S20, 2016.

Ostoja-Starzewski, M. Material spatial randomness: From statistical to representative volume element. **Probabilistic Engineering Mechanics**, v. 21, n. 2, p. 112 – 132, 2006.

Park, K.; Paulino, G. H. Cohesive zone models: A critical review of traction-separation relationships across fracture surfaces. **Applied Mechanics Reviews**, 2013.

Plimpton, S. Fast parallel algorithms for short-range molecular dynamics. **Journal of Computational Physics**, v. 117, n. 1, p. 1–19, 1995.

Prada, D. M.; Galvis, A. F.; Alcântara, A. C. S.; Sollero, P. 3d boundary element meshing for multiscale bone anisotropic analysis. **European Journal of Comput Mech.**, v. 27, n. 5-6, p. 425–442, 2018.

- Prada, D. M.; Galvis, A. F.; Miller, J.; Foster, J. M.; Zavaglia, C. Multiscale stiffness characterisation of both healthy and osteoporotic bone tissue using subject-specific data. **J Mech Behav Biomed Mater**, v. 135, p. 105431, 2022.
- Rachner, T. D.; Khosla, S.; Hofbauer, L. C. Osteoporosis: now and the future. **The Lancet**, v. 377, n. 9773, p. 1276–1287, 2011.
- Reber, K. C.; König, H.-H.; Becker, C.; Rapp, K.; Büchele, G.; Mächler, S.; Lindlbauer, I. Development of a risk assessment tool for osteoporotic fracture prevention: A claims data approach. **Bone**, v. 110, p. 170 – 176, 2018.
- R. O. Ritchie, M. J. B.; Hansma, P. Plasticity and toughness in bone. **Physics Today**, 2009.
- Schileo, E.; Pitocchi, J.; Falcinelli, C.; Taddei, F. Cortical bone mapping improves finite element strain prediction accuracy at the proximal femur. **Bone**, v. 136, p. 115348, 2020.
- Sfantos, G.; Aliabadi, M. Multi-scale boundary element modelling of material degradation and fracture. **Computer Methods in Applied Mechanics and Engineering**, v. 196, n. 7, p. 1310–1329, 2007.
- Sfantos, G. K.; Aliabadi, M. H. A boundary cohesive grain element formulation for modelling intergranular microfracture in polycrystalline brittle materials. **International Journal for Numerical Methods in Engineering**, v. 69, n. 8, p. 1590–1626, 2007.
- Taddei, F.; Pancanti, A.; Viceconti, M. An improved method for the automatic mapping of computed tomography numbers onto finite element models. **Med Eng Phys.**, v. 26, n. 1, p. 61 – 69, 2004, <[https://doi.org/10.1016/S1350-4533\(03\)00138-3](https://doi.org/10.1016/S1350-4533(03)00138-3)>.
- Taddei, F.; Schileo, E.; Helgason, B.; Cristofolini, L.; Viceconti, M. The material mapping strategy influences the accuracy of ct-based finite element models of bones: An evaluation against experimental measurements. **Med Eng Phys.**, v. 29, n. 9, p. 973 – 979, 2007, <<https://doi.org/10.1016/j.medengphy.2006.10.014>>.
- Taesun You, Yong-Rak Kim and Taehyo Park. Two-way coupled multiscale model for predicting mechanical behavior of bone subjected to viscoelastic deformation and fracture damage. **Journal of Engineering Materials and Technology**, 2016.
- Tan, C.; Shiah, Y.; Wang, C. Boundary element elastic stress analysis of 3d generally anisotropic solids using fundamental solutions based on fourier series. **Int J Solids Struct.**, v. 50, n. 16, p. 2701 – 2711, 2013, <<https://doi.org/10.1016/j.ijsolstr.2013.04.026>>.
- Thompson, A. P.; Aktulga, H. M.; Berger, R.; Bolintineanu, D. S.; Brown, W. M.; Crozier, P. S.; Veld, P. J. in 't; Kohlmeyer, A.; Moore, S. G.; Nguyen, T. D.; Shan, R.; Stevens, M. J.; Tranchida, J.; Trott, C.; Plimpton, S. J. LAMMPS - a flexible simulation tool for particle-based materials modeling at the atomic, meso, and continuum scales. **Comp. Phys. Comm.**, v. 271, p. 108171, 2022.
- Ural, A.; Mischinski, S. Multiscale modeling of bone fracture using cohesive finite elements. **Engineering Fracture Mechanics**, v. 103, p. 141 – 152, 2013.
- Yamakov, V.; Saether, E.; Phillips, D.; Glaessgen, E. Molecular-dynamics simulation-based cohesive zone representation of intergranular fracture processes in aluminum. **Journal of the Mechanics and Physics of Solids**, v. 54, n. 9, p. 1899–1928, 2006.

Zannoni, C.; Mantovani, R.; Viceconti, M. Material properties assignment to finite element models of bone structures: a new method. **Med Eng Phys.**, v. 20, n. 10, p. 735 – 740, 1999, <[https://doi.org/10.1016/S1350-4533\(98\)00081-2](https://doi.org/10.1016/S1350-4533(98)00081-2)>.

Zhou, Z.; Qian, D.; Minary-Jolandan, M. Clustering of hydroxyapatite on a super-twisted collagen microfibril under mechanical tension. **J. Mater. Chem. B**, v. 5, p. 2235–2244, 2017.

†, S. D. M.; Padbidri, J. Minimal kinematic boundary conditions for simulations of disordered microstructures. **Philosophical Magazine**, v. 85, n. 1, p. 65–78, 2005.